



**HAL**  
open science

# Role of HSPA5 and the unfolded protein Response in Group 3 Medulloblastoma

Liliana Mirabal Ortega

► **To cite this version:**

Liliana Mirabal Ortega. Role of HSPA5 and the unfolded protein Response in Group 3 Medulloblastoma. Cancer. Université Paris Cité, 2023. English. NNT : 2023UNIP5210 . tel-04819197

**HAL Id: tel-04819197**

**<https://theses.hal.science/tel-04819197v1>**

Submitted on 4 Dec 2024

**HAL** is a multi-disciplinary open access archive for the deposit and dissemination of scientific research documents, whether they are published or not. The documents may come from teaching and research institutions in France or abroad, or from public or private research centers.

L'archive ouverte pluridisciplinaire **HAL**, est destinée au dépôt et à la diffusion de documents scientifiques de niveau recherche, publiés ou non, émanant des établissements d'enseignement et de recherche français ou étrangers, des laboratoires publics ou privés.

Université Paris Cité

École doctorale Hématologie, Oncogénèse et Biothérapies (ED 561)  
Signalisation, Radiobiologie et Cancer (UMR 3347 / U 1021)

# Role of HSPA5 and the Unfolded Protein Response in Group 3 Medulloblastoma

Par **Liliana MIRABAL ORTEGA**

Thèse de doctorat d'Oncogénèse

Dirigée par **Celio POUPONNOT**

Présentée et soutenue **publiquement**

le 20 Décembre 2023

Devant un jury composé de :

**Fredrik SWARTLING**, Associate Professor, Uppsala University, SWEDEN,  
Rapporteur

**Agnès DELAUNAY-MOISAN**, DR, Université Paris-Saclay, Rapporteur

**Eric CHEVET**, DR, Université Rennes 1, Examineur

**Servane TAUSZIG-DELAMASURE**, DR, Université Claude Bernard Lyon 1,  
Examineur

**Michaela FONTENAY**, PUPH, Université Paris Cité, Examineur

**Celio POUPONNOT**, DR, Institut Curie/CNRS, Directeur de thèse



## RESUME SUBSTANTIEL

---

Le médulloblastome (MB) est une tumeur embryonnaire provenant du cervelet. Il représente la tumeur cérébrale maligne la plus courante de l'enfance. Le MB est une maladie hétérogène et quatre groupes moléculaires ont été identifiés : WNT, SHH, Groupe 3 (G3) et Groupe 4 (G4). Ces groupes diffèrent en termes de caractéristiques moléculaires et cliniques. La survie globale (SG) des patients est d'environ 70 à 80 %, mais le pronostic varie en fonction du groupe moléculaire, des variants histopathologiques et des caractéristiques cliniques, notamment l'âge, la présence de métastases et l'étendue de la résection tumorale. Il est important de noter que les traitements causent de graves effets secondaires. Le G3 est le groupe le plus agressif avec le taux métastatique le plus élevé (40 à 50 %) et la SG à 5 ans la plus faible (<60 %). Malgré des recherches intensives, aucun « driver » commun n'a été identifié pour les tumeurs de G3 en dehors de la surexpression de MYC, MYC étant amplifié chez 15 à 20 % des patients de G3. Conformément à la surexpression de MYC, ces tumeurs présentent des signatures transcriptomiques et protéomiques liées au processing, à la transcription et à la traduction de l'ARNm. Les tumeurs qui présentent une amplification ou une amplification du gène c-MYC ont un pronostic particulièrement sombre. Malgré ces connaissances et l'orientation des recherches sur le G3 MB, la biologie de ce groupe reste mal comprise.

HSPA5, également connue sous le nom de GRP78 (Glucose- Related Protein 78) ou BiP (Immunoglobulin heavy chain Binding Protein), est une chaperonne du réticulum endoplasmique (RE). HSPA5 est aussi le régulateur principal de l'UPR (Unfolded protein Response), un mécanisme important qui permet aux cellules de faire face au stress du RE dû à l'accumulation de protéines mal repliées. Dans des conditions physiologiques normales, HSPA5 est liée aux trois effecteurs de l'UPR empêchant leur activation : ATF6 (Activating Transcription Factor 6), PERK (PRKR-like ER kinase) et IRE1 $\alpha$  (Inositol-requiring protein 1 $\alpha$ ). Dans des conditions de stress du RE, la chaperonne se dissocie de ces effecteurs permettant leur activation avec l'initiation de la voie de signalisation en aval.

IRE1 $\alpha$  est une protéine kinase transmembranaire dotée d'une activité endoribonucléase. L'activation d'IRE1 $\alpha$  dans des conditions de stress de l'ER conduit

au clivage d'un intron de 26 nucléotides de l'ARNm de la protéine de liaison X-box 1 (XBP1), produisant la forme épissée du facteur de transcription sXBP1. sXBP1 joue un rôle clé dans l'UPR en contrôlant l'expression de gènes impliqués dans le repliement des protéines, la sécrétion, la dégradation associée au réticulum endoplasmique (ERAD) et la synthèse des lipides. L'activité endoribonucléase de IRE1 $\alpha$  est également impliquée dans le clivage et la dégradation de certains ARNm et/ou microARN, un processus connu sous le nom de Regulated IRE1-Dependent Decay (RIDD). Pour son activation, ATF6 $\alpha$  est exporté du RE vers le complexe de Golgi où il est clivé par les protéases S1P et S2P. Le facteur de transcription actif ATF6 $\alpha$  régule des programmes transcriptionnels spécifiques impliqués dans le contrôle de la qualité des protéines et ERAD comme HERPUD1. ATF6 $\alpha$  est également responsable de l'induction transcriptionnelle de la plupart des chaperons du RE, y compris HSPA5. L'activation de PERK entraîne la phosphorylation de la sous-unité 1 du facteur d'initiation de la traduction eucaryote 2 (P-eIF2 $\alpha$ /EIF2S1), entraînant une atténuation transitoire de la synthèse protéique globale mais cette phosphorylation d'eIF2 $\alpha$  conduit également à la traduction d'ARNm spécifiques, dont le facteur de transcription ATF4, qui à son tour induira l'expression de CHOP (CAAT/enhancer-binding protéine (C/EBP)/ GADD153). ATF4 et CHOP contrôlent l'expression de gènes impliqués dans le repliement des protéines, les réponses antioxydantes, l'autophagie et le métabolisme des acides aminés.

L'UPR est considérée comme un mécanisme cytoprotecteur lorsque son activation conduit à la résolution du stress du RE. Cependant, lorsque la réponse est intense et trop soutenue, elle devient cytotoxique en induisant la mort cellulaire. L'induction du facteur de transcription pro-apoptotique CHOP en aval de PERK/P-eIF2 $\alpha$ /ATF4 est l'une des principales voies impliquées dans l'apoptose induite par l'UPR. CHOP peut induire l'expression des protéines BH3-only de la famille BCL-2 et réguler négativement l'expression de la protéine anti-apoptotique Bcl-2. Il a également été proposé qu'ATF4/CHOP puisse induire la mort cellulaire en augmentant la synthèse protéique, ce qui entraîne un stress oxydatif mortel et une déplétion en ATP.

De nombreux types de cancer possèdent des niveaux de stress basaux du RE qui peuvent résulter de facteurs intrinsèques ou extrinsèques et dépendent de l'activation de l'UPR pour survivre et continuer à croître. Cette caractéristique spécifique des cellules cancéreuses ouvre une fenêtre thérapeutique pour manipuler

l'activation de l'UPR. Ceci a été réalisé soit en inhibant les voies de signalisation en aval de l'UPR favorables à la survie, soit en favorisant la mort cellulaire suite à une suractivation de l'UPR. Par exemple, HA15, un inhibiteur de HSPA5, induit un très fort niveau de mort cellulaire dans les cellules de mélanome, mais pas dans les cellules normales, en induisant une réponse UPR forte et soutenue. Dans cette étude, grâce à un criblage par siARN conduisant à l'identification de HSPA5 en tant que vulnérabilité dans G3 MB, nous avons étudié le rôle de l'UPR dans G3 MB.

Pour identifier de nouvelles vulnérabilités dans le MB de G3, nous avons effectué un criblage ciblé par siRNA dans une lignée cellulaire de G3. Nous avons évalué l'effet du knock-down (KD) de différents gènes sélectionnés sur la viabilité de la lignée cellulaire G3 HD-MB03, conduisant à l'identification de HSPA5 comme un potentiel hit. Nous avons validé la sensibilité des cellules du G3 à l'inhibition de HSPA5 en utilisant le HA15, une drogue qui inhibe spécifiquement la chaperonne. Le traitement des cellules avec le HA15 diminue fortement la viabilité des cellules du G3 alors que des cellules n'appartenant pas au G3 (non-G3) ou normales ne répondent presque pas à cette drogue. Nous avons réalisé le KD de l'expression de HSPA5 par shRNA dans deux lignées cellulaires de G3. Le KD de HSPA5 induit une forte diminution de la viabilité des cellules D458Med liée à une apoptose importante. Nous avons greffé orthotopiquement les cellules D458Med-Luc transduites avec différents shRNA dans le cervelet de souris nues. Le KD de HSPA5 retarde la croissance tumorale et augmente la survie chez les souris greffées avec des cellules HSPA5-KD. Des résultats similaires ont été obtenus avec des cellules D425-Luc et deux modèles de xénogreffes dérivées de patients de G3 (PDX-3 et PDX-7). Ces résultats indiquent que HSPA5 est une vulnérabilité potentielle pour le G3.

Une analyse RNASeq nous a permis de montrer que les gènes dérégulés participent principalement aux réponses au stress du RE et de l'UPR, avec l'activation des trois bras de l'UPR. Nous avons constaté un fort enrichissement de la signature des gènes de l'UPR dans les cellules KD par rapport au contrôle. De même, nous avons constaté que les signatures géniques d'activation de chaque bras, à savoir PERK, IRE1 $\alpha$  et ATF6 $\alpha$ , étaient également enrichies dans les cellules KD. Nous avons également vérifié l'activation des 3 bras par Western Blot. Le KD de HSPA5 induit fortement l'expression de cibles de chaque bras, à savoir HERPUD1 (bras ATF6) et la forme épissée de XBP1 (bras IRE1a). Dans le cas du bras PERK, nous avons examiné

le niveau de phosphorylation de eIF2 $\alpha$  par rapport au eIF2 $\alpha$  total comme première mesure de l'activation de la voie. Nous avons également examiné l'induction d'ATF4/CHOP comme confirmation de l'activation de ce bras, ce qui est également le cas après HSPA5 KD. Ces résultats indiquent que l'inhibition de HSPA5 induit les trois bras de l'UPR dans les cellules G3, couplés à l'induction de la mort cellulaire.

Pour confirmer la sensibilité globale des cellules de G3 à l'activation de l'UPR à plus grande échelle, nous avons effectué un criblage avec des composés connus pour induire ou inhiber le stress RE et l'UPR. Nous avons constaté que les lignées cellulaires de G3 sont plus sensibles à l'induction de l'activation de l'UPR que les lignées cellulaires de non-G3, alors qu'aucune différence n'a été observée entre les deux groupes avec des composés qui inhibent l'UPR. Ces résultats ont montré que les cellules G3 sont plus sensibles à la mort cellulaire médiée par l'UPR.

Pour déterminer quel bras de l'UPR est responsable de l'induction de la mort cellulaire dans les cellules HSPA5 KD G3, nous avons inhibé chaque bras individuellement en utilisant des inhibiteurs spécifiques. Nous avons constaté que l'inhibition des bras IRE1 $\alpha$  (MKC8806) et ATF6 $\alpha$  (Ceapin-A7) n'avait aucun effet sur la mort cellulaire. Au contraire, l'inhibition de PERK par le GSK2606414 a prévenu la mort cellulaire dans les cellules HSPA5 KD. Nous avons étudié si le KD d'ATF4 ou CHOP pouvait sauver (« rescuer ») la mort cellulaire, car il a été démontré qu'ils étaient impliqués dans l'apoptose médiée par l'UPR. Étonnamment, ni le KD d'ATF4 ni de CHOP n'étaient suffisants pour empêcher l'induction de la mort cellulaire dans les cellules HSPA5 KD.

Pour déterminer si l'inhibition de eIF2 $\alpha$  par le bras PERK pourrait prévenir l'effet de HSPA5 KD, nous avons traité les cellules avec l'ISRIB. L'ISRIB est une petite molécule qui permet aux cellules de contourner l'inhibition de eIF2 $\alpha$  par phosphorylation et de rétablir la synthèse protéique. Le traitement par ISRIB des cellules HSPA5 KD a partiellement prévenu la mort cellulaire, indiquant que les cellules de G3 sont sensibles à l'inhibition de eIF2 $\alpha$ . Pour identifier les gènes impliqués dans cette réponse, nous avons effectué une analyse par RNASeq des cellules HSPA5 KD traitées ou non à l'ISRIB. Nous avons identifié 37 gènes différentiellement exprimés régulés négativement dans les cellules shHSPA5 KD traitées avec ISRIB par rapport aux cellules traitées au DMSO. Les gènes dérégulés sont liés au transport des acides aminés, à la biosynthèse et, dans une moindre mesure, à l'homéostasie lipidique ainsi qu'aux voies de réponse au stress du RE. ISRIB n'a induit aucun changement majeur

dans la signature générale de l'UPR, ni de celle des bras ATF6 $\alpha$  ou IRE1 $\alpha$ . En revanche, l'expression des gènes de la signature d'activation de PERK étaient diminués dans les cellules HSPA5 KD traitées avec ISRIB. Ces résultats confirment que la mort cellulaire médiée par HSPA5 KD était liée à l'activation du bras PERK et suggèrent que l'inhibition de eIF2 $\alpha$  est un mécanisme de régulation important dans le G3.

La phosphorylation de eIF2 $\alpha$  semblant être un mécanisme de régulation important dans le G3, nous avons étudié le rôle de ses deux phosphatases : GADD34 (PPP1R15A), qui est induite par le bras PERK comme mécanisme de rétrocontrôle, et la phosphatase eIF2 $\alpha$  constitutive, CReP (PPP1R15B). L'analyse transcriptomique de données publiques obtenues sur 762 MB a montré que l'expression de PPP1R15B était plus élevée dans le G3 que dans les autres groupes et dans le cervelet fœtal normal. Son expression est particulièrement enrichie dans le sous-type G3- $\delta$  qui correspond aux tumeurs amplifiées par MYC de mauvais pronostics. En conséquence, l'expression de PPP1R15B a une valeur pronostique, les patients présentant des niveaux élevés de PPP1R15B affichant un mauvais pronostic.

Nous avons réalisé le KD de PPP1R15B par shRNA et découvert que le KD de PPP1R15B entraînait une diminution importante de la viabilité avec une forte induction d'ATF4 et de CHOP. Il est important de noter que nous avons greffé des cellules D425-Luc KD et contrôle de manière orthotopique chez des souris nues. Nous avons constaté que les tumeurs KD se développent plus lentement que les tumeurs témoins, ce qui entraîne une amélioration de la survie. Des résultats similaires ont été obtenus dans deux PDX de G3 (PDX-3, PDX-7). Dans l'ensemble, ces résultats suggèrent que la phosphorylation de eIF2 $\alpha$  représente un mécanisme de régulation central dans MB de G3.

En conclusion, mes travaux ont montré que les cellules G3 MB sont très sensibles à l'activation de l'UPR et notamment à travers le contrôle de l'activité de eIF2 $\alpha$  par phosphorylation. Cela ouvre une perspective thérapeutique pour le traitement des patients G3 MB.

# RESUME

---

## **Titre : HSPA5 et la réponse au stress du réticulum endoplasmique dans le Médulloblastome de Groupe 3**

Le médulloblastome (MB) est une tumeur embryonnaire du cervelet. C'est la tumeur cérébrale maligne la plus fréquente de l'enfance. Le MB est un cancer hétérogène et quatre groupes moléculaires ont été identifiés : WNT, SHH, Groupe 3 (G3) et Groupe 4 (G4). Ces groupes sont différents en termes de caractéristiques moléculaires et cliniques. Les traitements actuels ont amélioré la survie globale des patients jusqu'à environ 70 à 80 %, mais au prix d'effets secondaires graves. Mon travail porte sur le groupe G3, dont la biologie reste mal comprise et qui présente le pire pronostic, avec des taux élevés de métastases au moment du diagnostic et des rechutes fréquentes. Par conséquent, des thérapies plus ciblées avec moins d'effets secondaires sont nécessaires de toute urgence.

Notre équipe a identifié HSPA5 (Heat Shock Protein 5) comme une vulnérabilité du G3 grâce à un criblage fonctionnel basé sur l'ARNi. HSPA5 est le régulateur principal de la réponse au stress dans le réticulum endoplasmique (Unfolded Protein Response (UPR)). Les principaux objectifs de mon travail de thèse étaient de comprendre pourquoi HSPA5 est essentiel pour la biologie du G3 et en étudiant les mécanismes moléculaires impliqués pour identifier de nouvelles informations sur la vulnérabilité du G3.

Mes travaux ont montré que les cellules de G3 sont très sensibles à l'inhibition de HSPA5 en utilisant le composé HA15 ou des shRNA *in vitro* et *in vivo*. L'extinction de l'expression (knock-down (KD)) de HSPA5 conduit à l'activation des trois branches de l'UPR mais seul le bras PERK de l'UPR est responsable de la mort cellulaire induite suite au KD de HSPA5. La régulation de la phosphorylation de eIF2 $\alpha$  semble être un nœud essentiel pour les cellules de G3 car son maintien, soit par l'activation de kinases, soit par inhibition des phosphatases impliquées dans sa régulation, entraîne une diminution de la croissance des cellules de G3 *in vitro*. J'ai identifié CReP, codé par le gène PPP1R15B, comme une phosphatase essentielle pour le maintien de eIF2 $\alpha$  sous sa forme non phosphorylée dans le G3. Dans ce cadre, le KD de la

phosphatase CReP (PPP1R15B) prolonge la survie des souris greffées par différents modèles de G3 montrant son importance.

En conclusion, mes travaux ont montré que les cellules G3 MB sont très sensibles à l'activation de l'UPR et notamment à travers le contrôle de l'activité de eIF2 $\alpha$  par phosphorylation. Cela ouvre une perspective thérapeutique pour le traitement des patients G3 MB.

**Mots clefs : Médulloblastome, HSPA5, UPR, eIF2alpha, CREP**

## ABSTRACT

---

### **Title : Role of HSPA5 and the Unfolded Protein Response in Group 3 Medulloblastoma**

Medulloblastoma (MB) is an embryonal tumor originating in the cerebellum and the most common malignant brain tumor of childhood. MB is a heterogeneous disease and four molecular groups are identified: WNT, SHH, Group 3 (G3) and Group 4 (G4). These groups are different in terms of molecular and clinical features. Current treatments have improved the overall survival (OS) of patients to ~70-80% but at the cost of severe side effects. My work focuses on G3, which is still poorly understood despite of displaying the worst prognosis, including high rates of metastasis at diagnosis and frequent relapses. Therefore, a more directed therapies with less side effects are urgently needed.

Our team identified the Heat Shock Protein 5 (HSPA5) as a vulnerability in G3 through a targeted functional RNAi screen. HSPA5 is the master regulator of the Unfolded Protein Response (UPR), a mechanism triggered by the cells to cope with stress in endoplasmic reticulum (ER) stress. The main objectives of my PhD work were to investigate the mechanisms by which HSPA5 is a dependency in G3 tumors to provide new insights about G3 vulnerabilities.

My work showed that G3 cells are highly sensitive to the inhibition of HSPA5 using the tool compound HA15 or shRNA *in vitro* and *in vivo*. HSPA5 knock-down (KD) induced the activation of the three branches of the UPR. Interesting, only the PERK arm of UPR is responsible for the cell death induced after UPR activation in HSPA5 KD cells. The regulation of eIF2 $\alpha$  phosphorylation seems to be an essential node for G3 cells, since its induction either through kinases activation or through the inhibition of the phosphatases involved in its regulation, lead to a decrease of G3 cells viability *in vitro*. I showed that this phosphorylation is kept in check in G3 cells by the CReP phosphatase encoded by PPP1R15B. Accordingly, CReP KD improves the survival of mice grafted by different G3 models, showing the key role of this gene in MB growth *in vivo*.

In conclusion, my work showed that G3 MB cells are highly sensitive to UPR activation and especially through the control of eIF2 $\alpha$  phosphorylation. This opens a therapeutic perspective for the treatment of G3 MB patients.

**Keywords : Medulloblastoma, HSPA5, UPR, eIF2alpha, CREP**

## **ACKNOWLEDGEMENTS**

---

This section of the manuscript will be modified before the final version is submitted to the University. However, I would like to thank very much to Pr. Fredrik J. Swartling and Dr. Agnès Delaunay-Moisan for accepting to be part of my jury and especially, to review my thesis manuscript. I'm waiting forward to receive your feedback about the document.



# TABLE OF CONTENTS

---

RESUME SUBSTANTIEL.....	2
RESUME.....	7
ABSTRACT.....	9
ACKNOWLEDGEMENTS.....	11
PREFACE.....	14
ABBREVIATION LIST.....	16
INDEX OF FIGURES AND TABLES.....	18
<b>1 INTRODUCTION.....</b>	<b>19</b>
<b>1. Medulloblastoma.....</b>	<b>19</b>
1.1. Cerebellum.....	20
1.2. Medulloblastoma Recurrence and Metastases.....	23
1.3. Treatment.....	24
1.3.1. Surgery.....	24
1.3.1.1. Risk stratification.....	24
1.4. MB groups.....	27
1.4.1. WNT.....	28
1.4.2. SHH.....	31
1.4.3. Group 4.....	34
1.4.4. Group 3.....	37
1.5. MB subtypes.....	41
1.6. Targeted therapies.....	42
1.7. Structure.....	44
1.8. Cellular localization.....	45
1.9. HSPA5 is an essential gene during development.....	46
1.10. Functions.....	46
1.11. HSPA5 in cancer.....	48
1.11.1. Tumor initiation.....	48
1.11.2. Metastasis.....	48
1.11.3. Resistance to therapy.....	49
<b>3. UPR.....</b>	<b>51</b>
3.1. UPR signaling to resolve ER stress.....	53
3.1.1. PERK arm.....	53
3.1.2. IRE1 $\alpha$ arm.....	54
3.1.3. ATF6 arm.....	55

3.2.	<b>UPR-induced cell death</b>	56
3.3.	<b>UPR in cancer</b>	58
3.3.1.	<b>Oncogenic transformation and proteotoxic stress</b>	59
3.3.2.	<b>Angiogenesis</b>	60
3.3.3.	<b>Hypoxia and oxidative stress</b>	60
3.3.4.	<b>Metabolism</b>	61
3.4.	<b>UPR in MB</b>	63
3.5.	<b>Targeting the UPR</b>	64
3.5.1.	<b>Inhibition of basal UPR activation:</b>	64
3.5.2.	<b>Overactivation of basal UPR activation:</b>	65
2	<b>RESULTS</b>	68
1.1.	<b>Article 1: In preparation</b>	70
3	<b>DISCUSSION</b>	131
1.1.	<b>siRNA-based screen to identify new vulnerabilities in G3 MB</b>	132
1.2.	<b>G3 MB cells require HSPA5 to survive</b>	133
1.3.	<b>G3 cells are sensitive to UPR activation</b>	134
1.4.	<b>PERK activation/ eIF2<math>\alpha</math> phosphorylation are the main mediators of the UPR induced cell death</b>	136
1.5.	<b>G3 cells require hypo-phosphorylated eIF2<math>\alpha</math>: a CReP dependency</b>	140
1.6.	<b>eIF2<math>\alpha</math> phosphorylated status control by MYC?</b>	142
1.7.	<b>General conclusion</b>	143
4	<b>PERSPECTIVES</b>	144
5	<b>BIBLIOGRAPHY</b>	146
6	<b>APPENDICES</b>	168
1.	<b>Appendix 1 Co-author paper 1</b>	169
2.	<b>Appendix 2 Co-author paper 2</b>	183
3.	<b>Appendix 3 First author Book Chapter</b>	204
4.	<b>Appendix 4 Co-author paper 3</b>	226

# PREFACE

---

## Context

Medulloblastoma (MB) is a pediatric tumor of the cerebellum. It represents the most frequent malignant brain tumor in childhood (Ostrom et al., 2021). MB is a heterogeneous disease and four molecular groups are defined: WNT, SHH, Group 3 (G3) and Group 4 (G4) (Cho et al., 2011; Kool et al., 2008; Northcott et al., 2011). These groups are different in terms of molecular and clinical features as it will be further discussed. The overall survival (OS) of patients is around ~70-80%, but the prognosis varies according to the molecular group, histopathological variants and clinical features including age, metastatic disease and extent of tumor resection (Northcott et al., 2019). Besides, survivors suffer from severe side effects that compromise their quality of life. My work focuses on G3, which is the group with the worst prognosis, including high rates of metastasis at diagnosis and frequent relapses. Therefore, a more directed therapies with less side effects are urgently needed.

Our team identified the Heat Shock Protein 5 (HSPA5) as a potential target for G3 through a targeted functional RNAi screen. HSPA5 is the master regulator of the Unfolded Protein Response (UPR), a mechanism triggered by the cells to cope with stress in endoplasmic reticulum (ER).

In recent years, the mechanisms of UPR triggered by ER stress in cancer cells have gained attention from a therapeutic view. When UPR activation is strong, sustained and uncontrolled, instead of being cytoprotective, it leads to cell death through apoptosis and/or autophagy. Hence, strong and sustained activation of UPR beyond a “cytoprotective threshold” could be of therapeutic interest by killing cancer cells.

## Objectives:

Since UPR has been demonstrated to exert a dual role in cancer (1/ protective and protumorigenic when controlled and 2/ antitumorigenic leading to cell death when strongly activated), we hypothesized that G3 MB tumors are sensitive to the an overactivation of UPR through HSPA5 inhibition.

The aim of this project is to investigate:

1. if HSPA5 could be considered as a new dependency for G3 tumors and
2. what are the molecular mechanisms involved in the response to HSPA5 inhibition that can provide new insights about G3 vulnerabilities.

I performed my PhD thesis in the team Signaling and cancer progression, under the supervision of Celio Pouponnot (team leader) at Institute Curie, Orsay (U1021/UMR3347). I started my PhD in October 2018 (career break from June 2022 to March 2023, twin pregnancy). This work has been presented at different meetings and congress (see below). I supervised a Master 2 student and collaborated with different projects inside and outside our team, some of them already published (see Appendices). I also wrote together with other colleagues in the team a chapter about Modeling MB in vivo for the Neuromethods book Brain Tumors.

- 5<sup>th</sup> edition of the React4Kids “Understand to Treat” meeting, Marseille, France. October 2023.
- 16<sup>th</sup> International PhD Student Cancer Conference, Cambridge, UK. Poster presentation. July 2023
- 5<sup>th</sup> CRCL International Cancer Symposium. Lyon, France. Oral communication (presented by Celio Pouponnot since I was in maternity leave). November 2022.
- International school « Development and Cancer » for Master students Paris-Saclay University 1st Prize Poster presentation. Orsay, France. November 2021.
- Endoplasmic Reticulum: Functions in Physiology and Pathology. ITMO BCDE. Paris, France. Poster Prize. October 2021.

## ABBREVIATION LIST

---

<b>BHLHZ</b>	Basic Helix-Loop-Helix-Zipper
<b>BZIP</b>	Basic Leucine Zipper
<b>CNS</b>	Central Nervous System
<b>CSF</b>	Cerebro-Spinal Fluid
<b>CSI</b>	Cranio-Spinal Irradiation
<b>DEG</b>	Differentially Expressed Genes
<b>DPC</b>	Days Post Conception
<b>E</b>	Embryonal day
<b>EGL</b>	External Granule cell Layer
<b>ER</b>	Endoplasmic Reticulum
<b>ERAD</b>	ER-Associated protein Degradation
<b>FBS</b>	Fetal Bovine Serum
<b>GBM</b>	Glioblastoma
<b>GO</b>	Gene Ontology analysis
<b>GTR</b>	Gross Total Resection
<b>HCC</b>	Hepatocellular Carcinoma
<b>IGL</b>	Internal Granule cell Layer
<b>KD</b>	Knock-down/Knock-downed
<b>LRL</b>	Lower Rhombic Lip
<b>MAM</b>	Mitochondria-associated ER Membranes
<b>MB</b>	Medulloblastoma
<b>NBD</b>	Nucleotide-Binding Domain
<b>NTR</b>	Near-Total Resection
<b>ORF</b>	Open Reading Frame
<b>OS</b>	Overall Survival
<b>PC</b>	Purkinje Cells
<b>PCA</b>	Prostate Cancer
<b>PCW</b>	Post-Conceptional Weeks
<b>PDX</b>	Patient Derived Xenograft
<b>RIDD</b>	Regulated IRE1-Dependent Decay of mRNA

<b>RL</b>	Rhombic Lip
<b>SBD</b>	Substrate Binding Domain
<b>STR</b>	Sub-Total Resection
<b>SVZ</b>	Subventricular Zone
<b>TAG</b>	Triacylglycerols
<b>TF</b>	Transcription Factor
<b>TNBC</b>	Triple Negative Breast Cancer
<b>UBC</b>	Unipolar Brush Cells
<b>UORF</b>	Upstream Open Reading Frame
<b>UPR</b>	Unfolded Protein Response
<b>URL</b>	Upper Rhombic Lip
<b>UTR</b>	Untranslated Region
<b>VZ</b>	Ventricular Zone
<b>WHO</b>	World Health Organization

## INDEX OF FIGURES AND TABLES

---

<b>Figure 1</b>	<b>Magnetic resonance imaging (MRI) images of MB and metastasis.....</b>	<b>16</b>
<b>Figure 2</b>	<b>Schematic sagittal sections of the developing cerebellum.....</b>	<b>18</b>
<b>Figure 3</b>	<b>Adult cerebellum.....</b>	<b>19</b>
<b>Figure 4</b>	<b>Dose distribution of radiation.....</b>	<b>22</b>
<b>Figure 5</b>	<b>Histological classification of MB tumors.....</b>	<b>24</b>
<b>Figure 6</b>	<b>Wnt/<math>\beta</math>-catenin signaling pathway.....</b>	<b>26</b>
<b>Figure 7</b>	<b>SHH signaling pathway.....</b>	<b>29</b>
<b>Figure 8</b>	<b>PRDM6 enhancer hijacking.....</b>	<b>32</b>
<b>Figure 9</b>	<b>HSPA5 structure.....</b>	<b>42</b>
<b>Figure 10</b>	<b>Unfolded Protein Response signaling pathways.....</b>	<b>50</b>
<b>Figure 11</b>	<b>UPR-induced cell death.....</b>	<b>55</b>
<b>Table 1</b>	<b>Classification of MB patients according to the metastasis stage.....</b>	<b>20</b>
<b>Table 2</b>	<b>Clinical and molecular characteristics of WNT group.....</b>	<b>27</b>
<b>Table 3</b>	<b>Clinical and molecular characteristics of SHH group.....</b>	<b>30</b>
<b>Table 4</b>	<b>Clinical and molecular characteristics of G4 group .....</b>	<b>33</b>
<b>Table 5</b>	<b>Clinical and molecular characteristics of G3 group.....</b>	<b>37</b>



# 1 INTRODUCTION

---

## 1. Medulloblastoma

Medulloblastoma (MB) is an embryonal tumor originating in the cerebellum (Fig. 1a) with metastasis mainly found in the cerebrospinal axis (Fig. 1b). It is the most common pediatric brain tumor of childhood, representing 25% of all pediatric brain tumors and ~69% of all embryonal tumors in children and adolescents (0-19 years) (Ostrom et al., 2021). MB incidence decrease with age with the highest incidence between 5-9 years: 0.61 per 100,000 population. MB is more common in males than in females (Ostrom et al., 2021). Initially, patients present milder symptoms like headache, nausea and vomiting, fatigue and others. As the disease progresses, more severe and specific symptoms will appear. Essentially, motor skills will be affected with problems to walk, hand writing, ataxia, and vision (Northcott et al., 2019).

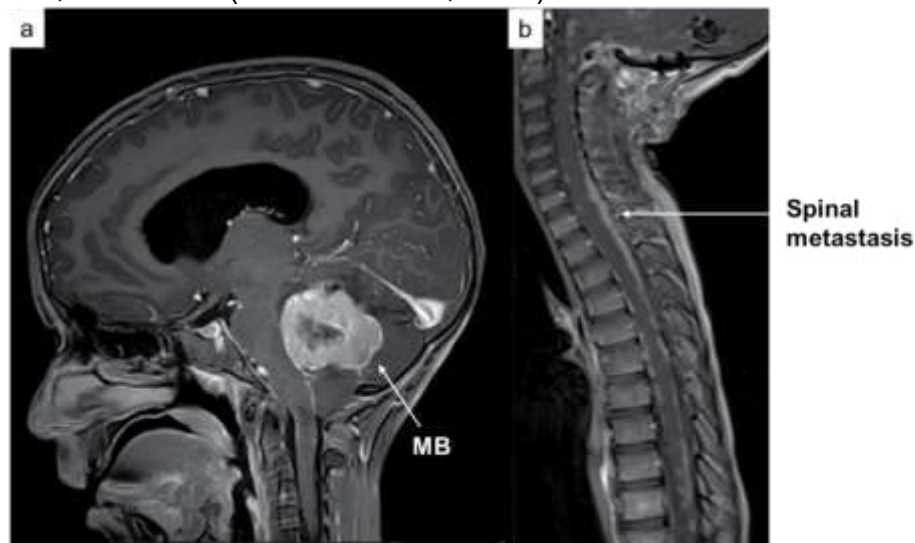


**Figure 1: Magnetic resonance imaging (MRI) images of MB and metastasis:** a. Cranial MRI image of a patient with MB (sagittal plane); b. Spinal MRI of patient with multiple metastatic lesions within the spinal canal (*adapted from Northcott et al., 2019*).

To better understand the biology of these tumors including established and potential cell of origins of the different groups, a brief description of the developing and adult cerebellum will be presented here.

## 1.1. Cerebellum

Cerebellum is a structure derived from the dorsal part of the anterior hindbrain. The adult's cerebellum is the result of a complex pattern of neurogenesis and cell movement during development which is similar between the mouse and the human with some small differences. All the cells that are present in the mature cerebellum are derived from three germinative zones: the ventricular zone (VZ), the rhombic lip (RL) and the external granule cell layer (EGL) (Fig. 3) (Leto et al., 2016). The VZ generates all GABAergic neurons and most glial cells: the Purkinje cells (PCs), neurons of the cerebellar nuclei and different populations of cerebellar interneurons (Golgi, baskets and stellate cells). At early stages of development, the rhombic lip can be subdivided into the upper rhombic lip (URL), corresponding to the rhombomere 1, and the lower rhombic lip (LRL) corresponding to rhombomeres 2-8. The URL (RL for the rest of the text) produces all cerebellar glutamatergic neurons: a subpopulation of neurons of the cerebellar nuclei are generated first, followed by granule cell progenitors (GCPs) of the EGL, which proliferate, differentiate and migrate radially to form the internal granule layer (IGL). The unipolar brush cells (UBC) which are also generated from this zone arrive at last (reviewed in Holgado et al., 2017).

Human cerebellar development is a long process that starts early on after conception (30 days post conception (dpc)) and is complete during the second postnatal year. The cerebellar VZ is split into a VZ and a subventricular zone (SVZ) which is composed mainly of mitotic radial glial-like progenitors that disappears by the end of the embryonic state (56dpc). The human embryonic RL is compartmentalized with a ventricular (RL<sup>VZ</sup>) and subventricular RL (RL<sup>SVZ</sup>) that are molecularly distinct. The RL<sup>VZ</sup> contains mainly SOX2<sup>+</sup> stem cells. The RL<sup>SVZ</sup> contains SOX2<sup>-</sup> proliferative progenitors that will differentiate into TBR2<sup>+</sup> UBC or ATOH1<sup>+</sup> GCPs, that will migrate onto the surface to form the EGL (Haldipur et al., 2020). The EGL is evident from 8 post conceptional weeks (pcw), lying near the PCs which secrete Sonic hedgehog (SHH) to induce proliferation of GCPs. The peak of proliferation of the EGL occurs from 26-32pcw. By 40pcw the EGL is thin but remains present until the end of the first postnatal year (Haldipur et al., 2020).

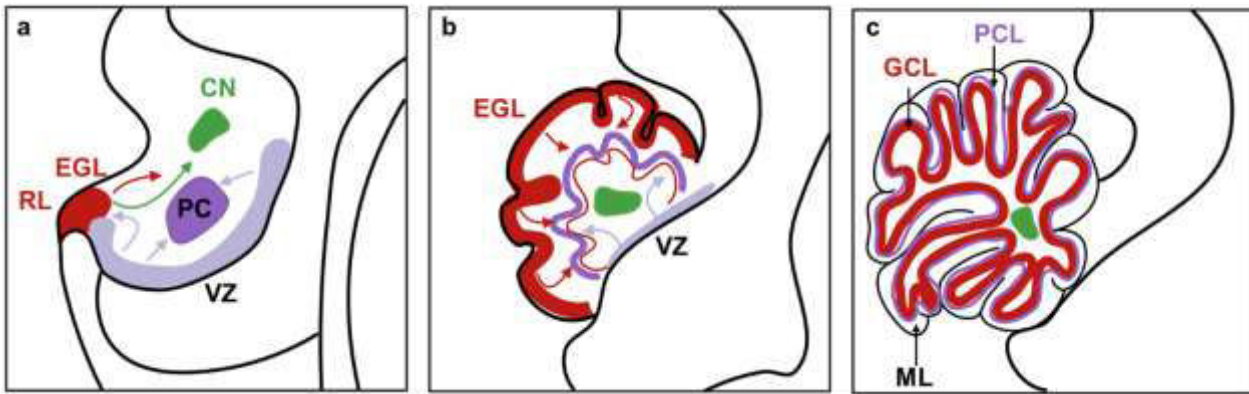


**Figure 2. Schematic sagittal sections of the developing cerebellum:** a. three germinative zones give rise to all cells of the mature cerebellum: neural stem cells in the ventricular zone (VZ, in light purple) give rise to GABAergic neurons including Purkinje cells (PC, in purple); the rhombic lip (RL, in red) produces granule cell progenitors (GCPs) that will form the external granular layer (EGL, in red) and neurons that will form the cerebellar nuclei (CN, in green); b. later in development, GCPs in the EGL stop proliferating and migrate radially to give birth to granule neurons forming the internal granule layer; c. the mature cerebellum is laminated composed of different layers: the molecular layer (ML, white space), the Purkinje cell layer (PCL, in purple) and the granule cell layer (GCL, in red) (adapted from *Holgado et al., 2017; Marzban et al., 2015*).

Mouse cerebellar development is already complete by postnatal day 15 (P15). The mouse VZ does not contain a SVZ. Contrary to the human RL, mouse RL is small, does not have structural compartmentalization and disappears at birth (e19/postnatal (P) day 0). The EGL is evident by embryonal day 12.5 (E12.5) with the peak of proliferation occurring at P6-8, induced by SHH which is secreted by the PCs.

The adult cerebellum is a foliated structure divided into two cerebellar hemispheres connected by the vermis. It is organized into the cerebellar cortex and the cerebellar nuclei (CN) (Fig.4). The cerebellar cortex is laminated, composed of three layers: 1. the molecular layer (ML) containing stellate and basket cells; 2. The Purkinje cell layer (PCL) containing Purkinje cells and candelabrum cells and 3. the granular cell layer (GCL) containing cerebellar granule neurons, which represents the most abundant neuron type; the GCL also contains Golgi cells, UBC and Lugaro cells. The cerebellar nuclei are mainly composed of projection neurons. Neurons in the cerebellum can be classified as inhibitory or GABAergic: PCs, basket, stellate, Golgi and Lugaro cells and excitatory or Glutamatergic: granule cells, UBCs and excitatory projection neurons.

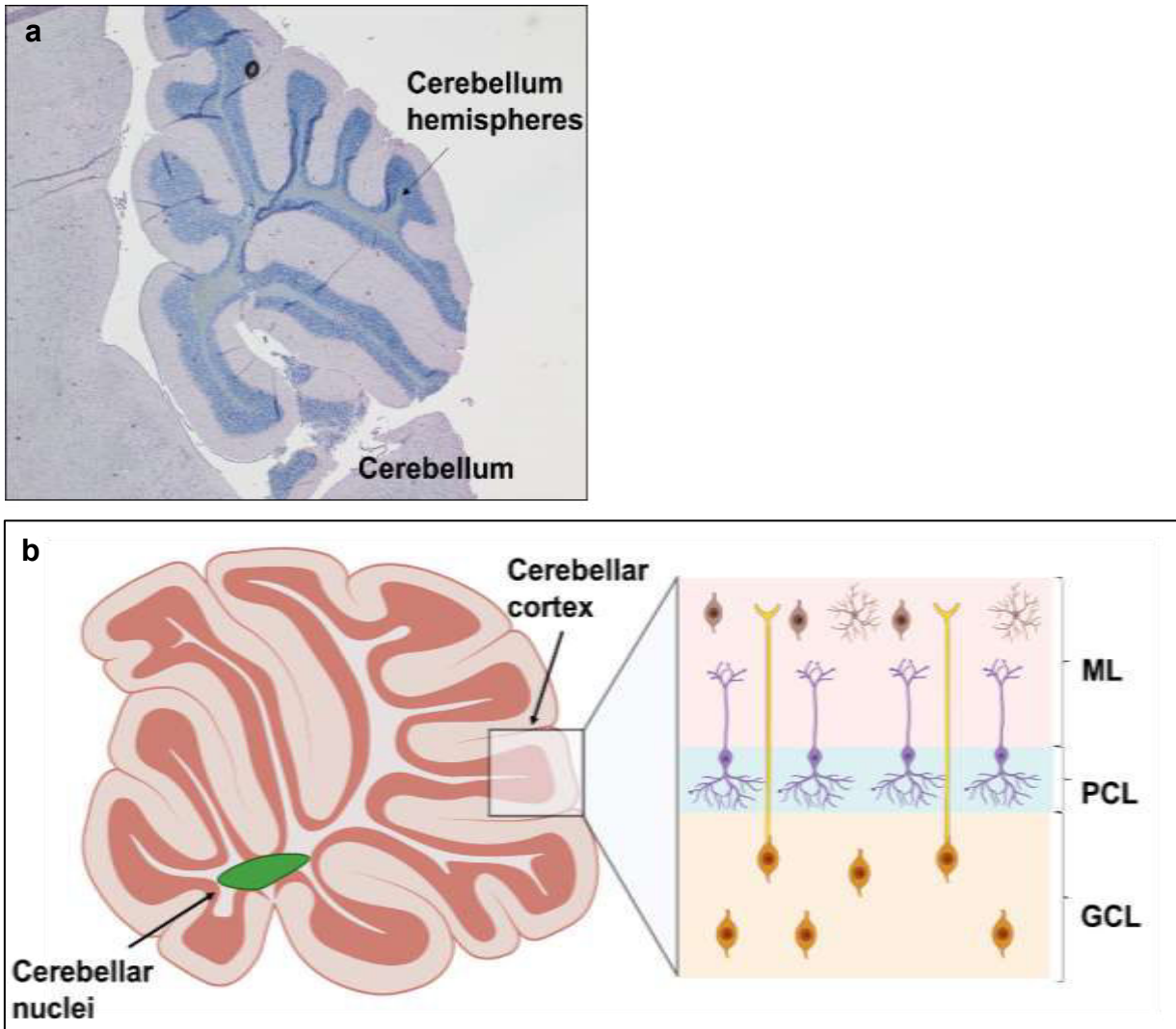


**Figure 3. Adult cerebellum:** a. sagittal section of a mouse adult cerebellum; b. schematic representation of an adult cerebellum showing the organization in cerebellar cortex and cerebellar nuclei. The square shows a zoomed section with the different layers forming the cerebellar cortex. ML: molecular layer, PCL: Purkinje cell layer, GCL: Granular cell layer.

## 1.2. Medulloblastoma Recurrence and Metastases

Recurrences occur in ~30% of patients and if this occurs, the survival of patients is reduced to only 10%. Recurrences could be local (tumor bed only) or in other sites, metastatic recurrences. Molecular features of primary tumors are maintained in the relapses (Ramaswamy et al., 2013). MB metastases occur mainly through leptomeningeal dissemination and remains confined to the central nervous system (CNS) and the spinal cord in most of cases (Hovestadt et al., 2020). It has been suggested that an hematogenous spread can also occur (Garzia et al., 2018) and rare metastases can be found outside the CNS. Metastases are diagnosed through the cerebrospinal fluid (CSF) cytology combined with imaging and are classified as microscopic and macroscopic metastases. Patients are classified in five groups according to the stage of metastases from M0 to M4 (Table 1).

**Table 1. Classification of MB patients according to the metastasis stage (according to Chang et al., 1969).**

<b>M0</b>	Tumors with no evidence of metastasis
<b>M1</b>	Microscopic tumor cells detected in CSF
<b>M2</b>	Intracranial metastatic lesions independent of the primary tumor
<b>M3</b>	Metastatic lesions in the spinal space
<b>M4</b>	Metastasis outside the cerebrospinal axis

## **1.3. Treatment**

The current standard of care involves maximal resection of the tumor, followed by cranio-spinal irradiation (CSI) and chemotherapy adapted to risk stratified patients.

### **1.3.1. Surgery**

The extent of the surgery is classified as gross total resection (GTR, no residual tumor), near-total resection (NTR,  $<1.5 \text{ cm}^2$  tumor remaining), or sub-total resection (STR,  $\geq 1.5 \text{ cm}^2$  tumor remaining). Surgery leads to neurological morbidity in 24% of patients increasing to 44% after gross total resection (Thompson et al., 2016). Postoperative cerebellar mutism syndrome incidence also increases with the extent of resection. Without accounting for the molecular group, the extent of the resection will improve the outcome of patients in terms of both progression-free and overall survival (OS). However, no benefits could be associated with the extent of the resection when the molecular groups are considered. Only patients of G4 seems to benefit from a GTR compared to STR, especially when metastases were present but only regarding progression-free survival (Thompson et al., 2016). A balance should be established between the aggressiveness of the surgery and the benefits from patients, considering the strong sequelae that can derivate from it.

#### **1.3.1.1. Risk stratification**

Diagnosis of the lesion followed by surgery and tumor pathology studies allow to establish a risk stratification of patients that will further defined the rest of the therapy protocol and predict survival. Average or standard risk patients will include those without metastasis (M0) and GTR/NTR. High risk patients will be those presenting metastases at the moment of diagnosis (M1–3) and/or STR. Patients from the SHH that harbor TP53 mutation or G3 patients showing MYC amplification will be also considered of high risk (Northcott et al., 2019).

### **1.3.2. Radiotherapy**

Radiotherapy for MB patients involved irradiation of the entire cranio-spinal axis (CSI, cranio-spinal irradiation) with a focal boost to the primary tumor bed. Different types of irradiation can be used or are being investigated. Photon beam-based radiation is extensively used and is based in the use of high-energy electromagnetic waves

(Steinmeier et al., 2019). Severe secondary effects derived from the highly aggressive radiation of the CNS in young patients are a major problem in the management of MB including: neurocognitive and neuropsychological damages, neuroendocrine dysfunction, hearing loss, growth problems, and secondary malignancies. Due to these important sequelae, numerous studies have tried to establish new treatment protocols that allow to decrease the dose of irradiation delivered without compromising the positive effects on disease control.

**Figure 4: Dose distribution of radiation:** a. CSI using photon beam; b. CSI using proton



beam. The area and intensity of received radiation is indicated in color, from red (stronger) to blue (weaker) (*adapted from Padovani et al., 2019*).

The current protocol for management of standard risk patients is based on CSI of 23.4Gy with a boost of 30.6Gy for a total dose of 54Gy, followed by adjuvant chemotherapy. High-risk patients still receive the same initial protocol including high dose of CSI (36Gy) with an important boost in the posterior fossa (18-20Gy), with a total dose of 54-56Gy. In children younger than 3y, radiotherapy is avoided or delayed due to the important side effects. However, this results in OS lower than 30-50%. In the latest years, proton beam-based radiation has gained interest since it is based on the use of charged particles (hydrogen ions) that have the advantage of providing high doses delivery capacities while sparing the adjacent healthy tissue (Steinmeier et al., 2019). Recent studies focused in comparing the effects in term of disease cure and toxicity between photon and proton beam therapy (Padovani et al., 2019; Yip et al.,

2022). Most of the studies seems to indicate similar results in terms of OS between photon and proton therapies, but more investigation is needed to confirm the beneficial use of proton therapy in terms of secondary effects (Eaton et al., 2016).

### **1.3.3. Chemotherapy**

The addition of adjuvant chemotherapy to the standard of care of MB patients allowed to increase the OS of patients. Importantly, the combination of radio and chemotherapy was an important step in the radiation dose de-escalation for standard-risk patients. First successful trial combined a low dose of CSI (23.4 Gy) with a posterior fossa boost (55.8 Gy) and concurrent chemotherapy using vincristine and adjuvant lomustine or cyclophosphamide, vincristine and cisplatin (Packer et al., 2006). This treatment scheme leads to an OS of 87.8% at 5 years and 81.3% at 10 years (Packer et al., 2006, 2013) and has become the standard approach to treat standard-risk MB patients (Northcott et al., 2019).

## 1.4. MB groups

MB is a heterogeneous disease and researchers and clinicians agreed to establish an international consensus subdividing MB in four molecular groups: WNT, SHH, Group 3 (G3) and Group 4 (G4) (Cho et al., 2011; Kool et al., 2008; Northcott et al., 2011). These groups differ in terms of clinical characteristics, prognosis, genetic drivers and their cell of origin. Traditionally, MB tumors were classified based on histopathological analysis and four categories existed: classic, desmoplastic/nodular (DN), MB with extensive nodularity (MBEN), large cell and anaplastic (LC/A) histology (Fig.5) (Ellison, 2010; Northcott et al., 2019). The World Health Organization (WHO) classification 2021 of tumors of the CNS defined MB in terms of molecular features with three main subgroups: WNT-activated, SHH-activated and non-WNT/non-SHH, but also based on histology (Louis et al., 2021). Importantly, this updated version indicated that the combination of histologically and genetically defined variants should be integrated in the diagnosis of new patients.

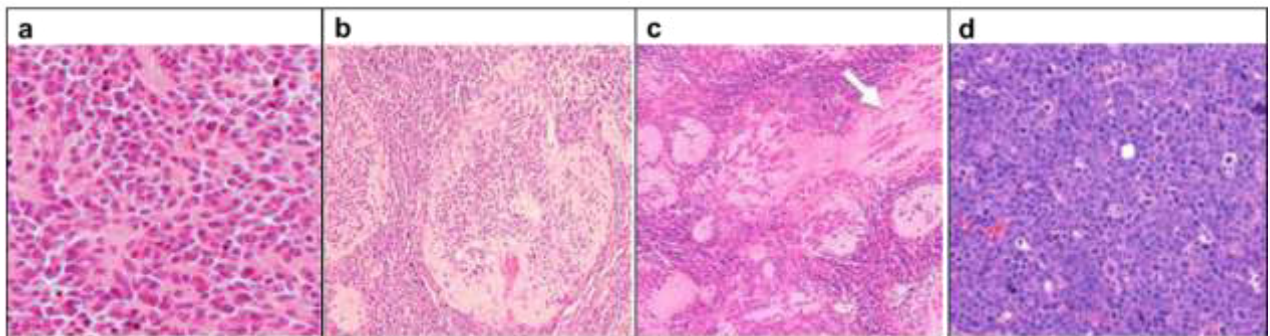


**Figure 5. Histological classification of MB tumors:** a. classic; b. desmoplastic/nodular (DN); c. MB with extensive nodularity (MBEN); d. large cell and anaplastic (LC/A) MB histology (a-c: from Ellison, 2010, d: from Northcott et al., 2019).

### 1.4.1.WNT

The WNT group corresponds to ~10% of MB cases and it is mostly found in teenagers and adults. In this group, metastases rarely occur with 5-10% patients presenting metastases at diagnosis (Table 2). In general, WNT tumors are considered of very good prognosis with a 5-years OS >95%. This is particularly true for patients younger than 16 years old, while adults have an intermediate prognosis (Schwalbe et al., 2017).

These tumors are characterized by the activation of the Wnt/ $\beta$ -catenin pathway (Fig.6) (Northcott et al., 2017; Thompson et al., 2006). In normal conditions, the activation of the canonical Wnt/ $\beta$ -catenin pathway involved the binding of the Wnt proteins to the membrane receptors Frizzeld and LRP5/6. When the ligand is bound, the “destruction complex” formed by: APC, AXIN, CK1 and GSK-3 is recruited to the membrane leading to its inhibition. This allows for  $\beta$ -catenin stabilization that will then be translocated to the nucleus where it activates target genes via the TFs T-cell factor/lymphoid enhancer-binding factor (TCF/LEF). Targets genes of the pathway (Cyclin D1, c-Myc and MMPs) are involved in cell proliferation, survival, differentiation and migration (Liu et al., 2022a). ~90% of WNT tumors carry somatic mutations in the CTNNB1 gene encoding for  $\beta$ -catenin. This mutation leads to constitutively activation of the WNT- $\beta$ -catenin pathway by stabilization of  $\beta$ -catenin and its accumulation in the nucleus where it activates target genes through the TFs TCF/LEF, activating programs of cell growth and proliferation. Most of WNT tumors that do not have the mutated CTNNB1 will present inactivating mutations in the tumor suppressor gene APC and these mutations are mutually exclusive. Other mutated genes included DDX3X (36%), SMARC4 (19%), TP53(14%), SNK2B (14%), PIK3CA (11%) and EPHA7 (8%). In addition, monosomy of chromosome 6 is present in ~80-85% of WNT patients (Northcott et al., 2017).

A mouse model allowed to propose the cell of origin of these tumors (Gibson et al., 2010). It was based on the expression of a Blbp-Cre-dependent mutant allele of Ctnnb1 in progenitor cell populations across the hindbrain. Activating mutation in Ctnnb1 lead to aberrant accumulation of cells in the embryonic dorsal brainstem that persisted into the adult. These cells stained positive for Olig3 and Pax6, indicating they are derived from progenitors of the LRL. When combined with Tp53 deletion, these lesions progressed to form tumors that recapitulated the anatomy and the gene expression profiles of WNT MB. This work allowed to established that WNT tumors are originating

from progenitor cells in the lower rhombic lip in the developing brainstem (Gibson et al., 2010).

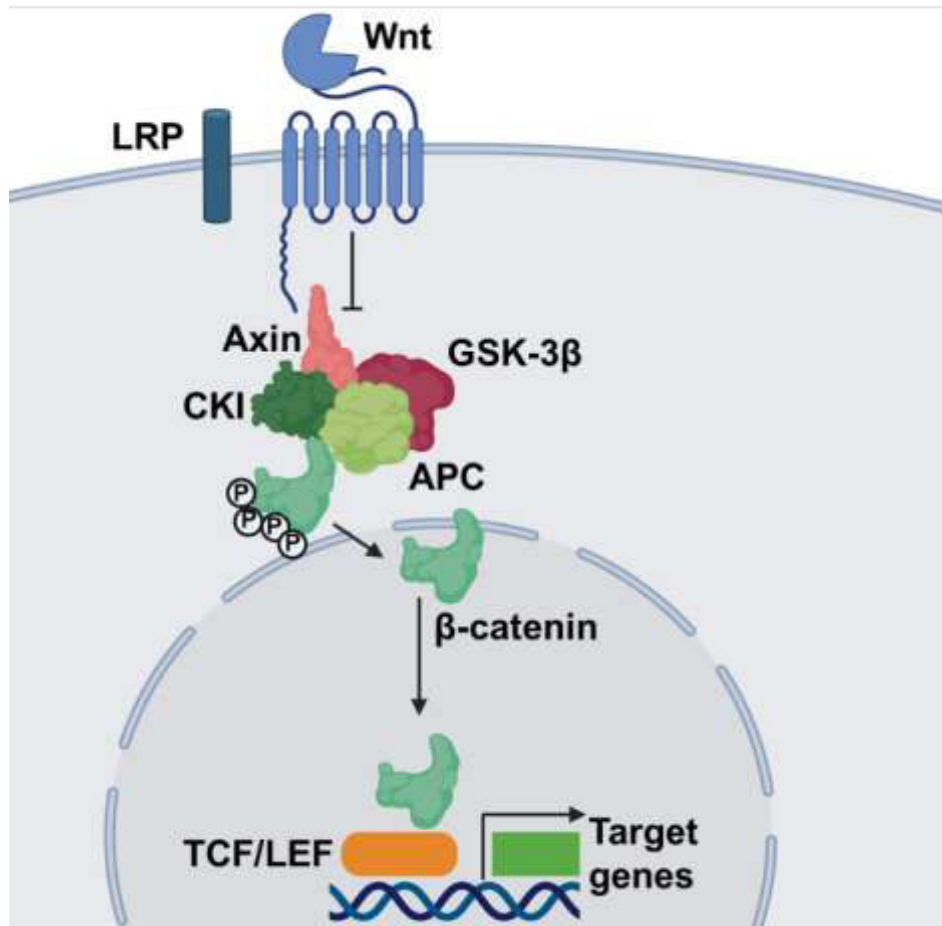


**Figure 6. Wnt/β-catenin signaling pathway:** Binding of the Wnt proteins to the membrane receptors Frizzled and LRP recruits the complex conformed by: APC, AXIN, CK1 and GSK-3 to the membrane, preventing degradation of β-catenin. Stabilized β-catenin is translocated to the nucleus to activate target genes in collaboration with the TFs TCF/LEF.

**Table 2. Clinical and molecular characteristics of WNT group**

<b>Clinical characteristics</b>			
<b>Age at diagnosis</b>	<b>Incidence</b>	<b>Metastasis at diagnosis</b>	<b>Overall survival (5 years)</b>
Children and adults	10-15%	5-10%	Very good/95%
<b>Molecular characteristics</b>			
<b>Proposed cell of origin</b>	<b>Main molecular drivers</b>	<b>Recurrent genetic alterations</b>	<b>Cytogenetic events</b>
Lower rhombic lip progenitors	Wnt/ $\beta$ -catenin pathway overactivation	<ul style="list-style-type: none"> <li>CTNNB1, DDX3X, SMARC4, TP53, SNK2B, PIK3CA, EPHA7 SNVs</li> </ul>	Loss chr. 6

### 1.4.2.SHH

Patients of the SHH group represent ~25-30% of MB and most of the infants (<3 years old) and adults belong to this group. Metastases are present in ~20% of patients at diagnosis and this group is considered of intermediate prognosis depending on age, histology, metastasis status and genotype (Table 3).

The most predominant feature of SHH tumors molecularly are germline or somatic mutations in components of the SHH signaling pathway (Fig.7). In the absence of SHH ligands, the membrane receptor Patched 1 (PTCH1) is inhibiting Smoothed (SMO) at the membrane. SMO inhibition leads to the induction by Suppressor of fused (SUFU) of the phosphorylation of GLI transcription. After phosphorylation, GLI undergoes proteasomal degradation and its target genes are not transcribed. In the presence of SHH, the inhibition on SMO by PTCH is removed and subsequently, SUFU is inhibited. There is increasing concentrations of SMO at the membrane, leading to the stabilization and activation of GLI TFs, that will be translocated to the nucleus to activate SHH-dependent gene expression. GLI1/2 are the main effectors of the SHH pathway and some of the target genes include stemness self-renewal related factors such as Nanog, MYCN and BMI (Lospinoso Severini et al., 2020).

In SHH MB tumors, inactivating mutations or deletions in PTCH1 (43%) and SUFU (10%) are present. Activating mutations of SMO are also found in 9% of cases. Amplifications of GLI and GLI2 and MYCN are present in 9% and 7% of patients, respectively (Kool et al., 2014; Northcott et al., 2017). These alterations lead to the constitutive SHH-independent activation of the pathway, driving the activation of SHH target genes involved in cell growth and proliferation. Recurrent alterations in TP53 are found in ~30% of patients. Mutations in the TERT promoter are also found in (39% of patients), being represented in up to 98% of adult SHH patients (Lindsey et al., 2014; Northcott et al., 2012, 2017). Cytogenetic events can also be found in these tumors including losses of the long arms of chromosome 9 (9q) and 10 (10q). This can lead to the loss of heterozygosity of important tumor suppressor genes as PTCH1 and SUFU (Northcott et al., 2017).

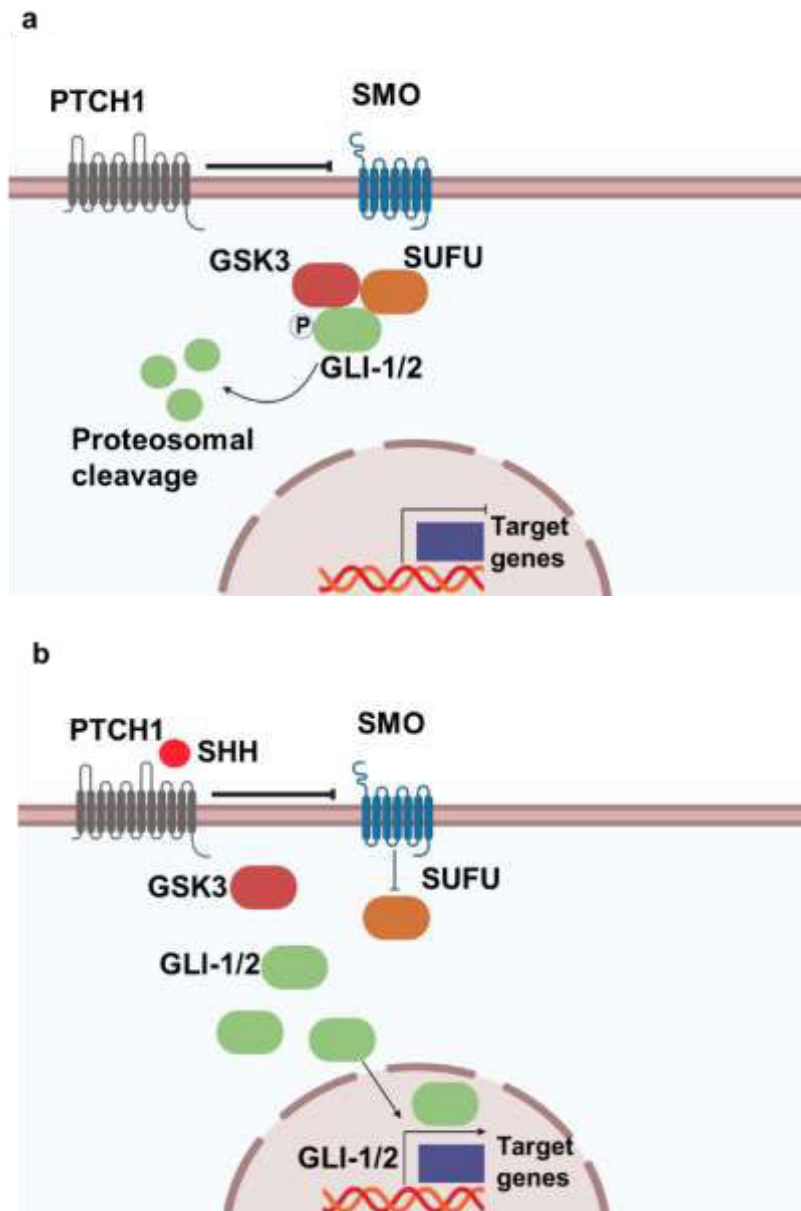


**Figure 7. SHH signaling pathway:** a: In the absence of the ligand SHH, Patched 1 (PTCH1) inhibits Smoothened (SMO) at the membrane, removing the repression on Suppressor of fused (SUFU) by SMO. SUFU induces the phosphorylation of GLI proteins by GSK3, inducing its proteasomal degradation; b: In the presence of SHH, PTCH1 leads to its internalization and degradation, removing the inhibition over SMO. SMO then inhibits SUFU, and GLI TFs are translocated to the nucleus to activate the expression of target genes.

Different animal models allowed to establish that the cell of origin for this group is the GCPs. For instance, deletion of PTCH1 or expression of an activated SMO in lineage-restricted GCPs produced tumors that resemble human SHH MB (Schüller et al., 2008; Yang et al., 2008). Many other studies using different mouse models have confirmed this idea. More recently, additional evidence has been added by single-cell transcriptomic studies showing that SHH tumors mirror the granule cell hierarchy (Vladoiu et al., 2019).

**Table 3. Clinical and molecular characteristics of SHH group**

<b>Clinical characteristics</b>			
<b>Age at diagnosis</b>	<b>Incidence</b>	<b>Metastasis at diagnosis</b>	<b>Overall survival (5 years)</b>
Infants, children and adults	25-30%	20%	Intermediate/75%
<b>Molecular characteristics</b>			
<b>Proposed cell of origin</b>	<b>Main molecular drivers</b>	<b>Recurrent genetic alterations</b>	<b>Cytogenetic events</b>
Granule cells progenitors	SHH pathway overactivation	<ul style="list-style-type: none"> <li>• PTCH1, SUFU, SMO, TP53, TERT SNVs</li> <li>• GLI and GLI2 and MYCN amplifications</li> </ul>	Loss 9q and 10q

### 1.4.3. Group 4

G4 is the most frequent MB groups, with 35-40% of patients that belong to this group. It represents ~50% of adolescent MB but can be also diagnosed during childhood. Around one third of G4 patients are metastatic at diagnosis and in general it is considered to have an intermediate outcome (Table 4).

G4 tumors, similar to what is found in G3, shows rare recurrent somatic mutations, with no gene that is mutated in more than 10% of cases and no specific deregulation in a given signaling pathway has been identified although recent data suggest that Src signaling could be an important driver pathway in G4. Most common alterations that are present in 6-9% of patients include somatic mutations in KDM6A, ZMYM3, KTM2C and KBTBD4. Amplification of MYCN and OTX2 are found in this group and amplification of CDK6 can be specifically detected in 6% of G4 tumors (Northcott et al., 2017, 2019). Enhancer hijacking mechanisms can be found and explain the overexpression of different genes in G3 and G4 tumors. These mechanisms can be explained by the existence of somatic structural variants that will juxtapose certain genes in a region proximal to active enhancer elements, including super-enhancers, instigating oncogenic activity. The existence of these elements allowed first to explain the overexpression of GFI1 and GFI1B in G3 and G4 (Northcott et al., 2014). The same events were found to occur in G4 tumors with a juxtaposition of the PRDM6 promoter close to the SNCAIP super-enhancer, explaining the upregulation of PRDM6 which is found in 17% of these patients (Fig.8) (Northcott et al., 2017). Recently, proteomic and phosphoproteomic analyses have identified the ERBB4-SRC signaling pathway to be deregulated in G4, likely constituting a potential oncogenic driver for this group (Forget et al., 2018). Cytogenetically, G4 tumors are characterized by isochromosome 17q, gain of chromosome 7 and 17q and loss of 8, 11 and the 17p chromosome.

There is no transgenic mouse model of G4 MB and the cell of origin for these tumors has not been clearly determined. Analyses of the medulloblastoma enhancer and super-enhancer landscape have allowed to identify LMX1A, EOMES and LHX2 (Lin et al., 2016; Northcott et al., 2019) as master regulators TFs of G4. These TFs have also crucial roles during cerebellar development. The expression of these genes is spatiotemporal restricted to neurons originated from progenitors of the URL (Lin et al., 2016; Northcott et al., 2019). The fact that these genes are master regulators of G4

tumors and during developing of the cerebellum in the URL, suggest that the cell of origin of these tumors is probably generated from this compartment. This idea is further supported by recent studies comparing MB tumors to the normal mouse and human cerebellum development. Indeed, transcriptome from G4 MB tumors align with the RL and to glutamatergic cerebellar nuclear neuron or UBCs (Smith et al., 2022; Vladioiu et al., 2019) .

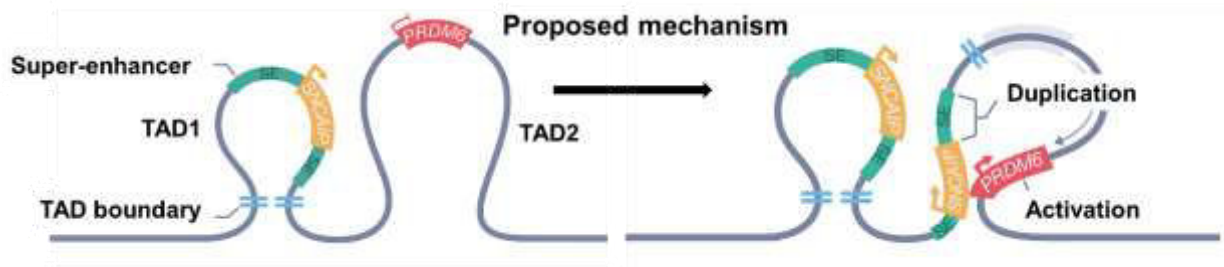


**Figure 8. PRDM6 enhancer hijacking:** Proposed model explaining the molecular basis of SNCAIP/PRDM6-associated enhancer hijacking (adapted from *Northcott et al., 2017*).

**Table 4. Clinical and molecular characteristics of G4 group**

<b>Clinical characteristics</b>			
<b>Age at diagnosis</b>	<b>Incidence</b>	<b>Metastasis at diagnosis</b>	<b>Overall survival (5 years)</b>
Children	35-40%	~ 35%	Intermediate/75%
<b>Molecular characteristics</b>			
<b>Proposed cell of origin</b>	<b>Main molecular drivers</b>	<b>Recurrent genetic alterations</b>	<b>Cytogenetic events</b>
Progenitors of the upper RL, UBC	PRDM6, ERBB4-SRC signaling pathway	<ul style="list-style-type: none"> <li>• MYCN and OTX2 amplification</li> <li>• KDM6A, ZMYM3, KTM2C and KBTBD4 SNVs</li> <li>• PRDM6 enhancer hijacking</li> </ul>	<ul style="list-style-type: none"> <li>• Isochr. 17q</li> <li>• Gain of chr. 7 and 17q</li> <li>• Loss of chr.8, 11 and 17p</li> </ul>

### 1.4.4. Group 3

G3 is the most aggressive group and represents ~20-25% of all MB cases. It is predominant in infants and early childhood. G3 is the group with the higher metastatic rate (40-50%) and the 5-years OS is <60% (Table 5).

Despite intensive research, no common driver pathway has been identified for G3 tumors. The most recurrent aberration is amplification of the oncogene MYC, present in 17% of G3 patients, even though MYC overexpression, caused by mechanisms not fully understood, is characteristic of all G3 tumors. In accordance with MYC overactivation, these tumors show transcriptomic and proteomic signatures related with mRNA processing, transcription and translation (Archer et al., 2018; Forget et al., 2018). Gene mutations that can be found in more than 5% of patients included: SMARC4, KBTBD4, CTNEP1 and KMT2D, although the biochemical and functional characterization of these mutations is lacking (Northcott et al., 2017).

Another important oncogenic event in G3 tumors which is also found in G4, is the overexpression of GFI1 and GFI1B factors as a consequence of enhancer hijacking events that occurs in 15-20% of patients. GFI1 and GFI1B are DNA-binding zinc finger TFs that are major regulators of hematopoiesis with a role in cell fate decision (Vassen et al., 2016). Both proteins act as epigenetic regulators by recruiting histone modifiers to repress the expression of target genes. The oncogenic role of these factors in G3 MB was demonstrated by the establishment of a mouse model in which the overexpression of either GFI1 or GFI1B together with MYC in neural stem cells lead to the formation of G3-like tumors (Northcott et al., 2014). Moreover, GFI1 and GFI1B are not only important for G3 MB tumor formation, but also for tumor maintenance (Lee et al., 2019).

Some G3 tumors are driven by MYCN (5%) and OTX2 (3%) amplifications (Northcott et al., 2017). OTX2 is a homeodomain-containing TFs which plays a critical role in forebrain, eye and pineal gland development. It has a crucial role in the specification and regionalization of the rostral central nervous system and it is expressed in the prospective cerebellum at early embryonic stages and in granule cells progenitor (Beby and Lamonerie, 2013). OTX2 is highly overexpressed in G3, G4 and WNT, despite of the genomic amplification events that could exist. This gene promotes cell proliferation mainly through the regulation of cell cycle genes and inhibits differentiation in G3 MBs

(Adamson et al., 2010; Bunt et al., 2012). OTX2 is important for maintaining the regulatory landscape of G3 tumors, being present at most active enhancers in these cells (Boulay et al., 2017). It has been proposed to participate in the expression of MYC (Adamson et al., 2010).

Our team has made major contributions to the understanding of G3 biology. Specifically, we have deciphered the role of the photoreceptor program (Cavalli et al., 2017; Cho et al., 2011; Kool et al., 2008) and the TGF- $\beta$  signaling pathway (Lin et al., 2016; Northcott et al., 2012, 2017) that were previously shown to be active in these tumors. Indeed, a subset of G3 tumors are characterized by the expression of a set of genes that are normally expressed in the retina and not in the cerebellum, which are known as the photoreceptor program. NRL, a lineage-restricted basic leucine zipper (bZIP) TF, and CRX an homeobox TF, are required for photoreceptor development. Both of them are under the control of OTX2 during retinal development (Swaroop et al., 2010). Our team showed that the high expression of NRL and CRX in G3 tumors is explained by their location close to G3 specific enhancers/super-enhancers and also through OTX2 regulation (Garancher et al., 2018). Importantly, it was shown that NRL and CRX are important for G3 MB growth *in vitro* and *in vivo*, and in particular that, NRL is mediating cell cycle progression and protecting G3 cells from apoptosis. Additionally, this work also showed that NRL was controlling the expression of the anti-apoptotic factor BCL-XL in G3 cells, providing a new vulnerability for these tumors that could be targeted by BCL inhibitors (Garancher et al., 2018).

Different genomic/epigenomic studies pointed to a deregulation of the TGF $\beta$ /Activin signaling pathway in some G3 tumors. Amplifications of some mediators of the pathway and the regulation through active enhancers suggested a putative oncogenic role for the TGF $\beta$  signaling pathway in G3 MB (Lin et al., 2016; Northcott et al., 2012, 2017). We have provided the proof of principle that this signaling pathway is active in a subset of G3 tumors (Morabito et al., 2019). Importantly, we also showed that the inhibition of the pathway decreased G3 cells proliferation *in vitro* and that treatment of orthotopically grafted mice with Galunisertib, a pharmacological inhibitor of the pathway, increased the survival of mice compared to non-treated animals, suggesting a potential therapeutic benefit for patients showing an activation of this pathway (Morabito et al., 2019).

Different cytogenetics events characterize G3 tumors, isochromosome 17q being the most representative one (40-50% of tumors), even though this alteration is most frequently found in G4. Additionally, loss of chromosome 8, 10q, 16q and gain of 1q, 7 and 18 can also be detected.

Several experiments using orthotopic transplants of virally infected cerebellar progenitors suggest that G3 tumors are originating from cerebellar neural stem cell populations. One of these models consists in the overexpression of MYC together with a dominant negative form of p53 in stem cells isolated from the postnatal cerebellum (CD133<sup>+</sup>)(Pei et al., 2012). Another model was based in the overexpression of MYC in GCPs isolated from p53 null mice (Kawauchi et al., 2012). In both cases, the tumors formed resembled human G3 MB, suggesting that these cells could represent the cell of origin of these tumors. It was also shown that different types of cerebellar neuron progenitors can be transformed by MYC overexpression and the dominant negative form of p53 including Pax6<sup>+</sup> GCPs and Pax2<sup>+</sup> inhibitory interneurons (Kawauchi et al., 2017). The combination of MYC and GFI1/GFI1B overexpression on GCPs, also allow G3 MB tumor formation in mouse, confirming these cells as starting point for G3 tumor formation (Northcott et al., 2014). Single-cell transcriptomic analysis of human G3 MB reveals an important resemblance to Nestin<sup>+</sup> cerebellar early stem cells, but also to GCP and UBC lineages, confirming this idea (Vladoiu et al., 2019).

**Table 5. Clinical and molecular characteristics of G3 group**

<b>Clinical characteristics</b>			
<b>Age at diagnosis</b>	<b>Incidence</b>	<b>Metastasis at diagnosis</b>	<b>Overall survival (5 years)</b>
Infants and children	20-25%	40-50%	Poor/50%
<b>Molecular characteristics</b>			
<b>Proposed cell of origin</b>	<b>Main molecular drivers</b>	<b>Recurrent genetic alterations</b>	<b>Cytogenetic events</b>
Neural stem cells	MYC	<ul style="list-style-type: none"> <li>• MYC, MYCN and OTX2 amplification</li> <li>• SMARC4, KBTBD4, CTNEP1 and KMT2D SNVs</li> <li>• GFI1 and GFI1B enhancer hijacking</li> </ul>	<ul style="list-style-type: none"> <li>• Isochr 17q</li> <li>• Loss of chr. 8 and 10q</li> <li>• Gain of chr. 7, 18, 16q and 1q</li> </ul>

## 1.5. MB subtypes

Several studies have described additional subtypes for each MB group (Cavalli et al., 2017; Northcott et al., 2012, 2017). For instance, Cavalli and colleagues have described 12 MB subtypes, two within the WNT group, four for SHH tumors, three in G3 and three in G4 group. These subtypes differ in terms of clinical and molecular features and provide deeper understanding of MB heterogeneity. In this way, WNT tumors are divided in  $\alpha$  and  $\beta$  subtypes. The  $\alpha$  subtype include mostly children and tumors harboring monosomy 6 while  $\beta$  tumors are mostly found in older patients. The survival of both subtypes is similar. In the case of SHH group, four additional subtypes have been described. The  $\alpha$  subtype include children and represents the patients with the worst prognosis in this group.  $\alpha$  tumors are associated with MYCN and GLI2 amplifications. Additionally, TP53 mutations are mostly found in  $\alpha$  tumors and only for this subtype this alteration has a prognostic value. SHH infants are mostly found in the  $\beta$  and  $\gamma$  subtypes.  $\beta$  tumors are frequently metastatic at diagnosis and are associated with PTEN deletions. These patients have in general a worse outcome than patients of  $\gamma$  subtype that have less genetic alterations. Last, the  $\delta$  subtype include adults and have the better prognosis among SHH patients. Most of the TERT promoter mutations are found in this subtype.

For G3 three additional subtypes have been described. Most of G3 infants are included in the  $\alpha$  subtype as well as children. These tumors are highly metastatic at diagnosis in a similar way than tumors from  $\gamma$  subtype and are associated with loss of 8q (MYC chromosome). The  $\beta$  subtype includes older G3 patients and is not as metastatic as the other subtypes of G3. These tumors are associated GFI/GFI1B overactivation and OTX2 amplifications. The  $\gamma$  subtype is the one with the worst prognosis and it is associated with increased copy number of MYC. These tumors are also enriched in isochromosome 17q and patients are mostly infants or children. G4 tumors have also been divided in three subtypes with patients of the  $\beta$  subtype being slightly older than patients from  $\alpha$  and  $\gamma$  subtypes that include mostly infants and children. In terms of genetic alterations, tumors from  $\alpha$  and  $\gamma$  subtypes are associated with CDK6 amplifications while isochromosome 17q is mostly found in tumors from the  $\beta$  subtype.

## 1.6. Targeted therapies

Uncovering the main molecular drivers in the different MB groups it is important not only to better understand tumor biology but also to come up and propose more directed therapies. These therapies should only benefit to a subset of MB patients but should have the advantage of targeting identified vulnerabilities in each tumor type while preventing the normal cells from toxic effects. Even though our understanding of the molecular events characterizing the different groups of MB has been in constant progression for the last years, there is only a reduced number of targeted therapies that have been or are in clinical trials for MB patients.

One of the first lines of targeted therapies evaluated in the context of MB are the inhibitors of the SHH pathway mediators. Especially, inhibitors of SMO have been tested in different clinical trials so far. Some examples are the molecules: Vismodegib (GDC-0449) (PBTC-025B, PBTC-032), Sonidegib (LDE225) (NCT01125800, NCT01708174) and LEQ506 (NCT01106508) (Robinson et al., 2015). As frequently found for other targeted therapies, resistance mechanisms have been found in these studies mainly related with the occurrence of new mutations in SMO that lead to a loss of activity of the inhibitors, or with the existence of alterations in the mediators of the pathway that are downstream of SMO. This led to the development of new molecules that could target for example the GLI TFs. This is the case of the drug Silmitasertib (CX-4945), which is a Casein Kinase 2 (CK2) inhibitor (NCT03904862) (Yao et al., 2022), and also the rationale to evaluate Arsenic Trioxide (NCT00024258), which is known to inhibit the activity of GLI proteins (Beauchamp et al., 2011; dos Santos Klinger et al., 2020). Another molecule in clinical trials for SHH patients that carry PTCH1 loss of function mutations is Taladegib (NCT05199584).

As it has been proposed in several studies, MB tumors can be driven by epigenetic alterations (Northcott et al., 2017, 2019). In line with this, molecules that target epigenetic factors are currently evaluated for MB patients. This is the case of the HDAC inhibitors Fimepinostat (NCT03893487) and Vorinostat (NCT00867178), the EZH2 inhibitor Tazemetostat (NCT03213665) and Bromodomain and BET Inhibitors (BMS-986158 and BMS-986378) (NCT03936465). BET inhibitors such as JQ1 have shown preclinical promise for MYC-driven MB tumors, mainly due to its effect in reducing the expression of MYC, of genes related with neuronal differentiation programs and

progression through the cell cycle (Bandopadhyay et al., 2019). Additional pathways that are currently under investigation include the PI3K/MTOR using Ribociclib and Everolimus (NCT03387020) and Samotolisib (NCT03213678). The Notch1 signaling pathway that can be targeted with the gamma secretase inhibitor RG-4733 (NCT01088763). The inhibition of the folate pathway have been shown to be very promising in preclinical studies (Morfouace et al., 2014) and the use of Pemetrexed (NCT01878617) combined with Gemcitabine in addition to standard chemotherapy is currently being evaluated for Intermediate- and high risk-MB patients.

Mediators of the cell cycle machinery also seems to be potential targets especially for the most aggressive type of tumors. Kinase inhibitors targeting checkpoint kinases 1 and 2 (CHK1/2), polo-like kinases (PLKs), cyclin-dependent kinases (CDKs), and Aurora (AUR) are promising molecules in this context (Endersby et al., 2021). Especially, the combination of the CHK1/2 inhibitor LY2606368 (Prexasertib) with DNA-damage inducing agents has strong activity in preclinical models for the most aggressive MB tumors (Endersby et al., 2021) and is currently being evaluated in patients from Group 3/Group 4 or SHH groups (NCT04023669). Another molecule under test is the Wee1-kinase inhibitor AZD1775 (MK-1775) (NCT02095132). Inhibitors of the CDK 4-6 kinases such as Palbociclib have been also tested (NCT0225546). The small molecule Ribociclib has been evaluated in combination with different agents: with Gemcitabine for G3/G4 patients, with trametinib for WNT/SHH or with Sonidegib for SHH-activated patients (NCT03434262).

In conclusion, MB tumors have been proven to be very different clinically and molecularly. Standard treatments do not include these differences and globally patients receive the same combination of multimodal treatments based on their risk factors. G3 is the group with the worse prognosis and there is an urgent need to better understand the biology of these tumors and identify new vulnerabilities that can be targeted. The work I have done during my thesis focused on investigating activation of the Unfolded Protein Response through HSPA5 inhibition or the activation of the eIF2 $\alpha$  pathway as potential therapeutic targets in G3 tumors.



## **HSPA5**

HSPA5 (Heat Shock Protein family A 5), also known as GRP78 (Glucose-related protein 78) was first discovered as one of two proteins which expression in fibroblasts was induced by glucose starvation (Shiu et al., 1977). In 1983, Munro and Pelham showed that it corresponds to the protein named BiP (Immunoglobulin heavy chain Binding Protein) found to be bound to the immunoglobulin heavy chains of pre-B cells (Haas and Wabl, 1983). HSPA5 belongs to the HSP70 family of proteins (Munro and Pelham, 1986). It is the fifth member of the Heat Shock Protein family A. HSPA5 is mainly found in the Endoplasmic Reticulum (ER), but can also be found at the Mitochondria-associated ER Membranes (MAMs) and the cell surface. This protein function as a chaperone of the ER: translocate proteins into the ER, fold and hold proteins in this organelle. HSPA5 also controls the Unfolded Protein Response (UPR) and assists the ER-associated protein degradation (ERAD).

### **1.7. Structure**

HSPA5 has 60% homology with HSP70, and as other members of this family contains a highly conserved N-terminal ATPase-binding domain or nucleotide-binding domain (NBD) required for the ATPase catalytic activity. It also contains a substrate binding domain (SBD) conformed of eight  $\beta$ -strands with a helical lid and an interdomain linker (Fig.9) (Wang et al., 2017). The interaction of the chaperone with its clients will be determined by an allosteric ATPase cycle in which co-chaperones and nucleotide exchange factors participate (Zhuravleva and Gierasch, 2015). In its ATP-bound state, the lid in the SDB is open, allowing the binding of substrates. ATP hydrolysis led to a closed lid conformation permitting a high affinity state with the client protein. Exchange of ADP for a new ATP molecule induce a conformational change leading substrate release and folding or targeting to degradation (Pobre et al., 2019). HSPA5 has also unique features that differentiate it from other members of the HSP70 family including an ER signal sequence and a KDEL retention signal that enable HSPA5 to translocate into the ER and remain there (Wang et al., 2017).

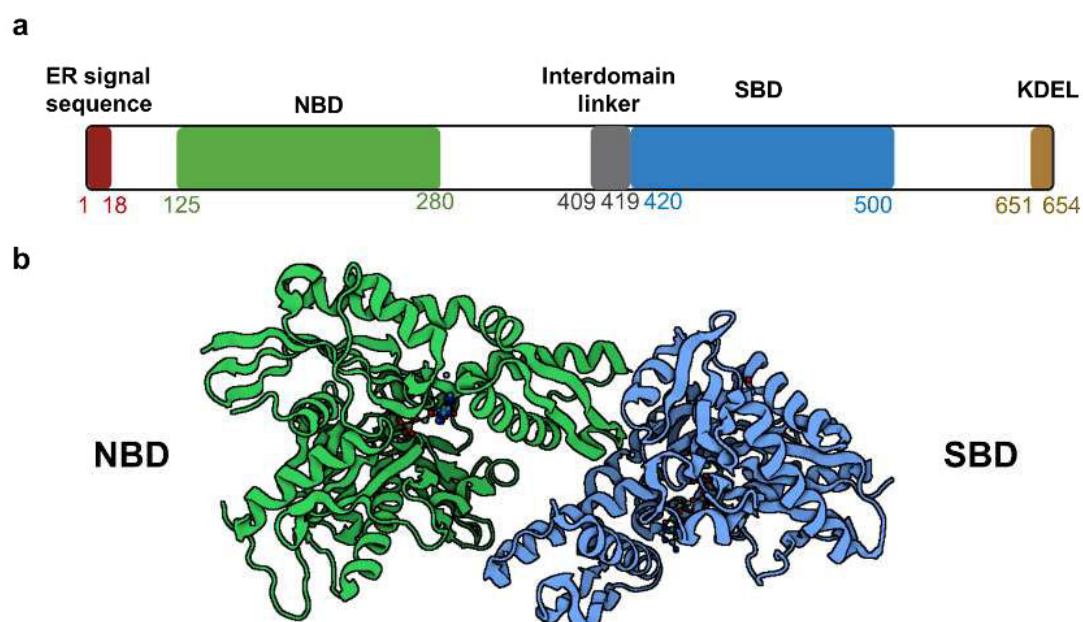


**Figure 9. HSPA5 structure:** a: Primary structure of HSPA5: N-terminal ATPase-binding domain or nucleotide-binding domain (NBD), substrate binding domain (SBD) with an interdomain linker. It also contains an ER signal sequence and a KDEL retention signal; b: secondary structure of HSPA5 showing the NBD and SBD. (Adapted from *Wang et al., 2017*, PDB: 3IUC).

## 1.8. Cellular localization

As an ER chaperone, HSPA5 is traditionally described as an ER-resident protein. However, it is now well accepted that in different stress conditions HSPA5 can have a wider number of functions and consequently, different localizations outside of the ER. For instance, it has been shown that in conditions of UPR activation, HSPA5 can be relocated to the mitochondria (Sun et al., 2006). The exact role of the mitochondria-resident HSPA5 is not completely understood but it could be related with the maintenance of cellular  $\text{Ca}^{2+}$  homeostasis or the extension of the UPR to this organelle. It has been also described the relocalization of HSPA5 to the cytosol in conditions of ER stress and/or proteasome inhibition as a part of the protein turnover mechanisms (Shim et al., 2018). Similarly, upregulation of cytosolic HSPA5 can occur in the presence of double stranded RNA (dsRNA) in cases of viral infection of cells (Jheng et al., 2016). Cell-surface expression of HSPA5 has been also described (Tsai et al., 2018; Yao et al., 2015; Zhang et al., 2010).

## **1.9. HSPA5 is an essential gene during development**

HSPA5 knockout mice die at embryonic day (E) 3.5 due to a defect in embryonic cell proliferation and an increased apoptosis of the inner cell mass indicating that, as other ER chaperones, HSPA5 is essential for embryonic development (Luo et al., 2006). It can be also important later on during development. For instance, inducible knockout of HSPA5 in Purkinje cells during the first postnatal days, affects its survival and induces cerebellar atrophy. On the contrary, the homozygous deletion of HSPA5 specifically in mouse prostate epithelium does not affect postnatal prostate development or growth (Fu et al., 2008). Similarly, the heterozygous conditional deletion of HSPA5 in the hematopoietic system in mice did not induce any abnormality compared to WT mice, exhibiting normal organ size and morphology, and no loss in total bone marrow cell number or hematopoietic stem cell population (Wey et al., 2012). These results suggest that while HSPA5 is essential for the embryologic development, the essential functions of HSPA5 in adult tissues seem to be cell type specific.

## **1.10. Functions**

HSPA5 has a major role in controlling protein homeostasis in the cell. As an ER-chaperone, HSPA5 functions involved folding, holding and translocation of proteins into the ER. The chaperone activity of HSPA5 relies on its ATP- and substrate binding domain and is regulated by co-chaperones, cofactors (ER-localized DnaJ cofactors (ERdjs)) and nucleotide exchange factors (Grp170/ORP150 and Sil1) (Pobre et al., 2019). Misfolded proteins are translocated to the cytosol to be degraded by the proteasome system in a process known as ER-associated protein degradation (ERAD) (Needham et al., 2019; Wang and Kaufman, 2016). HSPA5 protects the cells from a proteotoxic stress not only by its chaperone activity and its contribution to the degradation of misfolded proteins through ERAD. Recently, it has been also proposed that HSPA5 can have another activity as disaggregase, collaborating with the clearance of protein aggregates that can concentrate in the ER (Melo et al., 2022).

HSPA5 also contribute to keep cell homeostasis by regulating the  $\text{Ca}^{2+}$  level in the ER (Daverkausen-Fischer and Pröls, 2022).  $\text{Ca}^{2+}$  leakage to the cytosol constitute an apoptotic signal. In that way, HSPA5 plays an important role as it is a high capacity  $\text{Ca}^{2+}$ -binding protein, keeping it sequestered in the ER (Lièvremonet et al., 1997). HSPA5 also regulates  $\text{Ca}^{2+}$  levels by directly closing the Sec61 channel, together with

the cytosolic  $\text{Ca}^{2+}$ -calmodulin (CaM), preventing in that way  $\text{Ca}^{2+}$  leakage to the cytosol (Schäuble et al., 2012).  $\text{Ca}^{2+}$  flux from the ER to the mitochondria is also important for ATP balance and cell survival. This flux occurs at specific points of contacts between the ER and the mitochondria known as mitochondria-associated ER membranes (MAMs). Efficient  $\text{Ca}^{2+}$  flux from the ER to mitochondria is mediated via inositol 1,4,5-trisphosphate receptors (IP3Rs), the voltage dependent anion channel 1 (VDAC1) and mitochondrial  $\text{Ca}^{2+}$  uniporter 1 (MUC1) (Gutiérrez and Simmen, 2018). HSPA5 directly regulates IP3Rs by promoting the assembly of the tetrameric complex required to form an activated channel (Higo et al., 2010).

As previously mentioned, HSPA5 can also be preferentially expressed at the surface of cancer cells. At this site, it interacts with signaling molecules involved in different oncogenic processes including proliferation, invasion, inflammation and others (Tsai et al., 2018, 2015). For instance, HSPA5 at the cell surface of human prostate cancer cells and murine macrophages was shown to interact with the proteinase inhibitor  $\alpha 2$ -macroglobulin ( $\alpha 2\text{M}^*$ ) and to be essential for signal transduction downstream of this protein (Misra et al., 2002). Similarly, HSPA5 at the surface of macrophages was shown to interact with IGF-1 and was indispensable for M2 polarization and the proliferation and migration of lung cancer cells (Zhang et al., 2021b). Another partner of HSPA5 at the cell surface is the small signaling molecule Cripto which has important roles during embryogenesis but also in the progression of human tumors. It was shown that HSPA5 and Cripto at the cell membrane cooperate to attenuate TGF- $\beta$ -dependent growth-inhibitory effects in prostate cancer cells (Shani et al., 2008).

HSPA5 is the master regulator of the Unfolded Protein Response, an important mechanism that allows cells to cope with ER stress due to accumulation of misfolded/unfolded proteins in this organelle. In non-stressed conditions, HSPA5 is bound to the three effectors of the UPR, Activating Transcription Factor 6 (ATF6), PRKR-like ER kinase (PERK) and Inositol-requiring protein 1 $\alpha$  (IRE1 $\alpha$ ), preventing the activation of the downstream signaling pathways. In conditions of ER stress, the chaperone is titrated away from these effectors allowing for their activation with the initiation of the corresponding signaling pathways. UPR is considered as a cytoprotective mechanism when its activation lead to the resolution of ER stress. However, when the response is too strong and sustained, UPR activation through HSPA5 is cytotoxic.

## **1.11. HSPA5 in cancer**

HSPA5 is involved in different aspects of cancer development including initiation, growth and survival, metastasis and mechanisms of resistance to therapies. Extensive research has been done regarding these aspects, but only selected examples will be presented in this document.

### **1.11.1. Tumor initiation**

The role of HSPA5 in tumor formation has been extensively demonstrated. A few examples are provided here. Heterozygous HSPA5<sup>+/-</sup> mice crossed with different strains that allow for breast tumor development showed increased latency period for tumors formation and decreased of tumor growth (Dong et al., 2008). Conditional knockouts of both HSPA5 and PTEN in the prostate epithelium (Fu et al., 2008) or cells of the hematopoietic system (Wey et al., 2012) was enough to inhibit prostate tumorigenesis and leukemogenesis respectively through suppression of the PI3K/AKT activation initiated by PTEN loss. In a Kras-driven mouse model of pancreatic ductal adenocarcinoma HSPA5 haploinsufficiency lead to a reduction in the acinar-to-ductal metaplasia step, a key tumor initiation mechanism (Shen et al., 2017).

### **1.11.2. Metastasis**

The role of HSPA5 in mediating metastasis has been described for different types of cancer including, melanoma, human hepatocellular carcinoma (HCC), prostate, ovarian and breast cancer (Chen et al., 2015). HSPA5 heterozygosity is sufficient to decreased tumor angiogenesis and growth of metastatic lesions. MAb159, an antibody against HSPA5 decreased tumor growth and also metastasis formation in the liver and lungs in a orthotopic mouse model of breast adenocarcinoma and melanoma (Liu et al., 2013). Investigations on human hepatocellular carcinoma (HCC) have shown that HSPA5 at the cell surface interacts with  $\alpha 2M^*$ , and this interaction stimulates the invasion and metastasis of HCC cells (Zhao et al., 2015). HSPA5 upregulates the TF HOXB9, to promote HCC invasion and metastasis in recurrent HCC (Ying et al., 2017).

### 1.11.3. Resistance to therapy

HSPA5 upregulation in certain cancer cells has been related to resistance to treatments but the mechanisms are not completely understood. Some examples include the use of temozolomide or the inhibitor of the ubiquitin-activating enzyme 1 (UBA1), TAK-243, in glioma cells. In both cases it was shown that the level of expression of HSPA5 was negatively correlated with the sensitivity of the cells to the treatment. (Liu et al., 2021; Pyrko et al., 2007). Triple negative breast cancer (TNBC) cells resistant to pirarubicin, one of the main agents used in chemotherapy for this disease, showed higher level of expression of HSPA5 than sensitive cells, and the downregulation of HSPA5 using siRNA was sufficient to reestablish sensitivity to the compound (Liu et al., 2022b). The use of an antibody to block cell surface HSPA5 improved the response of cells to radiation, in two different tumor models, non-small cell lung cancer (NSCLC) and glioblastoma (GBM) multiforme (Dadey et al., 2017), indicating that the protein is also involved in the way the cells respond to radiotherapy.

The role of HSPA5 in resistance to treatments may be linked to the acquisition of a stemness phenotype of cancer cells. As it was shown in head and neck cancer (HNC) cells, where the knockdown of HSPA5 decreased the stemness characteristics of these cells with a decrease in the expression of the stem cell markers Oct-4 and Slug, while the keratinocyte differentiation markers CK18 and involucrin were increased indicating differentiation. Interestingly, CD24<sup>-</sup>/CD44<sup>+</sup>/HSPA5<sup>+</sup> were more chemo-resistant and invasive compared to the CD24<sup>-</sup>/CD44<sup>+</sup> only cells (Chiu et al., 2013). In breast cancer cells it was shown that HSPA5 is co-expressed and co-localizing with the transmembrane protein CD44 at the cell surface. Specially, HSPA5 interacts with an isoform of CD44 that has additional variable exons added to the extracellular juxtamembrane region, and that is frequently observed during cancer progression (CD44v). This interaction was particularly increased in tamoxifen-resistant models of breast cancer (Tseng et al., 2019).

In conclusion, HSPA5 is a chaperone of the endoplasmic reticulum involved in a wide range of processes in the cell independent of protein folding and response to ER stress. The pro-survival functions of HSPA5 may be crucial during cancer development and growth, metastasis and resistance to treatments. Accordingly, HSPA5 is an interesting target to new therapies.

Cancer cells are exposed to different intrinsic and extrinsic stresses such as hypoxia, glucose deprivation, acidosis, oxidative stress, oncogenic transformation, etc. These conditions make cancer cells to suffer from ER stress and induce the UPR as a cytoprotective mechanism. HSPA5, as the master regulator of the UPR, has a key role in promoting cancer cell survival through activation of this response. In the context of this thesis, the control of UPR activation by HSPA5 and its potential role as cytotoxic strategy for treatment of G3 MB cells is highly important and as so, the next chapter is dedicated to UPR mechanisms and how it can be involved in cancer



### 3. UPR

The endoplasmic reticulum (ER) is an essential organelle with multiple functions in the cell including folding and assembly of secreted and transmembrane proteins, regulation of the  $\text{Ca}^{2+}$  pool and flux in the cell, biosynthesis of lipid and sterol, communication between organelles and signaling (Chen and Cubillos-Ruiz, 2021; Hetz et al., 2020). Maintaining ER homeostasis is then vital for the cell. Numerous conditions including increased physiological demands or pathological dysregulations can alter ER homeostasis and lead to the accumulation of misfolded and/or unfolded proteins in the ER, inducing ER stress. Eukaryotic cells have evolved an adaptive response to cope with ER stress known as the Unfolded Protein Response, that involves the activation of different mechanisms that allow to reestablish the balance in the ER. These mechanisms lead to a transcriptional and translational reprogramming of the cell including induction of chaperones and folding enzymes, mRNA degradation, attenuation of protein synthesis and degradation of misfolded/unfolded proteins. If these responses are unable to resolve ER stress, UPR activation can also lead to the induction of cell death. In this way, UPR can be considered as a pro-survival mechanism if it allows to reestablish ER homeostasis, or cytotoxic if not. Constitutively activated or defective UPR has been associated with several pathological conditions including cancer (Chen and Cubillos-Ruiz, 2021). In this chapter I will describe how the UPR response function in normal conditions, how it has been related with cancer initiation and development and how it could be targeted as a strategy for cancer therapeutics.

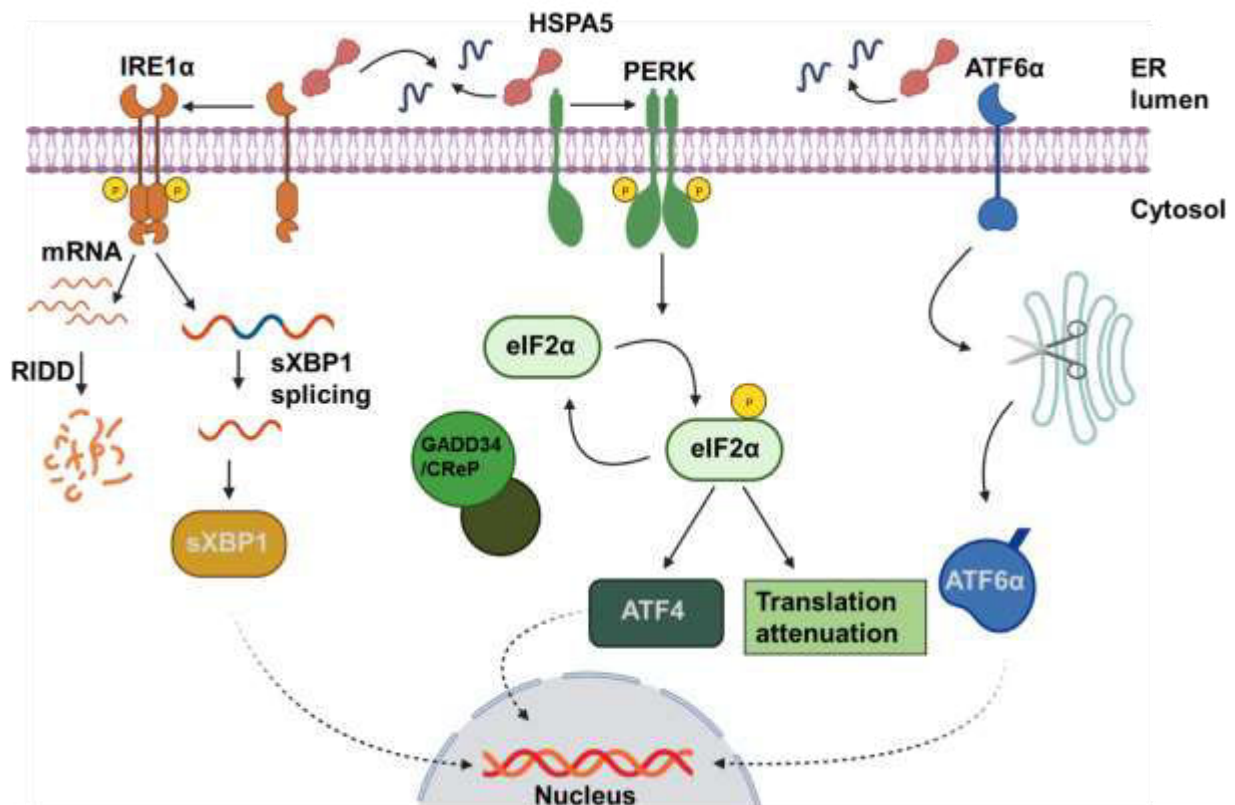


**Figure 10. Unfolded Protein Response signaling pathways:** ER stress results from an accumulation of unfolded/misfolded proteins in the endoplasmic reticulum (ER) which leads to the dissociation of the HSPA5 chaperone from the three effectors IRE1 $\alpha$ , ATF6 and PERK. IRE1 $\alpha$  functions as a kinase and an endoribonuclease. Through the latter activity, it catalyzes the cleavage of a 26-nucleotide intron from the unspliced X-box binding protein 1 (uXBP1) mRNA to produce the spliced form of the XBP1 (sXBP1). This TF is important in the regulation of genes involved in folding and degradation of unfolded proteins, process known as Endoplasmic-reticulum-associated protein degradation (ERAD). IRE1 $\alpha$  also mediates the Regulated IRE1-Dependent Decay of mRNA (RIDD). PERK is a kinase. Its activation involved its oligomerization and autophosphorylation. Activated PERK phosphorylates the translation initiation factor eIF2 $\alpha$ , which leads to a general decrease in global translation but a selective increase in ATF4 translation. ATF4 is also a TF that controls the expression of genes involved in folding, antioxidant responses, autophagy, amino acid metabolism, and apoptosis. Activation of ATF6 involved its translocation to the Golgi complex where it is cleaved by the proteases S1P and S2P and becomes activated. Its cytoplasmic domain is then translocated into the nucleus where it acts as a TF regulating the expression of genes participating in ER protein folding and the ERAD. These three arms of the UPR allow cells to adapt to stress conditions and survive. In the case of a strong and sustained UPR activation these same pathways can lead to cell death. (P: phosphorylated residue).

### **3.1. UPR signaling to resolve ER stress**

As briefly mentioned before, the chaperone HSPA5 (BiP/GRP78) is the master regulator of the UPR. In normal conditions, the chaperone is associated with the three main sensors of ER stress: Activating Transcription Factor 6 (ATF6), PRKR-like ER kinase (PERK) and Inositol-requiring protein 1 $\alpha$  (IRE1 $\alpha$ ), keeping them in their inactive forms. These proteins traverse the ER membrane and possess an ER luminal domain (LD) involved in detection of misfolded proteins, a transmembrane domain, and a cytosolic effector domain, that propagate the signal (Walter and Ron, 2011). The main mechanism proposed to explain UPR activation in conditions of ER stress, involved HSPA5 titration from these effectors due the highest affinity of the chaperone for misfolded/unfolded proteins accumulated in the ER, leading to the activation of the UPR. It has been shown that there is a direct noncanonical interaction between the ATPase domain of HSPA5 to the luminal domains of IRE1 $\alpha$  and PERK. When misfolded/unfolded proteins bind to the SBD of HSPA5, this latter is dissociated from the effectors, allowing for their activation (Carrara et al., 2015; Kopp et al., 2019). In this context, HSPA5 plays the central role in sensing ER stress and controlling UPR activation through the effector proteins. Some studies suggest that the effectors, in particular IRE1 $\alpha$  and PERK are able to directly sense and interact with unfolded proteins through the LD of both proteins that are very similar, leading to its activation independently of HSPA5 dissociation (Bashir et al., 2021; Kimata et al., 2007; Oikawa et al., 2009), but these mechanisms are not completely understood.

#### **3.1.1. PERK arm**

After dissociation from HSPA5, PERK dimerizes, auto-phosphorylates and becomes active. Activated PERK triggers the phosphorylation of the eukaryotic translation initiation factor 2 subunit 1 (P-eIF2 $\alpha$ /EIF2S1) leading to decreased levels of eIF2-GTP. This results in a transient attenuation of protein synthesis (Hetz et al., 2020; Walter and Ron, 2011). The decrease in translation after eIF2 $\alpha$  phosphorylation allows to restore ER homeostasis by decreasing the total amount of proteins entering this organelle. The phosphorylation of eIF2 $\alpha$  has another consequence, which is the selective translation of specific mRNAs by a mechanism that involves short upstream open reading frames (uORFs) in the 5' untranslated region (UTR) of these mRNAs. This is the case of the TF ATF4. The mRNA of ATF4 contains two uORFs in the 5'

UTR, uORF1 and uORF2. In non-stressed cells, abundant eIF2-GTP will scan downstream of uORF1 and reinitiate at the next coding region, uORF2, an inhibitory element that blocks ATF4 expression. Phosphorylation of eIF2 $\alpha$  increases the time required by the scanning ribosomes to initiate another round of scan, allowing ribosome to continue through the inhibitory uORF2 and reinitiate at the ATF4-coding region (Vattem and Wek, 2004). ATF4 will induce then the expression of the CAAT/enhancer-binding protein (C/EBP) homologous protein (CHOP)/GADD153. ATF4 and CHOP control the expression of genes involved in folding, antioxidant responses, autophagy, amino acid metabolism. ATF4 is also responsible for the upregulation of the protein phosphatase 1 (PP1) regulatory subunit GADD34 (encoded by the gene PPP1R15A), which forms a complex with PP1 to dephosphorylate eIF2 $\alpha$  in a feedback loop (Novoa et al., 2001). The constitutive repressor of eIF2 $\alpha$  phosphorylation (CReP, encoded by the gene PPP1R15B) can also recruit the phosphatase catalytic subunits of the PP1 to P-eIF2 $\alpha$  (Jousse et al., 2003). ATF4 and CHOP are also responsible for the induction of apoptosis if the ER stress cannot be resolved (Hetz et al., 2020).

### **3.1.2.IRE1 $\alpha$ arm**

IRE1 $\alpha$  is a transmembrane Ser/Thr protein kinase with additional endoribonuclease properties. The activation of IRE1 $\alpha$  under ER stress involves its dimerization and autophosphorylation leading to the activation of its endoribonuclease function. Through this latter activity, it catalyzes the cleavage of a 26-nucleotide intron from the X-box binding protein 1 (XBP1) mRNA. The product of the spliced form of XBP1 (sXBP1) is a basic leucine zipper (bZIP) TF. sXBP1 has a key role in UPR by controlling the expression of genes involved in protein folding, secretion, ERAD, and lipid synthesis. Interestingly, it has been shown that another branch of the UPR, ATF6, is involved in the production of sXBP1. The TF ATF6 is responsible for the increased transcription of the XBP1 mRNA, while IRE1 $\alpha$  is required for the splicing and production of the fully active sXBP1 (Lee et al., 2002; Yoshida et al., 2001). The endoribonuclease activity of IRE1 $\alpha$  is also involved in the cleavage and degradation of some mRNAs and or microRNAs, a process known as the regulated IRE1- dependent decay (RIDD) (Hollien and Weissman, 2006). mRNA degradation through RIDD can contribute to reestablish ER homeostasis by reducing the ER protein load.

### 3.1.3.ATF6 arm

After dissociation from HSPA5, ATF6 $\alpha$  is exported from the ER to the Golgi complex where it is cleaved by the proteases S1P and S2P (Ye et al., 2000). Cleavage by the proteases releases a fragment corresponding to the cytosolic N-terminal portion of the protein (cATF6) containing a transcriptional activation domain, a bZIP domain, a DNA-binding domain and nuclear localization signals (Almanza et al., 2019). The active ATF6 $\alpha$  migrates to the nucleus where it regulates specific transcriptional programs involved in protein quality control and ERAD. An important role for ATF6 $\alpha$  in the induction of major ER chaperones has been well established. Using primary mouse embryonic fibroblasts established from ATF6 $\alpha$ -knockout mice, it was showed that ATF6 $\alpha$  was responsible for the transcriptional induction of most ER chaperones, including HSPA5 (Yamamoto et al., 2007). Interestingly, in this work, authors also showed that ATF6 $\alpha$  heterodimerizes with XBP1 for the induction of ERAD components. As part of crosstalk mechanisms between the different arms of UPR, it has been recently shown that the ATF6 $\alpha$  branch is also important in the upregulation of CHOP after UPR induction. Precisely, it has been proposed that ATF6 $\alpha$  is responsible for the early induction of CHOP, while at latter time points this expression relies on ATF4 (Yang et al., 2020).

### 3.2. UPR-induced cell death

Unresolved ER stress and/or prolonged UPR activation can switch from a pro-survival response to the induction of cell death (Almanza et al., 2019; Hetz et al., 2020). Different mechanisms have been proposed to explain UPR-mediated cell death including apoptosis, necrosis/necroptosis and autophagy. In this manuscript I will mainly focus on UPR-mediated apoptosis.

Induction of both the intrinsic and extrinsic pathways of apoptosis can be induced and is mainly linked to IRE1 $\alpha$  and PERK activation. In particular, the induction of the pro-apoptotic TF CHOP downstream of PERK/P-eIF2 $\alpha$ /ATF4 is one of the main pathways involved in UPR-induced apoptosis (Zinszner et al., 1998). BH3- only proteins of the BCL-2 family, including BIM, PUMA, NOXA and BID are important players of the ER stress-mediated apoptosis and have been shown to be induced by CHOP, that can required to form heterodimers with C/EBP $\alpha$  to do so (Puthalakath et al., 2007). CHOP can also activate the extrinsic apoptotic pathway through the induction of the death receptor 4 (DR4) and DR5. Additionally, CHOP downregulates expression of the antiapoptotic protein Bcl-2 (McCullough et al., 2001). Interestingly, it has been proposed that the main mechanism responsible for ATF4/ CHOP -induced cell death is related with an increase in protein synthesis that results in a lethal oxidative stress and ATP depletion (Han et al., 2013). CHOP also induces the expression of ER oxidase 1 $\alpha$  (ERO1 $\alpha$ ), an oxidoreductase that produce hydrogen peroxide during disulfide bond formation, producing reactive oxygen species (ROS) and inositol-1,4,5-trisphosphate receptor (IP3R)-mediated Ca<sup>2+</sup> efflux from the ER. Ca<sup>2+</sup> released from the ER is recovered by the mitochondria, leading to the production of ROS also in the mitochondria, producing oxidative stress, stimulating cytochrome c release, and impairing mitochondrial function. All of these lead to CHOP-dependent cell death (Wang and Kaufman, 2016).

IRE1 $\alpha$  interacts with the tumor necrosis factor receptor associated factor 2 (TRAF2). This can stimulate the activity of the apoptosis signal-regulating kinase 1 (ASK1), which in turns will activate (c-Jun amino terminal kinase) JNK and the p38 MAPK to promote apoptosis. Phosphorylation by JNK will lead to inhibition of BCL-2, BCL-XL and MCL-1 and activation of BIM and BID. p38 MAPK can also lead to CHOP activation. Through its RIDD function, IRE1 $\alpha$  can also lead to the degradation of some miRNAs that

negatively regulates apoptosis as Caspase 2 and the thioredoxin-interacting protein (TXNIP), inducing inflammation and NLRP3 inflammasome activation leading to cell death. HSPA5 has been described to be a RIDD substrate, which degradation led to the induction of apoptosis (Han et al., 2009).

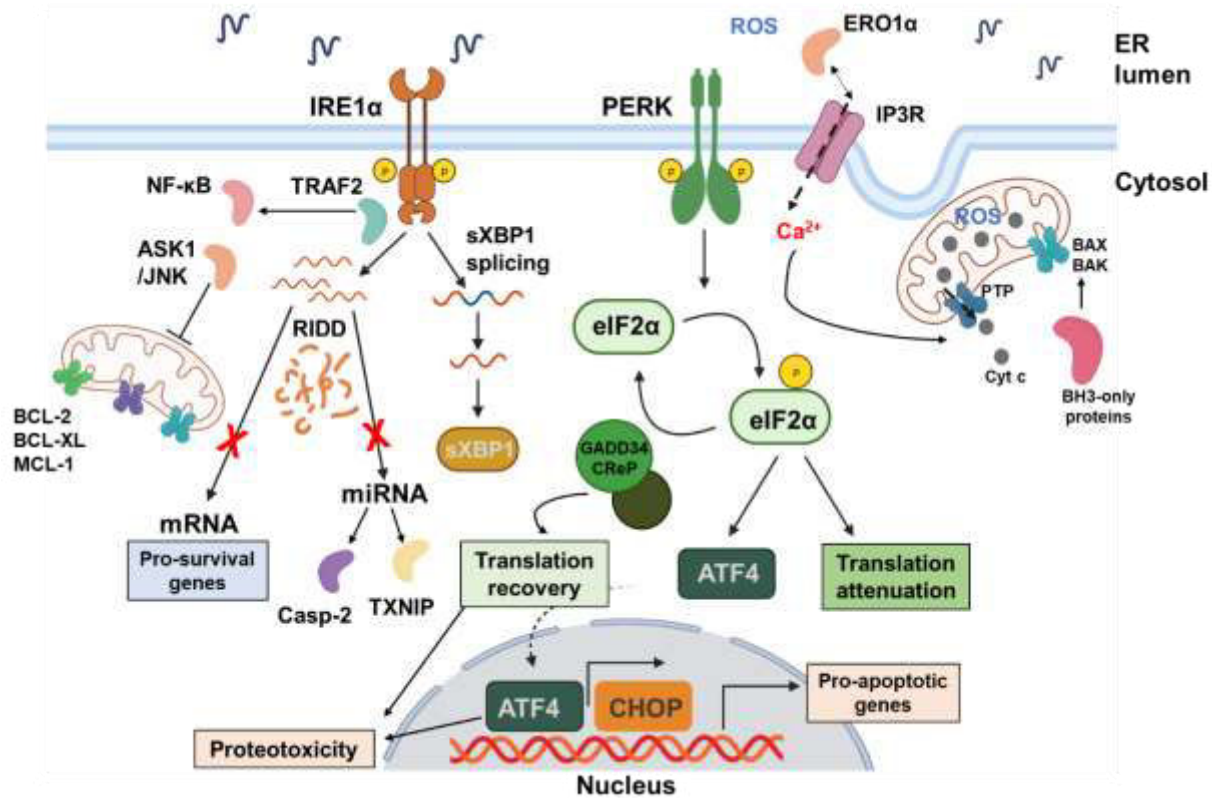


**Figure 11. UPR-induced cell death:** Signaling pathways activated downstream of PERK and IRE1α leading to cell death.

### 3.3. UPR in cancer

An altered ER function and dysregulated UPR have been related with several human pathologies including metabolic diseases, neurodegeneration and cancer. I will only present its role in Cancer. Cancer cells growth in a stressful environment characterized by nutrient deprivation, low oxygen, oxidative conditions, etc. Moreover, the oncogenic transformation process imposes highly metabolic demands with increasing protein synthesis rates and biogenic processes. All of these elements constitute bona fide triggers of ER stress and UPR activation. When UPR-induced responses allow tumor cells to adapt to these conditions, this mechanism contributes to oncogenic transformation, tumor development, angiogenesis and invasion. To note that some studies have shown the implication of only one of the UPR arms while others showed the importance of the crosstalk between the different arms to promote cancer growth. In this chapter I will briefly review how ER stress and UPR have been associated with cancer development, and then the therapeutic options based on targeting this response.

Several studies have confirmed the role of UPR in promoting different cancers (Cai et al., 2021; Ghaddar et al., 2021; Li et al., 2017; Lin et al., 2021; Tay et al., 2014). Interestingly, in some cases, the different arms of UPR seems to have an opposite role for cancer cell growth. For instance, in prostate cancer cells it was shown that the activation of the IRE1 $\alpha$  branch with a concomitant inhibition of PERK signaling were required to promote growth and survival (Sheng et al., 2015). In different models of pancreatic neuroendocrine tumors it was shown that the modulation of either IRE1 $\alpha$  or PERK (genetic and pharmacologically) resulted in a strong activation of the other arm and the induction of apoptosis (Moore et al., 2019), adding complexity to the regulation of these pathways.

The kinetic of UPR activation was investigated using an orthotopic mouse model for hepatocarcinogenesis, with IRE1 $\alpha$  signaling detected during tumor initiation and robust PERK activation in established tumors. Interestingly, only the inhibition of PERK was able to reduce the burden of hepatocellular carcinoma in animals suggesting that even though distinct arms of UPR are activated during the different phases of tumor development, in this case only PERK was important for tumor maintenance (Vandewynckel et al., 2015).

### 3.3.1. Oncogenic transformation and proteotoxic stress

Oncogenic transformation is a multistep process highly stressful for the cells. Different oncogenic events have been shown to rely in stress response pathways, including UPR, to survive. For instance, oncogenic MYC transformation induces proteotoxic stress through the activation of genes involved in ribosome biogenesis, amino acid metabolism and increasing protein synthesis rates. To cope with this and prevent proteotoxic-induced apoptosis, MYC hijack the different branches of the UPR to maintain ER homeostasis. The activation of UPR have been documented in different MYC-driven cancers including lymphomas, prostate and breast cancer, neuroblastomas and malignant rhabdoid tumors (MRTs). A Smarcb1-deficient mouse model of MRTs showed ER stress, UPR and autophagy activation as an adaptation of the cells to the proteotoxic stress induced by MYC activation (Carugo et al., 2019). The transformation of cells using the E $\mu$ -myc transgenic mouse model of lymphomagenesis, is another example of how UPR is induced following MYC activation to promote survival of the cells (Hart et al., 2012). Here, MYC activation led to the induction of ATF4 downstream of the PERK arm of UPR, promoting survival in hypoxic and nutrient deprivation conditions and regulating protein synthesis levels to prevent proteotoxic stress.

The adequate control of protein synthesis ratio in transformed cells is also a crucial point for oncogenic induced tumorigenesis. Phosphorylation of eIF2 $\alpha$  by different kinases including PERK and GCN2 is a strategic mechanism induced by MYC to prevent proteotoxic induced cell death. This has been nicely shown in a study using murine and humanized models of prostate cancer (PCa) that rely on the loss of PTEN and activation of MYC. In this work, authors showed that activation of the PERK/eIF2 $\alpha$  arm of UPR was required to reset global protein synthesis to a level that is compatible with survival and aggressive tumor development (Nguyen et al., 2018). Another example of this negative feedback loop established between MYC activation and eIF2 $\alpha$  phosphorylation was provided in colorectal cancer (Schmidt et al., 2019). In this context, the break in protein synthesis could be achieved through eIF2 $\alpha$  phosphorylation, but also through the negative regulation of the mTOR pathway through the induction of ATF4 target genes as sestrin2 (SESN2) and 4EBP1 (Park et al., 2014; Tameire et al., 2019).

### **3.3.2. Angiogenesis.**

Angiogenesis is a key process in promoting tumor growth and metastasis. Activation of the different arms of UPR have been related with this process. PERK arm of UPR has been linked to proangiogenic processes for a long time. Using K-Ras-transformed mouse embryonic fibroblast (MEFs) and a mouse model of angiogenesis, it was shown that PERK<sup>+/+</sup> tumors facilitated endothelial cell survival and functional vessel formation. Genes differentially regulated between PERK<sup>+/+</sup> and PERK<sup>-/-</sup> tumors included the proangiogenic genes vascular endothelial growth factor (VEGF) and type 1 collagen inducible protein (VCIP) (Blais et al., 2006). In GBM cells, it was recently showed that PERK induces the expression of the proangiogenic factor peptidylglycine  $\alpha$ -amidating monooxygenase (PAM) (Soni et al., 2020). PERK-eIF2 $\alpha$  axis of UPR regulates the mesenchymal-endothelial transition of cancer-associated fibroblasts (CAFs) that is responsible for tumor angiogenesis in the context of pancreatic ductal adenocarcinoma (PDAC) (Cai et al., 2021).

In GBM cells, a dual role for the IRE1 $\alpha$  RNase activity concerning the function on invasion processes was described. This work demonstrated that the IRE1 $\alpha$ /sXBP1 axis was pro-tumorigenic by promoting tumor infiltration by immune cells, angiogenesis and invasion. Strikingly, the degradation of mRNAs through RIDD could antagonize tumor invasion and angiogenesis, showing antagonistic roles of the downstream effectors of IRE1 $\alpha$  in tumors (Lhomond et al., 2018). Breast cancer cells also exhibit constitutive IRE1 $\alpha$  RNase activity with an elevated IRE1 $\alpha$  gene signature associated with a more mesenchymal-like phenotype, increased invasiveness and a worse clinical outcome (Logue et al., 2018).

### **3.3.3. Hypoxia and oxidative stress**

Adaptation of cancer cells to hypoxic conditions has been related with the activation of the different arms of UPR. For instance, the induction of PERK and phosphorylation of eIF2 $\alpha$  leading to a decrease protein synthesis was shown to be critical in adaptation to hypoxia in different cancer cells (Blais et al., 2004; Koumenis et al., 2002). Similarly, other studies showed that sXBP1, activated downstream of IRE1 $\alpha$ , was important for the survival of RAS- and MYC-transformed cancer cells in hypoxic conditions *in vitro* and *in vivo* (Romero-Ramirez et al., 2004). This role was further confirmed in different *in vitro* and *in vivo* models of TNBC, showing that XBP1

was involved in TNBC tumorigenicity by assembling a transcriptional complex with HIF1 $\alpha$  to regulate the expression of HIF1 $\alpha$  targets (Chen et al., 2014).

The activation of PERK can also be involved in the regulation of different steps of tumor progression and survival to stressful conditions. In particular, PERK has been related with antioxidant responses in stressed cells mainly through activation of the P-eIF2 $\alpha$ /ATF4 axis. Specifically, ATF4 controls the expression of genes that contribute to maintain the redox balance in the cell and increase the biosynthesis of the antioxidant glutathione (Harding et al., 2003; Rouschop et al., 2013). Another role of PERK in protecting cells from oxidative stress is achieved through an eIF2 $\alpha$ -independent activation and nuclear import of the Nrf2 TF, regulating genes involved in anti-oxidant responses (Cullinan et al., 2003). In this case, Nrf2 was demonstrated to be a direct substrate of PERK, with phosphorylation by this kinase leading to the activation of the protein.

### **3.3.4. Metabolism**

Specific metabolic addictions of some types of tumors have been described, including MYC-driven tumors. Glutamine (Gln) for example, is used as a building block for proteins but also serves as a carbon and nitrogen donor for amino acid synthesis and nucleotide biogenesis. This is also the case for glycine and serine which are required to maintain and increase the flux through the one-carbon and methionine cycles (Wortel et al., 2017). In different models of MYC-driven cell transformation and lymphomagenesis it was shown that MYC activates ATF4 to control the expression of genes involved in the regulation of amino acid and protein synthesis (Tameire et al., 2019). ATF4 is known to control genes participating in amino acid metabolism and in this context, it has been shown to play a critical role in sustaining survival of MYC-driven Neuroblastoma (NB) cells subjected to glutamine deprivation. Also using NB cells, it was shown that -NMYC amplified cells showed increased transcriptional activation of the serine-glycine one-carbon (SGOC) biosynthetic pathway and an increased dependence on this pathway for supplying glucose-derived carbon for serine and glycine synthesis. ATF4 was required in these cells for the transcriptional activation of the SGOC pathway (Xia et al., 2019).

Similarly, c-MYC- and N-MYC-driven cancers, including Burkitt's lymphoma (BL) and NB respectively, rely on the IRE1 $\alpha$ /XBP1 pathway of the UPR. In this case,

the IRE1 $\alpha$ /XBP1 signaling pathway induced stearoyl-CoA desaturase (SCD) transcription, which generates unsaturated lipids required for ER membrane homeostasis. Here, the activation of the IRE1 $\alpha$ /XBP1 pathway was involved in the regulation of lipid metabolism to promote cell growth (Xie et al., 2018). Further understanding of the role of IRE $\alpha$  in controlling lipid metabolism was provided recently. DGAT2 mRNA, encoding the rate-limiting enzyme in triacylglycerols (TAG) biosynthesis was confirmed to be a RIDD target. Inhibition of IRE1 $\alpha$ , leads to DGAT2-dependent accumulation of TAGs in lipid droplets and sensitizes TNBC cells to nutritional stress (Almanza et al., 2022).

### 3.4. UPR in MB

Only few studies have assessed the role of UPR in MB tumors and they concern only data related with the SHH driven group. In an interferon- $\gamma$  (IFN $\gamma$ )-induced mouse model of SHH MB, it was shown that activation of the PERK arm of UPR was related with tumor development through the induction of VEGF-A and promotion of angiogenesis. Interestingly, the inactivation of GADD34 enhanced PERK expression and contributed to MB formation (Lin et al., 2011a). Using non-G3 cell lines of MB, it was shown that PERK/eIF2 $\alpha$  pathway activation promoted MB cell migration and invasion through induction of VEGF-A (Jamison et al., 2015).

Additional data was obtained using the Patched1 heterozygous deficient (Ptch1<sup>+/-</sup>) mouse model of MB. Here, authors demonstrated the activation of the PERK arm on premalignant GCPs in young Ptch1<sup>+/-</sup> mice and MB cells in adult mice. Interestingly, PERK haploinsufficiency decreased the incidence of Ptch1<sup>+/-</sup>-driven MB and led to increased apoptosis in GCPs cells, indicating that PERK contributes to SHH MB formation through inhibition of apoptosis (Ho et al., 2016). Another study investigated the role of GADD34 in this context. Interestingly, a heterozygous mutation of GADD34 enhanced PERK activation and increased the incidence of SHH MB in adult mice while the homozygous mutation greatly increased PERK activation but decreased the incidence of MB in adult mice. The homozygous mutation led to an increased apoptosis of premalignant GCPs, while neither the homozygous nor the heterozygous mutation of GADD34 had an effect on MB cells in the adult Ptch1<sup>+/-</sup> mice (Stone et al., 2016). These results suggest a role for the PERK signaling pathway activation during SHH MB tumor formation. A finetune regulation of the activity of the pathway seems to be required since a modest activation potentiates tumor formation while a complete unleash can lead to apoptotic cell death and decreased incidence.

Recently, germline loss-of-function variants of *ELP1* were reported in 14% of pediatric patients of the SHH MB group. ELP1 is the largest subunit of the Elongator complex, which catalyzes translational elongation. ELP1-associated SHH MB tumors showed translational deregulation and UPR activation, suggesting that disruption of protein homeostasis could have a pathogenic role in SHH MB (Waszak et al., 2020).

### 3.5. Targeting the UPR

Numerous types of cancer showed basal ER stress that can result from intrinsic or extrinsic factors, and rely on the activation of UPR to survive and continue to growth. From here, the idea of inhibiting pro-survival UPR downstream signaling pathways or enhancing cell death inducing mechanisms represent promising strategies for cancer treatment. The existence of a basal ER stress with a constitutively activated UPR in cancer cells make these cells more prone to bypass the threshold defining the survival-death response. This idea has been exploited as a therapeutic strategy for different type of cancers.

#### 3.5.1. Inhibition of basal UPR activation:

The two activities of IRE1 $\alpha$  can be targeted with pharmacological inhibitors (Raymundo et al., 2020). However, inhibition of the kinase activity has not been largely exploited, especially in the context of cancer. Kinase-inhibiting RNase-Attenuators (KIRAs) inhibitors are some of the molecules developed to inhibit IRE1 $\alpha$  kinase activity. In the contrary, inhibition of the endoribonuclease activity has helped to elucidate the role of this pathway in different cancers and served to demonstrate the therapeutical potential of its inhibition. The endoribonuclease inhibitor 4 $\mu$ 8C (Cross et al., 2012) suppressed the proliferation of colon cancer cells *in vitro* and xenograft growth *in vivo* (Li et al., 2017). Inhibition of IRE1 $\alpha$  using this inhibitor was shown to reduce tumor burden in a chemically induced mouse model of HCC (Pavlović et al., 2020). B-I09 is another inhibitor of IRE1 $\alpha$  RNase activity that effectively induced leukemic regression in a mouse model of chronic lymphocytic leukemia (CLL) (Tang et al., 2014). It has been also successfully used to suppress CARM1-expressing ovarian cancer, with an interestingly synergism with immune checkpoint blockade (Lin et al., 2021). The IRE1 $\alpha$  RNase-specific inhibitor MKC8866 has been used in different models of breast and prostate cancer, contributing in both cases to show the dependence of MYC-driven cancers on the activation of the IRE1 $\alpha$  /XBP1 pathway (Sheng et al., 2019; Zhao et al., 2018). Interestingly, this drug was recently shown to be efficient in sensitizing GBM cells to chemo/radiotherapy in a preclinical model of GBM (Le Reste et al., 2020).

PERK kinase inhibitors have been also developed. For instance, GSK2606414 is an orally available, potent selective inhibitor of PERK that has been mostly studied as a memory-enhancing drug. However, it has also shown efficacy in decreasing tumor

growth in a subcutaneous mouse model of pancreatic adenocarcinoma (Axten et al., 2012). GSK2606414 was also used recently in mutant KRAS-driven mouse models of lung tumor to evidence the potential of targeting the PERK/eIF2 $\alpha$  axis in for the treatment of lung cancer (Ghaddar et al., 2021). GSK2656157 is an ATP-competitive inhibitor of PERK that led to the inhibition of multiple human tumor xenografts growth in mice. In these models, the effect of PERK inhibition was linked to an altered amino acid metabolism, decreased blood vessel density, and vascular perfusion (Atkins et al., 2013).

The inhibition of the translational repression induced by P-eIF2 $\alpha$  is another strategy that is being explored from therapeutic point of view for cancer treatment. ISRIB, is a small molecule known to revert the effect of eIF2 $\alpha$  phosphorylation by promoting eIF2B dimerization, increasing its GEF activity and desensitizing it to inhibition by P-eIF2 $\alpha$  (Sidrauski et al., 2013, 2015). ISRIB has shown sensitizing properties in different models of pancreatic cancer that were resistant to Gemcitabine (Palam et al., 2015). Interestingly, the activation of the PERK/eIF2 $\alpha$  arm of UPR was shown to be crucial to reset global protein synthesis to a level compatible with survival in prostate cancer (PCa) cells driven by the loss of PTEN and activation of MYC. In this context, reverting the effect of eIF2 $\alpha$  phosphorylation using ISRIB triggered cytotoxicity against and aggressive model of metastatic prostate cancer (Nguyen et al., 2018).

### **3.5.2. Overactivation of basal UPR activation:**

As described before, UPR activation induced by ER stress will lead to different transcriptional and translational responses in the cell that will restore homeostasis and promote survival of the cells. However, when ER stress is unmanageable and/or UPR activation is too long and strong, cell death mechanisms will be induced. From here, another strategy to target UPR in cancer, is based on the use of molecules that will enhance this response. This is of particular interest in in cells that have a basal level of activation of UPR, making them more prone to bypass the cytoprotective threshold and induce cell death.

This strategy has been validated with the use of molecules that inhibit chaperones, interfere with the process of protein degradation, like inhibitors of the proteasome system, or other compounds that can enhance ER stress and UPR activation by disturbing Ca<sup>2+</sup> signaling, for example.

HSPA5 is the main ER chaperone and has a major role as controlling UPR pathways activation as described before. Inhibition of the chaperone activity of HSPA5 has been investigated as an approach to induce cytotoxic UPR. HA15 is one of the best examples of HSPA5 inhibitors described so far. This compound was shown to induce melanoma cell death by apoptosis and autophagy that resulted from the induction of a massive ER stress and UPR. In addition to melanoma, the efficacy of HA15 in inducing cancer cell death has been assessed in different models including breast cancer, human colorectal adenocarcinoma and pancreatic cancer (Cerezo et al., 2016). Other chaperones residing in the ER include GRP94, another “glucose-regulated” chaperone, calreticulin and calnexin, which are Ca<sup>2+</sup>-binding chaperones and protein disulfide isomerases, chaperones belonging to the thioredoxin superfamily. All of these chaperones are important players of the UPR, and protect cells from ER stress-induced cell death. Similarly, HSP70 and HSP90 which are cytosolic chaperones, are induced to help the cells to cope with proteotoxic stress (Kabakov et al., 2020). Conceptually, inhibition of all of these chaperones can lead to a non-resolvable ER stress and induced cancer cell death.

A similar strategy consists to disturb the process of protein degradation to induce an abnormal accumulation of unfolded/misfolded proteins and activate cytotoxic mechanisms. The therapeutic potential of targeting the ubiquitin proteasome system has been investigated in numerous cancers (Marciniak et al., 2022). Bortezomib, carfilzomib and ixazomib belong to the first-generation proteasome inhibitors and currently approved for the treatment of multiple myeloma or mantle-cell lymphoma (MCL) (Manasanch and Orłowski, 2017). Novel proteasome inhibitors include the orally bioavailable boronate ixazomib, oprozomib, marizomib, and the boronate delanzomib. From these inhibitors, ixazomib is the first oral second-generation proteasome inhibitor that was approved by the FDA for the treatment of relapsed/refractory multiple myeloma (Facon et al., 2021). Oprozomib and marizomib are in early-phase clinical trials for cancer treatment (Manasanch and Orłowski, 2017). Marizomib is able to penetrate the blood brain barrier and its efficacy is being investigated in GBM patients (Bota et al., 2021; Di et al., 2016). Interestingly, the mechanism of action of Marizomib is linked to the induction of a strong UPR leading to cell death (Lin et al., 2019).

In conclusion, activation of the different arms UPR as a mechanism responding to different stresses has been shown to be crucial for the survival and adaptation of

different types of tumor cells. In this way, inhibition of these signaling pathways has a therapeutic potential. More interestingly, since cancer cells have a basal ER stress and show a constitutive activated UPR, these cells are more sensitive to a complete unleashing of the system to induce cell death. This second aspect also results very attracting for the research and development of new therapeutic strategies for cancer treatment.



## 2 RESULTS

---

Medulloblastoma (MB) is an embryonal tumor originating in the cerebellum and the most common pediatric brain tumor of childhood. It is a very heterogeneous disease with four molecular groups that have been further subdivided in subtypes. Patients from G3 have the worse prognosis and the biology of this group is not completely understood. Extensive research has been made to try to identify oncogenic hits that can cooperate with MYC to produce Group 3 tumors or to decipher new vulnerabilities that could be therapeutically targeted. With this aim, we made a RNAi-based targeted screen in a G3 cell line, to identify new potential therapeutic targets. We found that HSPA5 is an interesting hit, since its downregulation decreased the proliferation of cells. HSPA5 is the master regulator of the UPR, a pivotal mechanism that can help cells to survive in stressful conditions but can also induce cell death, opening a therapeutic window. UPR is an endoplasmic stress response mediated by three main effectors downstream of HSPA5: Activating Transcription Factor 6 (ATF6), PRKR-like ER kinase (PERK) and Inositol-requiring protein 1 $\alpha$  (IRE1 $\alpha$ ). After activation, the PERK kinase will phosphorylate the translation initiation factor eIF2 $\alpha$ , resulting in the decrease in global protein synthesis with the concomitant translation of specific mRNA like ATF4 and CHOP. If ER stress cannot be resolved, these same effectors can induce cell death. In general, cancer cells are exposed to stressful conditions and rely in stress response mechanisms to survive. It is thought that cancer cells can have a basal level of ER stress and UPR activation, that could make them more sensitive to an overactivation of these pathways.

In this context, the objective of my PhD is to investigate:

3. if HSPA5 could be considered as a new dependency for G3 tumors and
4. what are the molecular mechanisms involved in the response to HSPA5 inhibition that can provide new insights about G3 vulnerabilities.

To answer these questions, I used different G3 and non G3 cell lines, Patient Derived Xenografts (PDXs) and mouse models, to assess the role of HSPA5 and the UPR in G3 MB.

### **1. G3 cells are dependent on HSPA5 to survive.**

The inhibition of HSPA5 using the tool compound HA15 or shRNA lead to a decrease of G3 cell growth *in vitro*. This decrease seems to be the result of apoptosis induction with no effect on cell cycle. The knock-down (KD) of HSPA5 also lead to a delay in tumor growth in orthotopic models of G3 tumors in mice, increasing the survival of mice that were grafted with HSPA5-KD cells, indicating that indeed G3 tumor cells depend on HSPA5 to survive.

### **2. HSPA5 KD induced Unfolded Protein Response (UPR) activation.**

HSPA5 KD induced the activation of the three branches of the UPR as confirmed by RNA-seq analysis and Western blots. Interesting, only the PERK arm of UPR is responsible for the cell death induced after UPR activation in HSPA5 KD cells. G3 cells are highly sensitive to UPR activation either through HSPA5 KD or using drugs that lead to activation of this response.

### **3. Phosphorylation of eIF2 $\alpha$ could be a crucial node of regulation of G3 cells**

The phosphorylated status of eIF2 $\alpha$  seems to be an essential node of regulation for G3 cells, since its activation either through kinases activation or through the inhibition of the phosphatases involved in its regulation, lead to a decrease of G3 cells growth *in vitro*. The KD of the CReP (PPP1R15B) phosphatase lead to a delay in tumor growth and an increase in mice survival when G3 cells are grafted in cerebellum of immunocompromised mice.

**1.1. Article 1: In preparation**



**Title: Control of eIF2 $\alpha$  dephosphorylation by CReP is a central node in G3 MB.**

**Authors:** Liliana Mirabal-Ortega<sup>1,2,3,4,5,6</sup>, Sabine Druillennec<sup>1,2,3,4,5,6</sup>, Laurence Mery<sup>1,2,3,4,5,6</sup>, Magalie Larcher<sup>1,2,3,4,5,6</sup>, Dave Yong Xiang Ng<sup>1,2,3,4,5,6</sup>, Kevin Muller<sup>7</sup>, Marie-Pierre Montero<sup>7</sup>, Sofia Gaid<sup>1,2,3,4,5,6</sup>, Sophie Leboucher<sup>1,4</sup>, Bertrand Duvillie<sup>1,2,3,4,5,6</sup>, Franck Bourdeaut<sup>5,8,9,10</sup>, François Doz<sup>5,8,9,10</sup>, Véronique Marsaud<sup>1,2,3,4,5</sup>, Jacob Torrejon<sup>1,2,3,4,5</sup>, Olivier Ayrault<sup>1,2,3,4,5</sup>, Alain Eychene<sup>1,2,3,4,5,6</sup>, Rachid Benhida<sup>11,12</sup>, Stéphane Rocchi<sup>11,12,13,14,15</sup>, Eric Chevet<sup>16,17,18</sup>, Eddy Pasquier<sup>7</sup>, Celio Pouponnot<sup>1,2,3,4,5,6\*</sup>

**Affiliations:**

<sup>1</sup>Institut Curie, Orsay, France, <sup>2</sup>CNRS UMR 3347, Centre Universitaire, Orsay, France, <sup>3</sup>INSERM U1021, Centre Universitaire, Orsay, France, <sup>4</sup>University Paris-Saclay, Orsay, France, <sup>5</sup>PSL Research University; Paris, France, <sup>6</sup>Equipe labélisée Ligue Contre le Cancer (LCC), <sup>7</sup>Reverse Molecular Pharmacology in Pediatric Oncology, Centre de Recherche en Cancérologie de Marseille (CRCM), Aix-Marseille Université, CNRS, Inserm, Institut Paoli Calmettes ; Marseille, France, <sup>8</sup>Institut Curie, Paris, France, <sup>9</sup>SIREDO Oncology Center (Pediatric, Adolescent and Young Adults Oncology), Institut Curie, Paris, France, <sup>10</sup>INSERM U830, Institut Curie, Paris, France, <sup>11</sup>Institut de Chimie de Nice UMR UNS-CNRS 7272, Nice, France, <sup>12</sup>Université Nice Sophia Antipolis, Nice, France, <sup>13</sup>INSERM U1065, Nice, France, <sup>14</sup>Centre Méditerranéen de Médecine Moléculaire (C3M), Nice, France, <sup>15</sup>Service de Dermatologie, Hôpital Archet II, Nice, France, <sup>16</sup>INSERM U1242, Rennes, France, <sup>17</sup>Université de Rennes 1, Rennes, France, <sup>18</sup>Centre de Lutte Contre le Cancer Eugène Marquis, Rennes, France

\*Corresponding author. Email: celio.pouponnot@curie.fr.

**One Sentence Summary:** eIF2 $\alpha$  represents the central node of UPR-mediated cell death after HSPA5 inhibition in Group 3 Medulloblastoma

**Abstract:**

Medulloblastoma (MB) is the most frequent malignant brain tumor in childhood with group 3 (G3) patients having the worst prognosis. Through a targeted siRNA-based screen, we identified HSPA5 (Heat Shock Protein 5) as a potential vulnerability in G3 MB. As a known regulator of the unfolded protein response (UPR), knock-down (KD) of HSPA5 leads to activation of the three arms of this pathway, namely ATF6, IRE1 $\alpha$  and PERK. HSPA5 KD induces cell death and slows down G3 MB growth *in vivo*. Accordingly, using a targeted pharmacological screen, we showed that G3 MB cells are particularly sensitive to UPR inducers, the PERK arm being the main mediator of cell death induction. This arm inactivates global translation through eIF2 $\alpha$  phosphorylation, leading to the specific translation of ATF4 and CHOP. Unexpectedly, KD of ATF4 or CHOP does not rescue cell death. In contrast, our results point to the inactivation of eIF2 $\alpha$  by phosphorylation as the central mechanism of this response. We identified PPP1R15B, an eIF2 $\alpha$  phosphatase also known as CreP, as the main phosphatase that keeps eIF2 $\alpha$  in its active form in basal conditions, protecting MB cells from apoptosis and is required for MB growth *in vivo*. Taken together, our work established that G3 MB cells are particularly sensitive to UPR activation due to their sensitivity to eIF2 $\alpha$  inactivation, likely highlighting their dependence on translation. Regulation of eIF2 $\alpha$  phosphorylation represents a crucial node in G3 MB making these tumors vulnerable to different mediators of this phosphorylation including CReP inactivation.

## INTRODUCTION

Medulloblastoma (MB) is the most frequent malignant brain tumor in childhood (1). It is an embryonic tumor originating in the cerebellum. MB is a heterogeneous disease and four molecular groups have been identified: WNT, SHH, Group 3 (G3) and Group 4 (G4) (2–4). These groups differ in terms of molecular and clinical features. The overall survival (OS) of patients is around ~70-80%, but the prognosis varies according to the molecular group, histopathological variants and clinical features including age, metastatic disease and extent of tumor resection (5). Importantly, survivors suffer from severe side effects including: neurocognitive and neuropsychological damages, neuroendocrine dysfunction, hearing loss, growth problems, and secondary malignancies.

G3 is the most aggressive group and represents ~20-25% of all MB cases. It is predominant in infants and early childhood. G3 is the group with the highest metastatic rate (40-50%) and the poorest 5-years OS (<60%). Despite intensive research, no common driver pathway has been identified for G3 tumors besides MYC overexpression, with MYC being amplified in 15-20% of G3 patients. In accordance with MYC overexpression, these tumors show transcriptomic and proteomic signatures related to mRNA processing, transcription and translation (6, 7). Among other alterations, the most prevalent oncogenic hit in G3 leads to the overexpression of GF11 and GF11B transcription factors as a consequence of enhancer hijacking events that occurs in ~20% of patients (8, 9). Recently, subclassification in subtypes has shown that tumors which harbor MYC amplification or MYC overexpression are of particular poor prognoses (10). Despite this knowledge and the focus of research on G3 MB, the biology of this group remains poorly understood. G3 patients continue to receive aggressive and toxic treatment regimens that do not consider their molecular features.

HSPA5, also known as GRP78 (Glucose-related protein 78) or BiP (Immunoglobulin heavy chain Binding Protein) (11, 12), is a chaperone of the endoplasmic reticulum (ER). As an ER-chaperone, HSPA5 functions involved folding, holding and translocating the newly synthesized polypeptides across the ER membrane. It also contributes to clearance of unfolded proteins by targeting them for ER-associated degradation (ERAD) and to maintain  $Ca^{2+}$  homeostasis in this organelle. HSPA5 is the master regulator of the Unfolded Protein Response (UPR), an important mechanism that allows cells to cope with

ER stress due to the accumulation of misfolded/unfolded proteins. In normal physiological conditions, HSPA5 is bound to the three effectors of the UPR, Activating Transcription Factor 6 (ATF6), PRKR-like ER kinase (PERK) and Inositol-requiring protein 1 $\alpha$  (IRE1 $\alpha$ ), preventing their activation. In conditions of ER stress, the chaperone is relieved from these effectors allowing their activation with the initiation of the downstream signaling pathways (13, 14).

IRE1 $\alpha$  is a transmembrane protein kinase with endoribonuclease activity. The activation of IRE1 $\alpha$  under ER stress leads to the cleavage of a 26-nucleotide intron from the X-box binding protein 1 (XBP1) mRNA, producing the spliced form of the sXBP1 transcription factor. sXBP1 has a key role in UPR by controlling the expression of genes involved in protein folding, secretion, endoplasmic reticulum-associated degradation (ERAD), and lipid synthesis. The endoribonuclease activity of IRE1 $\alpha$  is also involved in the cleavage and degradation of some mRNAs and/ or microRNAs, a process known as the regulated IRE1- dependent decay (RIDD) (15). For its activation, ATF6 $\alpha$  is exported from the ER to the Golgi complex where it is cleaved by the proteases S1P and S2P (16). The active ATF6 $\alpha$  transcription factor regulates specific transcriptional programs involved in protein quality control and ERAD as HERPUD1. ATF6 $\alpha$  is also responsible for the transcriptional induction of most ER chaperones, including HSPA5 (17). Activated PERK triggers the phosphorylation of the eukaryotic translation initiation factor 2 subunit 1 (P-eIF2 $\alpha$ /EIF2S1), resulting in a transient attenuation of protein synthesis (18, 19). The phosphorylation of eIF2 $\alpha$  also leads to the translation of specific mRNAs including the transcription factor ATF4 which in turn will induce the expression of the CAAT/enhancer-binding protein (C/EBP) homologous protein (CHOP)/GADD153. ATF4 and CHOP control the expression of genes involved in protein folding, antioxidant responses, autophagy and amino acid metabolism (18).

UPR is considered as a cytoprotective mechanism when its activation leads to the resolution of ER stress. However, when the response is intense and over-sustained, it becomes cytotoxic by inducing cell death (20, 21). The induction of the pro-apoptotic transcription factor CHOP downstream of PERK/P-eIF2 $\alpha$ /ATF4 is one of the main pathways involved in UPR-induced apoptosis (22, 23). CHOP can induce the expression of BH3- only proteins of the BCL-2 family and downregulates the expression of the anti-

apoptotic protein Bcl-2 (24). It has also been proposed that ATF4/CHOP can induce cell death by increasing protein synthesis that results in lethal oxidative stress and ATP depletion (25).

Numerous types of cancer possess basal ER stress levels that can result from intrinsic or extrinsic factors and rely on the activation of the UPR to survive and continue to grow. This specific characteristic of cancer cells opens a therapeutic window for manipulating UPR activation. This has been achieved either by inhibiting the pro-survival UPR downstream signaling pathways or by enhancing cell death following overactivation of the UPR (26, 27). For example, HA15, a HSPA5 inhibitor, has been characterized and shown to induce a dramatic level of cell death in melanoma cells but not in normal cells by inducing a strong and sustained UPR (28).

In this study, through an siRNA screen leading to the identification of HSPA5 as a vulnerability in G3 MB, we investigated the role of UPR in G3 MB.

## RESULTS

### G3 MB cells are sensitive to HSPA5 inhibition

To identify new potential vulnerabilities in G3 MB, we performed an siRNA-based targeted screen in a G3 cell line. We evaluated the effect of the knock-down (KD) of different selected genes on the viability of the G3 HD-MB03 cell line using CellTiter-Glo and IncuCyte® (Fig.1A). A total of 62 genes were included in the screen (Supp Table 1). This led to the identification of HSPA5 (Fig.1B, Fig Supp.1), a chaperone of the ER and the master regulator of UPR. To confirm the sensitivity of G3 cells to HSPA5 inhibition, we used HA15 (28), a direct inhibitor of HSPA5 ATPase activity, as a tool compound. G3 cell growth (D283Med, D425Med, D458Med and HDMB03) was negatively impacted by HA15 in a dose dependent manner while non-G3 cells (ONS-76) and the non-cancerous cell line RPE1 were mostly unaffected by this treatment (Fig.1C). IC50 values were between 2 to 5  $\mu$ M for G3 cells, while 86 $\mu$ M and 20 $\mu$ M and were required to achieve the 50% inhibition of cell growth for ONS-76 and RPE-1 (Fig.1D, Table 1). These results suggest that G3 MB cells are more sensitive to HSPA5 inhibition than non-G3 and non-cancerous cells.

### HSPA5 is important for G3 MB growth *in vitro* and *in vivo*

To confirm HSPA5 as a potential therapeutic hit for G3 cells, we identified two shRNAs (shHSPA5#2 and shHSPA5#5) which efficiently knocked-down (KD) HSPA5 expression in two different G3 cell lines, D458Med (Fig.2A) and D425Med (Fig Supp.2A). We evaluated their effects on cell growth (Fig.2B and Fig Supp.2B). HSPA5 KD induced a strong decrease in D458Med cell viability (Fig.2B). Cell cycle analyses revealed no major differences in the number of cells in the different phases of the cycle (Fig.2C). To investigate how HSPA5 KD was inducing decreased cell growth, we analyzed the occurrence of apoptosis by flow cytometry and found an important increase in the number of cells positive for Caspase 3 staining in the HSPA5 KD cells compared to the control cells (Fig.2D). Similar results were obtained in D425Med cells (Fig Supp.2A-D), another G3 cell line, further validating that HSPA5 is important for G3 cell growth by protecting cells from apoptosis.

To confirm this dependency *in vivo*, we orthotopically grafted D458Med-Luc cells transduced with the different shRNAs in the cerebellum of nude mice (Fig.2E). Tumor growth was followed by bioluminescence imaging (BLI) (Fig.2F-G). HSPA5 KD delayed tumor growth as evidenced by BLI signals (Fig.2G) and histological analyses (Fig.2H-I). The tumor growth delay was translated into a survival increase in mice that were grafted with HSPA5-KD cells (Fig.2J). Similar results were obtained with D425-Luc cells (Fig Supp.2E-F), and importantly in two G3 patient-derived xenograft (PDX) models (PDX-3, Fig2K-M and PDX-7 Fig Supp.2G). Taken together, these results indicate HSPA5 as a potential vulnerability for G3 MB as suggested by the initial siRNA screen.

### **HSPA5 KD induces the activation of the three arms of UPR**

To explore the molecular mechanisms that could explain the effects of HSPA5 KD in D425Med cells, we performed RNA-seq analysis. A total of 40 genes were found to be significantly differentially expressed genes (DEG) between the KD condition compared to control cells (Fig.3A-B). Gene ontology (GO) analysis revealed that deregulated genes participate mainly in ER stress and UPR responses, with activation of the three arms of UPR (Fig.3C). We performed gene expression analysis (GSEA, Gene set enrichment analysis) using a list of genes that are known to be specifically activated by the UPR, refer as the “UPR gene signature” from here (29). We found a strong enrichment of the UPR gene signature in the KD cells as compared to control (Fig.3D-E). Similarly, we found that the signature of each individual arms, namely PERK, IRE1 $\alpha$  and ATF6 $\alpha$ , were also enriched in KD cells (Fig Supp.3A-B).

To confirm UPR activation upon HSPA5 KD, we performed western blot analysis in two different G3 cell lines and one G3 PDX (Fig.4A-C). The KD of HSPA5 strongly induced the expression of downstream targets of each arm, namely HERPUD1 (ATF6 arm) and the spliced form of XBP1 (IRE1a arm). In the case of the PERK arm, we looked at the level of eIF2 $\alpha$  phosphorylation compared to the total eIF2 $\alpha$  as a first readout of the activation of the pathway. Since this modification can be transient and difficult to detect as it has been previously described (30), we also looked at the induction of ATF4/CHOP as a confirmation of the activation of this arm, which is also the case after HSPA5 KD.

Altogether, this indicated that HSPA5 inhibition efficiently induced the three arms of UPR in G3 cells coupled with the induction of cell death.

To confirm the overall sensitivity of G3 cells to UPR activation in a larger scale, we performed a screen based on cell viability with selected compounds known to either promote ER stress/UPR or, in contrast, inhibit these pathways (Fig.4D). We found that G3 MB cell lines are more sensitive to the induction of UPR activation as compared to non-G3 MB cell lines (Fig.4E), while no difference was observed between the two groups with compounds that inhibit UPR (Fig.4F). Taken together, our results showed that G3 cells are more sensitive to UPR-mediated cell death.

### **The inhibition of PERK rescues HSPA5 KD-induced cell death**

To further determine which specific arm of UPR is responsible for cell death induction in HSPA5 KD G3 cells, we inhibited each individual arm using specific inhibitors in D458Med (Fig.5) and in D425Med (Fig Supp.4). The different inhibitors did not have a major effect in control conditions, suggesting that none of the 3 arms play a major cytoprotective role in G3 MB basal conditions (Fig.5A, Fig Supp.4A). We found that whereas inhibition of the IRE1 $\alpha$  (MKC8806) and ATF6 $\alpha$  arms (Ceapin-A7) has no effect on cell death, PERK inhibition using GSK2606414 in contrast, rescued cell death in HSPA5 KD cells. The effective inhibition of the corresponding arm by each inhibitor was confirmed by western blot (Fig.5B, Fig Supp.4B). To further probe into the mechanisms of cell death induction, we investigated whether KD of the downstream effector of PERK, ATF4 or CHOP can rescue cell death since they have been shown to be involved in UPR-mediated apoptosis in previous reports (23, 28). Surprisingly, neither the KD of ATF4 (Fig.5C-D, Fig Supp.4C-D), nor CHOP (Fig.5E-F, Fig Supp.4E-F), was sufficient to rescue cell death induction in HSPA5 KD cells.

### **ISRIB treatment partially rescues HSPA5 KD-induced cell death**

To investigate if the inhibition of eIF2 $\alpha$  by the PERK arm could rescue the effect of HSPA5 KD, we treated the D458Med (Fig.6) and D425Med (Fig Supp.5) cells with ISRIB. ISRIB is a small molecule that allows cells to bypass the inhibition of eIF2 $\alpha$  by phosphorylation and to re-establish protein synthesis. We monitored the effect of ISRIB in HSPA5 KD cells by the decrease of ATF4 and CHOP expression (Fig.6B and Fig

Supp.5B). Treatment with ISRIB in HSPA5 KD cells partially rescued cell death (Fig.6A and Fig Supp.6A), indicating that G3 cells are sensitive to eIF2 $\alpha$  inhibition.

To identify the genes that were involved in this response, we performed an RNA-seq analysis in shHSPA5 KD and control cells treated with DMSO or ISRIB. We identified 37 differentially expressed genes that were downregulated in the shHSPA5 KD cells treated with ISRIB compared to the DMSO treated cells and performed GO analyses. Genes deregulated in the ISRIB-treated cells are related with amino acid transport, biosynthesis and to a lesser extent in lipid homeostasis as well as ER stress response pathways (Fig.6C-D). ISRIB did not induce any major changes in the general UPR signature (Fig.6E), nor in the ATF6 $\alpha$  or IRE1 $\alpha$  arms (Fig Supp 5.C-D). In contrast, the PERK signature genes were decreased in the HSPA5 KD cells treated with ISRIB (Fig.6F). This last result was also confirmed by gene expression analysis (Fig.6G). These results confirm that HSPA5 KD-mediated cell death was linked to the activation of the PERK arm and point towards the notion that the inhibition of eIF2 $\alpha$  is an important regulatory mechanism in G3 MB.

To further confirm the key role of eIF2 $\alpha$  phosphorylation in G3 MB, we investigated the effect of different drugs known to modulate it. Salubrinal is a dual inhibitor of the two eIF2 $\alpha$  phosphatases, Raphin1, an inhibitor of CReP (PPP1R15B), BTdCPU, a potent heme-regulated inhibitor kinase (HRI) activator, another eIF2 $\alpha$  kinase, and GSK-621, which is a specific AMPK activator which strongly induces eIF2 $\alpha$  phosphorylation. We found that in general, G3 cell lines (orange) tended to be more sensitive to these different compounds than non G3 cells (blue and dark) (Fig.7A). We verified that each of these drugs effectively induced eIF2 $\alpha$  phosphorylation, leading to ATF4 and CHOP induction (Fig.7B). These results confirm that the regulation of eIF2 $\alpha$  by phosphorylation represents a central node in G3 MB.

### **KD of CReP, the constitutive eIF2 $\alpha$ phosphatase, decreases G3 cell growth and delays tumor growth *in vivo***

With phosphorylation-mediated eIF2 $\alpha$  inhibition appearing to be an important regulatory mechanism in G3 MB, we thus investigated the role of its phosphatases in G3 cells. Two eIF2 $\alpha$  phosphatases are well characterized: GADD34 (PPP1R15A), which is

induced by the PERK arm as a retro-control mechanism, and the constitutive eIF2 $\alpha$  phosphatase, CReP (PPP1R15B). We first investigated their expression in MB patient samples. Transcriptomic analysis of 762 tumors (10) showed that PPP1R15A expression has no specific patterns across MB groups and subtypes (Fig Supp.6A). In contrast, PPP1R15B expression was higher in G3 tumors as compared to other groups and normal fetal cerebella. Importantly, its expression is particularly enriched in G3- $\delta$  subtype (Fig.8A) which corresponds to MYC-amplified tumors with the worst prognoses (10). Accordingly, the expression of PPP1R15B has a prognostic value, with patients harboring high PPP1R15B levels displaying a worse prognosis (Fig.8B). WB analysis showed that our panel of G3 cell lines express higher levels of the CReP protein (encoded by PPP1R15B) as compared to non-Group 3 cell lines. Interestingly, this higher level is correlated with a concomitant low level of P-eIF2 $\alpha$  (Fig.8C). This suggests a potential need for G3 cells to maintain low levels of P-eIF2 $\alpha$  to maintain survival.

To investigate whether CReP is a key phosphatase keeping eIF2 $\alpha$  in its unphosphorylated active form, we performed KD of PPP1R15B using shRNA. We found that the KD of PPP1R15B by two independent shRNAs (sh15B#3 and #5) led to an important decrease in D425Med cell viability (Fig.8D). PPP1R15B KD led to the activation of known eIF2 $\alpha$  downstream targets as expected, with a strong induction of ATF4 and CHOP (Fig.8E). Similar results were obtained using the D458Med G3 cell line (Fig.8F-G). Importantly, we wanted to confirm this dependency of G3 cells *in vivo*. We grafted D425-Luc control (shCtrl) and KD (sh15B) cells orthotopically in nude mice. Tumor growth was followed by BLI and mice survival. We found that KD tumors grow more slowly than control tumors (Fig.8H), which resulted in an improved survival of these mice (Fig.8I). Similar results were obtained in two other models of G3 MB tumors, using PDX-3 and PDX-7 cells (Fig.8J-K). Taken together, these results suggested that eIF2 $\alpha$  phosphorylation represents a central regulatory mechanism in G3 MB. This phosphorylation can be mediated by PERK or inhibited by CReP.

## DISCUSSION

G3 MB is a highly aggressive pediatric brain tumor whose biology is not completely understood despite intensive research. The oncogene MYC is the main molecular driver of these types of tumors, but as a transcription factor, it remains difficult to target therapeutically. There is an urgent need to better understand the biology of G3 tumors in order to identify new vulnerabilities. Through a siRNA screen, we identified the UPR regulator HSPA5 as a dependency in G3 MB. We investigated the underlying mechanisms of this dependency. Our work showed that G3 MB cells are highly sensitive to UPR activation *in vitro* and *in vivo*. Interestingly, we found that UPR-mediated cell death is dependent on the activation of the PERK arm of UPR with a central role played by the inactivation of eIF2 $\alpha$  by phosphorylation. The level of eIF2 $\alpha$  phosphorylation is kept at a low level by the CReP phosphatase encoded by the PPP1R15B gene. PPP1R15B expression is enriched in the G3- $\delta$  subtype of MB and is thus associated with a poor prognostic outcome. We further showed that modulation of eIF2 $\alpha$  phosphorylation either by inhibiting CReP or activation of its kinases is of therapeutic interest.

We performed an siRNA-targeted screen in a G3 cell line to identify new genes important for the survival of G3 tumors and we identified HSPA5 as an interesting hit. HSPA5 is overexpressed in several tumor types and it has been linked to different processes during tumor initiation and development (21, 31). To our knowledge, no previous studies have linked HSPA5 to MB, nor specifically to G3 tumors. We showed that G3 growth is highly dependent on HSPA5. Using the tool compound HA15, we showed that G3 cells are more sensitive to HSPA5 inhibition than non-G3 cells. We established that HSPA5 is a dependency in G3 cells using a genetic approach with shRNA-mediated KD. HSPA5 KD led to a massive induction of cell death *in vitro* and delayed tumor growth in different models of G3 tumors including cell lines as well as importantly in our more recapitulative PDX models.

We investigated the underlying mechanism. Using RNAseq analysis and WB, we showed that HSPA5 KD in G3 cells led to a strong activation of the 3 arms of UPR, namely IRE1 $\alpha$ , ATF6 $\alpha$  and PERK. It is well established that UPR can have a dual role. It can be cytoprotective by helping to resolve ER stress or cytotoxic when pushed and prolonged

(23). To further confirm the sensitivity of G3 cells to UPR, we performed a chemical screen with UPR inhibitors or inducers. We did not reveal any specific sensitivity of G3 cells to UPR inhibitors suggesting that UPR does not play a major cytoprotective role in G3 MB. These results were in line with our experiments with inhibitors of each individual UPR arm, revealing that the lack of cytoprotectivity was regardless of the UPR arms. Indeed, no induction of cell death was observed upon inhibition of IRE1 $\alpha$  (MKC8866), ATF6 $\alpha$  (Ceapin-A7) and PERK (GSK260614) in shRNA control condition. This contrasts with what can be observed in other cancers. For example, the IRE1 $\alpha$  arm has been shown to play a cytoprotective role in glioblastoma or breast cancer (32–34) and the PERK arm in SHH MB (35). Instead, we revealed a higher sensitivity of G3 cells to chemical UPR activators, in agreement with our results showing that HSPA5 KD mediates a strong induction of cell death concomitantly with UPR induction.

UPR mediating cell death is often associated with the PERK arm through the induction of CHOP (22, 23). Accordingly, we showed that the PERK arm is the main mediator of cell death in HSPA5 KD G3 cells. Indeed, treatment of HSPA5 KD cells with a PERK inhibitor (GSK260641) rescued cell death while neither IRE1 $\alpha$  nor ATF6 $\alpha$  inhibitors did. Unexpectedly, KD of CHOP (nor ATF4) was not able to prevent cell death in this condition, which too, contrasts with many observations in different cancers (23, 28). However, while our results showed that CHOP is not sufficient to rescue cell death, they do not exclude that CHOP is involved. In any case, our results with ISRIB suggest that the nodal point is eIF2 $\alpha$  inactivation by phosphorylation. This is sustained by different observations. Besides the rescue by ISRIB, we showed that G3 cells are sensitive to different compounds that induce eIF2 $\alpha$  phosphorylation either by activating its kinases, including HRI, or inhibition of its phosphatases. Beyond this, our results suggest that G3 cells are sensitive to kinases involved in the integrated stress response (ISR) which are able to phosphorylate and inactivate eIF2 $\alpha$  (36). In addition to ER stress, G3 cells may, thus, be particularly sensitive to different stresses which induce the activation of these kinases including nutrient deprivation, double stranded RNA and heme deficiency. This raises the question of how G3 MB can cope with these high sensitivities. We showed that in basal conditions, G3 MB expresses high levels of PPP1R15B encoding CReP, an

eIF2 $\alpha$  phosphatase, maintaining a low level of eIF2 $\alpha$  phosphorylation. KD of CReP increased eIF2 $\alpha$  phosphorylation in tandem with cell death induction. We also showed that CReP is required for G3 MB growth *in vivo*.

The key role of eIF2 $\alpha$  translational factor, maintained in its active form by CReP, likely highlights a G3 MB dependency on translation. Indeed, it is well established that MYC oncogenic transformation leads to a boost in protein synthesis to provide sufficient material to growth. This is exemplified by the enrichment of ribosomal RNAs in G3 MB (7). Moreover, as recently demonstrated for some N-MYC driven MB tumor models (37), keeping the translation machinery active may allow for production of proteins that could help to prevent proteotoxic stress created by oncogenic insults. All of this may explain why MYC-driven cancers, as in G3 MB, depend on a high rate of protein synthesis, likely explaining their requirement for the low basal level of eIF2 $\alpha$  phosphorylation and their sensitivity to the inactivating phosphorylation of eIF2 $\alpha$ . More work is required to accurately assess the potential link between MYC and eIF2 $\alpha$  phosphorylation, but our study nevertheless highlights the key role of eIF2 $\alpha$  in G3 MB.

Our results point to regulation of eIF2 $\alpha$  as a central node in G3 MB cells with a key role the CReP phosphatase which maintains this translational factor in its unphosphorylated active form. We showed a dependency of G3 tumors to inhibitors of eIF2 $\alpha$ , either by kinase activators or phosphatase inhibitors which promote its inactivation by phosphorylation. Preclinical confirmation of this hypothesis by using drugs that can lead to eIF2 $\alpha$  phosphorylation is essential to proving the therapeutic potential of targeting this axis for G3 MB tumors.

## **MATERIALS AND METHODS**

### **Cell lines and culture conditions**

Human G3 MB cell lines D458Med and D425Med (obtained from Dr. Bigner) (He et al., 1991) were cultured in Improved MEM medium (Gibco) supplemented with 10% fetal bovine serum (FBS) (Sigma), 100 units/ml penicillin-streptomycin (Gibco), 1.25 µg/ml fungizone (Gibco). D425-Luc and D458-Luc cells were generated in our lab by transduction with lentiviral particles coding for the GFP/Luciferase genes. D283Med (ATCC) cells were cultured in MEM medium (Gibco), supplemented with 10% FBS, 100 units/ml penicillin-streptomycin, 1.25 µg/ml fungizone, 0.1mM non-essential amino acids (Gibco) and 1mM sodium pyruvate (Gibco). HD-MB03 cells (DSMZ) were cultured in RPMI 1640 medium (Gibco) supplemented with 10% FBS, 100 units/ml penicillin-streptomycin, 1.25 µg/ml fungizone and 0.1mM non-essential amino acids. D341Med cells (ATCC) were cultured in MEM medium (Gibco), supplemented with 20% FBS, 100 units/ml penicillin-streptomycin, 1.25 µg/ml fungizone, 0.1mM non-essential amino acids (Gibco) and 1mM sodium pyruvate (Gibco). DAOY (ATCC), ONS-76 (ATCC) and UW-228 (ATCC) cells were cultured as described in (38). hTERT-RPE1 (RPE1) cells (Clontech) were culture in DMEM:F-12 Glutamax medium (Gibco), supplemented with 10% FBS, 15Mm HEPES, 100 units/ml penicillin-streptomycin, 1.25 µg/ml fungizone. All cells were cultured at 37°C in humidified atmosphere containing 5% CO<sub>2</sub>. HD-MB03 and RPE1 cells grow in adherent conditions and D283Med, D341Med, D425Med and D458Med cell lines grow in suspension. All cells were tested for mycoplasma contamination.

## Chemicals

Drug	Provider	Reference
HA15	Provided by Stephan Rocchi's lab (28)	
GSK2606414	Selleckchem	S7307
MK-8866	Provided by Eric Chevet's lab	
Ceapin-A7	Sigma aldrich	SML2330
Salubrinal	MedChemExpress	HY-15486
Raphin1	MedChemExpress	HY-123960A
BTdCPU	MedChemExpress	HY-1182665
GSK-621	MedChemExpress	HY-100548

## siRNA screen

HD-MB03 cells were seeded at  $0.5 \times 10^6$  cells/ml (final volume of 100 $\mu$ L for 96-well plates) and transfected with a custom-made siRNA library and the DharmaFECT transfection reagent 3 according to manufacturer's instructions (Dharmacon). Cells were transfected with ON-TARGETplus SMARTpool siRNA against genes of interest. siRNAs were used at a final concentration of 25nM. Cells were incubated with siRNAs 72h for cell proliferation analysis. Experiments were performed in triplicates.

## Cell confluence and cell death detection through PI staining with IncuCyte®

Cell growth analyses were performed using the IncuCyte® S3 System (Essen BioScience, Sartorius). For drug experiments, cells were seeded in 96-well plates (HD-MB03: 100 000 cells/ml; D28Med, D425Med and D458Med cells: 150 000 cells/ml; ONS-76: 30 000 cells/ml; RPE1: 35 000 cells/ml) 24h before treatment. shRNA transduced cells were seeded 72h after infection at the concentrations mentioned before. Cell death was measured by adding PI to the medium at 2.5 $\mu$ g/ml at the same moment than drugs or at the moment of cell seeding for shRNA experiments. Plates were transferred to the IncuCyte® and incubated up to 72h at 37°C in humidified atmosphere containing 5%

CO2. Phase-contrast images (cell confluence) and Red fluorescence signal (cell death) were automatically acquired every 3 hours and the quantified confluence or fluorescence curves were generated by the software IncuCyte® S3 2022B Rev2. Experiments were performed in triplicates.

### **Cell Viability**

Cell viability was measured using the CellTiter Glo® assay. Cells were seeded and treated as described before. Luminescence signal was detected at different time points following manufacturer's instructions. Experiments were performed in triplicates.

### **Apoptosis and Cell Cycle Analyses by Flow Cytometry**

D425Med and D458Med cells were seeded at 250 000 cells/ml 72h after infection. 48h hours later, apoptosis was measured using the FITC-coupled anti-Caspase-3 active form (cleaved caspase-3 (cC3)) monoclonal antibody from the FITC Active Caspase-3 Apoptosis Kit (BD Biosciences) according to manufacturer's instructions. Signals were detected by a FACScanto cytometer (BD Biosciences) and the percentage of apoptotic cells was determined by using FlowJo software (Tree Star).

For cell cycle analysis, cells were incubated with 10µM of 5-Bromo-2'-deoxy-uridine (BrdU) for 30 minutes and then, cell cycle analysis was performed using the FITC-coupled anti-BrdU antibody from the FITC-BrdU Flow Kit (BD Bioscience) according to manufacturer's instructions. After fixation, permeabilization and incubation with the FITC-coupled anti-BrdU antibody, cells were incubated for 5 minutes with the ready-to-use nucleic acid dye 7-Amino-Actinomycin D (7AAD) (BD Biosciences) for DNA staining. Signals were detected by a FACScanto cytometer (BD Biosciences) and analyzed using FlowJo software (Tree Star).

### **Lentiviral (shRNA) production and infection**

Lentiviral vectors encoding shRNA against different genes were obtained from SIGMA library (<https://www.sigmaaldrich.com/life-science/functional-genomics-and-rnai/shrna/library-information/vector-map.html>). A list with shRNA sequences is presented in Table 2. Viral particles were produced in 293T cells by co-transfection with pLKO-shRNA containing vectors and the packaging plasmids pS-PAX2 and pMD2-

VSVG, using lipofectamine 2000 (Invitrogen). Lentiviral particles were harvested three times between 48 and 72 h post-transfection and were used to infect the cell of interest.

### **Patient-derived xenograft (PDX)**

Patient-derived xenograft (PDX) were established by Ayrault's team (Institute Curie) from tumor tissues freshly isolated from untreated patients (38). They are inoculated and maintained into nude mice, usually NSG mice, where they can be maintained and serially passaged either subcutaneously or orthotopically in the cerebellum. PDX3 and PDX7 correspond to ICN-MB-PDX-3 and ICN-MB-PDX-7, respectively. PDX were maintained, dissociated and cultured as described in (38).

### **Western blots**

Cell extracts and Western blot experiments were performed as previously described (39). The list of primary and secondary antibodies is presented in Table 3. Signals were obtained using a Vilber Fusion FX SPECTRA machine. Signal images are analyzed and quantified using ImageJ 1.53q. Quantifications will be provided in Supplementary File 1.

### **IHC and tumor area measurement**

To determine the tumor area by IHC analysis in HSPA5 KD experiments, 5-7 mice per group were euthanized when mice in the Control group reached the survival ethic end point. The brains were collected after tissue fixation by intracardiac perfusion (4% formaldehyde/PBS). Tissues were fixed during 24h at room temperature, embedded in paraffin and cut at 7 $\mu$ m-thick. After dewax and rehydration, heat mediated antigen retrieval was performed using Citrate buffer pH 6,0 for 20 minutes. Slides were incubated with Ki-67 primary antibody (Rat monoclonal SolA15 eBioscience, ThermoFisher, 1:500) over night at 4°C. ImmPRESS™-AP (alkaline phosphatase) Polymer Anti-Rat IgG (Vector Labs MP5404) was used to detect the primary antibody and visualized using an Alkaline Phosphatase (Red AP) Substrate Kit (Vector Labs SK-5100). The sections were finally counterstained with hematoxylin and mounted with aqueous mounting medium (Aquatex, Merck). Tumor size and IHC staining were assessed using ImageJ software. To quantify the Ki67 (pink staining) on images, the area corresponding to Ki67 is determined as follow

by using Fiji software. First, the colour deconvolution plugin is used to separate the original RGB image into 3 individual channels according to colour vectors  $[[r1]=0.45 [g1]=0.76 [b1]=0.45 [r2]=0.74 [g2]=0.57 [b2]=0.33 [r3]=0.55 [g3]=0.65 [b3]=0.51]$ . The channel 1 is used to extract the colour represented by Ki67. A threshold is then fixed to create a mask of segmentation. Close operation followed by a fill hole operation produce a solid mask of the Ki67 signal. At the end, the percentage of Ki67 per image is calculated by Analyze Particles function with minimum objects' size of 5 pixels<sup>2</sup>.

### **RNA-seq and Bioinformatic analysis**

First RNA-seq analysis was performed on D425Med cells transduced with shCtrl, shHSPA5#2 and shHSPA5#5 encoding lentiviral particles. Transduced cells were seeded 72h after infection and RNA was isolated 48h later. Total RNAs were isolated using the NucleoSpin RNA, Mini kit for RNA purification (Macherey-Nagel). RNA Quality was evaluated by Bioanalyzer (Agilent Technologies) and samples with RNA integrity > 7 were used for library construction. RNA-sequencing libraries were prepared from 1µg of total RNA using the TruSeq Stranded mRNA kit following manufacturer's protocols. For the second RNA-seq analysis, D458Med transduced cells were seeded 72h. RNA was isolated 6h after DMSO or ISRIB (0,5µM) for 6h treatment. RNAs were prepared as previously described. RNA-sequencing libraries were prepared from 1µg of total RNA following the Illumina stranded mRNA prep Ligation protocol.

Sequencing was carried out on a NovaSeq 6000 instrument from Illumina (S1-PE100, paired-end reads). Raw sequencing reads were first checked for quality with Fastqc (0.11.8) and trimmed for adapter sequences with cutadapt using the TrimGalore (0.6.2) wrapper. Trimmed reads were subsequently aligned to the complete human ribosomal RNA sequence with bowtie (2.4.2). Reads that did not align to rRNA were then mapped to the human reference genome hg38 and read counts per gene were generated with STAR mapper (2.6.1a\_08-27). The bioinformatics pipelines used for these tasks are available online (RNAseq v3.1.7: <https://gitlab.curie.fr/data-analysis/RNA-seq>, doi: 10.5281/zenodo.7443721). RNA sequencing data will be available under Gene Expression Omnibus series accession number GSEXXXX (reviewer token: xxx). Counts were normalized using TMM normalization from EdgeR (v 3.42.4). Differential gene expression was assessed with the Limma voom framework (v 3.56.2). Genes with an

absolute fold-change  $\geq 1.5$  and an adjusted p-value  $< 0.05$  were labeled significant by using R (v 4.3.1). Gene Ontology analyses were performed by using clusterProfiler package (v 4.8.3). Gene Sets Enrichment Analyses (GSEA, <http://software.broadinstitute.org/gsea>) were run using signal-to-noise for the ranking gene metric and 1000 permutations. The UPR signature as well as specific UPR-arm signatures used as gene set references are described in Plate *et al*, 2016 (29).

PPP1R15A and B expression and overall survival analyses were obtained with R (v 4.3.1) and GraphPad Prism tools (v 10.0.2) from transcriptomic data generated with 763 MB patients and 9 normal fetal cerebellums samples (Data from Cavalli's lab (10)).

### **Drug screening**

Briefly, 3000 living MB cells were seeded per well with the Certus Flex® (GyGer) in 384-well plates (Corning, #3830). Cells were incubated in the presence of a custom-made drug library containing 27 pharmacological drugs targeting UPR (MedChem Express). Stock solutions were at 10mM in DMSO and compounds were distributed with the Echo 550 liquid dispenser® (Labcyte) at 6 different concentrations covering 3 logs (100 nM–100  $\mu$ M) in constant DMSO. Cell viability was measured using CellTiter-Glo® 2.0 Cell Viability Assay (Promega, #G9243) after 72 h of drug incubation in a humidified environment at 37°C and 5% CO<sub>2</sub>. Luminescence was measured using a PHERAstar® plate reader (BMG). Data were normalized to negative control wells (DMSO only). IC<sub>50</sub>, defined as half maximal inhibitory concentration values, and AUC (Area Under the dose response Curve —  $\% \cdot \text{mol} \cdot \text{L}^{-1}$ ) were obtained using library (ic50), library (drc), library (ggplot2) and library (PharmacoGx) packages from R studio.

### **Animal experiments**

Animal studies are performed in accordance with the recommendations of the European Community (2010/63/UE) for the care and use of laboratory animals. All experiments presented in this work were authorized by the ethics committee of the Institut Curie CEEA-IC\_2014\_002 (Authorization 02382.02) and CEEA-IC\_2021\_009 (Authorization #31999-2021061422359754 v2) given by National Authority.

Orthotopic grafts are performed in 7 weeks-old NMRI Nude female mice (Janvier Labs). 100 000 cells for cell lines or 300 000 cells for PDX are grafted in 5 $\mu$  of PBS directly

in the cerebellum of mice as described in (38). D425Med and D458Med cells express the Luciferase gene allowing for tumor growth follow-up by measuring Bioluminescence (BLI) through the luciferase activity. Bioluminescence imaging and quantification are performed at different time points using the Living Image software. IVIS imaging of animals is performed 15 minutes after an intraperitoneal administration of Luciferine (30mg/ml 50 $\mu$ l, Perkin Elmer).

### **Statistical analyses**

Statistical information can be found in figures and figure legends. A  $P \leq 0.05$  is considered as significant. All experiments were performed at least in triplicates. Results are presented as the average  $\pm$  SEM. Statistical analyses were performed using GraphPad Prism version 10.0.0 for Windows and the exact p values will be provided in Supplementary File 2.

### **List of Supplementary Materials**

Fig. S1 to Fig S6

Table S1

Data file S1 to S2

## References

1. Q. T. Ostrom, G. Cioffi, K. Waite, C. Kruchko, J. S. Barnholtz-Sloan, CBTRUS Statistical Report: Primary Brain and Other Central Nervous System Tumors Diagnosed in the United States in 2014-2018. *Neuro. Oncol.* **23**, III1–III105 (2021).
2. Y. J. Cho, A. Tsherniak, P. Tamayo, S. Santagata, A. Ligon, H. Greulich, R. Berhoukim, V. Amani, L. Goumnerova, C. G. Eberhart, C. C. Lau, J. M. Olson, R. J. Gilbertson, A. Gajjar, O. Delattre, M. Kool, K. Ligon, M. Meyerson, J. P. Mesirov, S. L. Pomeroy, Integrative genomic analysis of medulloblastoma identifies a molecular subgroup that drives poor clinical outcome. *J. Clin. Oncol.* **29**, 1424–1430 (2011).
3. M. Kool, J. Koster, J. Bunt, N. E. Hasselt, A. Lakeman, P. van Sluis, D. Troost, N. Schouten-van Meeteren, H. N. Caron, J. Cloos, A. Mr??i??, B. Ylstra, W. Grajkowska, W. Hartmann, T. Pietsch, D. Ellison, S. C. Clifford, R. Versteeg, Integrated genomics identifies five medulloblastoma subtypes with distinct genetic profiles, pathway signatures and clinicopathological features. *PLoS One.* **3** (2008), doi:10.1371/journal.pone.0003088.
4. P. A. Northcott, A. Korshunov, H. Witt, T. Hielscher, C. G. Eberhart, S. Mack, E. Bouffet, S. C. Clifford, C. E. Hawkins, P. French, J. T. Rutka, S. Pfister, M. D. Taylor, Medulloblastoma comprises four distinct molecular variants. *J. Clin. Oncol.* **29**, 1408–1414 (2011).
5. P. A. Northcott, G. W. Robinson, C. P. Kratz, D. J. Mabbott, S. L. Pomeroy, S. C. Clifford, S. Rutkowski, D. W. Ellison, D. Malkin, M. D. Taylor, A. Gajjar, S. M. Pfister, Medulloblastoma. *Nat. Rev. Dis. Prim.* **5** (2019), doi:10.1038/s41572-019-0063-6.
6. T. C. Archer, T. Ehrenberger, F. Mundt, M. P. Gold, K. Krug, C. K. Mah, E. L. Mahoney, C. J. Daniel, A. LeNail, D. Ramamoorthy, P. Mertins, D. R. Mani, H. Zhang, M. A. Gillette, K. Clauser, M. Noble, L. C. Tang, J. Pierre-François, J. Silterra, J. Jensen, P. Tamayo, A. Korshunov, S. M. Pfister, M. Kool, P. A.

- Northcott, R. C. Sears, J. O. Lipton, S. A. Carr, J. P. Mesirov, S. L. Pomeroy, E. Fraenkel, Proteomics, Post-translational Modifications, and Integrative Analyses Reveal Molecular Heterogeneity within Medulloblastoma Subgroups. *Cancer Cell*. **34**, 396-410.e8 (2018).
7. A. Forget, L. Martignetti, S. Puget, L. Calzone, S. Brabetz, D. Picard, A. Montagud, S. Liva, A. Sta, F. Dingli, G. Arras, J. Rivera, D. Loew, A. Besnard, J. Lacombe, M. Pagès, P. Varlet, C. Dufour, H. Yu, A. L. Mercier, E. Indersie, A. Chivet, S. Leboucher, L. Sieber, K. Beccaria, M. Gombert, F. D. Meyer, N. Qin, J. Bartl, L. Chavez, K. Okonechnikov, T. Sharma, V. Thatikonda, F. Bourdeaut, C. Pouponnot, V. Ramaswamy, A. Korshunov, A. Borkhardt, G. Reifenberger, P. Pouillet, M. D. Taylor, M. Kool, S. M. Pfister, D. Kawauchi, E. Barillot, M. Remke, O. Ayrault, Aberrant ERBB4-SRC Signaling as a Hallmark of Group 4 Medulloblastoma Revealed by Integrative Phosphoproteomic Profiling. *Cancer Cell*. **34**, 379-395.e7 (2018).
8. P. A. Northcott, C. Lee, T. Zichner, A. M. Stütz, S. Erkek, D. Kawauchi, D. J. H. Shih, V. Hovestadt, M. Zapatka, D. Sturm, D. T. W. Jones, M. Kool, M. Remke, F. M. G. Cavalli, S. Zuyderduyn, G. D. Bader, S. Vandenberg, L. A. Esparza, M. Ryzhova, W. Wang, A. Wittmann, S. Stark, L. Sieber, H. Seker-Cin, L. Linke, F. Kratochwil, N. Jäger, I. Buchhalter, C. D. Imbusch, G. Zipprich, B. Raeder, S. Schmidt, N. Diessl, S. Wolf, S. Wiemann, B. Brors, C. Lawerenz, J. Eils, H. J. Warnatz, T. Risch, M. L. Yaspo, U. D. Weber, C. C. Bartholomae, C. Von Kalle, E. Turányi, P. Hauser, E. Sanden, A. Darabi, P. Siesjö, J. Sterba, K. Zitterbart, D. Sumerauer, P. Van Sluis, R. Versteeg, R. Volckmann, J. Koster, M. U. Schuhmann, M. Ebinger, H. L. Grimes, G. W. Robinson, A. Gajjar, M. Mynarek, K. Von Hoff, S. Rutkowski, T. Pietsch, W. Scheurlen, J. Felsberg, G. Reifenberger, A. E. Kulozik, A. Von Deimling, O. Witt, R. Eils, R. J. Gilbertson, A. Korshunov, M. D. Taylor, P. Lichter, J. O. Korbel, R. J. Wechsler-Reya, S. M. Pfister, Enhancer hijacking activates GFI1 family oncogenes in medulloblastoma. *Nature*. **511**, 428–434 (2014).
9. C. Lee, V. A. Rudneva, S. Erkek, M. Zapatka, L. Q. Chau, S. K. Tacheva-

- Grigороva, A. Garancher, J. M. Rusert, O. Aksoy, R. Lea, H. P. Mohammad, J. Wang, W. A. Weiss, H. L. Grimes, S. M. Pfister, P. A. Northcott, R. J. Wechsler-Reya, Lsd1 as a therapeutic target in Gfi1-activated medulloblastoma. *Nat. Commun.* **10**, 1–13 (2019).
10. F. M. G. Cavalli, M. Remke, L. Rampasek, J. Peacock, D. J. H. Shih, B. Luu, L. Garzia, J. Torchia, C. Nor, A. S. Morrissy, S. Agnihotri, Y. Y. Thompson, C. M. Kuzan-Fischer, H. Farooq, K. Isaev, C. Daniels, B. K. Cho, S. K. Kim, K. C. Wang, J. Y. Lee, W. A. Grajkowska, M. Perek-Polnik, A. Vasiljevic, C. Faure-Conter, A. Jouvét, C. Giannini, A. A. Nageswara Rao, K. K. W. Li, H. K. Ng, C. G. Eberhart, I. F. Pollack, R. L. Hamilton, G. Y. Gillespie, J. M. Olson, S. Leary, W. A. Weiss, B. Lach, L. B. Chambless, R. C. Thompson, M. K. Cooper, R. Vibhakar, P. Hauser, M. L. C. van Veelen, J. M. Kros, P. J. French, Y. S. Ra, T. Kumabe, E. López-Aguilar, K. Zitterbart, J. Sterba, G. Finocchiaro, M. Massimino, E. G. Van Meir, S. Osuka, T. Shofuda, A. Klekner, M. Zollo, J. R. Leonard, J. B. Rubin, N. Jabado, S. Albrecht, J. Mora, T. E. Van Meter, S. Jung, A. S. Moore, A. R. Hallahan, J. A. Chan, D. P. C. Tirapelli, C. G. Carlotti, M. Fouladi, J. Pimentel, C. C. Faria, A. G. Saad, L. Massimi, L. M. Liau, H. Wheeler, H. Nakamura, S. K. Elbabaa, M. Perezpeña-Diazconti, F. Chico Ponce de León, S. Robinson, M. Zapotocky, A. Lassaletta, A. Huang, C. E. Hawkins, U. Tabori, E. Bouffet, U. Bartels, P. B. Dirks, J. T. Rutka, G. D. Bader, J. Reimand, A. Goldenberg, V. Ramaswamy, M. D. Taylor, Intertumoral Heterogeneity within Medulloblastoma Subgroups. *Cancer Cell.* **31**, 737-754.e6 (2017).
  11. R. P. C. Shiu, J. Pouyssegur, I. Pastan, Glucose depletion accounts for the induction of two transformation-sensitive membrane proteins in Rous sarcoma virus-transformed chick embryo fibroblasts. *Proc. Natl. Acad. Sci. U. S. A.* **74**, 3840–3844 (1977).
  12. I. G. Haas, M. Wabl, Immunoglobulin heavy chain binding protein. *Nature* (1983), doi:10.1038/306387a0.
  13. M. Carrara, F. Prischi, P. R. Nowak, M. C. Kopp, M. M. U. Ali, Noncanonical binding of BiP ATPase domain to Ire1 and Perk is dissociated by unfolded protein

- CH1 to initiate ER stress signaling. *Elife*. **2015**, 1–16 (2015).
14. M. C. Kopp, N. Larburu, V. Durairaj, C. J. Adams, M. M. U. Ali, UPR proteins IRE1 and PERK switch BiP from chaperone to ER stress sensor. *Nat. Struct. Mol. Biol.* **26**, 1053–1062 (2019).
  15. J. Hollien, J. S. Weissman, Decay of Endoplasmic Reticulum-Localized mRNAs During the Unfolded Protein Response. *Science (80-. )*. **313**, 104–107 (2006).
  16. J. Ye, R. B. Rawson, R. Komuro, X. Chen, U. P. Davé, R. Prywes, M. S. Brown, J. L. Goldstein, ER stress induces cleavage of membrane-bound ATF6 by the same proteases that process SREBPs. *Mol. Cell*. **6**, 1355–1364 (2000).
  17. K. Yamamoto, T. Sato, T. Matsui, M. Sato, T. Okada, H. Yoshida, A. Harada, K. Mori, Transcriptional Induction of Mammalian ER Quality Control Proteins Is Mediated by Single or Combined Action of ATF6 and XBP1. *Dev. Cell*. **13**, 365–376 (2007).
  18. C. Hetz, K. Zhang, R. J. Kaufman, Mechanisms, regulation and functions of the unfolded protein response. *Nat. Rev. Mol. Cell Biol.* **21**, 421–438 (2020).
  19. P. Walter, D. Ron, The Unfolded Protein Response: From Stress Pathway to Homeostatic Regulation. *Science (80-. )*. **334**, 1081–1086 (2011).
  20. C. Bailly, M. J. Waring, Pharmacological effectors of GRP78 chaperone in cancers. *Biochem. Pharmacol.* **163**, 269–278 (2019).
  21. A. S. Lee, Glucose-regulated proteins in cancer: Molecular mechanisms and therapeutic potential. *Nat. Rev. Cancer*. **14**, 263–276 (2014).
  22. H. Zinszner, M. Kuroda, X. Z. Wang, N. Batchvarova, R. T. Lightfoot, H. Remotti, J. L. Stevens, D. Ron, CHOP is implicated in programmed cell death in response to impaired function of the endoplasmic reticulum. *Genes Dev.* **12**, 982–995 (1998).
  23. H. Urra, E. Dufey, F. Lisbona, D. Rojas-Rivera, C. Hetz, When ER stress reaches a dead end. *Biochim. Biophys. Acta - Mol. Cell Res.* **1833**, 3507–3517 (2013).
  24. K. D. McCullough, J. L. Martindale, L.-O. Klotz, T.-Y. Aw, N. J. Holbrook,

- Gadd153 Sensitizes Cells to Endoplasmic Reticulum Stress by Down-Regulating Bcl2 and Perturbing the Cellular Redox State. *Mol. Cell. Biol.* **21**, 1249–1259 (2001).
25. J. Han, S. H. Back, J. Hur, Y. H. Lin, R. Gildersleeve, J. Shan, C. L. Yuan, D. Krokowski, S. Wang, M. Hatzoglou, M. S. Kilberg, M. A. Sartor, R. J. Kaufman, ER-stress-induced transcriptional regulation increases protein synthesis leading to cell death. *Nat. Cell Biol.* **15**, 481–490 (2013).
  26. E. Chevet, C. Hetz, A. Samali, Endoplasmic reticulum stress–activated cell reprogramming in oncogenesis. *Cancer Discov.* **5**, 586–597 (2016).
  27. S. J. Marciniak, J. E. Chambers, D. Ron, Pharmacological targeting of endoplasmic reticulum stress in disease. *Nat. Rev. Drug Discov.* **21**, 115–140 (2022).
  28. M. Cerezo, A. Lehraiki, A. Millet, F. Rouaud, M. Plaisant, E. Jaune, T. Botton, C. Ronco, P. Abbe, H. Amdouni, T. Passeron, V. Hofman, B. Mograbi, A. S. Dabert-Gay, D. Debayle, D. Alcor, N. Rabhi, J. S. Annicotte, L. Héliot, M. Gonzalez-Pisfil, C. Robert, S. Moréra, A. Virougoux, P. Gual, M. M. U. Ali, C. Bertolotto, P. Hofman, R. Ballotti, R. Benhida, S. Rocchi, Compounds Triggering ER Stress Exert Anti-Melanoma Effects and Overcome BRAF Inhibitor Resistance. *Cancer Cell.* **29**, 805–819 (2016).
  29. L. Plate, C. B. Cooley, J. J. Chen, R. J. Paxman, C. M. Gallagher, F. Madoux, J. C. Genereux, W. Dobbs, D. Garza, T. P. Spicer, L. Scampavia, S. J. Brown, H. Rosen, E. T. Powers, P. Walter, P. Hodder, R. Luke Wiseman, J. W. Kelly, Small molecule proteostasis regulators that reprogram the ER to reduce extracellular protein aggregation. *Elife.* **5**, 1–26 (2016).
  30. A. Krzyzosiak, A. P. Pitera, A. Bertolotti, An Overview of Methods for Detecting eIF2 $\alpha$  Phosphorylation and the Integrated Stress Response. *Methods Mol. Biol.* **2428**, 3–18 (2022).
  31. A. O. Akinyemi, K. E. Simpson, S. F. Oyelere, M. Nur, C. M. Ngule, B. C. D. Owoyemi, V. A. Ayarick, F. F. Oyelami, O. Obaleye, D. P. Esoe, X. Liu, Z. Li,

- Unveiling the dark side of glucose-regulated protein 78 (GRP78) in cancers and other human pathology: a systematic review. *Mol. Med.* **29**, 112 (2023).
32. S. E. Logue, E. P. McGrath, P. Cleary, S. Greene, K. Mnich, A. Almanza, E. Chevet, R. M. Dwyer, A. Oommen, P. Legembre, F. Godey, E. C. Madden, B. Leuzzi, J. Obacz, Q. Zeng, J. B. Patterson, R. Jäger, A. M. Gorman, A. Samali, Inhibition of IRE1 RNase activity modulates the tumor cell secretome and enhances response to chemotherapy. *Nat. Commun.* **9** (2018), doi:10.1038/s41467-018-05763-8.
  33. S. Lhomond, T. Avril, N. Dejeans, K. Voutetakis, D. Doultinos, M. McMahon, R. Pineau, J. Obacz, O. Papadodima, F. Jouan, H. Bourien, M. Logotheti, G. Jégou, N. Pallares-Lupon, K. Schmit, P. Le Reste, A. Etcheverry, J. Mosser, K. Barroso, E. Vauléon, M. Maurel, A. Samali, J. B. Patterson, O. Pluquet, C. Hetz, V. Quillien, A. Chatziioannou, E. Chevet, Dual IRE 1 RN ase functions dictate glioblastoma development . *EMBO Mol. Med.* **10**, 1–28 (2018).
  34. P. J. Le Reste, R. Pineau, K. Voutetakis, J. Samal, G. Jégou, S. Lhomond, A. M. Gorman, A. Samali, J. B. Patterson, Q. Zeng, A. Pandit, M. Aubry, N. Soriano, A. Etcheverry, A. Chatziioannou, J. Mosser, T. Avril, E. Chevet, Local intracerebral inhibition of IRE1 by MKC8866 sensitizes glioblastoma to irradiation/chemotherapy in vivo. *Cancer Lett.* **494**, 73–83 (2020).
  35. Y. Ho, X. Li, S. Jamison, H. P. Harding, P. J. McKinnon, D. Ron, W. Lin, PERK Activation Promotes Medulloblastoma Tumorigenesis by Attenuating Premalignant Granule Cell Precursor Apoptosis. *Am. J. Pathol.* **186**, 1939–1951 (2016).
  36. M. Costa-Mattioli, P. Walter, The integrated stress response: From mechanism to disease. *Science.* **368** (2020), doi:10.1126/SCIENCE.AAT5314.
  37. D. Kuzuoglu-ozturk, O. Aksoy, C. Schmidt, R. Lea, J. D. Larson, R. R. L. Phelps, N. Nasholm, M. Holt, A. Contreras, M. Huang, S. Wong-michalak, H. Shao, R. Wechsler-reya, J. J. Phillips, J. E. Gestwicki, D. Ruggero, W. A. Weiss, N-myc – Mediated Translation Control Is a Therapeutic Vulnerability in Medulloblastoma

(2023), doi:10.1158/0008-5472.CAN-22-0945.

38. A. Garancher, C. Y. Lin, M. Morabito, W. Richer, N. Rocques, M. Larcher, L. Bihannic, K. Smith, C. Miquel, S. Leboucher, N. I. Herath, F. Dupuy, P. Varlet, C. Haberler, C. Walczak, N. El Tayara, A. Volk, S. Puget, F. Doz, O. Delattre, S. Druillennec, O. Ayrault, R. J. Wechsler-Reya, A. Eychène, F. Bourdeaut, P. A. Northcott, C. Pouponnot, NRL and CRX Define Photoreceptor Identity and Reveal Subgroup-Specific Dependencies in Medulloblastoma. *Cancer Cell*. **33**, 435-449.e6 (2018).
39. N. Rocques, N. Abou Zeid, K. Sii-Felice, L. Lecoin, M.-P. Felder-Schmittbuhl, A. Eychène, C. Pouponnot, GSK-3-Mediated Phosphorylation Enhances Maf-Transforming Activity. *Mol. Cell*. **28**, 584–597 (2007).

**Acknowledgments:** We would like to thank members of our laboratory for helpful advice and comments, C. Lasgi for her assistance in FACS analyses. V. Dangles-Marie, E. Belloir, C. Alberti and C. Lantoine at the Institut Curie mouse facilities. The authors greatly acknowledge L. Besse and C. Messaoudi from Multimodal Imaging Center - CNRS UAR2016 / Inserm US43 / Institut Curie / Université Paris-Saclay - for useful advices on image processing.

**Funding:** We would like to thanks to all of our founding sources.

Ligue Contre le Cancer (LCC), Val d'Oise; GEFLUC; Aïda; Fondation ARC pour la recherche sur le Cancer PJA20191209652; Consortium INCA PEDIAC; Ministère Français de l'Enseignement Supérieur, de la Recherche et de l'Innovation, PhD fellowship (LMO); Fondation pour la Recherche Médicale (FRM), End of PhD fellowship FDT202106013153 (LMO).

**Author contributions:**

Conceptualization: CP and LMO

Methodology: CP, LMO, SD, LM, EP

Investigation: LMO, SD, LM, ML, DYXN, KM, MPM, SG, SL, VM, JT

Funding acquisition: CP, AE

Project administration: CP, AE

Supervision: CP, AE, OA, EP, FD, FB, RB, SR, EC

Writing – original draft: LMO, CP, SD, BD

Writing – review & editing: LMO, CP, SD, LM

**Competing interests:**

The authors declare that they have no conflict of interest.

**Data and materials availability:** RNA sequencing data will be uploaded before submission of the article and accession number will be then provided. For the present PhD thesis manuscript data could be provided under request. Western blot quantifications and exact p values of all statistical tests will be provided in Supplementary Excell files, but could be provided for the reviewers of the thesis under request. All other data is available in the main text or the supplementary materials.

## Figures and tables

**Fig. 1. G3 MB cells are sensitive to HSPA5 inhibition.** A: Schematic representation of the strategy used for the siRNA screening. B: siRNA effect on cell viability was measured at 72h using the CellTiter Glo® assay (Luminescence signal is directly proportional to cell viability). siOTX2 and siMYC are used as positive controls of the experiments since its downregulation is known to induce cell death in G3 MB cells. siGAPDH, siCyclophylin and siCtrl are used as negative controls. Fold change is determined with respect of siCtrl condition. C: G3 (D283Med, D425Med, D458Med, HD-MB03), non-G3 (ONS-76) and a non-cancer cell line (RPE1) were treated with increasing concentrations of HA15 or DMSO. The effect of the drugs on cell growth was measured using the IncuCyte® technology. Phase contrast images are taken every 3 hours and a customized mask is used to measure the % of cell confluence. % of cell confluence is normalized to 0 hours. D: IC50 values were determined from results presented in B. Fold change between values at 72h and 0h were determined. DMSO is considered to represent 100% of cell growth. Experiments were performed in triplicates. For the siRNA screening results, statistical differences were calculated by a Two-way ordinary ANOVA followed by a Dunnet's multiple comparison test. For HA15 effect on cell growth statistical differences were calculated at the end point of the experiments between the different concentrations and DMSO, using a One-way ANOVA test followed by a Dunnet's multiple comparison test. \*: P≤0.05; \*\*: P≤0.001, \*\*\*: P≤0.0005, \*\*\*\*: P≤0.0001, ns: non-significative.

**Fig. 2. HSPA5 KD decreased G3 MB cell growth *in vitro* and *in vivo*.** A: D458Med cells were transduced with shCtrl, shHSPA5#2 and shHSPA5#5 encoding lentiviral particles and the efficiency of the KD was determined by Western blot.  $\beta$ -actin was used as loading control. Signal quantification is presented below membranes. The ratio between proteins of interest and  $\beta$ -actin is calculated and normalized to shCtrl values. Experiments were performed in triplicates. Representative blots are shown. B: The effect of HSPA5 KD on cell viability was measured using CellTiter Glo® (Luminescence). Transduced cells are seeded 72h (Day 0) after infection with lentiviral particles and cell viability is measured 48h later (Day 2). C: Cell cycle analysis was performed by staining cells with 7-AAD and anti-BrdU antibody, followed by flow cytometric analysis. 72h after infection with shCtrl, shHSPA5#2 and shHSPA5#5 encoding lentiviral particles. D458Med

cells were seeded. 48h later the % of cells in the different phases (G0/G1, S, G2/M) of cell cycle was determined. D: The induction of apoptosis was measured by Cleaved-Caspase 3 (cC3+) staining. D458Med cells were seeded 72h after infection with shCtrl, shHSPA5#2 and shHSPA5#5 encoding lentiviral particles. 48h later the % of apoptotic cells was determined by FACS. E: D458Med cells stably expressing Luciferase (D458-Luc) cells were transduced with shCtrl, shHSPA5#2 and shHSPA5#5 encoding lentiviral particles and the efficiency of the KD was determined by Western blot. F: Transduced D458-Luc cells were grafted into the cerebellum of nude mice (n=8 for each group) and tumor growth was followed by Bioluminescence (BLI) signal. Images of representative mice obtained at D7 and D18 are presented. G: BLI signals obtained at D7, D11 and D18 were quantified using the Live Image software. H: Tumor area was measured by KI-67 staining by IHC. Counterstaining with hematoxylin was performed. Representative images of tumors from the three groups shCtrl, shHSPA5#2 and shHSPA5#5 are presented. I: KI-67 signal quantification is presented. J: Kaplan-Meier survival curves of mice orthotopically grafted with shCtrl, shHSPA5#2 and shHSPA5#5 D458-Luc cells. K: shCtrl, shHSPA5#2 and shHSPA5#5 transduced PDX-3 cells were grafted into the cerebellum of nude mice (n=8 for each group). Tumor area was measured by KI-67 staining by IHC. Counterstaining with hematoxylin was performed. Representative images of tumors from the three groups shCtrl, shHSPA5#2 and shHSPA5#5 are presented. L: KI-67 signal quantification is presented. M: Kaplan-Meier survival curves of mice orthotopically grafted with shCtrl, shHSPA5#2 and shHSPA5#5 PDX-3 cells. Kaplan-Meier survival curves are analyzed by a Log-rank (Mantel-Cox) test. BLI signal curves are analyzed using a Mixed-effects model test. The other comparisons are done using a Two-way ANOVA test followed by a Dunnet's multiple comparison test. \*:  $P \leq 0.05$ ; \*\*:  $P \leq 0.001$ , \*\*\*:  $P \leq 0.0005$ , \*\*\*\*:  $P \leq 0.0001$ , ns: non-significative.

**Figure 3 HSPA5 KD lead to activation of the three arms of UPR.** A: Volcano plot representing the differentially expressed genes (DEG) obtained from the RNA-seq analysis of shCtrl and shHSPA5 (sh#2 and #5 together) D425Med cells. The 40 significant DEG (absolute fold change  $\geq 1.5$  and p value adjusted (padj)  $< 0.05$ ) are highlighted in red. X axis indicated the log<sub>2</sub> fold change (FC) and Y axis the  $-\log_{10}$  of adjusted p-value. The non-axial vertical lines denote absolute fold change of 1.5 while the non-axial

horizontal line denotes the adjusted p-value of ratio significance of 0.05. B: Hierarchical clustering analysis showing the expression of the 40 DEG obtained from the RNA-seq analysis across the different conditions: shCtrl, shHSPA5#2, shHSPA5#5 (three replicates per condition). C: Gene ontology (GO) analysis performed from the DEG between the conditions shCtrl and shHSPA5 (sh#2 and #5 together). D: Gene set enrichment analysis (GSEA) showing the enrichment of genes from UPR gene signature (29) on the shHSPA5 condition compared to shCtrl condition. ES: Enrichment Score, NES: Normalized Enrichment Score, FDR: False discovery rate. E: Expression of the genes from the UPR gene signature (29) in the different conditions obtained by the RNA-seq analysis. Statistical differences between the level of expression of the UPR signature genes in shCtrl condition compared to shHSPA5#2 and #5 are calculated by a Paired t test analysis. \*:  $P \leq 0.05$ ; \*\*:  $P \leq 0.001$ , \*\*\*:  $P \leq 0.0005$ , \*\*\*\*:  $P \leq 0.0001$ , ns: non-significative.

**Figure 4 G3 MB cells are sensitive to UPR activation.** Western blot analyses performed in D425Med (Fig.4A), D458Med (Fig.4B) and PDX-3 (Fig.4C) cells transduced with shCtrl, shHSPA5#2 and shHSPA5#5 encoding lentiviral particles. Expression of UPR effectors is evaluated: HSPA5 and HERPUD1 (ATF6 $\alpha$  arm), P-eIF2 $\alpha$ / eIF2 $\alpha$ , ATF4 and CHOP (PERK arm) and the spliced-form of the XBP1 transcription factor (sXBP1).  $\beta$ -actin is used as loading control. For quantification, the ratio between the protein of interest and  $\beta$ -actin is calculated and then normalized to shCtrl. For P-eIF2 $\alpha$ / eIF2 $\alpha$ , first the ratio between the Phosphorylated form and the total form regarding  $\beta$ -actin is calculated, then the ratio between P-eIF2 $\alpha$ /eIF2 $\alpha$  is determined, and last, the values are normalized to shCtrl. Experiments were performed in triplicates. Representative blots are shown. D: D: G3, non-G3 and the non-cancer RPE1 cell line were treated with pharmacological agents that activate or inhibit UPR. Drug sensitivity, represented as the “Area under the curve” (AUC), is shown as a heatmap. AUC is calculated from the effect on cell viability at 6 different drug concentrations from 0.1-100 $\mu$ M (yellow: highly sensitive to blue: less sensitive). Cell viability was assessed after 72h of incubation using CellTiter Glo®. E-F: The average sensitivity of non-G3 and Group 3 cells to drugs that activate (E) or inhibit UPR (F) was compared. Statistical differences between G3 and non-G3 cells (E-F) was

calculated by a Paired t test analysis on 18 and 9 compounds for UPR activation and inhibition, respectively. \*\*:  $P \leq 0.001$ , ns: non-significative.

**Figure 5 The inhibition of PERK rescued the HSPA5 KD-induced cell death.** A: D458Med cells transduced with shCtrl and shHSPA5#5 encoding lentiviral particles are treated with DMSO or UPR arms specific inhibitors: GSK2606414 (PERK inhibitor, 0.2 $\mu$ M), MKC8866 (IRE1 $\alpha$  inhibitor, 10 $\mu$ M) and Ceapin-A7 (ATF6 $\alpha$  cleavage inhibitor, 10 $\mu$ M). The effect on cell death is evaluated by PI staining of cells measured by the IncuCyte®. Data represent the fold change at 48h (compared to 0h) and normalized to shCtrl-DMSO. B: the specific activity of each UPR inhibitors and the effect on D458Med cells transduced with shCtrl shHSPA5#2 and shHSPA5#5 encoding lentiviral particles are evaluated by western blot. Quantification is performed as previously described. Experiments were performed in triplicates. Representative blots are shown. C: ATF4 KD D458Med cells are transduced with shCtrl, shHSPA5#2 and shHSPA5#5 encoding lentiviral particles. Western blot is used to confirmed the KD of ATF4 and HSPA5. D: The effect of ATF4 KD on the cell death induced by HSPA5 KD is evaluated by PI staining of cells measured by the IncuCyte®. Data represent the fold change at 48h (compared to 0h) and normalized to shCtrl. E: CHOP KD D458Med cells are transduced with shCtrl, shHSPA5#2 and shHSPA5#5 encoding lentiviral particles. Western blot is used to confirmed the KD of CHOP and HSPA5. D: The effect of CHOP KD on the cell death induced by HSPA5 KD is evaluated by PI staining of cells measured by the IncuCyte®. Data represent the fold change at 48h (compared to 0h) and normalized to shCtrl. Experiments were performed in triplicates. Representative blots are shown.  $\beta$ -actin is used as loading control. Quantification is performed as described in the legend of Figure 3. Statistical differences were calculated by a One-way ANOVA test followed by a Dunnet's multiple comparison test. \*:  $P \leq 0.05$ ; \*\*:  $P \leq 0.001$ , \*\*\*:  $P \leq 0.0005$ , \*\*\*\*:  $P \leq 0.0001$ , ns: non-significative.

**Figure 6 ISRIB treatment partially rescued HSPA5 KD-induced cell death.** A: D458Med cells transduced with shCtrl, shHSPA5#2 and shHSPA5#5 encoding lentiviral

particles are treated with DMSO or ISRIB (0.5 $\mu$ M). The effect on cell death is evaluated by PI staining of cells measured by the IncuCyte®. Data represent the fold change at 48h (compared to 0h) and normalized to shCtrl-DMSO. B: The specific activity of ISRIB and the effect on transduced cells is evaluated by Western blot.  $\beta$ -actin is used as loading control. Quantification is performed as previously described. Experiments were performed in triplicates. Representative blots are shown. C: Volcano plot representing the most differentially expressed genes (DEG) obtained from the RNA-seq analysis on D458Med cells. The Volcano plot represents the 37 DEG (red dots) between the conditions HSPA5 KD (shHSPA5#2 and #5 together) treated with DMSO (shHSPA5-DMSO) or ISRIB (shHSPA5-ISRIB). X axis indicates the log<sub>2</sub> fold change (FC) and Y axis the log<sub>10</sub> of adjusted p-value. The non-axial vertical lines denote absolute fold change of 1.5 while the non-axial horizontal line denotes the adjusted p-value of ratio significance of 0.05. D: Gene ontology (GO) analysis performed from the DEG between the conditions shHSPA5-DMSO and shHSPA5-ISRIB. E: GSEA showing the enrichment of the genes that are specifically regulated downstream of PERK on shHSPA5-ISRIB condition compared to the shHSPA5-DMSO condition; ES: Enrichment Score, NES: Normalized Enrichment Score, FDR: False discovery rate. F-G: Expression of the genes from the UPR gene signature (29) in the different conditions obtained by the RNA-seq analysis. F: Expression of the entire UPR gene signature list. G: Expression of the list of genes that are specifically regulated downstream of PERK. For ISRIB effect on HSPA5 KD induced cell death, statistical differences were calculated by a One-way ANOVA test followed by a Dunnet's multiple comparison test. Statistical differences between the level of expression of the UPR signature genes in shCtrl, shHSPA5#2, shHSPA5#5 treated with DMSO versus treated with ISRIB, are calculated by a Paired t test analysis. \*: P $\leq$ 0.05; \*\*: P $\leq$ 0.001, \*\*\*: P $\leq$ 0.0005, \*\*\*\*: P $\leq$ 0.0001, ns: non-significative.

**Figure 7 G3 MB cells are sensitive to UPR activation, especially to eIF2 $\alpha$  phosphorylation.** A: Dose-response curves of the different cell lines to drugs that will lead to eIF2 $\alpha$  phosphorylation (Salubrinal, Raphin1, BTdCPU and GSK-621). The effect on cell viability is determined using the CellTiter Glo® assay. B: The phosphorylation of eIF2 $\alpha$  and the activation of the downstream targets after treatment with drugs shown in Fig.7A were evaluated by Western blot.  $\beta$ -actin is used as loading control. Quantification

is performed as previously described. Experiments were performed in triplicates. Representative blots are shown.

**Figure 8 KD of CReP, the constitutive eIF2 $\alpha$  phosphatase, decreased G3 cell growth and delayed tumor growth in vivo.** A: Expression of PPP1R15B (CReP) in tumors from the different MB groups (left) or subtypes (right). Transcriptomic data generated from 763 MB patients and normal fetal cerebellum (Data from Cavalli's lab, (10)). B: Kaplan-Meier survival curve (Overall survival probability) of MB patients according to the expression of PPP1R15B (CReP). Curve were generated using survival information from Cavalli's dataset. The median is used as a cutoff to define high and low expression of the gene C: Western blot showing the expression of CReP, P-eIF2 $\alpha$ /eIF2 $\alpha$  in G3 and non-G3 MB cell lines.  $\beta$ -actin is used as loading control. Quantification is performed as previously described. Experiments were performed in triplicates. Representative blots are shown. D-G: Effect of PPP1R15B (CReP) using shRNA on D425Med (D) and D458Med cells (F) viability, measured by CellTiter Glo $\text{\textcircled{R}}$  assays. PPP1R15B (CReP) KD and the activation of the P-eIF2 $\alpha$  downstream targets was verified by western blot (E&G, D425Med and D458Med respectively).  $\beta$ -actin is used as loading control. Quantification is performed as previously described. Experiments were performed in triplicates. Representative blots are shown. H-I: D425-Luc cells expressing luciferase and transduced with shCtrl, sh15B#3 and sh15B#5 lentiviral particles were orthotopically grafted in the cerebellum of nude mice. H: Quantification of BLI signal at different time points. I: Kaplan-Meier survival curve of mice grafted with shCtrl (n=8), sh15B#3 (n=7) and sh15B#5 (n=8)) transduced cells. J-K: Kaplan-Meier survival curve of mice grafted with shCtrl, sh15B#3 and sh15B#5 transduced PDX-3 (J) and PDX-7 (K) cells. Statistical differences between the level of expression of PPP1R15B across the different groups are calculated using a Mann-Whitney test. Only comparisons between G3 and the other groups are presented. Kaplan-Meier survival curves are analyzed by a Log-rank (Mantel-Cox) test. BLI signal curves are analyzed using a Mixed-effects model test. The other comparisons are done using a Two-way ANOVA test followed by a Dunnet's multiple comparison test. \*:  $P \leq 0.05$ ; \*\*:  $P \leq 0.001$ , \*\*\*:  $P \leq 0.0005$ , \*\*\*\*:  $P \leq 0.0001$ .

**Table 1 HA15 IC50 in different cell lines.** G3, non-G3 and a non-cancerous cell line were treated with increasing concentrations of HA15. The effect of the drug on cell growth was analyzed using the IncuCyte®. The curves used to calculate the IC50 are presented in the Figure 1D

**Table 2. List of shRNA sequences**

**Table 3. List of primary and secondary antibodies**

## Supplementary figures and tables

**Fig S1. siRNA-based targeted screen in a G3 MB cell line.** A: HD-MB03 cell line was transfected with a custom-made siRNA library. The effect on cell growth was analyzed using the CellTiter Glo assay (Figure 1A, B) and the IncuCyte®. The curves determined for interesting genes (A: EYA2, B: HSPA5 and C: CABP5) are represented. siOTX2 and siCtrl are used as positive and negative controls respectively. Statistical differences were calculated at the end point of the experiments using a One-way ANOVA test followed by a Dunnet's multiple comparison test. All curves are compared to siCtrl curve.  $P \leq 0.05$ ; \*\*:  $P \leq 0.001$ , \*\*\*:  $P \leq 0.0005$ , \*\*\*\*:  $P \leq 0.0001$ .

**Fig S2. HSPA5 KD decreased G3 MB cell growth *in vitro* and *in vivo*.** A: D425Med cells were transduced with shCtrl, shHSPA5#2 and shHSPA5#5 encoding lentiviral particles and the efficiency of the KD was determined by Western blot.  $\beta$ -actin was used as loading control. Quantification is performed as previously described. B: The effect of HSPA5 KD on cell viability was measured using CellTiter Glo® (Luminesce). Transduced cells are seeded 72h (Day 0) after infection with lentiviral particles and cell viability is measured 48h later (Day 2). C: Cell cycle analysis was performed by measuring BrdU incorporation by FACS. D: The induction of apoptosis was measured by Cleaved-Caspase 3 (cC3+) staining. E: D425Med cells stably expressing Luciferase (D425-Luc) and transduced with shCtrl (n=8), shHSPA5#2 (n=7) and shHSPA5#5 (n=8) encoding lentiviral particles were grafted in nude mice. Tumor growth was measured by quantification of BLI signal at indicated time points. F: Kaplan-Meier survival curves of mice orthotopically grafted with shCtrl, shHSPA5#2 and shHSPA5#5 D425-Luc cells. G: PDX-7 cells were transduced with shCtrl, shHSPA5#2 and shHSPA5#5 encoding lentiviral particles and grafted into the cerebellum of nude mice (shCtrl (n=8), shHSPA5#2 (n=7) and shHSPA5#5 (n=8)). Kaplan-Meier survival curves are analyzed by a Log-rank (Mantel-Cox) test. BLI signal curves are analyzed using a Mixed-effects model test. The other comparisons are done using a Two-way ANOVA test followed by a Dunnet's multiple comparison test. \*:  $P \leq 0.05$ ; \*\*:  $P \leq 0.001$ , \*\*\*:  $P \leq 0.0005$ , \*\*\*\*:  $P \leq 0.0001$ , ns: non-significant.

**Fig S3. HSPA5 KD lead to the activation of the three arms of UPR.** A: GSEA showing the enrichment of genes from UPR gene signature (29). ES: Enrichment Score, NES: Normalized Enrichment Score, FDR: False discovery rate. B: Expression of the genes from the PERK, sXBP1 and ATF6 signature, specifically regulated downstream of each UPR arm (29) in the different conditions obtained by the RNA-seq analysis. Statistical differences between the level of expression of the PERK, sXBP1 and ATF6 signature genes in shCtrl condition compared to shHSPA5#2 and #5 are calculated by a Paired t test analysis. \*:  $P \leq 0.05$ ; \*\*:  $P \leq 0.001$ , \*\*\*:  $P \leq 0.0005$ , \*\*\*\*:  $P \leq 0.0001$ , ns: non-significative.

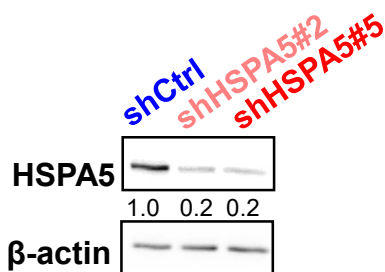
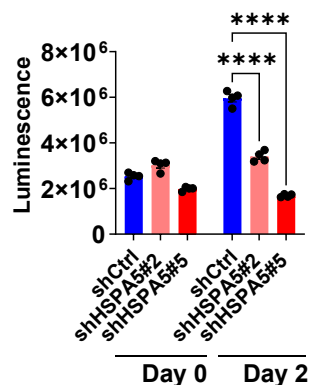
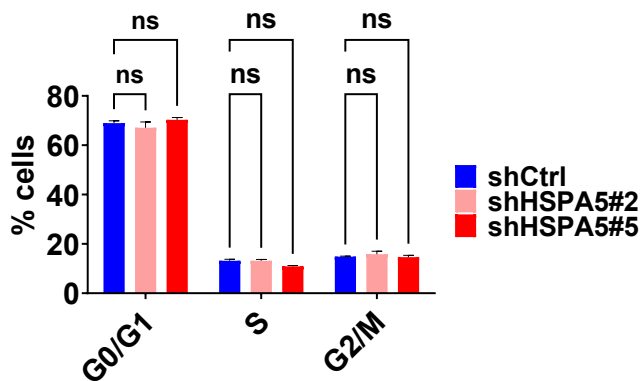
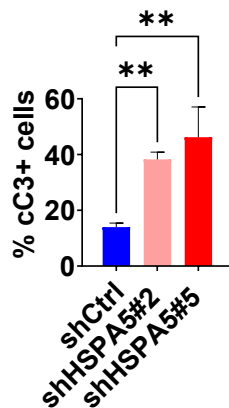
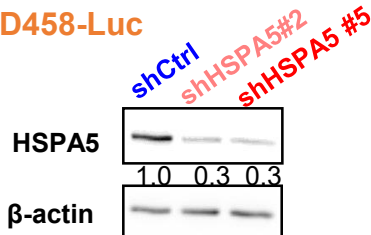
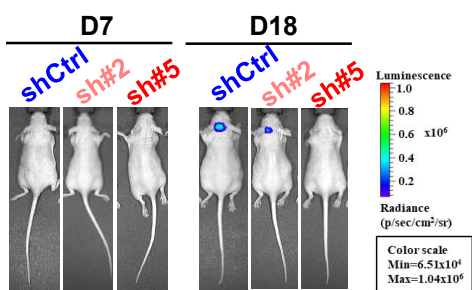
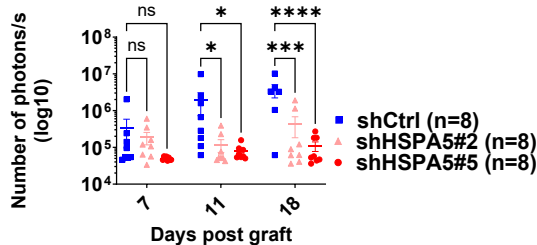
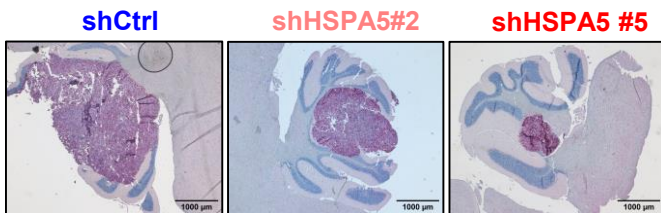
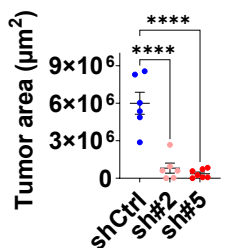
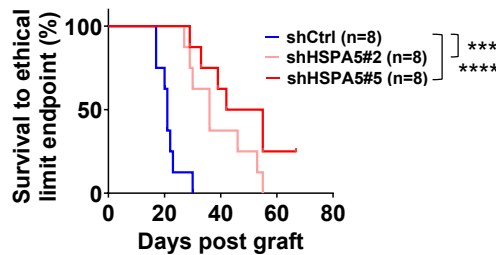
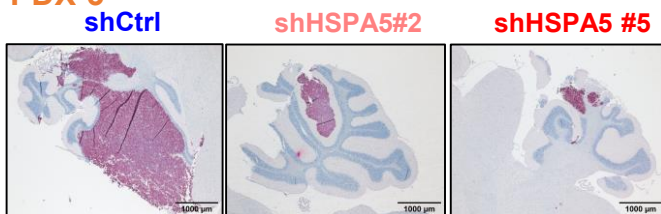
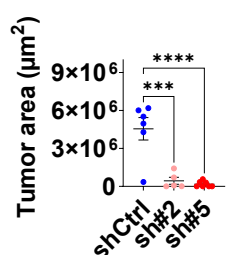
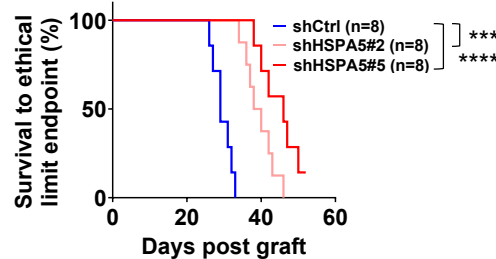
**Fig S4. The inhibition of PERK rescued the HSPA5 KD-induced cell death.** A: D425Med cells transduced with shCtrl, shHSPA5#2 and shHSPA5#5 encoding lentiviral particles are treated with DMSO or UPR arms specific inhibitors: GSK2606414 (PERK inhibitor,  $0.2\mu\text{M}$ ), MKC8866 (IRE1 $\alpha$  inhibitor,  $10\mu\text{M}$ ) and Ceapin-A7 (ATF6 $\alpha$  cleavage inhibitor,  $10\mu\text{M}$ ). The effect on cell death is evaluated by PI staining of cells measured by the IncuCyte®. Data represent the fold change at 48h (compared to 0h) and normalized to shCtrl-DMSO = 1. B: The specific activity of each UPR inhibitors and the effect on D458Med cells transduced with shCtrl, shHSPA5#2 and shHSPA5#5 encoding lentiviral particles was evaluated by Western blot. C: ATF4 KD D425Med cells are transduced with shCtrl, shHSPA5#2 and shHSPA5#5 encoding lentiviral particles. Western blot is used to confirmed the KD of ATF4 and HSPA5. D: The effect of ATF4 KD on the cell death induced by HSPA5 KD is evaluated by PI staining of cells measured by the IncuCyte®. Data represent the fold change at 48h (compared to 0h) and normalized to shCtrl. E: CHOP KD D425Med cells are transduced with shCtrl, shHSPA5#2 and shHSPA5#5 encoding lentiviral particles. Western blot is used to confirmed the KD of CHOP and HSPA5. D: The effect of CHOP KD on the cell death induced by HSPA5 KD is evaluated by PI staining of cells measured by the IncuCyte®. Data represent the fold change at 48h (compared to 0h) and normalized to shCtrl. Experiments were performed in triplicates.  $\beta$ -actin is used as loading control. Quantification is performed as described in the legend of Figure 3. Statistical differences were calculated by a One-way ANOVA test followed by a Dunnet's multiple comparison test. \*:  $P \leq 0.05$ ; \*\*:  $P \leq 0.001$ , \*\*\*:  $P \leq 0.0005$ , \*\*\*\*:  $P \leq 0.0001$ , ns: non-significative.

**Fig S5. ISRIB treatment partially rescued HSPA5 KD-induced cell death.** **A:** D425Med cells transduced with shCtrl, shHSPA5#2 and shHSPA5#5 encoding lentiviral particles are treated with DMSO or ISRIB (0.5 $\mu$ M). The effect on cell death is evaluated by PI staining of cells measured by the IncuCyte®. Data represent the fold change at 48h (compared to 0h) and normalized to shCtrl-DMSO. **B:** The specific activity of ISRIB and the effect on transduced cells is evaluated by Western blot.  $\beta$ -actin is used as loading control. Quantification is performed as previously described). Experiments were performed in triplicates. **C-D:** Expression of the list of genes that are specifically regulated downstream of ATF6 (C) and sXBP1 (D) (29) in the different conditions obtained by the RNA-seq analysis. For ISRIB effect on HSPA5 KD induced cell death, statistical differences were calculated by a One-way ANOVA test followed by a Dunnet's multiple comparison test. Statistical differences between the level of expression of the UPR signature genes in shCtrl, shHSPA5#2, shHSPA5#5 treated with DMSO versus treated with ISRIB, are calculated by a Paired t test analysis. \*:  $P \leq 0.05$ ; \*\*:  $P \leq 0.001$ , \*\*\*:  $P \leq 0.0005$ , \*\*\*\*:  $P \leq 0.0001$ , ns: non-significative.

**Fig S6. Expression of PPP1R15A in MB tumors.** Expression of PPP1R15A (GADD34) in tumors from the different MB groups (left) or subtypes (right). Transcriptomic data generated from 763 MB patients and normal fetal cerebellum (10). Statistical differences are calculated using a Mann-Whitney test. Only comparisons between G3 and the other groups are presented. \*:  $P \leq 0.05$ ; \*\*:  $P \leq 0.01$ , \*\*\*:  $P \leq 0.001$ , \*\*\*\*:  $P \leq 0.0001$ .

**Supplementary table 1** List of siRNA target genes used for siRNA screen presented in Figure 1B



**Figure 2****A****D458Med****B****C****D****E****D458-Luc****F****G****H****I****J****K****PDX-3****L****M**



**Figure 4**

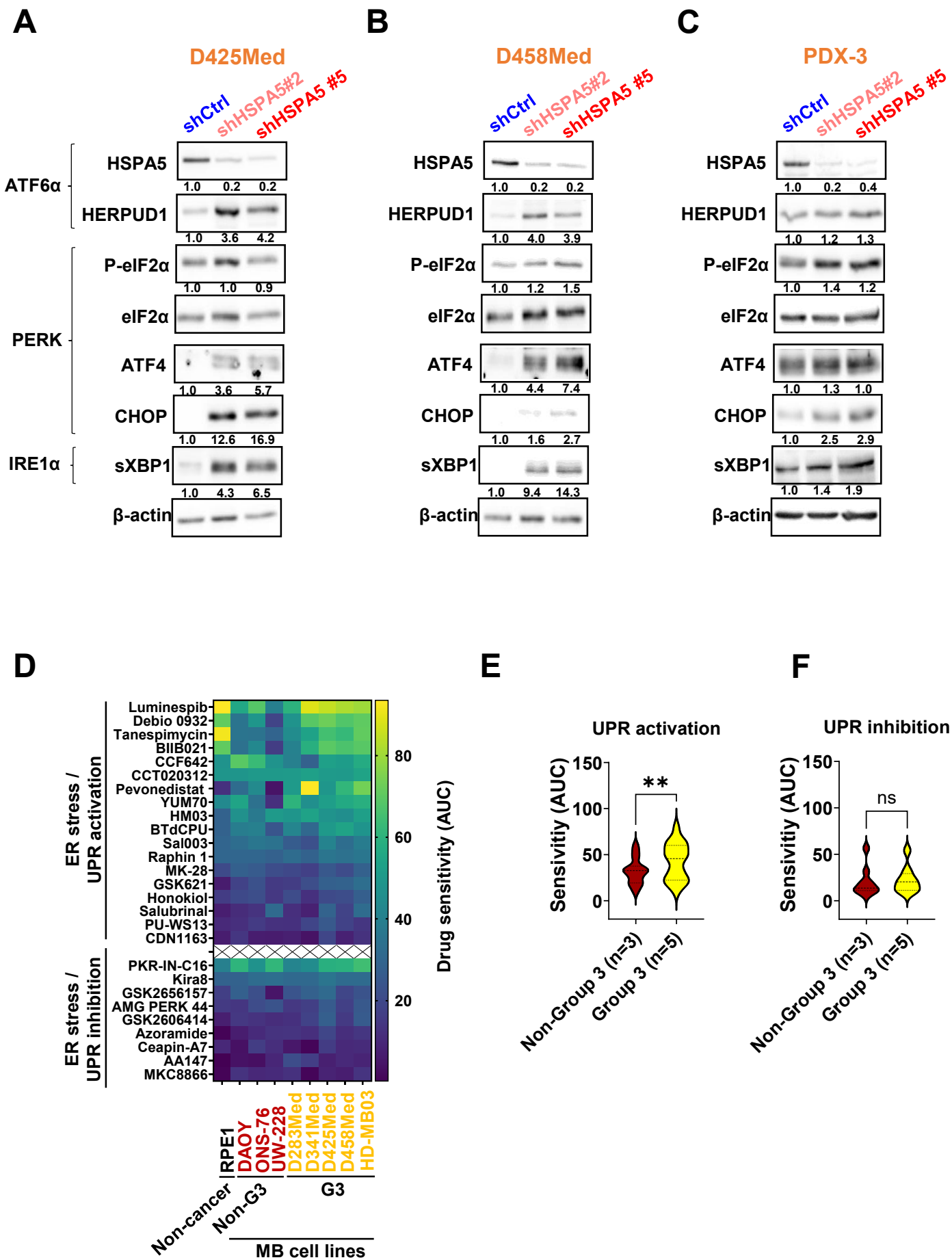
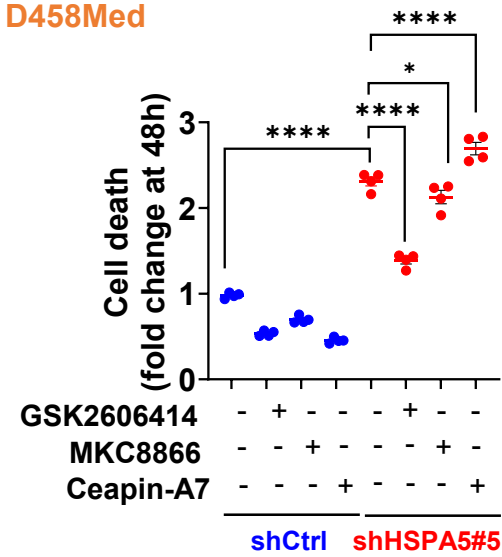


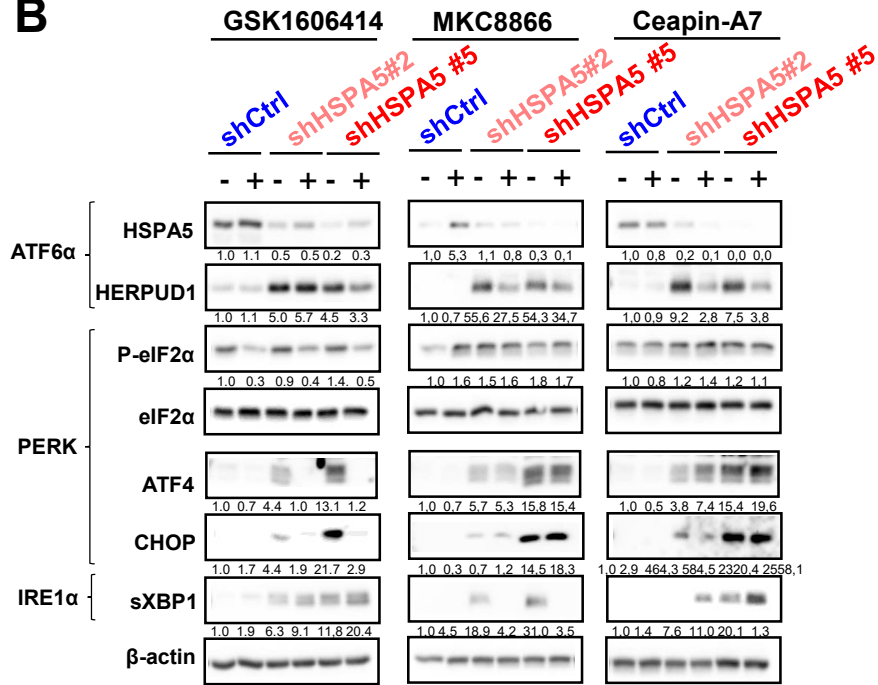
**Figure 5**

**A**

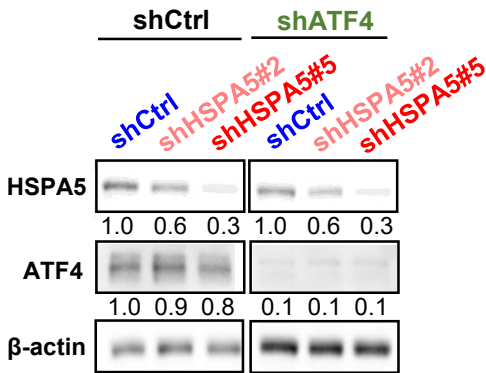
D458Med



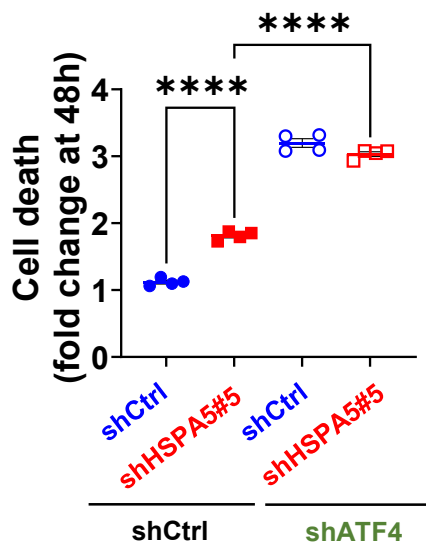
**B**



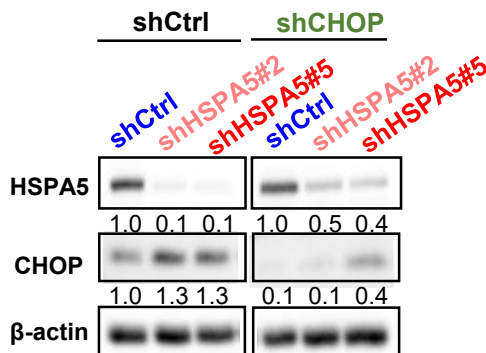
**C**



**D**



**E**



**F**

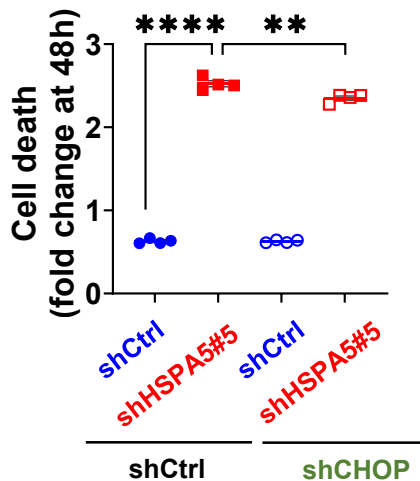
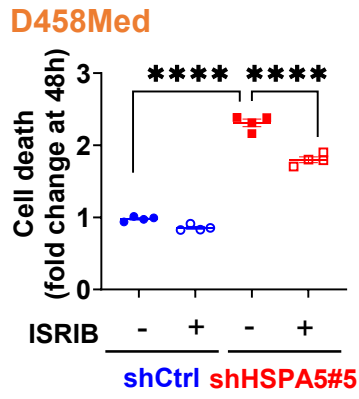
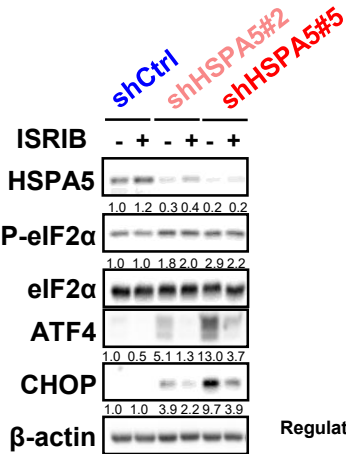


# Figure 6

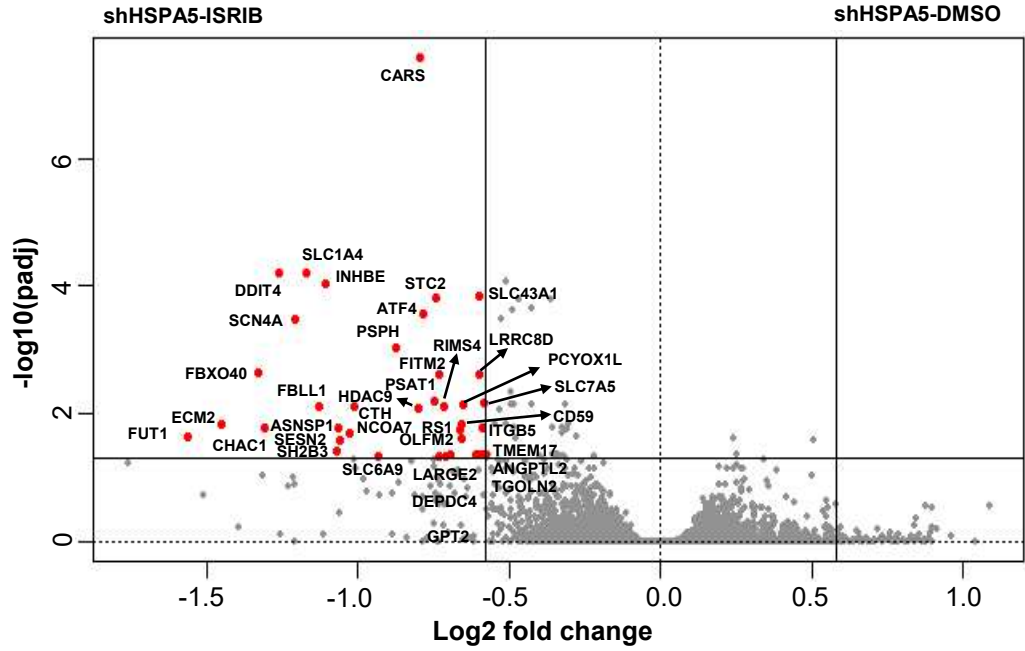
## A



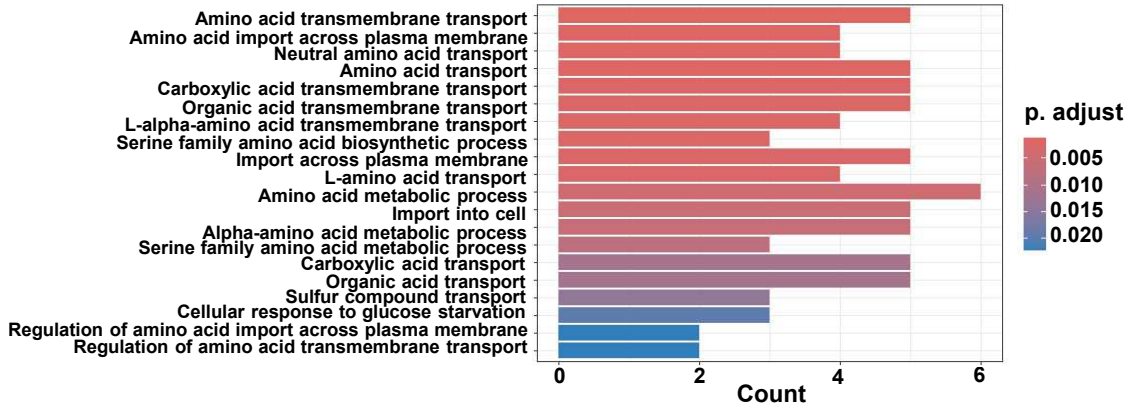
## B



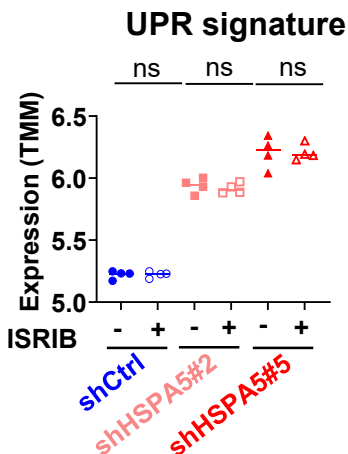
## C Most differentially expressed genes:



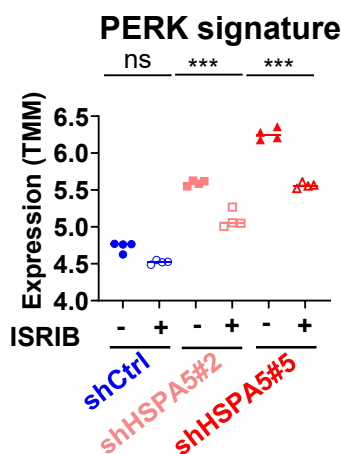
## D



## E



## F



## G

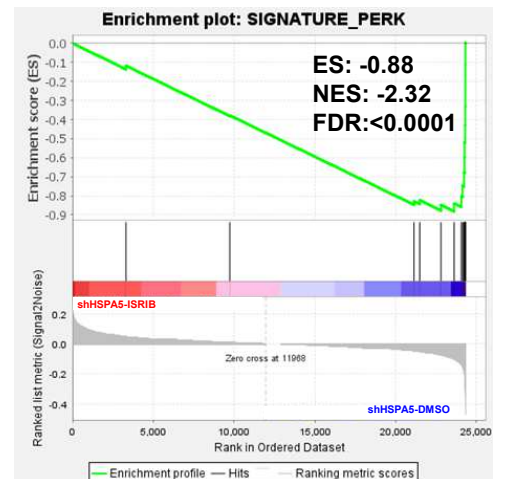


**Figure 7**

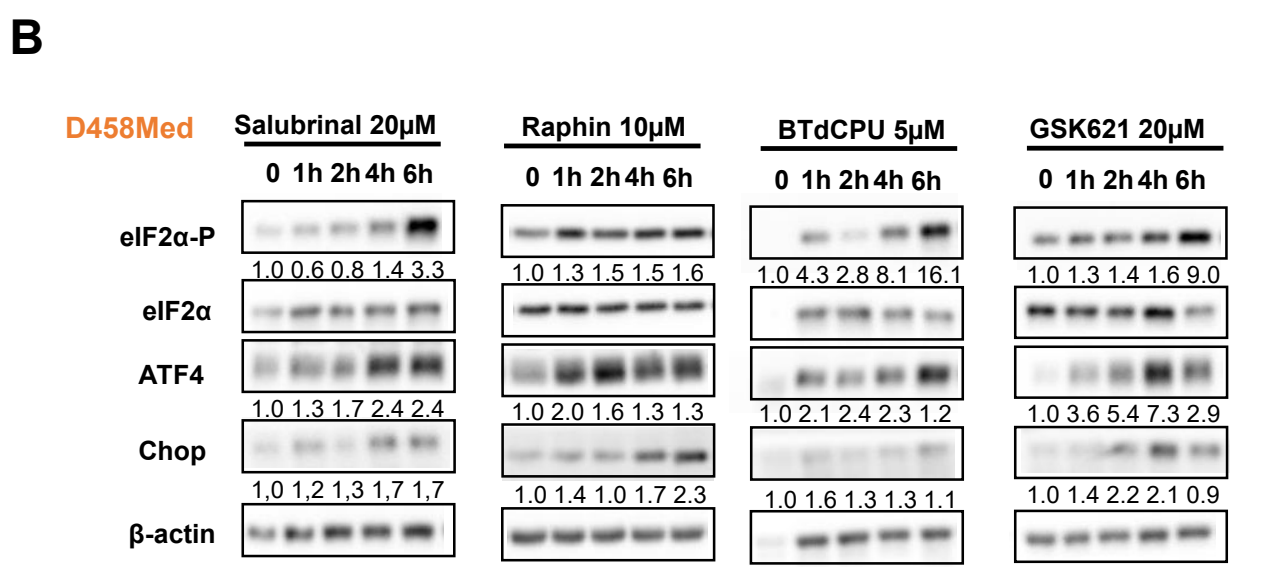
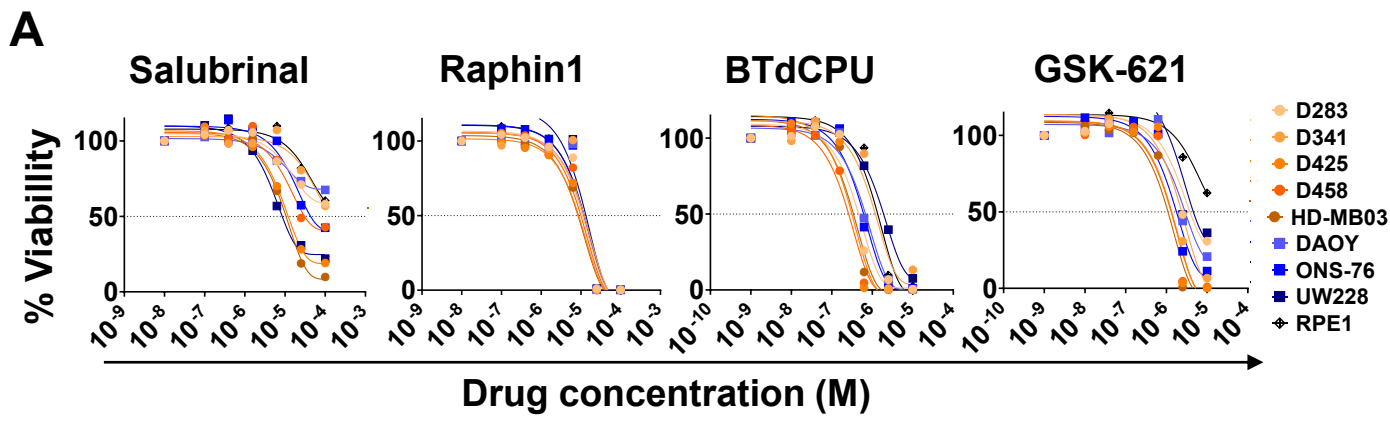


**Figure 8**

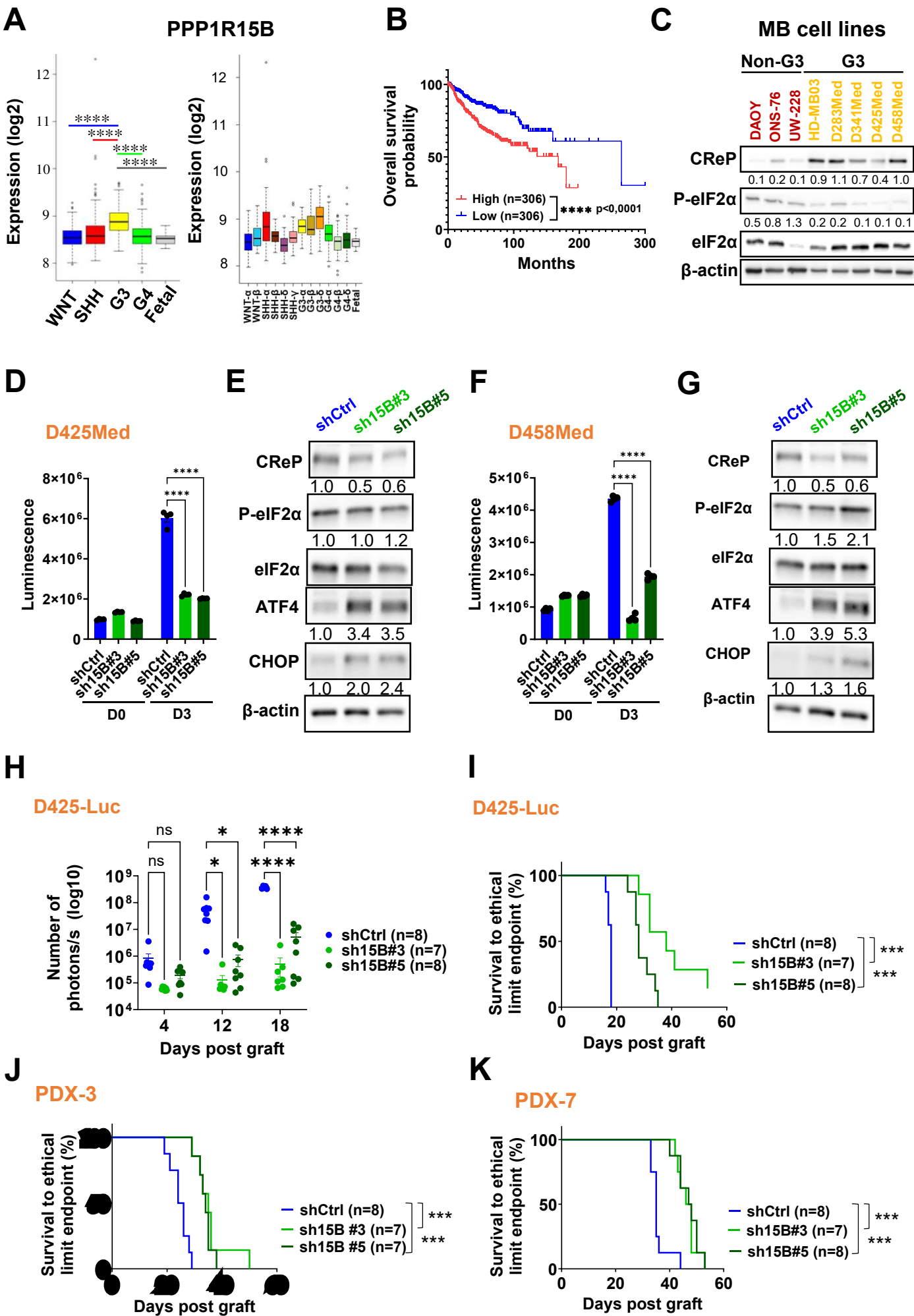
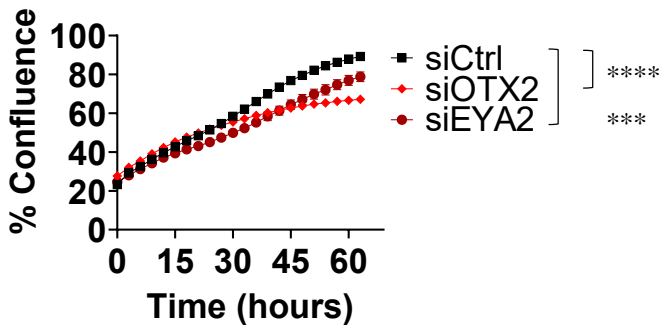
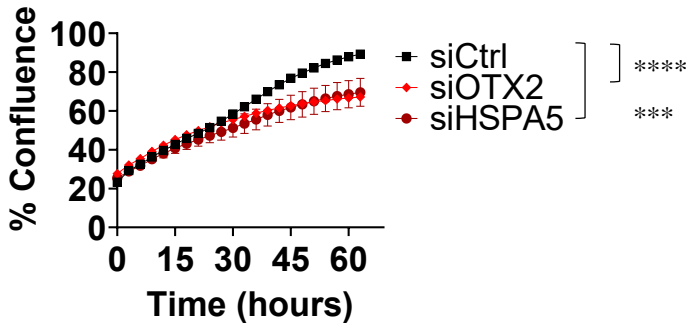


# Figure Supp 1

## A



## B



## C

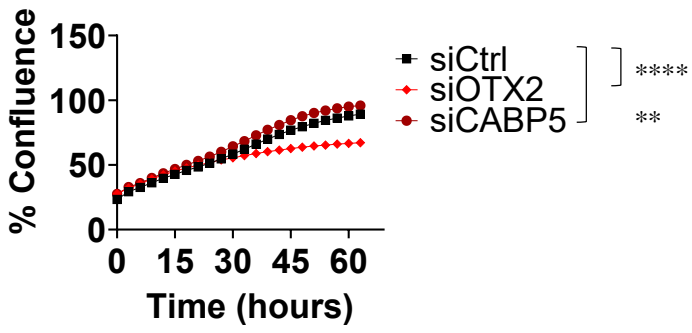
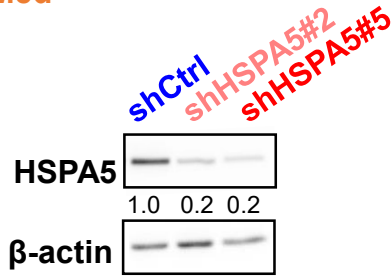
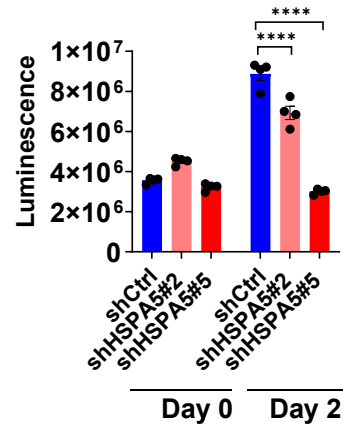


# Figure Supp 2

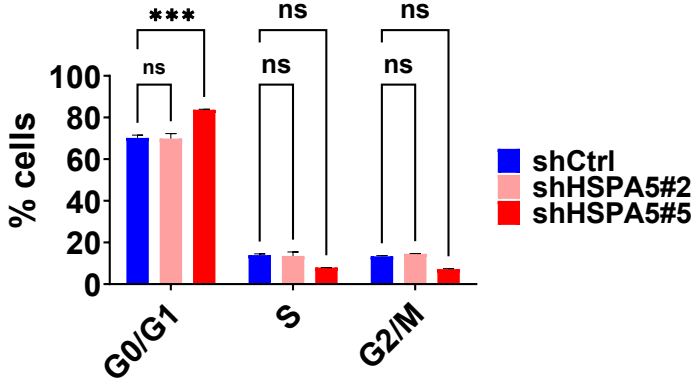
## A D425Med



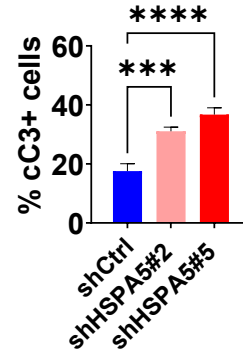
## B



## C

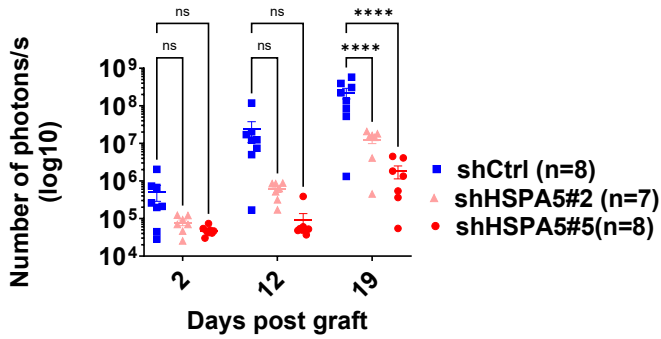


## D

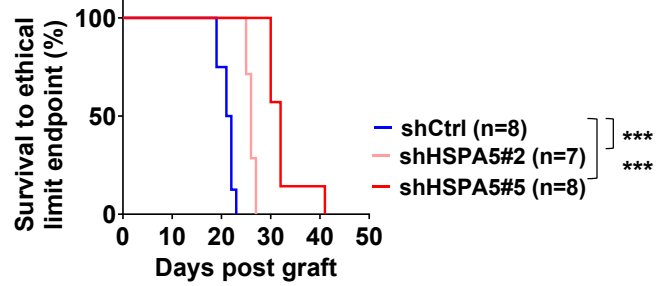


## E

### D425-Luc



## F



## G

### PDX-7

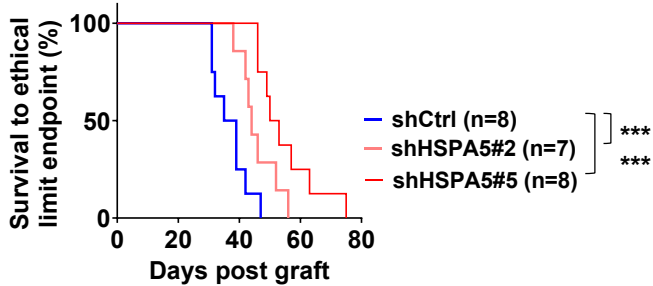
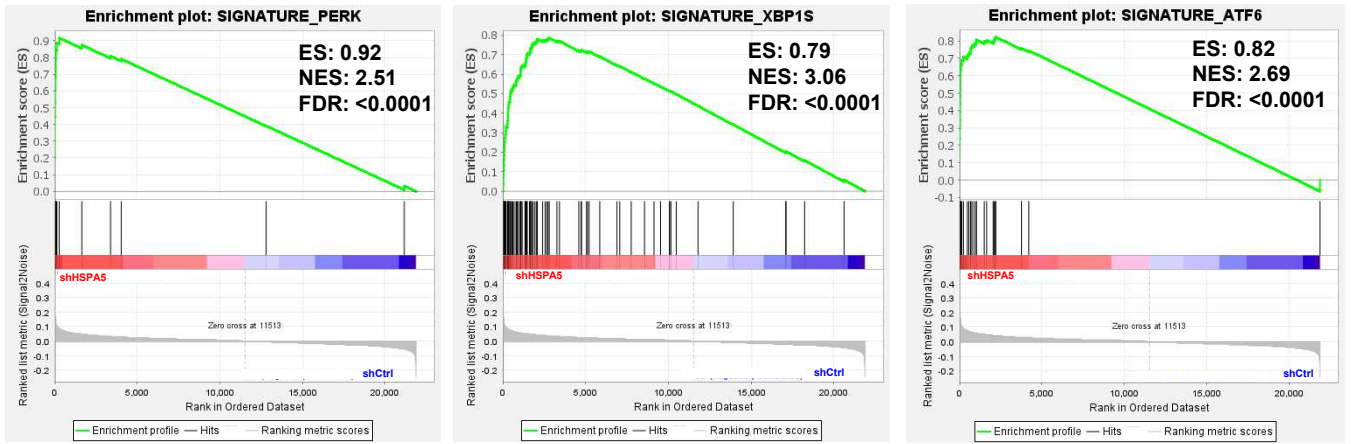


# Figure Supp 3

## A



## B

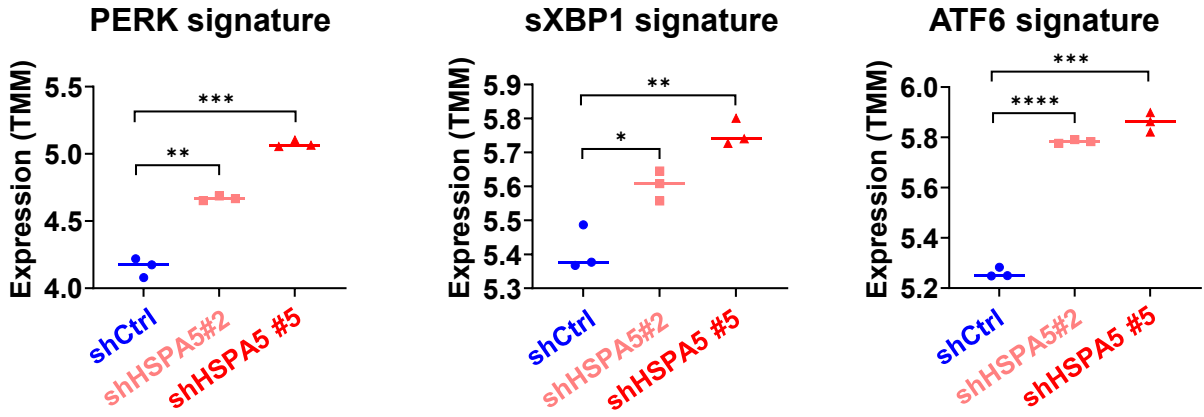
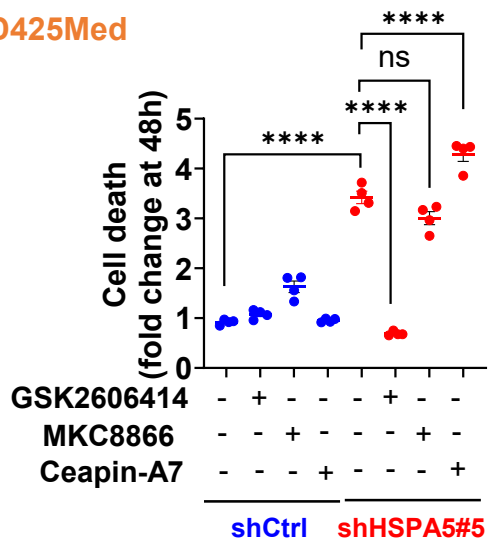


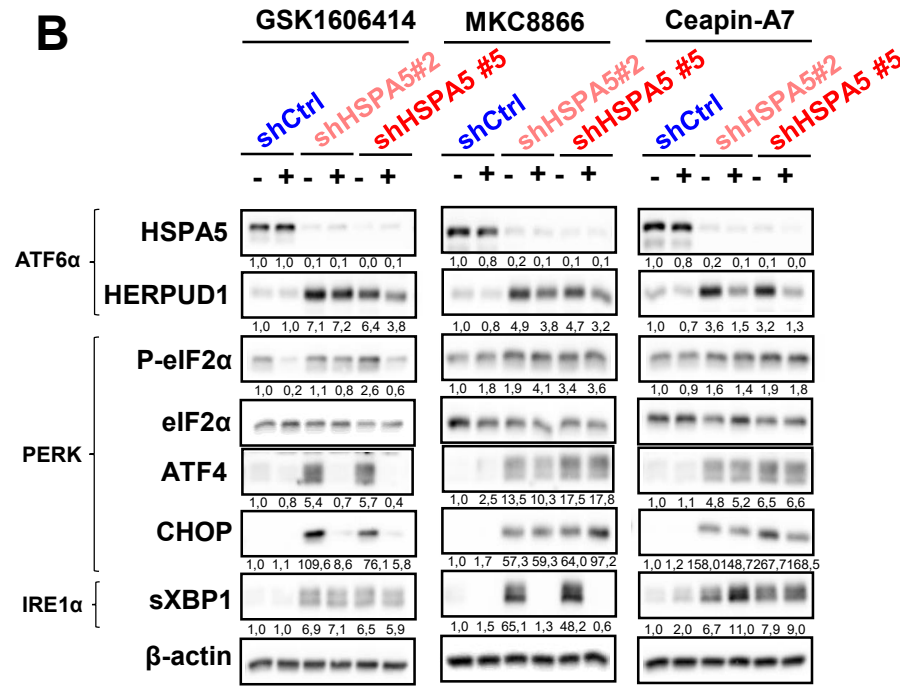
# Figure Supp 4

## A

D425Med



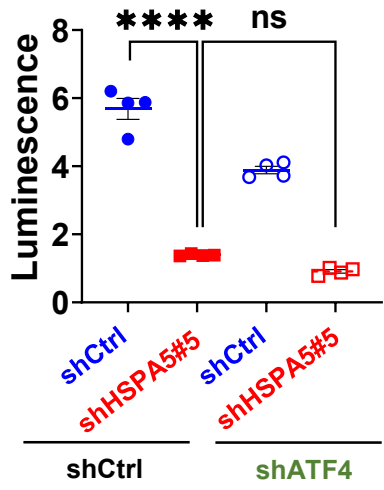
## B



## C



## D



## E



## F

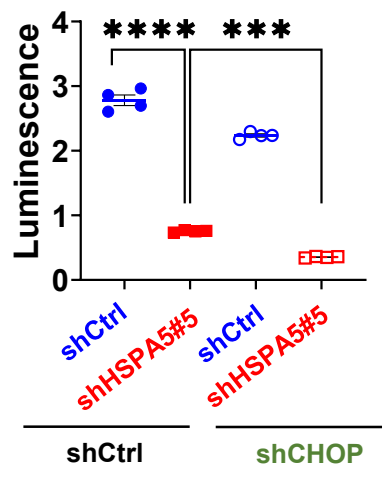
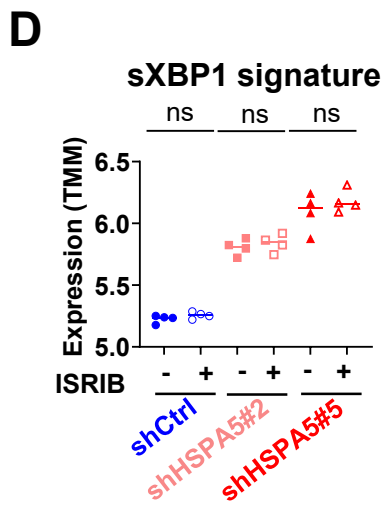
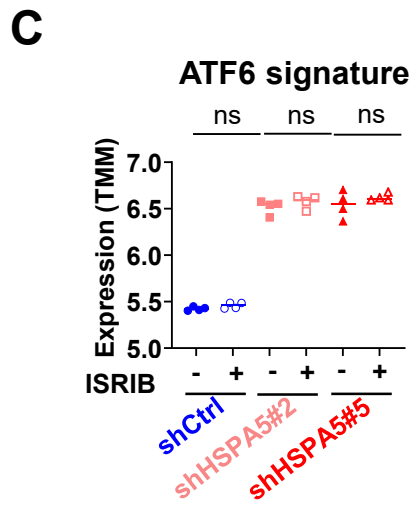
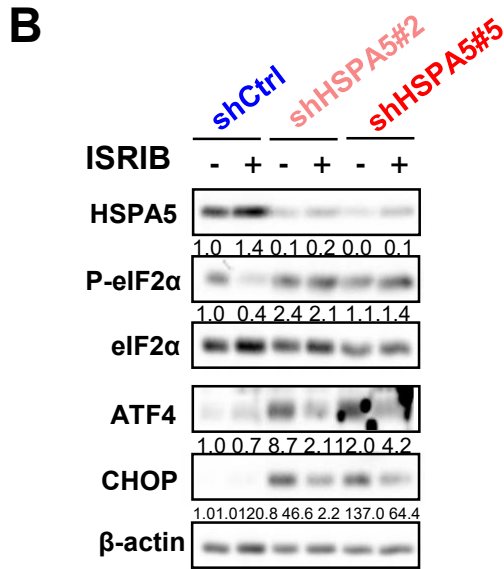
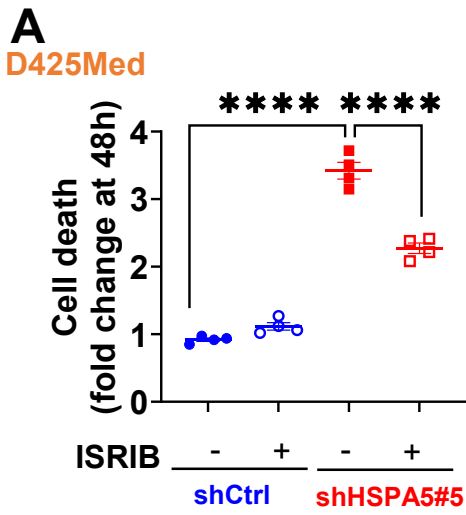
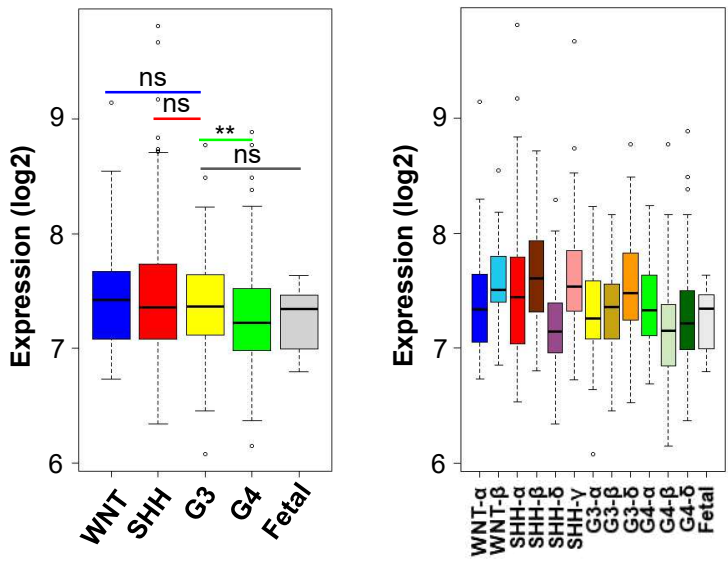


Figure Supp 5



A

PPP1R15A



**Table 1**

<b>Cell line</b>	<b>D283Med</b>	<b>D425Med</b>	<b>D458Med</b>	<b>HD-MB03</b>	<b>ONS-76</b>	<b>RPE1</b>
IC50	5,121	2,846	3,112	4,094	86,66	20,78

**Table 2**

<b>shRNA</b>	<b>Clone ID</b>
shHSPA5#2	TRCN0000231123
shHSPA5#5	TRCN0000218646
shATF4#3	TRCN0000013573
shCHOP#5	TRCN0000007267
sh15B#3	TRCN0000272634
sh15B#5	TRCN0000284798

**Table 3****Primary antibodies**

<b>Target</b>	<b>Name</b>	<b>Reference</b>	<b>Provider</b>
<i>HSPA5</i>	BiP/HSPA5 (C50B12) Rabbit mAb	3177S	Cell Signaling T
<i>HERPUD1</i>	HERPUD1 Rabbit Antibody	26730S	Cell Signaling T
<i>P-eIF2<math>\alpha</math></i>	Phospho-eIF2 $\alpha$ (Ser51) (D9G8) XP Rabbit mAb	3398S	Cell Signaling T
<i>eIF2<math>\alpha</math></i>	eIF2 $\alpha$ Rabbit Antibody	9722S	Cell Signaling T
<i>ATF4</i>	ATF-4 (D4B8) Rabbit mAb	11815S	Cell Signaling T
<i>CHOP</i>	CHOP (L63F7) Mouse mAb	2895S	Cell Signaling T
<i>sXBP1</i>	XBP-1s (D2C1F) Rabbit mAb	12782S	Cell Signaling T
<i>CReP</i>	PPP1R15B Rabbit Polyclonal antibody	PR-14634-1-AP	Proteintech
<i><math>\beta</math>-actin</i>	Anti- $\beta$ -Actin Mouse mAb	A1978	Sigma-Aldrich
<i>KI-67</i>	Ki-67 mAb (SoIA15), eBioscience™	14-5698-82	ThermoFischer

**Secondary antibodies**

<b>Target</b>	<b>Name</b>	<b>Reference</b>	<b>Provider</b>
<i>Anti-Rabbit</i>	Goat Anti-Rabbit IgG HRP Affinity Purified PAb, Goat IgG	HAF008	R&D Systems - Bio-Techne
<i>Anti-Mouse</i>	Goat Anti-Mouse IgG HRP Affinity Purified PAb, Goat IgG	HAF007	R&D Systems - Bio-Techne

# Supplementary Table 1

## List of siRNA target genes used for siRNA screen ON-TARGETplus SMARTpool siRNA (Dharmacon)

<b>Technical controls</b>	Non-targeting Control	<b>Genes involved in the photoreceptor program</b>	FOXG1	<b>Transcription factors and signaling molecules</b>	CTDNEP1	<b>Transcription factors and signaling molecules</b>	SMAD9
	GAPDH Control		RXRG		DEPTOR		MATK
	Cyclophilin Control		LIN28B		RASGRF2		PRMT5
	MYC		HLX		RALGPS2		EMP2
	OTX2		CASZ1		MAK		BSG
	TBR1		ARL4D		PTPRF		
	EYA2		ARL6		HSPB1		
	RREB1		DAND5		HSPA5		
	POU4F1		DUSP2		CPNE7		
	TAL2		DUSP7		CPNE6		
	BCL11B		SSTR2		IDH1		
	SMYD3		SEMA3F		GLUL		
	NEUROD1		NRP2		PALMD		
			GNB3		IMPG2		
			USP2		RD3		
		DOCK9	GSG1				
		PPP2R2B	USH2A				
		CABP5	SLC7A1				
		CAMKV	AIPL1				
		SERPINF1	TRIP10				
		NLK	PRICKLE2				
		SGK1	CACNA2D4				
		IQSEC1	SLC1A7				
		IQGAP2	PDE6A				
		NTN3					

### 3 DISCUSSION

---

G3 MB is a highly aggressive pediatric brain tumor whose biology is not completely understood despite intensive research. The oncogene MYC is the main molecular driver of these type of tumors, but as a TF is a hard to target. Besides, it is well known that MYC by itself is not enough to promote G3 MB formation. It requires additional oncogenic events to induce tumorigenesis. There is an urgent need to better understand the biology of G3 tumors and to identify new vulnerabilities.

During my PhD work, I tried to identify new therapeutic targets for G3 MB. To this end, we performed a siRNA-targeted screen in a G3 cell line. We identified the UPR regulator HSPA5 as a dependency in G3-MB. Our work showed that G3 MB cells are highly sensitive to UPR activation *in vitro* and *in vivo*. Interestingly, we have found that UPR-mediated cell death is dependent on the activation of the PERK arm of UPR and with a central role played by the inactivation of eIF2 $\alpha$  by phosphorylation. In line with this, we provide insights regarding a potential dependency of G3 cells on CReP, the phosphatase that control the basal phosphorylated status of eIF2 $\alpha$ . We showed that CReP is highly expressed in G3 cells, and its KD leads to a decrease in cell growth and an improvement of mice survival. These results are suggesting that eIF2 $\alpha$  phosphorylation is a point of vulnerability for G3 cells and using drugs that lead to eIF2 $\alpha$  phosphorylation could be of potential interest for therapy.

In this section I will proceed to discuss the main results of my work and will be divided in two main parts:

1. Important sensibility of G3 cells to UPR induction
2. eIF2 $\alpha$  as a central node of regulation for G3 cells.

Medulloblastoma is the most frequent malignant brain tumor in children with four molecular groups described. G3 is the group with the worse prognosis with less than 60% of OS at 5 years and less than 40% for the aggressive G3 $\gamma$  subtype (Cavalli et al., 2017). The oncogene MYC is the main molecular driver of these type of tumors. MYC is a basic helix-loop-helix-zipper (bHLHZ) TF that regulates genes involved in a large number of cellular processes including proliferation, apoptosis, metabolism, DNA repair and protein synthesis. As a TF is a hard molecule to target. Other genetic alterations in G3 tumors include overexpression of the TF GF11 and GF11B, amplifications of MYCN and OTX2, which are also TF (Juraschka and Taylor, 2019). This makes these types of tumors difficult to target with more directed therapies. Thus, an aggressive combination of surgery, chemotherapy and radiotherapy are used to treat G3 MB patients. In general, this multimodal treatment improved the survival of patients in the last decades but at the costs of severe side effects. Still patients that harbor MYC amplified tumors remain highly incurables. Extensive research is performed trying to identify new signaling pathways that could constitute potential vulnerabilities to target in these tumors.

### **1.1. siRNA-based screen to identify new vulnerabilities in G3 MB**

We performed an siRNA-targeted screen in a G3 cell line to identify new factors that could be important for G3 cells survival. The screen included a total of 62 genes that were selected based on two criteria. First, their expression was enriched in G3 tumors and second, they belong to one of the following functional groups: transcriptional regulators, signaling molecules and genes from the photoreceptor program. We found that the downregulation of one gene leads to an increase in G3 cell proliferation, CABP5. CABP5 is a calcium binding protein which expression is specific of the retina (Rieke et al., 2008). No data is available regarding a potential link of CABP5 in cancer. Two genes resulted important for the survival of G3 cells: EYA2 and HSPA5. Eyes Absent 2 (EYA2) is a transcriptional coactivator for the SIX family of homeoproteins and a tyrosine phosphatase. The EYA family of proteins has been linked with different types of cancers (Zhou et al., 2017) including breast cancer and GBM (Zhang et al., 2021a). It is highly expressed in Glioblastoma Stem Cells and the phosphatase inhibition affected cell growth *in vitro* and *in vivo*. Recently, EYA2 was

shown to directly regulate MYC transcription and stabilization in G3 MB, affecting tumor cells growth (Wolin et al., 2023). These results are in accordance with our siRNA screen, where EYA2 resulted in the decrease of G3 cells. For my PhD work I decided to investigate why HSPA5 was important for the survival of G3 cells since it was the strongest hit after different rounds of validation and also due the existence of pharmacological inhibitors as HA15 (Cerezo et al., 2016).

## **1.2. G3 MB cells require HSPA5 to survive**

To validate the results of the siRNA screen, I used an HSPA5 inhibitor, HA15, as a tool compound. HA15 is a specific inhibitor of the chaperone by acting on the ATPase activity of HSPA5. This drug has been used before and shown to induce melanoma cell death through the induction of apoptosis and autophagy (Cerezo and Rocchi, 2017; Cerezo et al., 2016). I showed that several G3 cell lines are highly sensitive to increasing concentrations of HA15. Interestingly, this effect seems to be specific of G3 cells since there is almost no effect when non-G3 cells as ONS-76 are treated with the same concentrations. These results indicate that HSPA5 is important for G3 MB cells growth. As previously shown, HA15 has no effect neither when used to treat the RPE1 cell line, which is a non-cancer cell model, confirming the idea that HSPA5 plays an important role in the survival of some types of cancer cells but not in normal cells, opening a therapeutic window.

HSPA5 is overexpressed in several tumor types and it has been linked to different processes during tumor initiation and development (Akinyemi et al., 2023; Lee, 2014). The knock-down or pharmacologically inhibition of the chaperone improved survival, decreased resistance to therapy and reduced metastasis in different preclinical tumor models. I also validated the importance of HSPA5 as a new dependency for G3 MB cells using shRNA to KD HSPA5 expression *in vitro*. Importantly, this was also confirmed *in vivo*, where mice that were orthotopically grafted with HSPA5 KD cells survived longer than mice that received control cells. These results were confirmed using two different G3 cell lines and two PDXs, more faithful model of G3 tumors. No studies have linked before HSPA5 to MB, and specifically to G3 tumors. Our results provide solid data about the sensitivity of G3 MB cells to HSPA5 KD *in vitro* and *in vivo*. Inhibition of the chaperone using HA15 showed that G3 cells are more sensitive than non-G3 cells to HSPA5 inhibition.

### **1.3. G3 cells are sensitive to UPR activation**

To understand the molecular mechanisms that were involved in the effect of HSPA5 KD in G3 cells, I performed an RNAseq analysis in the D425Med G3 cell line and compared HSPA5 KD cells to control cells. These analyses indicated that most of the genes that were differentially expressed between the two conditions were related with ER stress and UPR activation, including the activation of the three branches of UPR, namely IRE1 $\alpha$ , ATF6 $\alpha$  and PERK. I confirmed these results by western blot in two different G3 cell lines and one PDX, showing a strong induction of UPR after HSPA5 KD. Since HSPA5 is the master regulator of the UPR, we think that the activation of UPR after HSPA5 KD resulted from the release of the UPR effectors from the chaperone and/or to the induction of a massive ER stress due to the accumulation of unfolded/misfolded proteins in the ER (Kopp et al., 2019). In any case, these results suggest that G3 cells are highly sensitive to the induction of UPR, since there is a strong induction of cell death after UPR activation following HSPA5 KD.

The chaperone HSPA5 has many functions in the cell including folding, holding and translocating the newly synthesized polypeptides across the ER membrane. It also contributes to clearance of unfolded proteins by targeting them for ER-associated degradation (ERAD) and to maintain Ca<sup>2+</sup> homeostasis in this organelle (Schäuble et al., 2012). Since Ca<sup>2+</sup> leakage to the cytosol constitute an apoptotic signal, we can imagine that the cell death induced after HSPA5 KD may be linked to deregulated Ca<sup>2+</sup> flux to the cytosol. Additionally, it has been shown that during ER stress, HSPA5 may relocated to the surface of cancer cells, where it interacts with different signaling to activate processes involved in proliferation, invasion, inflammation and others (Tsai et al., 2018). From its role in all of these processes, we may also expect that the KD of the chaperone affect G3 MB cell growth. However, according to our data, the cell death induced after HSPA5 KD is mainly due to the activation of UPR and especially the PERK arm since the inhibition of PERK is sufficient to rescue cell death in HSPA5 KD cells.

To further confirm the sensitivity of G3 cells to UPR by performing a chemical screen with drugs that either activate or inhibit the UPR. For this screen we use a large panel of cell lines including five G3 MB cell lines, three non-G3 MB cell lines and one non-cancer cell line. According to the results with HSPA5 KD, drugs that induce UPR

had a strong effect on G3 cells compared to non-G3 cells and the normal cell line, confirming the hypothesis that G3 MB cells are highly sensitive to UPR activation. I have shown this through different means including HSPA5 KD, but also using drugs that are known to induce UPR.

UPR activation can have two biological functions. It can promote recovery from proteotoxic stress and help to reestablish homeostasis in the ER or it can induce a terminal apoptotic UPR (Hetz et al., 2015; Urrea et al., 2013). This concept has been exploited in the context of cancer therapeutics. For those cancer types where UPR has been shown to be protective, using drugs that inhibit the different pathways of UPR has been shown to be effective. In the other hand, it has been demonstrated that using genetic tools or drugs that will lead to an unresolvable ER stress and/or a complete unleashing of the UPR could also be of therapeutic interest. This is the case of the ER-resident chaperones inhibitors or proteasome inhibitors (Lin et al., 2019; Luo and Lee, 2013). This is also the case of drugs that will inhibit PERK or allow to bypass the phosphorylation of eIF2 $\alpha$  to reestablish protein synthesis, inducing lethal proteotoxic stress.

The drug-based screen did not reveal any specific sensitivity of G3 cells to UPR inhibitors. This result suggests that, in our hands, the different pathways of UPR are not playing a major cytoprotective role in G3 MB, since the use of different inhibitors did not affect the survival of cells. These results were in line with our experiments with inhibitors of each individual UPR arm. When I treated shRNA control cells with the specific inhibitors of each individual arm, namely, MKC8866 (IRE1 $\alpha$ ), Ceapin-A7 (ATF6 $\alpha$ ) and GSK260614 (PERK), no induction of cell death was observed. This result confirms that any UPR arm play a cytoprotective role in G3 MB.

This is in strike contrast with what can be observed in other cancers. Indeed, the existence of an adaptive and prosurvival basal activation of UPR has been largely demonstrated in different tumors. For example, the IRE1 $\alpha$  arm has been shown to play a cytoprotective role in GBM or breast cancer (Lhomond et al., 2018; Logue et al., 2018; Le Reste et al., 2020). This dependency mainly relies on the control of genes involved in protein folding, secretion, ERAD, and lipid synthesis by sXBP1 and the RIDD component of the pathway. Similarly, the PERK arm has been related with tumor survival by controlling genes involved in folding, antioxidant responses, autophagy,

amino acid metabolism, mainly through the induction of ATF4. The decrease in protein translation that results from the phosphorylation of eIF2 $\alpha$  by PERK, can also help cancer cells to cope with proteotoxic stress generated by the increased demands on biosynthetic processes. This has been nicely shown in prostate cancer and lymphoma MYC-driven tumor models where the activation of PERK and/or eIF2 $\alpha$  phosphorylation/ATF4 expression are required to control protein synthesis rates to a level that is compatible with life (Nguyen et al., 2018; Tameire et al., 2019). This seems not to be the case of G3 MB cells even though they are MYC-driven cancers. It is possible that G3 cells on the contrary, may require a fully active translational machinery to support tumor transformation and tumor growth driven by MYC. Active protein synthesis processes may provide the cells with specific molecules required for tumor survival. This may include, but not only, the expression of chaperones or ERAD related proteins that can help to cope with proteotoxic stress characteristic of the tumor growth.

A few studies have assessed the role of UPR in MB and are restricted to the SHH MB group. First results indicated that the activation of the PERK/eIF2 $\alpha$  arm promote MB cell migration and angiogenesis (Jamison et al., 2015; Lin et al., 2011b). Later, it was demonstrated that this arm was active not only in MB tumors but also in premalignant GCPs, suggesting a potential role of the PERK arm of UPR in MB tumor initiation (Ho et al., 2016). The importance of the pathway on SHH MB tumors was also investigated through GADD34 mutated models. GADD34 heterozygous mutation contribute to increase the activation of the PERK/eIF2 $\alpha$  arm but the homozygous mutation prevented MB formation, mainly through the induction of apoptosis in premalignant GCPs during transformation (Stone et al., 2016). These results suggest a dual role for the activation of the PERK arm of UPR in SHH MB. My work did not reveal such a protective role for UPR but, in contrast, a higher sensitivity of G3 cells to UPR activation, either by using chemical UPR activators, or through HSPA5 KD studies, with a strong cell death that is induced concomitantly with UPR induction.

#### **1.4. PERK activation/ eIF2 $\alpha$ phosphorylation are the main mediators of the UPR induced cell death**

My results showed that HSPA5 KD induced strong activation of the three arms of UPR and a massive cell death. Analysis of HSPA5 KD cells by flow cytometry revealed a positive staining with the anti-cleaved Caspase 3 antibody, suggesting

apoptotic cell death induction. These results are also confirmed by the RNAseq experiment. Gene ontology analysis showed activation of the apoptotic signaling pathway. UPR activation is an adaptive response of the cells under stressful environments to restore homeostasis in the ER. However, when ER stress cannot be resolved and UPR activation is too strong and sustained, cell death mechanisms could be activated (Hetz et al., 2020). The proapoptotic UPR mainly involve the IRE1 $\alpha$  and PERK arms. IRE1 $\alpha$  participates to cell death induction mainly through the activation of Caspase-2, Caspase-8 and BAX/BAK-dependent apoptosis. The PERK arm leads to the activation of the eIF2 $\alpha$ /ATF4 arm, resulting in the induction of the pro-apoptotic factor CHOP. CHOP is generally one of the main mediators of UPR-induced cell death. It plays this role through the induction of proteins of BCL-2 family, including BIM, PUMA, NOXA and BID. It can also activate the death receptor 4 (DR4) and DR5. CHOP will also induce the expression of GADD34, the ER-stress induced eIF2 $\alpha$  phosphatase, which lead to the reestablishing of protein synthesis, further contributing the proteotoxic stress. It has been also shown that CHOP may require additional elements to induce UPR-dependent cell death. For instance, it has been demonstrated that CHOP and ATF4 are both required to induce UPR-induced apoptotic cell death (Han et al., 2013). Counterintuitively, they do that by regulating genes that will promote protein synthesis to induce a proteotoxic stress that will conduct the cells to death.

To determine which arm of UPR was involved in the cell death that was induced after HSPA5 KD, I used specific inhibitors of each arm: MKC8866 (IRE1 $\alpha$ ), Ceapin-A7 (ATF6 $\alpha$ ) and GSK260614 (PERK) to treat control and HSPA5 KD cells. I showed that, while treatment of HSPA5 KD cells with IRE1 $\alpha$  or ATF6 $\alpha$  inhibitors had no effect, the use of the PERK inhibitor (GSK260641) rescued cell death. These results demonstrated the causal role of HSPA5 KD in inducing cell death through the PERK arm of UPR. The other two arms, while strongly activated, seem not to participate to cell death. Surprisingly, nor the KD of CHOP neither KD of ATF4 were able to prevent cell death induced by HSPA5 KD in two different G3 MB cell lines. This was an unexpected result since the participation of these two TFs in the UPR-induced cell death is largely demonstrated (Hetz et al., 2020; Urra et al., 2013). To cite one example, the KD of CHOP was sufficient to rescue UPR-induced cell death after HA15 treatment in melanoma cells (Cerezo et al., 2016). In this study, the KD of ATF4 also allowed to a partial recovery from HA15-induced cell death. However, while our results

showed that CHOP is not sufficient to rescue cell death. They do not exclude that CHOP is involved.

The rescue of HSPA5 KD phenotype by producing ATF4 KD cells was even more complex considering that the KD of ATF4 by itself leads to a decrease in G3 cell viability. ATF4 is a stress responsive TF induced in different conditions including ER stress, amino acid deprivation, oxidative stress and low oxygen conditions (Wortel et al., 2017). This TF will regulate genes that allow to adapt to different stresses and in this context, it can result essential to the survival of cells. However, ATF4 also participate to the induction of cell death, mainly through the induction of the proapoptotic factor CHOP. Although, it has been also demonstrated that both ATF4 and CHOP may cooperate in the regulation of genes that control protein synthesis. Indeed, both TFs induced cell death by promoting an uncontrolled increase in protein synthesis leading in ATP depletion and oxidative stress resulting in cell death (Han et al., 2013).

The contribution of ATF4 to cell fate decisions seems to be dependent on the cell type. This has been linked to oncogene transformation processes, in which it plays a role by controlling amino acid metabolism. In MYC-driven lymphoma cells, ATF4 has been shown to be activated by MYC to function as a rheostat to control protein synthesis rates and prevent lethal proteotoxicity (Tameire et al., 2019). On the contrary, in some models of MYC-driven neuroblastoma, ATF4 is induced in nutrient deprivation conditions to activate proapoptotic genes including NOXA, PUMA and TRIB3 (Xia et al., 2019). Considering this, it is not surprising to find that G3 MB cells die when ATF4 is KD. In G3 cells at basal states, ATF4 may act as a brake to prevent MYC-driven proteotoxicity as has been shown in other tumor models. This role could be particularly important during the early phases of tumor cell transformation. Considering this idea, during my PhD, I explored the potential effect of combining ATF4 and MYC overexpression on granule cell progenitors (GCPs) (ongoing experiments). However, more research is needed to better understand the role of this TF in G3 cells and a potential link with MYC.

In any case, my results point to eIF2 $\alpha$  inactivation by phosphorylation as a central node of regulation for G3 cells. HSPA5 KD cells were also treated with ISRIB, which is a small molecule that allows to bypass the blocking effect of eIF2 $\alpha$  phosphorylation and reestablish protein synthesis. When HSPA5 KD cells were treated

with ISRIB, there was also a partial rescue of cell death, confirming a crucial role for the eIF2 $\alpha$  phosphorylation in this phenotype. The main consequence of eIF2 $\alpha$  phosphorylation is an attenuation on global translation in cell, as a first attempt to reduce the protein burden during ER stress. At the same time, the translation of specific mRNAs like ATF4 and CHOP are favored during this phase of decreased protein synthesis. The activation of ATF4 and CHOP that occurred after HSPA5 KD, are also prevented as a secondary effect when cells are treated with ISRIB. This raises the question about the role of ATF4 and CHOP in the response. One cannot say if the decrease in ATF4 and CHOP induction after treatment of HSPA5 KD cells with ISRIB is simply the effect of the reestablishing of normal rates of protein synthesis or if they are indeed involved in the induction of cell death. The KD of ATF4, and specially CHOP may not be sufficient to prevent HSPA5 KD induced cell death but they could be involved somehow.

In the other hand, treatment of HSPA5 KD cells with ISRIB resulted in a partial rescue only. This fact raises the question of why while PERK inhibition completely rescued cell death, ISRIB treatment only allow a partial rescue? We may propose two hypotheses to this. The partial rescue by ISRIB suggests that cell death induction is a complex process that may implicate a transcriptional but also translational program after UPR activation. Indeed, we started to answer to this question and found that some pro and anti-apoptotic factors are regulated at different levels. For instance, our preliminary data is suggesting that the anti-apoptotic XIAP and MCL-1 are decreased after HSPA5 KD and increased by ISRIB treatment but only at the level of translation, while pro-apoptotic elements as PUMA, TRIB3, BID, NOXA, BIM seem to be regulated from the transcription point. Secondly, it has been demonstrated that ISRIB allows to bypass the blocking phosphorylation of eIF2 $\alpha$  while there are pools of free eIF2B molecules. Under UPR activation, ISRIB acts as an eIF2B activator that will force the GTP exchange factor to interact with eIF2 $\alpha$  and reestablish translation (Costa-Mattioli and Walter, 2020; Sidrauski et al., 2015). However, at certain level of UPR activation when there is no more eIF2B free pools, ISRIB is not able to do so anymore, explaining why when UPR activation is too strong, this molecule is not able to rescue from cell death.

## **1.5. G3 cells require hypo-phosphorylated eIF2 $\alpha$ : a CReP dependency**

My results showed that HSPA5 KD - induced cell death could be rescued by the use of the PERK inhibitor GSK2606414. This suggests that phosphorylation of eIF2 $\alpha$  is a major player in the effect of HSPA5 KD. This is also supported by experiments showing that treatment with ISRIB partially rescued HSPA5 KD induced cell death. These results suggest that G3 cells are sensitive to eIF2 $\alpha$  phosphorylation and may require mainly a hypo-phosphorylated eIF2 $\alpha$  to survive.

To go further and validate this hypothesis, I treated G3 cells with drugs that will result in a maintained phosphorylation of eIF2 $\alpha$ , either by activating the kinases that phosphorylate eIF2 $\alpha$  or by inhibiting the phosphatases. There are four eIF2 $\alpha$  specific kinases that will phosphorylate eIF2 $\alpha$  in response to different stresses, PERK, which is activated by ER stress and during the UPR, PKR (double-stranded RNA-dependent protein kinase), which is activated by double-stranded RNA, GCN2, which is activated by amino acid deprivation, and the heme-regulated HRI (heme-regulated inhibitor) (Costa-Mattioli and Walter, 2020). PERK is a common player between the UPR and the Integrated Stress Response (ISR) which involves also the other three kinases. Dephosphorylation of eIF2 $\alpha$  is assured by two heterodimeric phosphatases that comprises a regulatory subunit (PPP1R15A or GADD34 and PPP1R15B or CReP) and the catalytic subunit protein phosphatase 1 (PP1c) (Harding et al., 2009). GADD34 is induced during ER stress by CHOP, as a negative feedback loop that allows the reestablishment of protein synthesis when ER stress is resolved. CReP is the constitutively induced eIF2 $\alpha$  phosphatase that assures proper regulation of the eIF2 $\alpha$  phosphorylation status according to cell requirements.

I showed that treatment of G3 cells with BTdCPU, which is an activator of HRI, MK-28, an activator of PERK, GSK-621, which is a specific AMPK activator that results into eIF2 $\alpha$  phosphorylation, Salubrinal, which a dual inhibitor of CReP and GADD34, the two eIF2 $\alpha$  phosphatase and Raphin1, a specific CReP phosphatase, all resulted in a strong activation of the P-eIF2 $\alpha$  /ATF4/CHOP pathway with a strong induction of cell death. These results confirm eIF2 $\alpha$  as a sensitive node of regulation of G3 MB cells and may have identified a new vulnerability for these cells.

I focused my attention then to the phosphatases that may maintain the hypo-phosphorylated form of eIF2 $\alpha$ . Indeed, when we analyzed the level of expression of the two eIF2 $\alpha$  phosphatases in tumors from MB patients, we saw that there is not specific pattern of expression of PPP1R15A (GADD34) across groups. This result is not surprising since GADD34 is induced under stress and UPR activation conditions. It is not expected to be expressed at basal conditions. I performed shRNA mediated KD of GADD34 in G3 MB cell lines, and the decrease in the level of expression of the gene had no effect on cell viability as expected, confirming that G3 cells survival is not dependent on a basal activation of UPR pathways. In HSPA5 KD cells, the expression of PPP1R15A (GADD34) determined by RNAseq analysis is not induced compared to control cells. I did not succeed technically to evaluate if there was an increase in the level of the protein after HSPA5 KD. It is possible that PPP1R15A (GADD34) mRNA was specifically translated after UPR activation even if its transcription did not change. However, considering that PPP1R15A (GADD34) is direct target of CHOP, and that CHOP KD was not sufficient to rescue HSPA5 KD induced cell death, we can think that even if PPP1R15A (GADD34) is activated in these conditions, it is not contributing to the induction of cell death. As mentioned before, CHOP may induce UPR mediated cell death through the induction of proteins that favor increase in translation, including GADD34 that will remove the blocking phosphorylation of eIF2 $\alpha$  and reestablish protein synthesis (Marciniak et al., 2004; Urra et al., 2013).

In the other hand, PPP1R15B (CReP) is highly expressed in tumors from G3 and especially, tumors from the G3 $\gamma$  subtype. Patients from this subtype harbor MYC amplified tumors and display the worse prognosis. Interestingly, I showed that PPP1R15B expression has a prognostic value for MB patients, with patients harboring high level of expression getting a worse prognosis. I confirmed that the CReP protein is highly expressed in G3 cell lines compared to non-G3 MB cell lines. I also showed a low level of P-eIF2 $\alpha$  in G3 cell lines, contributing to the hypothesis that G3 cells may require a hypo-phosphorylated form of eIF2 $\alpha$  and that this may be maintained by the activity of CReP. It could be very interesting to validate this data in MB patient samples. During my thesis, we tried to do so using proteome and phosphoproteome data but it was not possible due to technical limitations of the approaches used to generate this data. Interestingly, my results also showed that G3 cells are dependent on CReP to survive since its KD induced cell death and increased the survival of mice grafted with

cell lines or PDXs where CReP expression was reduced. According to this, this work may have identified a new potential therapeutic target for G3 MB tumors.

### **1.6. eIF2 $\alpha$ phosphorylated status control by MYC?**

A dual role of P- eIF2 $\alpha$  in disease has been established. Indeed, loss or excess of eIF2 $\alpha$  phosphorylation resulting in its inactivation is incompatible with life. According to this, several studies have provided data demonstrating that some tumor types depend on the phosphorylation of eIF2 $\alpha$  to control protein synthesis rates and limit proteotoxic stress. In MYC-driven mouse models of lymphomas it was shown that MYC transformation induced activation of PERK and GCN2 leading to phosphorylation of eIF2 $\alpha$  and ATF4 expression as a rheostat to control protein synthesis rates and prevent apoptosis (Tameire et al., 2019). This is also the case of some prostate and colorectal cancer models in which eIF2 $\alpha$  phosphorylation is induced as a negative feedback loop by MYC to control protein synthesis (Nguyen et al., 2018; Schmidt et al., 2019). In the case of diseases characterized by accumulation of unfolded/misfolded proteins like Alzheimer or Charcot-Marie-Tooth 1B diseases, stimulating eIF2 $\alpha$  phosphorylation to attenuate translation and allow the cells to recovery from proteotoxic stress it is proposed to improve prognosis (Das et al., 2015).

The key role of eIF2 $\alpha$  translational factor, maintained in its active form by CReP, likely highlights a G3 MB dependency on translation. There is a potential link between the oncogene MYC which is the main driver of G3 MB tumors and the requirement of a hypo phosphorylated form of eIF2 $\alpha$ . It is well established that MYC, as a global TF, controls the expression of a high number of genes, but especially increase the synthesis of ribosomal proteins, eukaryotic translation initiation factors, rRNA and tRNAs. It rewires the entire protein synthesis machinery in favor of cell growth. This is very well exemplified by the enrichment of ribosomal RNAs in G3 MB (Forget et al., 2018). In other MYC-driven tumors it has been shown a dependency between MYC and eIF2 $\alpha$ . This is the case of MYC activated/PTEN loss driven prostate cancer model in which it was shown that MYC hijack the UPR, and specifically the PERK arm during tumor progression. PERK activation by MYC leads to an increase in the phosphorylation of eIF2 $\alpha$  as a mechanism to put a brake to protein synthesis and prevents apoptotic cell death.

The deleterious effect of eIF2 $\alpha$  phosphorylation has also been demonstrated on the neurodegenerative disease field, including prion disease, Alzheimer and Huntington diseases. In this context, defective mechanisms that are not completely understood lead to the accumulation of misfolded/unfolded proteins, activation of the UPR and especially PERK, and constitutive eIF2 $\alpha$  phosphorylation that result in neuronal cell death(Oliveira et al., 2021). In both cases, inhibition of PERK or reestablishing protein synthesis using molecules as ISRIB, has been shown to prevent or improve the conditions.

On the contrary, as recently demonstrated for some N-MYC driven MB tumor models (Kuzuoglu-ozturk et al., 2023), keeping the translation machinery active may allow for production of proteins that could help to prevent proteotoxic stress created by oncogenic insults. This may explain why MYC-driven cancers, as G3 MB, depend on high rate of protein synthesis likely explaining their requirement for low basal level of eIF2 $\alpha$  phosphorylation and their sensitivity to the inactivation of eIF2 $\alpha$  by phosphorylation. More work is required to accurately assess the potential link between MYC and eIF2 $\alpha$  phosphorylation but our study nevertheless highlights the key role of eIF2 $\alpha$  in G3 MB.

## **1.7. General conclusion**

My work showed that HSPA5 is important for the survival of G3 tumor cells. Importantly, by investigating the molecular mechanisms involved in the induction of cell death after HSPA5 KD, we have revealed an important sensitivity of these cells to the activation of UPR. More specifically, our results point to regulation of eIF2 $\alpha$  as a central node in G3 MB cells with a key role the CReP phosphatase which maintains this translational factor in its unphosphorylated active form. We show a dependency of G3 tumors to inhibitors of eIF2 $\alpha$ , whether by kinase activators or phosphatase inhibitors which promote its inactivation by phosphorylation. Preclinical confirmation of this hypothesis using drugs that could led to eIF2 $\alpha$  phosphorylation is an essential part to go further in proving the therapeutically potential of targeting eIF2 $\alpha$  phosphorylation for G3 MB tumors.



## 4 PERSPECTIVES

---

To go further and complete this work, a few aspects remains to be consolidated or investigated:

### **How cell death is induced after HSPA5 KD?**

The first part of my work showed that HSPA5 KD is inducing massive cell death in G3 MB cells. I investigated the molecular mechanisms that could explain this response. I found that, even if HSPA5 KD induced the three branches of UPR, the PERK arm was responsible for the induction of cell death. This was demonstrated using specific inhibitors of each arm, and confirmed by the use of ISRIB, showing that the phosphorylation of eIF2 $\alpha$  was a central point of regulation of the cell death. We also showed that cells died in part by Caspase 3 dependent apoptosis. However, a deeper understanding of the mechanisms leading to cell death should be explored. It has been described that the activation of PERK could result in decreased level of XIAP proteins, mostly through the phosphorylation of eIF2 $\alpha$  with consequent reduced protein synthesis (Hiramatsu et al., 2014). It is well known that the UPR is involved a transcriptional but also a translational response, and this could be the case in our model, with translational changes affecting the expression of anti or pro apoptotic proteins leading to cell death. During my thesis I did preliminary experiments to assess this question that need to be completed

### **HSPA5 KD is decreasing protein synthesis?**

Since our results are pointing to eIF2 $\alpha$  phosphorylation as the main mediator of HSPA5 KD induced cell death, and considering the effect that this phosphorylation has in protein synthesis, it would be interesting to look if indeed, this is the case in our conditions. This could help to understand how cells dye after HSPA5 KD, and potentially validate the dependence of MYC-driven G3 cells on protein synthesis and explain the sensibility to eIF2 $\alpha$  phosphorylation. I tried to answer this aspect during my thesis using methionine analogs or puromycin to label nascent proteins but the experiments were not convincing. Translatome experiments may be more accurate to precisely analyze the effect of HSPA5 KD in G3 cells.

## **Is there a link between MYC and eIF2 $\alpha$ in G3 MB cells?**

The results of my work indicate that G3 MB are highly sensitive to the phosphorylation of eIF2 $\alpha$ , either by the activation of UPR through HSPA5 KD, by inhibiting or the KD of CReP, the constitutive eIF2 $\alpha$  phosphatase or by activation of the kinases that phosphorylate eIF2 $\alpha$ . It has been shown that some tumor types driven by MYC rely on the phosphorylation eIF2 $\alpha$  as a rheostat to prevent proteotoxic induced cell death (Nguyen et al., 2018). On the contrary, an active translation machinery could be vital for other MYC-driven cancers (Kuzuoglu-ozturk et al., 2023). We need to further investigate what happen in the case of G3 MB cells and could be the potential link between MYC and eIF2 $\alpha$  in G3 MB cells and linked whit this, try to understand why PPP1R15B (CReP) is highly expressed in these cells.

## **Role of eIF2 $\alpha$ during G3 MB tumor formation**

In accordance with the previous ideas, it may be also interesting to investigate if eIF2 $\alpha$  could play any role during G3 MB formation. It is known that MYC is the main oncogenic driver of G3 MB tumors, but it is also known that it requires additional events to induce tumor formation. We can think that a tight control of the phosphorylated status of eIF2 $\alpha$  could be of particular importance during these phases. Experiments that investigate the effect of the combination of MYC overexpression together with non-phosphorylatable forms of eIF2 $\alpha$  in G3 MB tumor formation could be very interesting. I started to work in this during my thesis but it needs to be completed.

## **eIF2 $\alpha$ phosphorylation as a potential therapeutic target**

Last, it would be pertinent to evaluate if indeed, eIF2 $\alpha$  regulation is relevant for the treatment of G3 MB tumors. My work showed that these cells are highly sensitive to the phosphorylation of eIF2 $\alpha$  either by the use of drugs that activate the kinases or by inhibiting the phosphatases, especially CReP. Preclinical evaluation of the use of the different drugs in G3 tumor growth is still required.

## 5 BIBLIOGRAPHY

---

- Adamson, D.C., Shi, Q., Wortham, M., Northcott, P.A., Di, C., Duncan, C.G., Li, J., McLendon, R.E., Bigner, D.D., Taylor, M.D., et al. (2010). OTX2 is critical for the maintenance and progression of Shh-independent medulloblastomas. *Cancer Res.* *70*, 181–191.
- Akinyemi, A.O., Simpson, K.E., Oyelere, S.F., Nur, M., Ngule, C.M., Owoyemi, B.C.D., Ayarick, V.A., Oyelami, F.F., Obaleye, O., Esoe, D.P., et al. (2023). Unveiling the dark side of glucose-regulated protein 78 (GRP78) in cancers and other human pathology: a systematic review. *Mol. Med.* *29*, 112.
- Almanza, A., Carlesso, A., Chintia, C., Creedican, S., Doultinos, D., Leuzzi, B., Luís, A., McCarthy, N., Montibeller, L., More, S., et al. (2019). Endoplasmic reticulum stress signalling – from basic mechanisms to clinical applications. *FEBS J.* *286*, 241–278.
- Almanza, A., Mních, K., Blomme, A., Robinson, C.M., Rodriguez-Blanco, G., Kierszniowska, S., McGrath, E.P., Le Gallo, M., Pilalis, E., Swinnen, J. V., et al. (2022). Regulated IRE1 $\alpha$ -dependent decay (RIDD)-mediated reprogramming of lipid metabolism in cancer. *Nat. Commun.* *13*, 2493.
- Archer, T.C., Ehrenberger, T., Mundt, F., Gold, M.P., Krug, K., Mah, C.K., Mahoney, E.L., Daniel, C.J., LeNail, A., Ramamoorthy, D., et al. (2018). Proteomics, Post-translational Modifications, and Integrative Analyses Reveal Molecular Heterogeneity within Medulloblastoma Subgroups. *Cancer Cell* *34*, 396-410.e8.
- Atkins, C., Liu, Q., Minthorn, E., Zhang, S.Y., Figueroa, D.J., Moss, K., Stanley, T.B., Sanders, B., Goetz, A., Gaul, N., et al. (2013). Characterization of a novel PERK kinase inhibitor with antitumor and antiangiogenic activity. *Cancer Res.* *73*, 1993–2002.
- Axten, J.M., Medina, J.R., Feng, Y., Shu, A., Romeril, S.P., Grant, S.W., Li, W.H.H., Heering, D.A., Minthorn, E., Mencken, T., et al. (2012). Discovery of 7-methyl-5-(1-[[3-(trifluoromethyl)phenyl]acetyl]-2,3-dihydro-1H-indol-5-yl)-7H-pyrrolo[2,3-d]pyrimidin-4-amine (GSK2606414), a potent and selective first-in-class inhibitor of protein kinase R (PKR)-like endoplasmic reticulum kinase (PERK). *J. Med. Chem.* *55*, 7193–7207.

- Bandopadhyay, P., Piccioni, F., O'Rourke, R., Ho, P., Gonzalez, E.M., Buchan, G., Qian, K., Gionet, G., Girard, E., Coxon, M., et al. (2019). Neuronal differentiation and cell-cycle programs mediate response to BET-bromodomain inhibition in MYC-driven medulloblastoma. *Nat. Commun.* *10*.
- Bashir, S., Banday, M., Qadri, O., Bashir, A., Hilal, N., Nida-i-Fatima, Rader, S., and Fazili, K.M. (2021). The molecular mechanism and functional diversity of UPR signaling sensor IRE1. *Life Sci.* *265*, 118740.
- Beauchamp, E.M., Ringer, L., Bulut, G., Sajwan, K.P., Hall, M.D., Lee, Y.C., Peaceman, D., Özdemirli, M., Rodriguez, O., Macdonald, T.J., et al. (2011). Arsenic trioxide inhibits human cancer cell growth and tumor development in mice by blocking Hedgehog/GLI pathway. *J. Clin. Invest.* *121*, 148–160.
- Beby, F., and Lamonerie, T. (2013). The homeobox gene *Otx2* in development and disease. *Exp. Eye Res.* *111*, 9–16.
- Blais, J., Filipenko, V., Bi, M., and Harding, H. (2004). Activating Transcription Factor 4 is translationally regulated by hypoxic stress. *Mol. Cell. Biol.* *24*, 7469–7482.
- Blais, J.D., Addison, C.L., Edge, R., Falls, T., Zhao, H., Wary, K., Koumenis, C., Harding, H.P., Ron, D., Holcik, M., et al. (2006). Perk-Dependent Translational Regulation Promotes Tumor Cell Adaptation and Angiogenesis in Response to Hypoxic Stress. *Mol. Cell. Biol.* *26*, 9517–9532.
- Bota, D.A., Mason, W., Kesari, S., Magge, R., Winograd, B., Elias, I., Reich, S.D., Levin, N., Trikha, M., and Desjardins, A. (2021). Marizomib alone or in combination with bevacizumab in patients with recurrent glioblastoma: Phase I/II clinical trial data. *Neuro-Oncology Adv.* *3*, 1–10.
- Boulay, G., Awad, M.E., Riggi, N., Archer, T.C., Iyer, S., Boonseng, W.E., Rossetti, N.E., Naigles, B., Rengarajan, S., Volorio, A., et al. (2017). OTX2 activity at distal regulatory elements shapes the chromatin landscape of group 3 medulloblastoma. *Cancer Discov.* *7*, 288–301.
- Bunt, J., Hasselt, N.E., Zwijnenburg, D.A., Hamdi, M., Koster, J., Versteeg, R., and Kool, M. (2012). OTX2 directly activates cell cycle genes and inhibits differentiation in medulloblastoma cells. *Int. J. Cancer* *131*.

- Cai, W., Sun, X., Jin, F., Xiao, D., Li, H., Sun, H., Wang, Y., Lu, Y., Liu, J., Huang, C., et al. (2021). PERK-eIF2 $\alpha$ -ERK1/2 axis drives mesenchymal-endothelial transition of cancer-associated fibroblasts in pancreatic cancer. *Cancer Lett.* 515, 86–95.
- Carrara, M., Prischi, F., Nowak, P.R., Kopp, M.C., and Ali, M.M.U. (2015). Noncanonical binding of BiP ATPase domain to Ire1 and Perk is dissociated by unfolded protein CH1 to initiate ER stress signaling. *Elife* 2015, 1–16.
- Carugo, A., Minelli, R., Sapio, L., Soeung, M., Carbone, F., Robinson, F.S., Tepper, J., Chen, Z., Lovisa, S., Svelto, M., et al. (2019). p53 Is a Master Regulator of Proteostasis in SMARCB1-Deficient Malignant Rhabdoid Tumors. *Cancer Cell* 35, 204-220.e9.
- Cavalli, F.M.G., Remke, M., Rampasek, L., Peacock, J., Shih, D.J.H., Luu, B., Garzia, L., Torchia, J., Nor, C., Morrissy, A.S., et al. (2017). Intertumoral Heterogeneity within Medulloblastoma Subgroups. *Cancer Cell* 31, 737-754.e6.
- Cerezo, M., and Rocchi, S. (2017). New anti-cancer molecules targeting HSPA5/BIP to induce endoplasmic reticulum stress, autophagy and apoptosis. *Autophagy* 13, 216–217.
- Cerezo, M., Lehraiki, A., Millet, A., Rouaud, F., Plaisant, M., Jaune, E., Botton, T., Ronco, C., Abbe, P., Amdouni, H., et al. (2016). Compounds Triggering ER Stress Exert Anti-Melanoma Effects and Overcome BRAF Inhibitor Resistance. *Cancer Cell* 29, 805–819.
- Chang, C.H., Housepian, E.M., and Herbert, C. (1969). An operative staging system and a megavoltage radiotherapeutic technic for cerebellar medulloblastomas. *Radiology* 93, 1351–1359.
- Chen, X., and Cubillos-Ruiz, J.R. (2021). Endoplasmic reticulum stress signals in the tumour and its microenvironment. *Nat. Rev. Cancer* 21, 71–88.
- Chen, H.A., Chang, Y.W., Tseng, C.F., Chiu, C.F., Hong, C.C., Wang, W., Wang, M.Y., Hsiao, M., Ma, J.T., Chen, C.H., et al. (2015). E1A-Mediated Inhibition of HSPA5 Suppresses Cell Migration and Invasion in Triple-Negative Breast Cancer. *Ann. Surg. Oncol.* 22, 889–898.
- Chen, X., Iliopoulos, D., Zhang, Q., Tang, Q., Greenblatt, M.B., Hatziapostolou, M., Lim, E., Tam, W.L., Ni, M., Chen, Y., et al. (2014). XBP1 promotes triple-negative breast

cancer by controlling the HIF1 $\alpha$  pathway. *Nature* 508, 103–107.

Chiu, C.C., Lee, L.Y., Li, Y.C., Chen, Y.J., Lu, Y.C., Li, Y.L., Wang, H.M., Chang, J.T., and Cheng, A.J. (2013). Grp78 as a therapeutic target for refractory head-neck cancer with CD24- CD44+ stemness phenotype. *Cancer Gene Ther.* 20, 606–615.

Cho, Y.J., Tsherniak, A., Tamayo, P., Santagata, S., Ligon, A., Greulich, H., Berhoukim, R., Amani, V., Goumnerova, L., Eberhart, C.G., et al. (2011). Integrative genomic analysis of medulloblastoma identifies a molecular subgroup that drives poor clinical outcome. *J. Clin. Oncol.* 29, 1424–1430.

Costa-Mattioli, M., and Walter, P. (2020). The integrated stress response: From mechanism to disease. *Science* 368.

Cross, B.C.S., Bond, P.J., Sadowski, P.G., Jha, B.K., Zak, J., Goodman, J.M., Silverman, R.H., Neubert, T.A., Baxendale, I.R., Ron, D., et al. (2012). The molecular basis for selective inhibition of unconventional mRNA splicing by an IRE1-binding small molecule. *Proc. Natl. Acad. Sci. U. S. A.* 109, 869–878.

Cullinan, S.B., Zhang, D., Hannink, M., Arvisais, E., Kaufman, R.J., and Diehl, J.A. (2003). Nrf2 Is a Direct PERK Substrate and Effector of PERK-Dependent Cell Survival. *Mol. Cell. Biol.* 23, 7198–7209.

Dadey, D.Y.A., Kapoor, V., Hoye, K., Khudanyan, A., Collins, A., Thotala, D., and Hallahan, D.E. (2017). Antibody targeting GRP78 enhances the efficacy of radiation therapy in human glioblastoma and non-small cell lung cancer cell lines and tumor models. *Clin. Cancer Res.* 23, 2556–2564.

Das, I., Krzyzosiak, A., Schneider, K., Wrabetz, L., D'Antonio, M., Barry, N., Sigurdardottir, A., and Bertolotti, A. (2015). Preventing proteostasis diseases by selective inhibition of a phosphatase regulatory subunit. *Science* (80-. ). 348, 239–242.

Daverkausen-Fischer, L., and Pröls, F. (2022). Regulation of calcium homeostasis and flux between the endoplasmic reticulum and the cytosol. *J. Biol. Chem.* 298, 102061.

Di, K., Lloyd, G.K., Abraham, V., Maclaren, A., Burrows, F.J., Desjardins, A., Trikha, M., and Bota, D.A. (2016). Marizomib activity as a single agent in malignant gliomas: Ability to cross the blood-brain barrier. *Neuro. Oncol.* 18, 840–848.

Dong, D., Ni, M., Li, J., Xiong, S., Ye, W., Virrey, J.J., Mao, C., Ye, R., Wang, M., Pen, L.,

et al. (2008). Critical role of the stress chaperone GRP78/BiP in tumor proliferation, survival, and tumor angiogenesis in transgene-induced mammary tumor development. *Cancer Res.* 68, 498–505.

Eaton, B.R., Esiashvili, N., Kim, S., Weyman, E.A., Thornton, L.T., Mazewski, C., MacDonald, T., Ebb, D., MacDonald, S.M., Tarbell, N.J., et al. (2016). Clinical outcomes among children with standard-risk medulloblastoma treated with proton and photon radiation therapy: A comparison of disease control and overall survival the study was presented in oral form at the annual meeting of international society . *Int. J. Radiat. Oncol. Biol. Phys.* 94, 133–138.

Ellison, D.W. (2010). Childhood medulloblastoma: Novel approaches to the classification of a heterogeneous disease. *Acta Neuropathol.* 120, 305–316.

Endersby, R., Whitehouse, J., Pribnow, A., Kuchibhotla, M., Hii, H., Carline, B., Gande, S., Stripay, J., Ancliffe, M., Howlett, M., et al. (2021). Small-molecule screen reveals synergy of cell cycle checkpoint kinase inhibitors with DNA-damaging chemotherapies in medulloblastoma. *Sci. Transl. Med.* 13.

Facon, T., Venner, C.P., Bahlis, N.J., Offner, F., White, D.J., Karlin, L., Benboubker, L., Rigaudeau, S., Rodon, P., Voog, E., et al. (2021). Oral ixazomib, lenalidomide, and dexamethasone for transplant-ineligible patients with newly diagnosed multiple myeloma. *Blood* 137, 3616–3628.

Forget, A., Martignetti, L., Puget, S., Calzone, L., Brabetz, S., Picard, D., Montagud, A., Liva, S., Sta, A., Dingli, F., et al. (2018). Aberrant ERBB4-SRC Signaling as a Hallmark of Group 4 Medulloblastoma Revealed by Integrative Phosphoproteomic Profiling. *Cancer Cell* 34, 379-395.e7.

Fu, Y., Wey, S., Wang, M., Ye, R., Liao, C.P., Roy-Burman, P., and Lee, A.S. (2008). Pten null prostate tumorigenesis and AKT activation are blocked by targeted knockout of ER chaperone GRP78/BiP in prostate epithelium. *Proc. Natl. Acad. Sci. U. S. A.* 105, 19444–19449.

Garancher, A., Lin, C.Y., Morabito, M., Richer, W., Rocques, N., Larcher, M., Bihannic, L., Smith, K., Miquel, C., Leboucher, S., et al. (2018). NRL and CRX Define Photoreceptor Identity and Reveal Subgroup-Specific Dependencies in Medulloblastoma. *Cancer Cell* 33, 435-449.e6.

- Garzia, L., Kijima, N., Morrissy, A.S., De Antonellis, P., Guerreiro-Stucklin, A., Holgado, B.L., Wu, X., Wang, X., Parsons, M., Zayne, K., et al. (2018). A Hematogenous Route for Medulloblastoma Leptomeningeal Metastases. *Cell* 172, 1050-1062.e14.
- Ghaddar, N., Wang, S., Woodvine, B., Krishnamoorthy, J., van Hoef, V., Darini, C., Kazimierczak, U., Ah-son, N., Popper, H., Johnson, M., et al. (2021). The integrated stress response is tumorigenic and constitutes a therapeutic liability in KRAS-driven lung cancer. *Nat. Commun.* 12, 1–15.
- Gibson, P., Tong, Y., Robinson, G., Thompson, M.C., Currle, D.S., Eden, C., Kranenburg, T.A., Hogg, T., Poppleton, H., Martin, J., et al. (2010). Subtypes of medulloblastoma have distinct developmental origins. *Nature* 468, 1095–1099.
- Gutiérrez, T., and Simmen, T. (2018). Endoplasmic reticulum chaperones tweak the mitochondrial calcium rheostat to control metabolism and cell death. *Cell Calcium* 70, 64–75.
- Haas, I.G., and Wabl, M. (1983). Immunoglobulin heavy chain binding protein. *Nature*.
- Haldipur, P., Aldinger, K.A., Bernardo, S., Deng, M., Timms, A.E., Overman, L.M., Winter, C., Lisgo, S.N., Razavi, F., Manganaro, L., et al. (2020). Spatiotemporal expansion of primary progenitor zones in the developin human cerebellum. *Science* (80-. ). 366, 454–460.
- Han, D., Lerner, A.G., Vande Walle, L., Upton, J.P., Xu, W., Hagen, A., Backes, B.J., Oakes, S.A., and Papa, F.R. (2009). IRE1 $\alpha$  Kinase Activation Modes Control Alternate Endoribonuclease Outputs to Determine Divergent Cell Fates. *Cell* 138, 562–575.
- Han, J., Back, S.H., Hur, J., Lin, Y.H., Gildersleeve, R., Shan, J., Yuan, C.L., Krokowski, D., Wang, S., Hatzoglou, M., et al. (2013). ER-stress-induced transcriptional regulation increases protein synthesis leading to cell death. *Nat. Cell Biol.* 15, 481–490.
- Harding, H.P., Zhang, Y., Zeng, H., Novoa, I., Lu, P.D., Calfon, M., Sadri, N., Yun, C., Popko, B., Paules, R., et al. (2003). An integrated stress response regulates amino acid metabolism and resistance to oxidative stress. *Mol. Cell* 11, 619–633.
- Harding, H.P., Zhang, Y., Scheuner, D., Chen, J.J., Kaufman, R.J., and Ron, D. (2009). Ppp1r15 gene knockout reveals an essential role for translation initiation factor 2 alpha (eIF2 $\alpha$ ) dephosphorylation in mammalian development. *Proc. Natl. Acad. Sci. U. S. A.*

106, 1832–1837.

- Hart, L.S., Cunningham, J.T., Datta, T., Dey, S., Tameire, F., Lehman, S.L., Qiu, B., Zhang, H., Cerniglia, G., Bi, M., et al. (2012). ER stress-mediated autophagy promotes Myc-dependent transformation and tumor growth. *J. Clin. Invest.* *122*, 4621–4634.
- Hetz, C., Chevet, E., and Oakes, S.A. (2015). Proteostasis control by the unfolded protein response. *Nat. Cell Biol.* *17*, 829–838.
- Hetz, C., Zhang, K., and Kaufman, R.J. (2020). Mechanisms, regulation and functions of the unfolded protein response. *Nat. Rev. Mol. Cell Biol.* *21*, 421–438.
- Higo, T., Hamada, K., Hisatsune, C., Nukina, N., Hashikawa, T., Hattori, M., Nakamura, T., and Mikoshiba, K. (2010). Mechanism of ER Stress-Induced Brain Damage by IP3 Receptor. *Neuron* *68*, 865–878.
- Hiramatsu, N., Messah, C., Han, J., LaVail, M.M., Kaufman, R.J., and Lin, J.H. (2014). Translational and posttranslational regulation of XIAP by eIF2 $\alpha$  and ATF4 promotes ER stress-induced cell death during the unfolded protein response. *Mol. Biol. Cell* *25*, 1411–1420.
- Ho, Y., Li, X., Jamison, S., Harding, H.P., McKinnon, P.J., Ron, D., and Lin, W. (2016). PERK Activation Promotes Medulloblastoma Tumorigenesis by Attenuating Premalignant Granule Cell Precursor Apoptosis. *Am. J. Pathol.* *186*, 1939–1951.
- Holgado, B.L., Guerreiro Stucklin, A., Garzia, L., Daniels, C., and Taylor, M.D. (2017a). Tailoring Medulloblastoma treatment through genomics: making a change, one subgroup at a time. *Annu. Rev. Genomics Hum. Genet.* *18*, annurev-genom-091416-035434.
- Holgado, B.L., Guerreiro Stucklin, A., Garzia, L., Daniels, C., and Taylor, M.D. (2017b). Tailoring Medulloblastoma Treatment Through Genomics: Making a Change, One Subgroup at a Time. *Annu. Rev. Genomics Hum. Genet.* *18*, 143–166.
- Hollien, J., and Weissman, J.S. (2006). Decay of Endoplasmic Reticulum-Localized mRNAs During the Unfolded Protein Response. *Science (80-. )*. *313*, 104–107.
- Hovestadt, V., Ayrault, O., Swartling, F.J., Robinson, G.W., Pfister, S.M., and Northcott, P.A. (2020). Medulloblastomics revisited: biological and clinical insights from thousands of patients. *Nat. Rev. Cancer* *20*, 42–56.

- Jamison, S., Lin, Y., and Lin, W. (2015). Pancreatic Endoplasmic Reticulum Kinase Activation Promotes Medulloblastoma Cell Migration and Invasion through Induction of Vascular Endothelial Growth Factor A. *PLoS One* 10, e0120252.
- Jheng, J.R., Wang, S.C., Jheng, C.R., and Horng, J.T. (2016). Enterovirus 71 induces dsRNA/PKR-dependent cytoplasmic redistribution of GRP78/BiP to promote viral replication. *Emerg. Microbes Infect.* 5, e23.
- Jousse, C., Oyadomari, S., Novoa, I., Lu, P., Zhang, Y., Harding, H.P., and Ron, D. (2003). Inhibition of a constitutive translation initiation factor 2 $\alpha$  phosphatase, CReP, promotes survival of stressed cells. *J. Cell Biol.* 163, 767–775.
- Juraschka, K., and Taylor, M.D. (2019). Medulloblastoma in the age of molecular subgroups: A review: JNSPG 75th Anniversary invited review article. *J. Neurosurg. Pediatr.* 24, 353–363.
- Kabakov, A., Yakimova, A., and Matchuk, O. (2020). Molecular Chaperones in Cancer Stem Cells: Determinants of Stemness and Potential Targets for Antitumor Therapy. *Cells* 9, 1–53.
- Kawauchi, D., Robinson, G., Uziel, T., Gibson, P., Rehg, J., Gao, C., Finkelstein, D., Qu, C., Pounds, S., Ellison, D.W., et al. (2012). A mouse model of the most aggressive subgroup of human Medulloblastoma. *Cancer Cell* 21, 168–180.
- Kawauchi, D., Ogg, R.J., Liu, L., Shih, D.J.H., Finkelstein, D., Murphy, B.L., Rehg, J.E., Korshunov, A., Calabrese, C., Zindy, F., et al. (2017). Novel MYC-driven medulloblastoma models from multiple embryonic cerebellar cells. *Oncogene* 36, 5231–5242.
- Kimata, Y., Ishiwata-Kimata, Y., Ito, T., Hirata, A., Suzuki, T., Oikawa, D., Takeuchi, M., and Kohno, K. (2007). Two regulatory steps of ER-stress sensor Ire1 involving its cluster formation and interaction with unfolded proteins. *J. Cell Biol.* 179, 75–86.
- Kool, M., Koster, J., Bunt, J., Hasselt, N.E., Lakeman, A., van Sluis, P., Troost, D., Schouten-van Meeteren, N., Caron, H.N., Cloos, J., et al. (2008). Integrated genomics identifies five medulloblastoma subtypes with distinct genetic profiles, pathway signatures and clinicopathological features. *PLoS One* 3.
- Kool, M., Jones, D.T.W., Jäger, N., Northcott, P.A., Pugh, T.J., Hovestadt, V., Piro, R.M.,

- Esparza, L.A., Markant, S.L., Remke, M., et al. (2014). Genome Sequencing of SHH Medulloblastoma Predicts Genotype-Related Response to Smoothed Inhibition. *Cancer Cell* 25, 393–405.
- Kopp, M.C., Larburu, N., Durairaj, V., Adams, C.J., and Ali, M.M.U. (2019). UPR proteins IRE1 and PERK switch BiP from chaperone to ER stress sensor. *Nat. Struct. Mol. Biol.* 26, 1053–1062.
- Koumenis, C., Naczki, C., Koritzinsky, M., Rastani, S., Diehl, A., Sonenberg, N., Koromilas, A., and Wouters, B.G. (2002). Regulation of Protein Synthesis by Hypoxia via Activation of the Endoplasmic Reticulum Kinase PERK and Phosphorylation of the Translation Initiation Factor eIF2 $\alpha$ . *Mol. Cell. Biol.* 22, 7405–7416.
- Kuzuoglu-ozturk, D., Aksoy, O., Schmidt, C., Lea, R., Larson, J.D., Phelps, R.R.L., Nasholm, N., Holt, M., Contreras, A., Huang, M., et al. (2023). N-myc – Mediated Translation Control Is a Therapeutic Vulnerability in Medulloblastoma.
- Lee, A.S. (2014). Glucose-regulated proteins in cancer: Molecular mechanisms and therapeutic potential. *Nat. Rev. Cancer* 14, 263–276.
- Lee, C., Rudneva, V.A., Erkek, S., Zaparka, M., Chau, L.Q., Tacheva-Grigороva, S.K., Garancher, A., Rusert, J.M., Aksoy, O., Lea, R., et al. (2019). Lsd1 as a therapeutic target in Gfi1-activated medulloblastoma. *Nat. Commun.* 10, 1–13.
- Lee, K., Tirasophon, W., Shen, X., Michalak, M., Prywes, R., Okada, T., Yoshida, H., Mori, K., and Kaufman, R.J. (2002). IRE1-mediated unconventional mRNA splicing and S2P-mediated ATF6 cleavage merge to regulate XBP1 in signaling the unfolded protein response. *Genes Dev.* 16, 452–466.
- Leto, K., Arancillo, M., Becker, E.B.E., Buffo, A., Chiang, C., Ding, B., Dobyns, W.B., Dusart, I., Haldipur, P., Hatten, M.E., et al. (2016). Consensus Paper: Cerebellar Development. *Cerebellum* 15, 789–828.
- Lhomond, S., Avril, T., Dejeans, N., Voutetakis, K., Doultinos, D., McMahon, M., Pineau, R., Obacz, J., Papadodima, O., Jouan, F., et al. (2018). Dual IRE 1 RN ase functions dictate glioblastoma development . *EMBO Mol. Med.* 10, 1–28.
- Li, X.-X., Zhang, H.-S., Xu, Y.-M., Zhang, R.-J., Chen, Y., Fan, L., Qin, Y.-Q., Liu, Y., Li, M., and Fang, J. (2017). Knockdown of IRE1 $\alpha$  inhibits colonic tumorigenesis through

decreasing  $\beta$ -catenin and IRE1 $\alpha$  targeting suppresses colon cancer cells. *Oncogene* 36, 6738–6746.

Lièvreumont, J.P., Rizzuto, R., Hendershot, L., and Meldolesi, J. (1997). BiP, a major chaperone protein of the endoplasmic reticulum lumen, plays a direct and important role in the storage of the rapidly exchanging pool of Ca<sup>2+</sup>. *J. Biol. Chem.* 272, 30873–30879.

Lin, C.Y., Erkek, S., Tong, Y., Yin, L., Federation, A.J., Zaparka, M., Haldipur, P., Kawauchi, D., Risch, T., Warnatz, H.J., et al. (2016). Active medulloblastoma enhancers reveal subgroup-specific cellular origins. *Nature* 530, 57–62.

Lin, G.L., Wilson, K.M., Ceribelli, M., Stanton, B.Z., Woo, P.J., Kreimer, S., Qin, E.Y., Zhang, X., Lennon, J., Nagaraja, S., et al. (2019). Therapeutic strategies for diffuse midline glioma from high-throughput combination drug screening. *Sci. Transl. Med.* 11.

Lin, J., Liu, H., Fukumoto, T., Zundell, J., Yan, Q., Tang, C.H.A., Wu, S., Zhou, W., Guo, D., Karakashev, S., et al. (2021). Targeting the IRE1 $\alpha$ /XBP1s pathway suppresses CARM1-expressing ovarian cancer. *Nat. Commun.* 12, 5321.

Lin, W., Lin, Y., Li, J., Harding, H.P., Ron, D., and Jamison, S. (2011a). A deregulated integrated stress response promotes interferon- $\gamma$ -induced medulloblastoma. *J. Neurosci. Res.* 89, 1586–1595.

Lin, W., Lin, Y., Li, J., Harding, H.P., Ron, D., and Jamison, S. (2011b). A deregulated integrated stress response promotes interferon- $\gamma$ -induced medulloblastoma. *J. Neurosci. Res.* 89, 1586–1595.

Lindsey, J.C., Schwalbe, E.C., Potluri, S., Bailey, S., Williamson, D., and Clifford, S.C. (2014). TERT promoter mutation and aberrant hypermethylation are associated with elevated expression in medulloblastoma and characterise the majority of non-infant SHH subgroup tumours. *Acta Neuropathol.* 127, 307–309.

Liu, G., Yu, J., Wu, R., Shi, L., Zhang, X., Zhang, W., Zhong, X., Wang, Y., Li, H., Shen, Y., et al. (2021). GRP78 determines glioblastoma sensitivity to UBA1 inhibition-induced UPR signaling and cell death. *Cell Death Dis.* 12, 1–13.

Liu, J., Xiao, Q., Xiao, J., Niu, C., Li, Y., Zhang, X., Zhou, Z., Shu, G., and Yin, G. (2022a). Wnt/ $\beta$ -catenin signalling: function, biological mechanisms, and therapeutic

opportunities. *Signal Transduct. Target. Ther.* 7, 3.

Liu, M., Yang, J., Lv, W., Wang, S., Du, T., Zhang, K., Wu, Y., and Feng, X. (2022b). Down-regulating GRP78 reverses pirarubicin resistance of triple negative breast cancer by miR-495-3p mimics and involves the p-AKT/mTOR pathway. *Biosci. Rep.* 42.

Liu, R., Li, X., Gao, W., Zhou, Y., Wey, S., Mitra, S.K., Krasnoperov, V., Dong, D., Liu, S., Li, D., et al. (2013). Monoclonal antibody against cell surface GRP78 as a novel agent in suppressing PI3K/AKT signaling, tumor growth, and metastasis. *Clin. Cancer Res.* 19, 6802–6811.

Logue, S.E., McGrath, E.P., Cleary, P., Greene, S., Mnich, K., Almanza, A., Chevet, E., Dwyer, R.M., Oommen, A., Legembre, P., et al. (2018). Inhibition of IRE1 RNase activity modulates the tumor cell secretome and enhances response to chemotherapy. *Nat. Commun.* 9.

Lospinoso Severini, L., Ghirga, F., Bufalieri, F., Quaglio, D., Infante, P., and Di Marcotullio, L. (2020). The SHH/GLI signaling pathway: a therapeutic target for medulloblastoma. *Expert Opin. Ther. Targets* 24, 1159–1181.

Louis, D.N., Perry, A., Wesseling, P., Brat, D.J., Cree, I.A., Figarella-Branger, D., Hawkins, C., Ng, H.K., Pfister, S.M., Reifenberger, G., et al. (2021). The 2021 WHO classification of tumors of the central nervous system: A summary. *Neuro. Oncol.* 23, 1231–1251.

Luo, B., and Lee, A.S. (2013). The critical roles of endoplasmic reticulum chaperones and unfolded protein response in tumorigenesis and anticancer therapies. *Oncogene* 32, 805–818.

Luo, S., Mao, C., Lee, B., and Lee, A.S. (2006). GRP78/BiP Is Required for Cell Proliferation and Protecting the Inner Cell Mass from Apoptosis during Early Mouse Embryonic Development. *Mol. Cell. Biol.* 26, 5688–5697.

Manasanch, E.E., and Orlowski, R.Z. (2017). Proteasome inhibitors in cancer therapy. *Nat. Rev. Clin. Oncol.* 14, 417–433.

Marciniak, S.J., Yun, C.Y., Oyadomari, S., Novoa, I., Zhang, Y., Jungreis, R., Nagata, K., Harding, H.P., and Ron, D. (2004). CHOP induces death by promoting protein

synthesis and oxidation in the stressed endoplasmic reticulum. *Genes Dev.* *18*, 3066–3077.

Marciniak, S.J., Chambers, J.E., and Ron, D. (2022). Pharmacological targeting of endoplasmic reticulum stress in disease. *Nat. Rev. Drug Discov.* *21*, 115–140.

Marzban, H., Del Bigio, M.R., Alizadeh, J., Ghavami, S., Zachariah, R.M., and Rastegar, M. (2015). Cellular commitment in the developing cerebellum. *Front. Cell. Neurosci.* *8*, 1–26.

McCullough, K.D., Martindale, J.L., Klotz, L.-O., Aw, T.-Y., and Holbrook, N.J. (2001). Gadd153 Sensitizes Cells to Endoplasmic Reticulum Stress by Down-Regulating Bcl2 and Perturbing the Cellular Redox State. *Mol. Cell. Biol.* *21*, 1249–1259.

Melo, E.P., Konno, T., Farace, I., Awadelkareem, M.A., Skov, L.R., Teodoro, F., Sancho, T.P., Paton, A.W., Paton, J.C., Fares, M., et al. (2022). Stress-induced protein disaggregation in the endoplasmic reticulum catalysed by BiP. *Nat. Commun.* *13*, 1–11.

Misra, U.K., Gonzalez-Gronow, M., Gawdi, G., Hart, J.P., Johnson, C.E., and Pizzo, S. V. (2002). The role of Grp 78 in  $\alpha$ 2-macroglobulin-induced signal transduction: Evidence from RNA interference that the low density lipoprotein receptor-related protein is associated with, but not necessary for, GRP 78-mediated signal transduction. *J. Biol. Chem.* *277*, 42082–42087.

Moore, P.C., Qi, J.Y., Thamsen, M., Ghosh, R., Peng, J., Gliedt, M.J., Meza-Acevedo, R., Warren, R.E., Hiniker, A., Kim, G.E., et al. (2019). Parallel signaling through IRE1a and PERK regulates pancreatic neuroendocrine tumor growth and survival. *Cancer Res.* *79*, 6190–6203.

Morabito, M., Larcher, M., Cavalli, F.M., Foray, C., Forget, A., Mirabal-Ortega, L., Andrianteranagna, M., Druillenec, S., Garancher, A., Masliah-Planchon, J., et al. (2019). An autocrine ActivinB mechanism drives TGF  $\beta$ /Activin signaling in Group 3 medulloblastoma. *EMBO Mol. Med.* *11*, 1–17.

Morfouace, M., Shelat, A., Jacus, M., Freeman, B.B., Turner, D., Robinson, S., Zindy, F., Wang, Y.D., Finkelstein, D., Ayrault, O., et al. (2014). Pemetrexed and gemcitabine as combination therapy for the treatment of group3 medulloblastoma. *Cancer Cell* *25*,

516–529.

- Munro, S., and Pelham, H.R.B. (1986). An hsp70-like protein in the ER: Identity with the 78 kd glucose-regulated protein and immunoglobulin heavy chain binding protein. *Cell* 46, 291–300.
- Needham, P.G., Guerriero, C.J., and Brodsky, J.L. (2019). Chaperoning endoplasmic reticulum– associated degradation (ERAD) and protein conformational diseases. *Cold Spring Harb. Perspect. Biol.* 11.
- Nguyen, H.G., Conn, C.S., Kye, Y., Xue, L., Forester, C.M., Cowan, J.E., Hsieh, A.C., Cunningham, J.T., Truillet, C., Tameire, F., et al. (2018). Development of a stress response therapy targeting aggressive prostate cancer. *Sci. Transl. Med.* 10, 1–12.
- Northcott, P.A., Korshunov, A., Witt, H., Hielscher, T., Eberhart, C.G., Mack, S., Bouffet, E., Clifford, S.C., Hawkins, C.E., French, P., et al. (2011). Medulloblastoma comprises four distinct molecular variants. *J. Clin. Oncol.* 29, 1408–1414.
- Northcott, P.A., Shih, D.J.H., Peacock, J., Garzia, L., Sorana Morrissy, A., Zichner, T., Stütz, A.M., Korshunov, A., Reimand, J., Schumacher, S.E., et al. (2012). Subgroup-specific structural variation across 1,000 medulloblastoma genomes. *Nature* 487, 49–56.
- Northcott, P.A., Lee, C., Zichner, T., Stütz, A.M., Erkek, S., Kawauchi, D., Shih, D.J.H., Hovestadt, V., Zapatka, M., Sturm, D., et al. (2014). Enhancer hijacking activates GF11 family oncogenes in medulloblastoma. *Nature* 511, 428–434.
- Northcott, P.A., Buchhalter, I., Morrissy, A.S., Hovestadt, V., Weischenfeldt, J., Ehrenberger, T., Gröbner, S., Segura-Wang, M., Zichner, T., Rudneva, V.A., et al. (2017). The whole-genome landscape of medulloblastoma subtypes. *Nature* 547, 311–317.
- Northcott, P.A., Robinson, G.W., Kratz, C.P., Mabbott, D.J., Pomeroy, S.L., Clifford, S.C., Rutkowski, S., Ellison, D.W., Malkin, D., Taylor, M.D., et al. (2019). Medulloblastoma. *Nat. Rev. Dis. Prim.* 5.
- Novoa, I., Zeng, H., Harding, H.P., and Ron, D. (2001). Feedback inhibition of the unfolded protein response by GADD34-mediated dephosphorylation of eIF2 $\alpha$ . *J. Cell Biol.* 153, 1011–1021.

- Oikawa, D., Kimata, Y., Kohno, K., and Iwawaki, T. (2009). Activation of mammalian IRE1 $\alpha$  upon ER stress depends on dissociation of BiP rather than on direct interaction with unfolded proteins. *Exp. Cell Res.* *315*, 2496–2504.
- Oliveira, M.M., Lourenco, M. V., Longo, F., Kasica, N.P., Yang, W., Ureta, G., Ferreira, D.D.P., Mendonça, P.H.J., Bernales, S., Ma, T., et al. (2021). Correction of eIF2-dependent defects in brain protein synthesis, synaptic plasticity, and memory in mouse models of Alzheimer's disease. *Sci. Signal.* *14*, 5429.
- Ostrom, Q.T., Cioffi, G., Waite, K., Kruchko, C., and Barnholtz-Sloan, J.S. (2021). CBTRUS Statistical Report: Primary Brain and Other Central Nervous System Tumors Diagnosed in the United States in 2014-2018. *Neuro. Oncol.* *23*, III1–III105.
- Packer, R.J., Gajjar, A., Vezina, G., Rorke-adams, L., Burger, P.C., Robertson, P.L., Bayer, L., Lafond, D., Donahue, B.R., Marymont, M.H., et al. (2006). Phase III Study of Craniospinal Radiation Therapy Followed by Adjuvant Chemotherapy for Newly Diagnosed. *J. Clin. Oncol.* *24*.
- Packer, R.J., Zhou, T., Holmes, E., Vezina, G., and Gajjar, A. (2013). Survival and secondary tumors in children with medulloblastoma receiving radiotherapy and adjuvant chemotherapy: Results of Children's Oncology Group trial A9961. *Neuro. Oncol.* *15*, 97–103.
- Padovani, L., Horan, G., and Ajithkumar, T. (2019). Radiotherapy Advances in Paediatric Medulloblastoma Treatment. *Clin. Oncol.* *31*, 171–181.
- Palam, L.R., Gore, J., Craven, K.E., Wilson, J.L., and Korc, M. (2015). Integrated stress response is critical for gemcitabine resistance in pancreatic ductal adenocarcinoma. *Cell Death Dis.* *6*, 1–13.
- Park, H.W., Park, H., Ro, S.H., Jang, I., Semple, I.A., Kim, D.N., Kim, M., Nam, M., Zhang, D., Yin, L., et al. (2014). Hepatoprotective role of Sestrin2 against chronic ER stress. *Nat. Commun.* *5*.
- Pavlović, N., Calitz, C., Thanapirom, K., Mazza, G., Rombouts, K., Gerwins, P., and Heindryckx, F. (2020). Inhibiting IRE1 $\alpha$ -endonuclease activity decreases tumor burden in a mouse model for hepatocellular carcinoma. *Elife* *9*, 1–64.
- Pei, Y., Moore, C.E., Wang, J., Tewari, A.K., Eroshkin, A., Cho, Y.J., Witt, H., Korshunov,

- A., Read, T.A., Sun, J.L., et al. (2012). An animal model of MYC-driven Medulloblastoma. *Cancer Cell* 21, 155–167.
- Pobre, K.F.R., Poet, G.J., and Hendershot, L.M. (2019). The endoplasmic reticulum (ER) chaperone BiP is a master regulator of ER functions: Getting by with a little help from ERdj friends. *J. Biol. Chem.* 294, 2098–2108.
- Puthalakath, H., O'Reilly, L.A., Gunn, P., Lee, L., Kelly, P.N., Huntington, N.D., Hughes, P.D., Michalak, E.M., McKimm-Breschkin, J., Motoyama, N., et al. (2007). ER Stress Triggers Apoptosis by Activating BH3-Only Protein Bim. *Cell* 129, 1337–1349.
- Pyrko, P., Schöntha, A.H., Hofman, F.M., Chen, T.C., and Lee, A.S. (2007). The unfolded protein response regulator GRP78/BiP as a novel target for increasing chemosensitivity in malignant gliomas. *Cancer Res.* 67, 9809–9816.
- Ramaswamy, V., Remke, M., Bouffet, E., Faria, C.C., Perreault, S., Cho, Y.J., Shih, D.J., Luu, B., Dubuc, A.M., Northcott, P.A., et al. (2013). Recurrence patterns across medulloblastoma subgroups: An integrated clinical and molecular analysis. *Lancet Oncol.* 14, 1200–1207.
- Raymundo, D.P., Doultinos, D., Guillory, X., Carlesso, A., Eriksson, L.A., and Chevet, E. (2020). Pharmacological Targeting of IRE1 in Cancer. *Trends in Cancer* 6, 1018–1030.
- Le Reste, P.J., Pineau, R., Voutetakis, K., Samal, J., Jégou, G., Lhomond, S., Gorman, A.M., Samali, A., Patterson, J.B., Zeng, Q., et al. (2020). Local intracerebral inhibition of IRE1 by MKC8866 sensitizes glioblastoma to irradiation/chemotherapy in vivo. *Cancer Lett.* 494, 73–83.
- Rieke, F., Lee, A., and Haeseleer, F. (2008). Characterization of Ca<sup>2+</sup>-Binding Protein 5 Knockout Mouse Retina. *Invest. Ophthalmol. Vis. Sci.* 49, 5126–5135.
- Robinson, G.W., Orr, B.A., Wu, G., Gururangan, S., Lin, T., Qaddoumi, I., Packer, R.J., Goldman, S., Prados, M.D., Desjardins, A., et al. (2015). Vismodegib exerts targeted efficacy against recurrent sonic hedgehog - Subgroup medulloblastoma: Results from phase II Pediatric Brain Tumor Consortium studies PBTC-025B and PBTC-032. *J. Clin. Oncol.* 33, 2646–2654.
- Romero-Ramirez, L., Cao, H., Nelson, D., Hammond, E., Lee, A.H., Yoshida, H., Mori,

- K., Glimcher, L.H., Denko, N.C., Giaccia, A.J., et al. (2004). XBP1 is essential for survival under hypoxic conditions and is required for tumor growth. *Cancer Res.* *64*, 5943–5947.
- Rouschop, K.M., Dubois, L.J., Keulers, T.G., van den Beucken, T., Lambin, P., Bussink, J., van der Kogel, A.J., Koritzinsky, M., and Wouters, B.G. (2013). PERK/eIF2 $\alpha$  signaling protects therapy resistant hypoxic cells through induction of glutathione synthesis and protection against ROS. *Proc. Natl. Acad. Sci.* *110*, 4622–4627.
- dos Santos Klinger, P.H., Delsin, L.E.A., Cruzeiro, G.A.V., Andrade, A.F., Lira, R.C.P., de Andrade, P.V., das Chagas, P.F., de Paula Queiroz, R.G., Trevisan, F.A., de Oliveira, R.S., et al. (2020). Arsenic Trioxide exerts cytotoxic and radiosensitizing effects in pediatric Medulloblastoma cell lines of SHH Subgroup. *Sci. Rep.* *10*, 6–11.
- Schäuble, N., Lang, S., Jung, M., Cappel, S., Schorr, S., Ulucan, Ö., Linxweiler, J., Dudek, J., Blum, R., Helms, V., et al. (2012). BiP-mediated closing of the Sec61 channel limits Ca<sup>2+</sup> leakage from the ER. *EMBO J.* *31*, 3282–3296.
- Schmidt, S., Gay, D., Uthe, F.W., Denk, S., Paauwe, M., Matthes, N., Diefenbacher, M.E., Bryson, S., Warrander, F.C., Erhard, F., et al. (2019). A MYC–GCN2–eIF2 $\alpha$  negative feedback loop limits protein synthesis to prevent MYC-dependent apoptosis in colorectal cancer. *Nat. Cell Biol.* *21*, 1413–1424.
- Schüller, U., Heine, V.M., Mao, J., Kho, A.T., Dillon, A.K., Han, Y.-G., Huillard, E., Sun, T., Ligon, A.H., Qian, Y., et al. (2008). Acquisition of Granule Neuron Precursor Identity Is a Critical Determinant of Progenitor Cell Competence to Form Shh-Induced Medulloblastoma. *Cancer Cell* *14*, 123–134.
- Shani, G., Fischer, W.H., Justice, N.J., Kelber, J.A., Vale, W., and Gray, P.C. (2008). GRP78 and Cripto Form a Complex at the Cell Surface and Collaborate To Inhibit Transforming Growth Factor Signaling and Enhance Cell Growth. *Mol. Cell. Biol.* *28*, 666–677.
- Shen, J., Ha, D.P., Zhu, G., Rangel, D.F., Kobiela, A., Gill, P.S., Groshen, S., Dubeau, L., and Lee, A.S. (2017). GRP78 haploinsufficiency suppresses acinar-to-ductal metaplasia, signaling, and mutant Kras-driven pancreatic tumorigenesis in mice. *Proc. Natl. Acad. Sci. U. S. A.* *114*, E4020–E4029.

- Sheng, X., Arnoldussen, Y.J., Storm, M., Tesikova, M., Nenseth, H.Z., Zhao, S., Fazli, L., Rennie, P., Risberg, B., Wæhre, H., et al. (2015). Divergent androgen regulation of unfolded protein response pathways drives prostate cancer. *EMBO Mol. Med.* 7, 788–801.
- Sheng, X., Nenseth, H.Z., Qu, S., Kuzu, O.F., Frahnw, T., Simon, L., Greene, S., Zeng, Q., Fazli, L., Rennie, P.S., et al. (2019). IRE1 $\alpha$ -XBP1s pathway promotes prostate cancer by activating c-MYC signaling. *Nat. Commun.* 10.
- Shim, S.M., Choi, H.R., Sung, K.W., Lee, Y.J., Kim, S.T., Kim, D., Mun, S.R., Hwang, J., Cha-Molstad, H., Ciechanover, A., et al. (2018). The endoplasmic reticulum-residing chaperone BiP is short-lived and metabolized through N-terminal arginylation. *Sci. Signal.* 11.
- Shiu, R.P.C., Pouyssegur, J., and Pastan, I. (1977). Glucose depletion accounts for the induction of two transformation-sensitive membrane proteins in Rous sarcoma virus-transformed chick embryo fibroblasts. *Proc. Natl. Acad. Sci. U. S. A.* 74, 3840–3844.
- Sidrauski, C., Acosta-Alvear, D., Khoutorsky, A., Vedantham, P., Hearn, B.R., Li, H., Gamache, K., Gallagher, C.M., Ang, K.K.H., Wilson, C., et al. (2013). Pharmacological brake-release of mRNA translation enhances cognitive memory. *Elife* 2013, 1–22.
- Sidrauski, C., McGeachy, A.M., Ingolia, N.T., and Walter, P. (2015). The small molecule ISRIB reverses the effects of eIF2 $\alpha$  phosphorylation on translation and stress granule assembly. *Elife* 2015.
- Smith, K.S., Bihannic, L., Gudenas, B.L., Haldipur, P., Tao, R., Gao, Q., Li, Y., Aldinger, K.A., Iskusnykh, I.Y., Chizhikov, V. V., et al. (2022). Unified rhombic lip origins of group 3 and group 4 medulloblastoma. *Nature* 609, 1012–1020.
- Soni, H., Bode, J., Nguyen, C.D.L., Puccio, L., Neßling, M., Piro, R.M., Bub, J., Phillips, E., Ahrends, R., Eipper, B.A., et al. (2020). PERK-mediated expression of peptidylglycine  $\alpha$ -amidating monooxygenase supports angiogenesis in glioblastoma. *Oncogenesis* 9.
- Steinmeier, T., Schulze Schleithoff, S., and Timmermann, B. (2019). Evolving Radiotherapy Techniques in Paediatric Oncology. *Clin. Oncol.* 31, 142–150.
- Stone, S., Ho, Y., Li, X., Jamison, S., Harding, H.P., Ron, D., and Lin, W. (2016). Dual

- role of the integrated stress response in medulloblastoma tumorigenesis. *Oncotarget* 7, 64124–64135.
- Sun, F.C., Wei, S., Li, C.W., Chang, Y.S., Chao, C.C., and Lai, Y.K. (2006). Localization of GRP78 to mitochondria under the unfolded protein response. *Biochem. J.* 396, 31–39.
- Swaroop, A., Kim, D., and Forrest, D. (2010). Transcriptional regulation of photoreceptor development and homeostasis in the mammalian retina. *Nat. Rev. Neurosci.* 11, 563–576.
- Tameire, F., Verginadis, I.I., Leli, N.M., Polte, C., Conn, C.S., Ojha, R., Salas Salinas, C., Chinga, F., Monroy, A.M., Fu, W., et al. (2019). ATF4 couples MYC-dependent translational activity to bioenergetic demands during tumour progression. *Nat. Cell Biol.* 21, 889–899.
- Tang, C.H.A., Ranatunga, S., Kriss, C.L., Cubitt, C.L., Tao, J., Pinilla-Ibarz, J.A., Del Valle, J.R., and Hu, C.C.A. (2014). Inhibition of ER stress-associated IRE-1/XBP-1 pathway reduces leukemic cell survival. *J. Clin. Invest.* 124, 2585–2598.
- Tay, K.H., Luan, Q., Croft, A., Jiang, C.C., Jin, L., Zhang, X.D., and Tseng, H.Y. (2014). Sustained IRE1 and ATF6 signaling is important for survival of melanoma cells undergoing ER stress. *Cell. Signal.* 26, 287–294.
- Thompson, E.M., Hielscher, T., Bouffet, E., Remke, M., Luu, B., Gururangan, S., McLendon, R.E., Bigner, D.D., Lipp, E.S., Perreault, S., et al. (2016). Prognostic value of medulloblastoma extent of resection after accounting for molecular subgroup: a retrospective integrated clinical and molecular analysis. *Lancet Oncol.* 17, 484–495.
- Thompson, M.C., Fuller, C., Hogg, T.L., Dalton, J., Finkelstein, D., Lau, C.C., Chintagumpala, M., Adesina, A., Ashley, D.M., Kellie, S.J., et al. (2006). Genomics identifies medulloblastoma subgroups that are enriched for specific genetic alterations. *J. Clin. Oncol.* 24, 1924–1931.
- Tsai, Y.-L., Ha, D.P., Zhao, H., Carlos, A.J., Wei, S., Pun, T.K., Wu, K., Zandi, E., Kelly, K., and Lee, A.S. (2018). Endoplasmic reticulum stress activates SRC, relocating chaperones to the cell surface where GRP78/CD109 blocks TGF- $\beta$  signaling. *Proc. Natl. Acad. Sci.* 115, E4245–E4254.

- Tsai, Y.L., Zhang, Y., Tseng, C.C., Stanciuskas, R., Pinaud, F., and Lee, A.S. (2015). Characterization and mechanism of stress-induced translocation of 78-kilodalton glucose-regulated protein (GRP78) to the cell surface. *J. Biol. Chem.* *290*, 8049–8064.
- Tseng, C.C., Stanciuskas, R., Zhang, P., Woo, D., Wu, K., Kelly, K., Gill, P.S., Yu, M., Pinaud, F., and Lee, A.S. (2019). GRP78 regulates CD44v membrane homeostasis and cell spreading in tamoxifen-resistant breast cancer. *Life Sci. Alliance* *2*, 1–16.
- Urrea, H., Dufey, E., Lisbona, F., Rojas-Rivera, D., and Hetz, C. (2013). When ER stress reaches a dead end. *Biochim. Biophys. Acta - Mol. Cell Res.* *1833*, 3507–3517.
- Vandewynckel, Y.P., Laukens, D., Bogaerts, E., Paridaens, A., Van den Bussche, A., Verhelst, X., Van Steenkiste, C., Descamps, B., Vanhove, C., Libbrecht, L., et al. (2015). Modulation of the unfolded protein response impedes tumor cell adaptation to proteotoxic stress: a PERK for hepatocellular carcinoma therapy. *Hepatol. Int.* *9*, 93–104.
- Vassen, L., Wilkes, B., and Khandanpour, C. (2016). Review Article From cytopenia to leukemia : the role of G fi 1 and G fi 1b in blood formation. *Blood* *126*, 2561–2570.
- Vattem, K.M., and Wek, R.C. (2004). Reinitiation involving upstream ORFs regulates ATF4 mRNA translation in mammalian cells. *Proc. Natl. Acad. Sci. U. S. A.* *101*, 11269–11274.
- Vladoiu, M.C., El-Hamamy, I., Donovan, L.K., Farooq, H., Holgado, B.L., Sundaravadanam, Y., Ramaswamy, V., Hendrikse, L.D., Kumar, S., Mack, S.C., et al. (2019). Childhood cerebellar tumours mirror conserved fetal transcriptional programs. *Nature* *572*, 67–73.
- Walter, P., and Ron, D. (2011). The Unfolded Protein Response: From Stress Pathway to Homeostatic Regulation. *Science (80- )*. *334*, 1081–1086.
- Wang, M., and Kaufman, R.J. (2016). Protein misfolding in the endoplasmic reticulum as a conduit to human disease. *Nature* *529*, 326–335.
- Wang, J., Lee, J., Liem, D., and Ping, P. (2017). HSPA5 Gene encoding Hsp70 chaperone BiP in the endoplasmic reticulum. *Gene* *618*, 14–23.
- Waszak, S.M., Robinson, G.W., Gudenas, B.L., Smith, K.S., Forget, A., Kojic, M., Garcia-Lopez, J., Hadley, J., Hamilton, K. V., Indersie, E., et al. (2020). Germline Elongator

mutations in Sonic Hedgehog medulloblastoma. *Nature* 580, 396–401.

Wey, S., Luo, B., Tseng, C.C., Ni, M., Zhou, H., Fu, Y., Bhojwani, D., Carroll, W.L., and Lee, A.S. (2012). Inducible knockout of GRP78/BiP in the hematopoietic system suppresses Pten-null leukemogenesis and AKT oncogenic signaling. *Blood* 119, 817–825.

Wolin, A.R., Vincent, M.Y., Hotz, T., Purdy, S.C., Rosenbaum, S.R., Hughes, C.J., Hsu, J.Y., Oliphant, M.U.J., Armstrong, B., Wessells, V., et al. (2023). EYA2 tyrosine phosphatase inhibition reduces MYC and prevents medulloblastoma progression. *Neuro. Oncol.*

Wortel, I.M.N., van der Meer, L.T., Kilberg, M.S., and van Leeuwen, F.N. (2017). Surviving Stress: Modulation of ATF4-Mediated Stress Responses in Normal and Malignant Cells. *Trends Endocrinol. Metab.* 28, 794–806.

Xia, Y., Ye, B., Ding, J., Yu, Y., Alptekin, A., Thangaraju, M., Prasad, P.D., Ding, Z.C., Park, E.J., Choi, J.H., et al. (2019). Metabolic reprogramming by MYCN confers dependence on the serine-glycine-one-carbon biosynthetic pathway. *Cancer Res.* 79, 3837–3850.

Xie, H., Hu, C.A., Simon, M.C., Xie, H., Tang, C.A., Song, J.H., Mancuso, A., Valle, J.R. Del, Cao, J., Xiang, Y., et al. (2018). IRE1 a RNase – dependent lipid homeostasis promotes survival in Myc-transformed cancers Find the latest version : IRE1  $\alpha$  RNase – dependent lipid homeostasis promotes survival in Myc-transformed cancers. *J Clin Invest.* 128, 1300–1316.

Yamamoto, K., Sato, T., Matsui, T., Sato, M., Okada, T., Yoshida, H., Harada, A., and Mori, K. (2007). Transcriptional Induction of Mammalian ER Quality Control Proteins Is Mediated by Single or Combined Action of ATF6 and XBP1. *Dev. Cell* 13, 365–376.

Yang, H., Niemeijer, M., van de Water, B., and Beltman, J.B. (2020). ATF6 Is a Critical Determinant of CHOP Dynamics during the Unfolded Protein Response. *IScience* 23, 100860.

Yang, Z.J., Ellis, T., Markant, S.L., Read, T.A., Kessler, J.D., Bourbonlous, M., Schüller, U., Machold, R., Fishell, G., Rowitch, D.H., et al. (2008). Medulloblastoma can be initiated by deletion of patched in lineage-restricted progenitors or stem cells. *Cancer*

Cell 14, 135–145.

Yao, X., Liu, H., Zhang, X., Zhang, L., Li, X., Wang, C., and Sun, S. (2015). Cell surface GRP78 accelerated breast cancer cell proliferation and migration by activating STAT3. *PLoS One* 10, 1–17.

Yao, Y.L., Wang, Y.X., Yang, F.C., Wang, C., Mao, M., Gai, Q.J., He, J., Qin, Y., Yao, X.X., Lan, X., et al. (2022). Targeting AKT and CK2 represents a novel therapeutic strategy for SMO constitutive activation-driven medulloblastoma. *CNS Neurosci. Ther.* 28, 1033–1044.

Ye, J., Rawson, R.B., Komuro, R., Chen, X., Davé, U.P., Prywes, R., Brown, M.S., and Goldstein, J.L. (2000). ER stress induces cleavage of membrane-bound ATF6 by the same proteases that process SREBPs. *Mol. Cell* 6, 1355–1364.

Ying, X., Han, S.X., He, C.C., Zhou, C.Y., Dong, Y.P., Cai, M.J., Sui, X., Ma, C.X., Sun, X., Zhang, Y.Y., et al. (2017). Autoantibodies against glucose-regulated protein 78 as serological biomarkers in metastatic and recurrent hepatocellular carcinoma. *Oncotarget* 8, 24828–24839.

Yip, A.T., Yu, J.D., Huynh-Le, M.P., Salans, M., Unnikrishnan, S., Qian, A.S., Xu, R., Kaner, R., MacEwan, I., Crawford, J.R., et al. (2022). Post-treatment neuroendocrine outcomes among pediatric brain tumor patients: Is there a difference between proton and photon therapy? *Clin. Transl. Radiat. Oncol.* 34, 37–41.

Yoshida, H., Matsui, T., Yamamoto, A., Okada, T., and Mori, K. (2001). XBP1 mRNA is induced by ATF6 and spliced by IRE1 in response to ER stress to produce a highly active transcription factor. *Cell* 107, 881–891.

Zhang, G., Dong, Z., Gimple, R., Wolin, A., Wu, Q., Qiu, Z., Wood, L., Shen, J., Jiang, L., Zhao, L., et al. (2021a). Targeting *eya2* tyrosine phosphatase activity in glioblastoma stem cells induces mitotic catastrophe. *J. Exp. Med.* 218.

Zhang, H., Wang, S.Q., Hang, L., Zhang, C.F., Wang, L., Duan, C.J., Cheng, Y. Da, Wu, D.K., and Chen, R. (2021b). GRP78 facilitates M2 macrophage polarization and tumour progression. *Cell. Mol. Life Sci.* 78, 7709–7732.

Zhang, Y., Liu, R., Ni, M., Gill, P., and Lee, A.S. (2010). Cell surface relocalization of the endoplasmic reticulum chaperone and unfolded protein response regulator

GRP78/BiP. *J. Biol. Chem.* **285**, 15065–15075.

Zhao, N., Lewis, M.T., Chen, X., Zhao, N., Cao, J., Xu, L., Tang, Q., Dobrolecki, L.E., Lv, X., Talukdar, M., et al. (2018). Pharmacological targeting of MYC-regulated IRE1 / XBP1 pathway suppresses MYC-driven breast cancer Find the latest version : Pharmacological targeting of MYC-regulated IRE1 / XBP1 pathway suppresses MYC-driven breast cancer. *J. Clin. Invest.* **128**, 1283–1299.

Zhao, S., Li, H., Wang, Q., Su, C., Wang, G., Song, H., Zhao, L., Luan, Z., and Su, R. (2015). The role of c-Src in the invasion and metastasis of hepatocellular carcinoma cells induced by association of cell surface GRP78 with activated  $\alpha$ 2M. *BMC Cancer* **15**, 1–14.

Zhou, H., Zhang, L., Vartuli, R.L., Ford, H.L., and Zhao, R. (2017). The Eya phosphatase\_ Its unique role in cancer.

Zhuravleva, A., and Gierasch, L.M. (2015). Substrate-binding domain conformational dynamics mediate Hsp70 allostery. *Proc. Natl. Acad. Sci. U. S. A.* **112**, E2865–E2873.

Zinszner, H., Kuroda, M., Wang, X.Z., Batchvarova, N., Lightfoot, R.T., Remotti, H., Stevens, J.L., and Ron, D. (1998). CHOP is implicated in programmed cell death in response to impaired function of the endoplasmic reticulum. *Genes Dev.* **12**, 982–995.

# 6 APPENDICES

---



## 1. Appendix 1 Co-author paper 1

During my PhD I signed as co-author of different scientific articles in our team and also through our collaborations directly related with MB or with other cancer diseases as Melanoma and Retinoblastoma. I also wrote a chapter of a Neuromethods book together with colleagues from our team about available methods to modeling G3 MB in animals. They will be presented here in chronologically order.

---

***MITF activity is regulated by a direct interaction with RAF proteins in melanoma cells.*** C. Estrada, L. Mirabal-Ortega, L. Méry, F. Dingli, L. Besse, C. Messaoudi, D. Loew, C. Pouponnot, C. Bertolotto, A. Eychène and Sabine Druillennec. (2022) Communications Biology ([doi.org/10.1038/s42003-022-03049-w](https://doi.org/10.1038/s42003-022-03049-w))

I had the opportunity to help finishing the work of a previous PhD student in the lab in which it was established a new level of regulation of the transcription factor MITF by the RAF family of kinases in Melanoma cells. My contribution to this work was mainly based in the validation of some experiments by western blot. I also contributed to the reviewing process of the article.



## MITF activity is regulated by a direct interaction with RAF proteins in melanoma cells

Charlène Estrada<sup>1,2,3,4,5</sup>, Liliana Mirabal-Ortega <sup>1,2,3,4,5,6</sup>, Laurence Méry<sup>1,2,3,4,5,6</sup>, Florent Dingli <sup>7</sup>, Laetitia Besse<sup>8,9</sup>, Cedric Messaoudi <sup>8,9</sup>, Damarys Loew <sup>7</sup>, Celio Pouponnot <sup>1,2,3,4,5,6</sup>, Corine Bertolotto<sup>10</sup>, Alain Eychène <sup>1,2,3,4,5,6</sup> & Sabine Druillennec <sup>1,2,3,4,5,6</sup> 

The MITF transcription factor and the RAS/RAF/MEK/ERK pathway are two interconnected main players in melanoma. Understanding how MITF activity is regulated represents a key question since its dynamic modulation is involved in the phenotypic plasticity of melanoma cells and their resistance to therapy. By investigating the role of ARAF in NRAS-driven mouse melanoma through mass spectrometry experiments followed by a functional siRNA-based screen, we unexpectedly identified MITF as a direct ARAF partner. Interestingly, this interaction is conserved among the RAF protein kinase family since BRAF/MITF and CRAF/MITF complexes were also observed in the cytosol of NRAS-mutated mouse melanoma cells. The interaction occurs through the kinase domain of RAF proteins. Importantly, endogenous BRAF/MITF complexes were also detected in BRAF-mutated human melanoma cells. RAF/MITF complexes modulate MITF nuclear localization by inducing an accumulation of MITF in the cytoplasm, thus negatively controlling its transcriptional activity. Taken together, our study highlights a new level of regulation between two major mediators of melanoma progression, MITF and the MAPK/ERK pathway, which appears more complex than previously anticipated.

<sup>1</sup>Institut Curie, Centre de Recherche, F-91405 Orsay, France. <sup>2</sup>INSERM U1021, Centre Universitaire, F-91405 Orsay, France. <sup>3</sup>CNRS UMR 3347, Centre Universitaire, F-91405 Orsay, France. <sup>4</sup>Université Paris-Saclay, F-91405 Orsay, France. <sup>5</sup>PSL Research University, F-75006 Paris, France. <sup>6</sup>Equipe Labellisée Ligue Nationale Contre le Cancer, F-91405 Orsay, France. <sup>7</sup>Institut Curie, PSL Research University, Centre de Recherche, Laboratoire de Spectrométrie de Masse Protéomique, 26 rue d'Ulm, 75248 Paris, Cedex05 France. <sup>8</sup>Institut Curie, PSL Research University, CNRS UMS 2016, F-91401 Orsay, France. <sup>9</sup>Université Paris-Saclay, INSERM US43, F-91401 Orsay, France. <sup>10</sup>Université Côte d'Azur, INSERM U1065, Centre Méditerranéen de Médecine Moléculaire (C3M), Nice, France. ✉email: [sabine.druillennec-rodriere@curie.fr](mailto:sabine.druillennec-rodriere@curie.fr)

Cutaneous melanoma is an aggressive tumor arising from malignant transformation of melanocytes<sup>1</sup>. The RAS/RAF/MEK/ERK is a key signaling pathway frequently mutated in cutaneous melanoma since activating mutations in either *NRAS* or *BRAF* genes occur in 15–20% and 40–50% of cases, respectively, the two main mutations being *NRAS*<sup>Q61K</sup> and *BRAF*<sup>V600E</sup><sup>2,3</sup>. RAS is a GTPase activated via membrane-bound receptors upon stimulation by growth factors. In its GTP-bound form, RAS recruits effectors at the membrane and stimulates a number of downstream intracellular signaling pathways, including the MAPK/ERK pathway<sup>4</sup>. The three RAF serine-threonine kinases, ARAF, BRAF and CRAF, conserved in vertebrates are among the main RAS effectors. RAF activation enables subsequent activation by phosphorylation of MEK1 and MEK2, which in turn activate ERK1 and ERK2<sup>5</sup>. Once activated, ERK phosphorylates cytoplasmic substrates and regulates a wide variety of transcription programs when translocated into the nucleus, thus leading to modulation of key biological processes such as cell proliferation, survival, migration or differentiation<sup>6</sup>.

Using conditional knockout of BRAF and/or CRAF in a mouse melanoma model induced by *NRAS*<sup>Q61K</sup>, we showed that while BRAF is required downstream of activated *NRAS* for tumor initiation, both BRAF and CRAF play compensatory functions during late phases of melanomagenesis, thus highlighting the addition of melanoma to the RAF/ERK pathway<sup>7</sup>. Interestingly, we demonstrated that in the absence of BRAF and CRAF, ARAF alone can sustain both ERK activation and proliferation in *NRAS*-mutated melanoma cells. In this context, we also observed that ARAF homodimers are sufficient to induce ERK paradoxical activation by Vemurafenib, an inhibitor of *BRAF*<sup>V600E</sup> kinase activity widely used in clinics. Our results suggested a dependency toward ARAF kinase, as well as a possible role of ARAF in resistance mechanisms in cutaneous melanoma. The potential role of ARAF in *NRAS*-induced melanoma was further strengthened by an *in silico* search in public databases that allowed to identify patients with metastatic melanomas harboring an ARAF mutation associated with activating *NRAS* mutations<sup>7</sup>. Moreover, these observations have recently gained credit with the identification of recurrent activating ARAF mutations in melanoma patients resistant to Belvarafenib, a RAF dimer inhibitor<sup>8</sup>. Nevertheless, ARAF remains the least studied member of the RAF family because: (i) ARAF displays the lowest kinase activity towards MEK compared to other RAF proteins<sup>9</sup>, (ii) in most cellular models, the role of ARAF is hidden by the predominant roles of BRAF and CRAF.

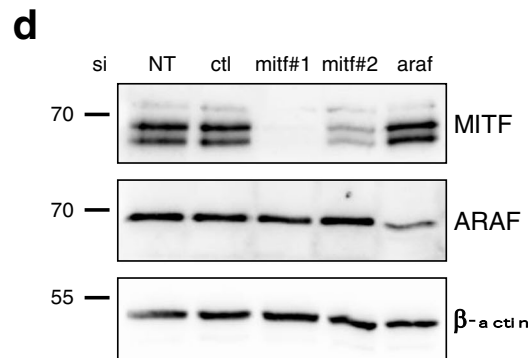
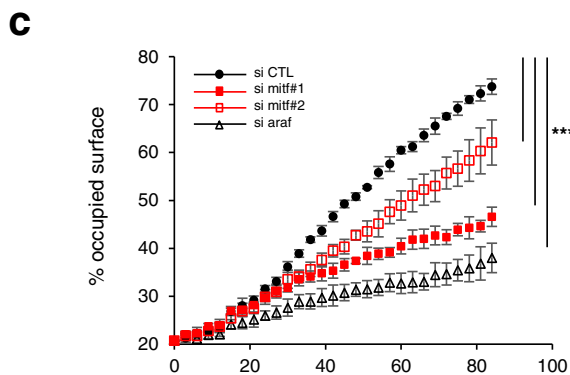
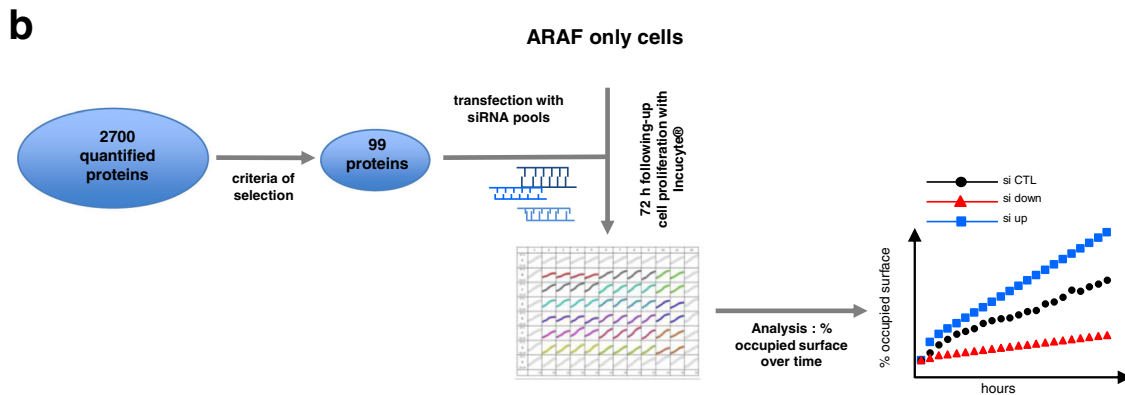
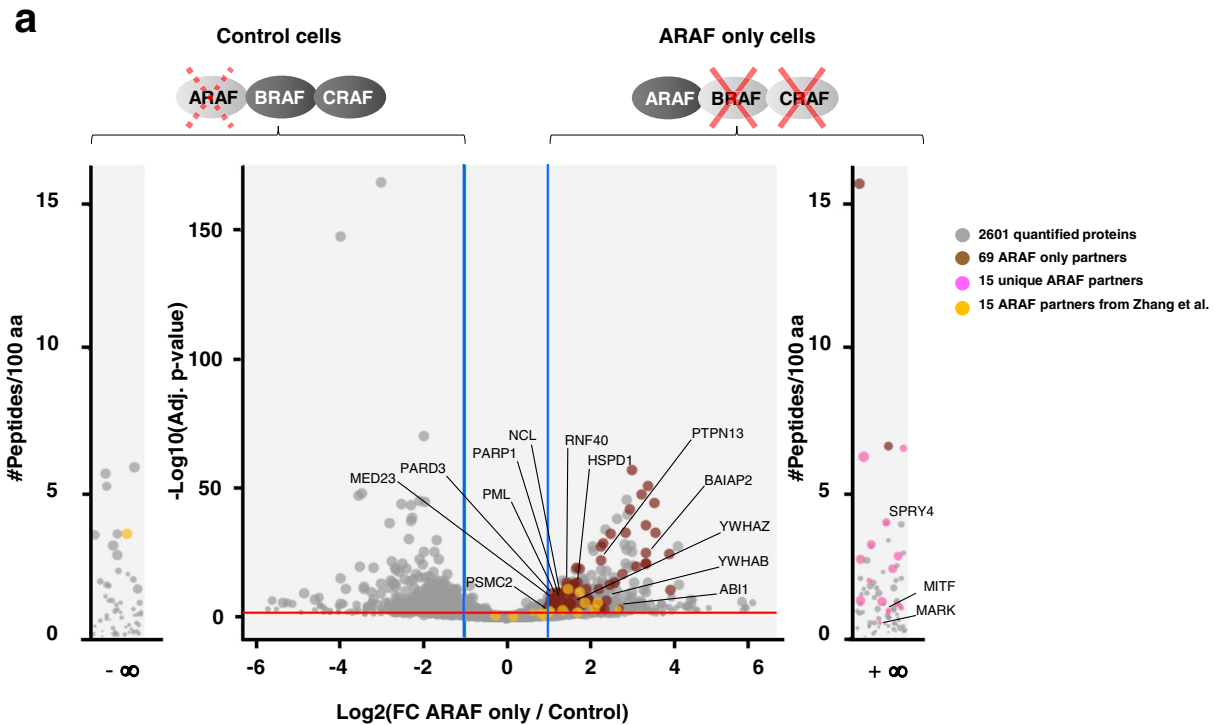
Microphtalmia-associated transcription factor (MITF) is a master regulator of the melanocytic lineage since it is essential for the differentiation, survival and proliferation of melanocytes<sup>10,11</sup>. MITF belongs to the MiT family, gathering bHLH-LZ domain transcription factors (TFEB, TFEC and TFE3), that can homo- or hetero-dimerize to regulate gene expression<sup>12</sup>. Expressed in about 80% of human melanoma<sup>13,14</sup>, MITF displays a central regulatory role in melanoma cell phenotypic plasticity. A proposed rheostat model suggests that the global level of MITF activity correlates with the phenotype of melanoma cells: at high levels of activity, MITF sustains the proliferative state of melanoma cells while at lower levels, MITF is associated with an invasive and stem-like phenotype<sup>15–18</sup>. In line with its central role, MITF is finely regulated to ensure the homeostasis of melanocytes or melanoma cells<sup>11</sup>. Among its numerous post-translational regulators, MITF is regulated by ERK2, that phosphorylates the S73 residue inducing both proteasome-mediated degradation and increased activity *via* the recruitment of p300/CBP transcription cofactor<sup>19–23</sup>. Altogether, the post-translational regulation of MITF by ERK pathway has complex consequences regarding MITF activity, depending on cellular context<sup>14</sup>.

To better characterize the role of ARAF in *NRAS*-driven melanoma, we searched for new ARAF interactors by mass spectrometry. Our results showed that ARAF directly binds to the transcription factor MITF. ARAF/MITF complexes were found in the cytosol of *NRAS*-mutated mouse melanoma cells. Not only ARAF, but also BRAF and CRAF interacted with MITF. Importantly, endogenous BRAF/MITF complexes were also evidenced in *BRAF*-mutated human melanoma cells, thus emphasizing the conservation of RAF/MITF interaction in human. At the functional level, RAF/MITF interaction modulates MITF nuclear localization, thus regulating its transcriptional activity. Taken together, these results highlight a new level of regulation of MITF by RAF, two key players of melanoma biology.

## Results and discussion

### Identification of new ARAF partners by large-scale analysis.

Although our knowledge of ARAF kinase has enlarged over the last decade<sup>24</sup>, ARAF remains understudied compared to the other members of RAF family. Owing to the redundant roles and the high homology of RAF kinases as well as the weak kinase activity of ARAF compared to BRAF and CRAF, it is challenging to study ARAF function in most cellular models where BRAF and CRAF are also expressed. In addition, attribution of a specific function to each RAF kinase is further hampered by their propensity to heterodimerize, especially when looking for binding partners. In the present study, we took advantage of a genetically engineered *NRAS*-driven melanoma mouse model allowing concomitant ablation of BRAF and CRAF to investigate the role of ARAF. Tumour cells derived from these mice constitute a well-adapted model to study ARAF function in the melanoma context in absence of BRAF and CRAF expression (ARAF-only cells)<sup>7</sup>. The ARAF interactome was established by immunoprecipitation of the endogenous ARAF protein from ARAF-only compared to control cells followed by analysis of the immune complexes by mass spectrometry in label-free conditions (Fig. 1). ARAF-only cells, which emerged after *braf* and *craf* genes ablation in melanoma cultures established from primary *NRAS*-induced tumors, are highly dependent on ARAF expression for their growth and survival<sup>7</sup>. Control cells display normal levels of BRAF and CRAF, but express low level of ARAF due to shRNA-mediated knock-down, thus allowing relative quantification of the data. The distribution of the 2700 ARAF-interacting proteins in ARAF-only or control cells (Supplementary Data 1) is illustrated by the volcano plot (Fig. 1a). We performed bioinformatics analysis using a subset of 431 interactors enriched in ARAF only cells and selected as follows: proteins with number of peptides  $\geq 9$ , ratio  $> 2$  and adjusted  $p$  value  $< 0.001$  and proteins exclusively identified in ARAF-only cells (359 and 72 proteins, respectively) (Supplementary Data 2). KEGG pathway visualization revealed an enrichment in the MAPK signaling pathway, in particular MEK1, the ARAF direct downstream substrate, thus strengthening the reliability of the experimental approach (Supplementary Fig. 1). Of note, *NRAS*, the direct upstream interactor of ARAF, is also found in the interactome but did not reach all the cut-offs. While the number of peptides and ratio were correct (peptides = 13, ratio = 12), the adjusted  $p$  value = 0.009 was above the selected cut-off. In addition, several 14-3-3 proteins (*Ywhab* and *Ywhaz* coding genes) are present in the 431 ARAF interactors subset. Although not included in the KEGG maps (Supplementary Fig. 1), 14-3-3 proteins are also involved in MAPK signaling by directly binding and regulating RAF kinases. We also performed process and pathway enrichment analysis as well as Protein-Protein Interaction (PPI) enrichment analysis with Metascape<sup>25</sup>. The most enriched process was related to Rho GTPases signaling (Supplementary Data 2). PPI enrichment analysis confirmed the



enrichment in Rho GTPases signaling network, but also highlighted mitochondrial processes, such as TCA cycle and respiratory electron transport, mitochondrial translation or fatty acid beta-oxidation (Supplementary Fig. 2). These observations are in agreement with previous published data. Indeed, among RAF family members, it has been described that CRAF regulates Rho signaling independently of its kinase activity by interacting and

controlling the subcellular localization of Rok- $\alpha$ <sup>26,27</sup>. Moreover, RAF proteins can be found localized at the mitochondria where they play a role in apoptotic processes or modulate metabolic cell activity<sup>28</sup>. ARAF and CRAF regulate apoptosis by interacting with apoptotic factors<sup>29-31</sup> and the activated form of BRAF has been found localized at the mitochondria where it regulates oxidative metabolism<sup>32</sup>.

**Fig. 1 Identification of MITF as an ARAF partner.** **a** Volcano plot representation of ARAF-binding proteins identified by proteomic analysis. Endogenous ARAF was immunoprecipitated from ARAF-only or control cells lysates. As indicated, ARAF-only cells are double knockout for BRAF and CRAF. Control cells display normal levels of BRAF and CRAF and low levels of ARAF. Binding partners were obtained by using quantitative label-free mass spectrometry analysis performed from five ARAF-only and four control cells replicates. The volcano plot represents the 2700 quantified proteins in control and ARAF-only cells with X axis indicating the log<sub>2</sub> fold change (FC) (ARAF-only versus control cells) and Y axis the -log<sub>10</sub> of adjusted *p* value. The non-axial vertical lines (in blue) denote absolute fold change of 2 while the non-axial horizontal line (in red) denotes the adjusted *p* value of ratio significance of 0.001. External plots show unique proteins with peptides identified only in one sample type (left in control and right in ARAF-only cells). **b** Schematic representation of the workflow to identify new relevant ARAF partners. The 99 proteins selected for further analysis through a siRNA based screen (Supplementary Data 3) are indicated in panel **a**: 69 proteins enriched in ARAF-only cells labeled in brown, 15 unique partners in ARAF-only cells in pink and 15 ARAF interactors published by Zhang *et al.*<sup>33</sup> in orange. ARAF-only cells proliferation was measured during 72 h by using IncuCyte® technology after transfection with siRNA pools targeting each of the 99 putative partners (Supplementary Fig. 3). The theoretical curve shows the percentage of occupied surface over time for a given knockdown target. siRNA having a pro-proliferative (si up) or anti-proliferative (si down) effect compared to a negative control (si CTL, black circles) are highlighted with blue squares and red triangles, respectively. **c** Proliferation of ARAF-only cells after transfection with a control siRNA (siCTL, black circles), individual siRNA against MITF (siMITF #1 or siMITF #2, in red squares) or siRNA pool against ARAF (siARAF, open black triangles). Data are the mean ± SD of four replicates (*n* = 4). \*\*\*\* *p* value < 0.0001 compared by a two-way ANOVA with Dunnett's multiple comparisons test. **d** Western blot analysis of MITF and ARAF protein levels in ARAF-only cells non-transfected (NT) or transfected with either siCTL, siMITF, or siARAF. β-actin is used as a loading control.

In order to identify ARAF relevant partners, which functionally impact melanoma cell proliferation, we developed a siRNA-based functional screen on 99 selected targets (Fig. 1b). These 99 interactors were selected as follows: 69 were chosen among the previously described 359 proteins enriched in ARAF-only cells and 15 were from the 72 proteins exclusively identified in ARAF-only cells (Supplementary Data 3). We also included 15 proteins that were found both in our current dataset and in the ARAF interactome published by Zhang *et al.*<sup>33</sup>. ARAF-only cells growth was followed upon knockdown of the selected partners by siRNA pools transfection (Supplementary Fig. 3). Among the 99 partners tested, 16 impacted the growth of ARAF only melanoma cells. It appeared that 11 ARAF partners had an anti-proliferative effect while 5 proteins were pro-proliferative (labeled in blue and red, respectively in Supplementary Data 3). Among the 132 interactors identified in the ARAF proteome by Zhang *et al.*<sup>33,34</sup>, 107 were commonly found in our dataset, showing the robustness of the approach. Twenty-four of the common identified partners were included in our screen: 9 were selected by the previously described parameters and 15 additional were chosen after bibliographic analysis. It should be noticed that Zhang *et al.* have validated their interactome by coimmunoprecipitation experiments on 12 out of 13 randomly selected ARAF interacting proteins with different functions<sup>33,34</sup>. Eight of these confirmed ARAF partners were tested in the siRNA-based screen and three appear to play a functional role in ARAF only cells: NCL, PARP and PSMC2.

Among the 16 partners that impact melanoma proliferation, we decided to focus on MITF since it represents a key transcription factor for melanoma progression that can be involved in therapy-resistance mechanism. It is also well known to be regulated by the MAPK/ERK pathway<sup>11,14</sup>. Of note, the ARAF interactome by Zhang *et al.* could not identify MITF as an ARAF partner since it was performed on a heterologous model overexpressing tagged ARAF in HEK293T cells that do not express MITF<sup>33,34</sup>. We next confirmed the pro-proliferative effect of MITF in ARAF-only cells by using two distinct siRNA against MITF in comparison to control siRNA. Since we previously demonstrated that ARAF-only cells rely on ARAF for their proliferation, we included a siRNA targeting ARAF as a positive control (Fig. 1c). Both siRNA against MITF decreased the growth of ARAF-only melanoma cells. Moreover, we observed a good correlation between the effect on cell proliferation and the level of extinction of MITF expression induced by the different siRNA (Fig. 1d), demonstrating that MITF is required for ARAF-only cells growth. We also showed that MITF is required in NRAS-

mutated mouse melanoma cells expressing normal levels of all RAF kinases (Supplementary Fig. 4a, b).

**ARAF directly interacts with MITF.** The interaction between ARAF and MITF was confirmed by coimmunoprecipitation experiments of endogenous proteins in ARAF-only cells (Fig. 2a). As shown in Fig. 2b, endogenous ARAF/MITF complexes were also detected by Proximity Ligation Assay (PLA) in ARAF-only cells, further revealing that this interaction occurred in the cytoplasm of melanoma cells. Importantly, this interaction appeared to be direct since complex formation was observed between ARAF and MITF human purified recombinant proteins, in an in vitro coimmunoprecipitation assay (Fig. 2c).

**Characterization of the RAF/MITF interaction.** While the connection between the ERK/MAPK pathway and MITF is well established in melanoma<sup>14</sup>, a direct interaction between RAF kinases and MITF has never been previously demonstrated. We tested whether this interaction was specific of ARAF or shared by all the RAF kinases. HEK293T cells were cotransfected with MITF and each of the three different HA-tagged RAF proteins. Anti-HA immune complexes were then probed with an anti-MITF antibody. Interestingly, we observed that MITF could interact not only with ARAF but also with BRAF and CRAF, the two other members of the RAF family (Fig. 3a–c). PLA experiments in NRAS-mutated murine melanoma cells confirmed the existence of endogenous BRAF/MITF and CRAF/MITF complexes located in the cytoplasm (Supplementary Fig. 4c and d, respectively). This is the first evidence of a direct interaction between RAF kinases family and MITF, two key players in melanoma cell biology. Although an MITF interactome has been previously reported, RAF kinases were not identified in this study since the authors focused specifically on nuclear interactors by performing nuclear purification<sup>35</sup>. The MAPK/ERK pathway being dysregulated by NRAS, but also BRAF mutations in melanoma, we investigated the ability of MITF to interact with the constitutively active BRAF<sup>V600E</sup> mutant (Fig. 3d). This is the most frequent BRAF mutation in human cancers, which is highly prevalent in melanoma and which markedly increases BRAF kinase activity<sup>36</sup>. We observed that MITF strongly interacts with BRAF<sup>V600E</sup> with an increased affinity compared to wild type BRAF. To evaluate the requirement of the RAF kinase activity, we also tested the interaction with the BRAF<sup>K483M</sup> kinase-dead mutant (BRAF<sup>KD</sup>) containing a Lys-to-Met substitution in its kinase domain (Fig. 3d). In contrast to BRAF<sup>V600E</sup>, the capacity

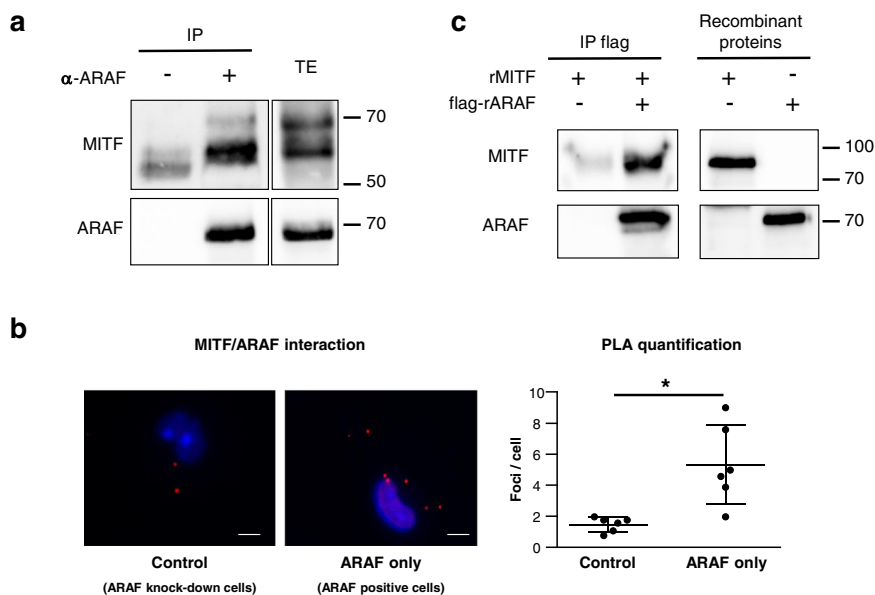


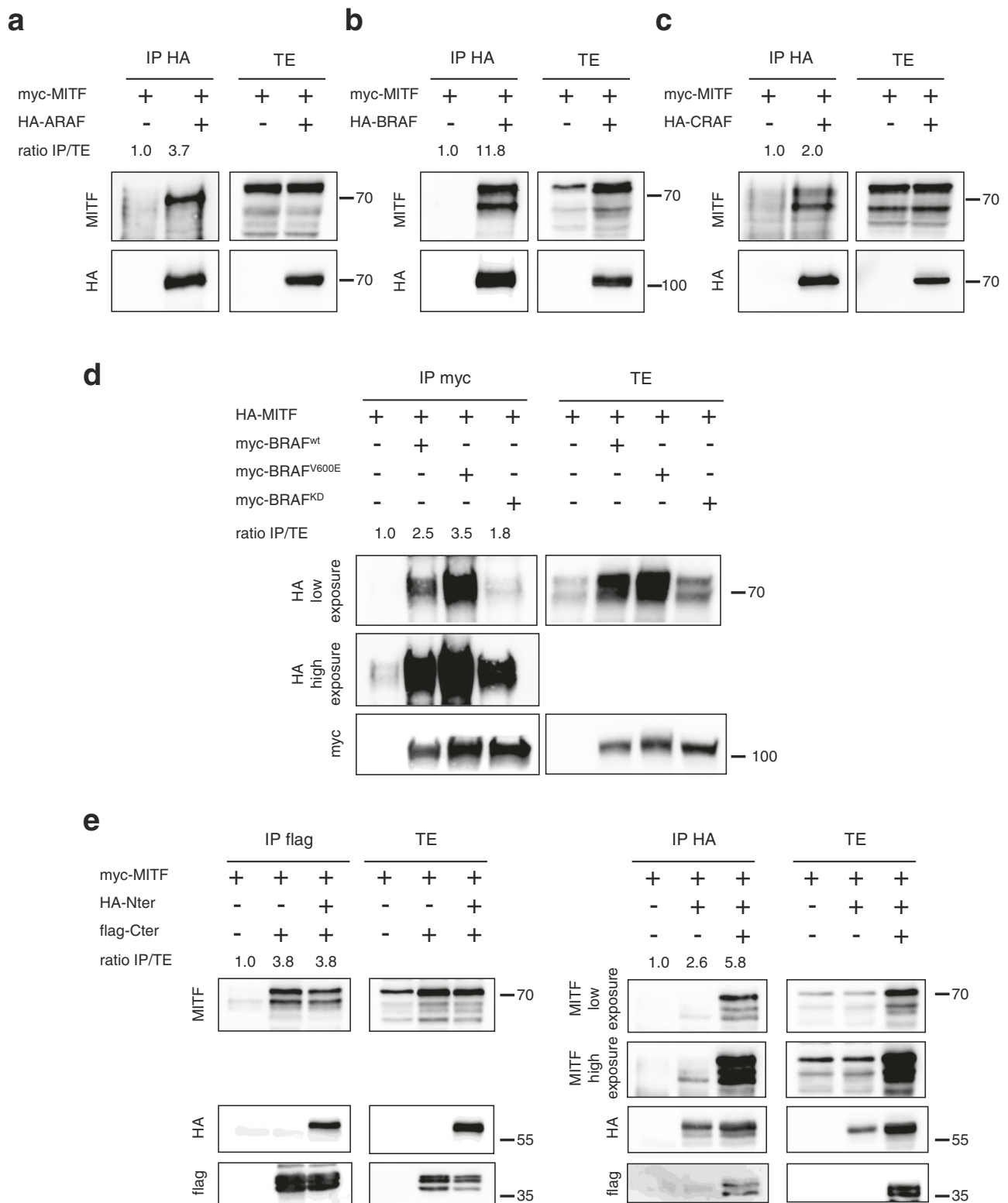
**Fig. 2 Validation of the ARAF/MITF interaction.** **a** Identification of endogenous ARAF/MITF complexes by co-immunoprecipitation. ARAF-only cells extracts were immunoprecipitated with an anti-ARAF antibody. Immune complexes (IP) and total extracts (TE) were immunoblotted with anti-MITF and anti-ARAF antibodies. **b** Identification of endogenous ARAF/MITF complexes by Proximity Ligation Assay. ARAF/MITF complexes were visualized as red dots in ARAF-only cells compared to control cells expressing an shRNA against ARAF by using a fluorescence microscope. Cell nuclei were stained with DAPI. Scatter plots show the average number of dots per cell (at least 148 nuclei were observed) from six microscopic fields and are representative of three different experiments. Means with standard deviations are shown. \* $p$  value = 0.0019 compared by unpaired  $t$  test with Welch's correction. Representative pictures from three independent experiments are shown. Scale bar: 100  $\mu$ m. **c** Identification of a direct ARAF/MITF interaction by in vitro coimmunoprecipitation. Recombinant MITF and flag-tagged ARAF proteins were incubated in NP40 Buffer. ARAF was immunoprecipitated with an anti-flag antibody. Immune complexes and recombinant proteins were blotted with anti-MITF and anti-ARAF antibodies.

of BRAF<sup>KD</sup> to bind to MITF was decreased as compared to wild type BRAF. Therefore, the strength of the binding directly correlates with the activation state of the RAF proteins since MITF strongly interacts with the activated mutant of BRAF, and much less with the BRAF kinase-dead mutant. These results suggest that not only an active form of the RAF kinase could be required to allow the interaction with MITF, but also that the MITF/BRAF complex formation can occur in a BRAF-mutated context.

We next investigated the role of the different domains of BRAF in the interaction with MITF, by using truncated forms of the protein (Fig. 3e). HEK293T cells were cotransfected with plasmids encoding MITF and either the C-terminus or N-terminus part of BRAF, or both. Of note, it was previously demonstrated that the N-terminus regulatory domain of RAF proteins binds to their C-terminus kinase domain in order to regulate their activity<sup>37</sup>. Accordingly, N- and C-terminus parts co-precipitated when co-expressed (Fig. 3e). Following C-terminus immunoprecipitation in the absence of the N-terminus, a strong interaction with MITF was observed indicating that the N-terminal part of BRAF is not required for MITF binding. Moreover, in these conditions, the presence of the N-terminus did not modify the interaction between MITF and the C-terminus (Fig. 3e, left panel). On the opposite, a weak interaction with MITF was seen when the N-terminal domain was immunoprecipitated in the absence of the C-terminus (Fig. 3e, right panel). However, complex formation between the N-terminus and MITF was strongly increased in the presence of the C-terminal part suggesting that, in this condition, the N-terminus does not interact directly with MITF but through the C-terminal domain. Altogether, the results indicate that complex formation with MITF involves the C-terminus region of RAF proteins that contains the kinase domain. These observations also suggest the requirement of a functional kinase domain to stabilize the interaction between RAF and MITF.

**Detection of endogenous RAF/MITF complexes in BRAF-mutated human melanoma cells.** To further substantiate our observations made in mouse melanoma, we evaluated the formation of RAF/MITF complex in three BRAF-mutated human melanoma cells. As shown in Fig. 4a–c, after immunoprecipitation of endogenous BRAF, we were able to detect MITF in all three different cell lines tested, thus confirming that the BRAF/MITF interaction is conserved in human. Since we observed a correlation between the kinase activity of RAF kinases and their binding to MITF (Fig. 3), BRAF-mutated human melanoma cells were treated with Vemurafenib, an ATP-competitive kinase inhibitor of BRAF. The inhibition of MAPK pathway following Vemurafenib treatment was confirmed by the decrease of ERK phosphorylation (Fig. 4d–f). In these conditions, we observed a slight decrease in the ability of MITF to interact with mutated BRAF compared to untreated cells. This demonstrates that the active site of RAF kinases is not the MITF binding domain and that the interaction does not require kinase activity. The lack of kinase activity requirement is also supported by results in Fig. 3e (left panel) showing that the N-terminus, known to decrease C-terminus kinase activity<sup>37–39</sup>, did not modify complex formation between the C-terminus and MITF. Accordingly, no phosphorylation sites or consensus for phosphorylation by RAF kinases, indicating that MITF could be a direct RAF substrate, have been reported. This also suggests that the ability of RAF kinases to bind MITF is not linked to a fully functional kinase active site, but rather due to conformational aspects.

**Functional role of RAF/MITF interaction.** We next investigated how the MITF/RAF complex formation could affect the respective subcellular localization of each partner, knowing that RAF kinases are cytosolic, whereas MITF can shuttle between the cytosol and the nucleus<sup>23</sup>. HEK293T cells were transfected with epitope-tagged MITF and ARAF, BRAF or CRAF and subcellular



localization was analysed by immunofluorescence (Fig. 5). When expressed alone, MITF was mainly nuclear while RAF proteins displayed a clear cytoplasmic localization. However, when co-expressed, a relocalization of MITF from nucleus to cytoplasm was observed, indicating that complexes between MITF and ARAF, BRAF or CRAF, are cytoplasmic in agreement with previous observations in PLA experiments (Fig. 2b, Supplementary Fig. 4a-b). MITF shuttling was also confirmed by fractionation

experiments showing an increase of cytoplasmic MITF when coexpressed with RAF proteins (Supplementary Fig. 5). This suggests that binding to RAF proteins may retain MITF in the cytoplasm.

To better understand the functional consequence of this cytoplasmic interaction, we next investigated how RAF proteins could affect MITF transcriptional activity. HEK293T cells were transfected by constructs encoding a luciferase reporter gene

**Fig. 3 Characterization of RAF/MITF interaction.** MITF interaction with ARAF (a), BRAF (b) or CRAF (c). HEK293T cells were cotransfected with the myc-MITF construct and each of the three HA-ARAF, HA-BRAF, or HA-CRAF constructs (panels a, b, c respectively). RAF proteins were immunoprecipitated with anti-HA antibody. Immune complexes and total extracts were immunoblotted with anti-myc or anti-HA antibodies. d HEK293T cells are cotransfected with the HA-MITF construct and each of the three myc-BRAF<sup>WT</sup>, myc-BRAF<sup>V600E</sup> or myc-BRAF<sup>KD</sup> constructs. Cell lysates were immunoprecipitated with anti-myc antibody. Immune complexes and total extracts were revealed with anti-HA and anti-myc antibodies. e HEK293T cells were cotransfected with the myc-MITF construct and HA-Nter or flag-Cter or both constructs. Cell lysates were immunoprecipitated either with anti-flag or anti-HA antibodies, and immune complexes were revealed with anti-MITF, anti-HA or anti-flag antibodies. Transfection efficiency was monitored by direct western blotting of total protein extracts. Coimmunoprecipitations were quantified using Image J software. The ratio of immunoprecipitated MITF over total MITF (IP/TE) was obtained by dividing the measured MITF signal intensity in immunoprecipitation (IP) by the MITF signal in the total extract (TE) for each condition and the ratio was set to 1 for the control condition. Coimmunoprecipitations are representative of at least three independent experiments.

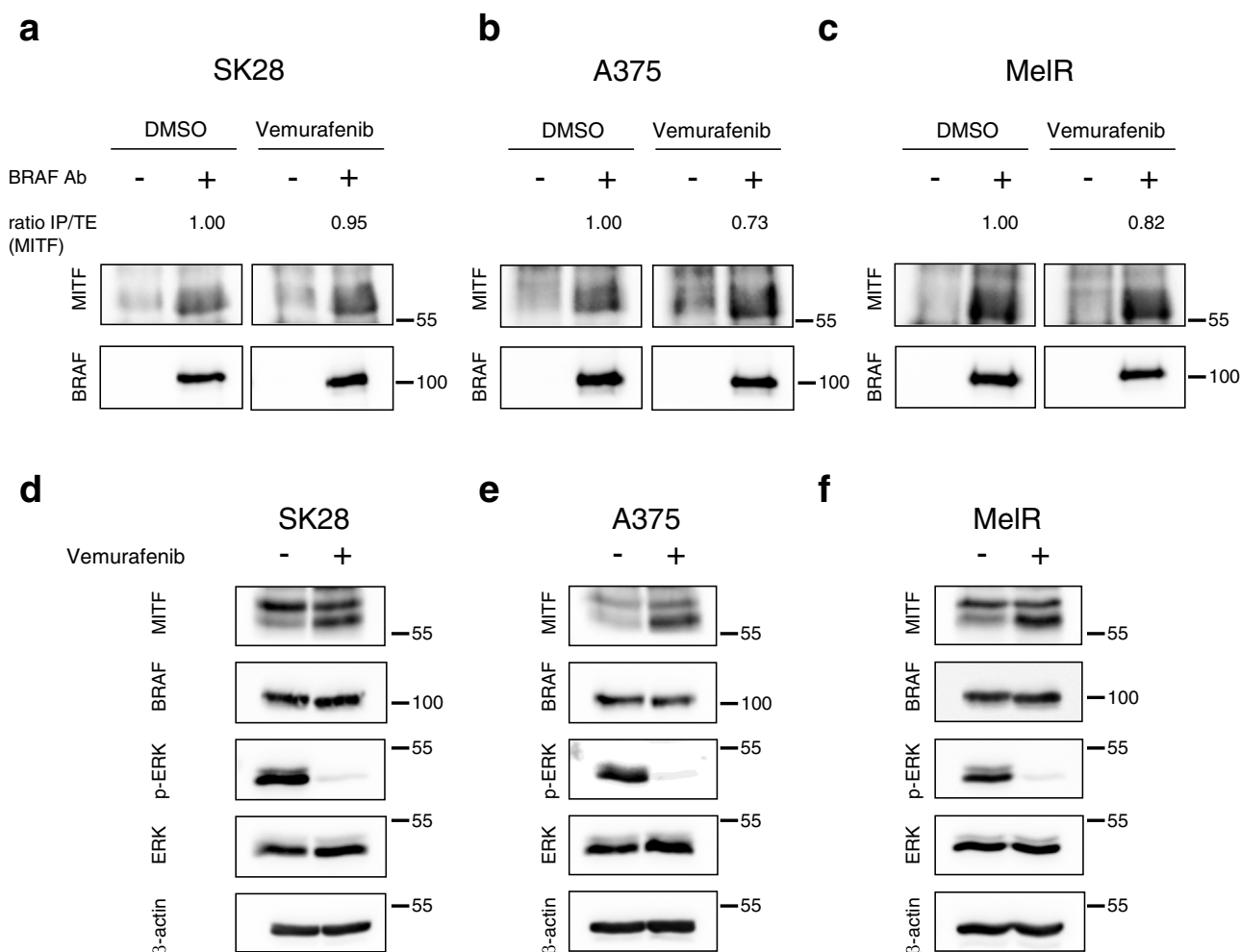


**Fig. 4 Identification of endogenous BRAF/MITF complexes in human melanoma cells.** Endogenous BRAF/MITF interaction in BRAF-mutated human melanoma cells. BRAF was immunoprecipitated with an anti-BRAF antibody in SK28 (a), A375 (b) and MelR (c) treated overnight with 1  $\mu$ M Vemurafenib or DMSO. Immune complexes were blotted with anti-MITF and anti-BRAF antibodies. Western blot analysis of MITF and BRAF protein expression and ERK activation (pERK) in SK28 (d), A375 (e) and MelR (f) melanoma cells after treatment with 1  $\mu$ M Vemurafenib or DMSO. Total ERK and  $\beta$ -actin are used as loading controls. The immunoprecipitated MITF over total MITF ratio (IP/TE(MITF)) was obtained by dividing the MITF signal intensity in immunoprecipitation by the MITF signal in the total extract for each condition. The IP/TE ratio was set to 1 in the DMSO control condition for each cell lines. Coimmunoprecipitations are representative of at least three independent experiments.

under the control of the MITF-regulated tyrosinase promoter, together with a constant amount of MITF plasmid and increasing amounts of plasmids encoding the RAF proteins (Fig. 6). Expression of MITF and RAF kinases was checked (Supplementary Fig. 6). We found that RAF kinases overexpression led to a decrease in MITF transcriptional activity, in a dose-dependent manner. Both BRAF and CRAF overexpression strongly suppressed MITF transcriptional activity while ARAF, which

possesses a weaker kinase activity, reduces MITF activity to a lesser extent (Fig. 6). Thus, the inhibition of MITF transcriptional activity by RAF proteins appears to be correlated with their ability to interact with MITF. Accordingly, the luciferase activity was highly decreased by BRAF<sup>V600E</sup> mutant, the strongest interactor, as compared to wild type BRAF while the BRAF kinase-dead mutant, the weakest interactor, had no effect on MITF transcriptional activity. These results showed that binding to RAF kinases

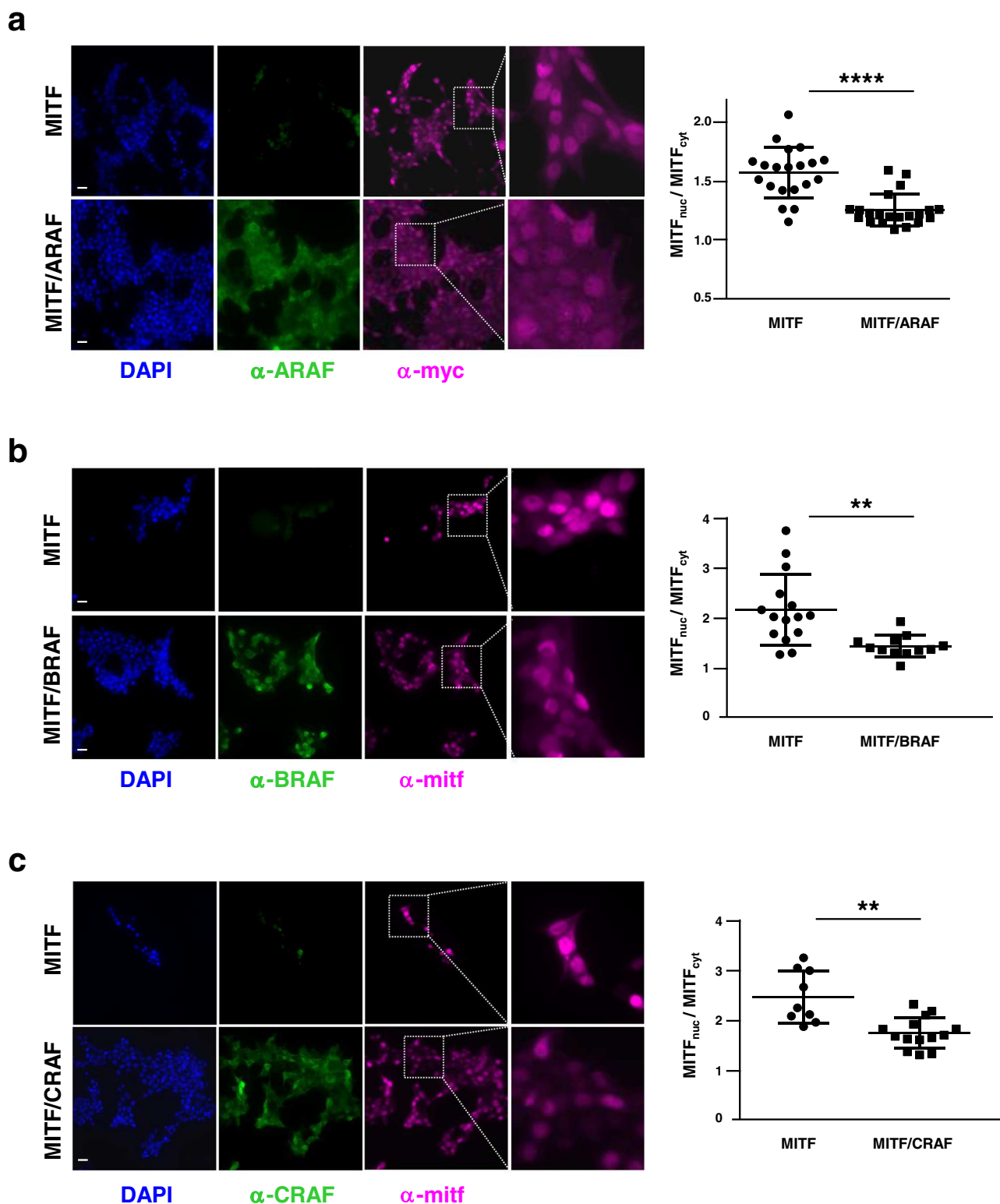


**Fig. 5 Effect of RAF proteins on MITF subcellular localization.** Subcellular localization of MITF in the presence of ARAF (a), BRAF (b) or CRAF (c). HEK293T cells were cotransfected with myc-MITF and HA-ARAF, HA-BRAF or HA-CRAF. Cell immunostaining was performed with anti-myc or anti-MITF and anti-ARAF, anti-BRAF or anti-CRAF. Scatter plots represent the ratio  $\text{MITF}_{\text{nuc}}/\text{MITF}_{\text{cyt}}$  calculated by measuring the quantity of nuclear MITF over cytoplasmic MITF. Means with standard deviations are shown. Scale bar: 200  $\mu\text{m}$ ; \*\*\*\*  $p$  value < 0.0001, \*\*  $p$  value = 0.014 or 0.029 (for BRAF and CRAF, respectively) compared by unpaired  $t$  test with Welch's correction.

negatively regulates MITF transcriptional activity. Taken together, these observations suggest a link between the intrinsic activating properties of RAF proteins, their ability to form complex with MITF and inhibition of MITF transcriptional activity.

MITF plays a critical role in melanoma cells homeostasis, acting as a master regulator of transcription of numerous target genes involved in a large panel of biological functions (proliferation, cell cycle control, survival, invasion, DNA repair,

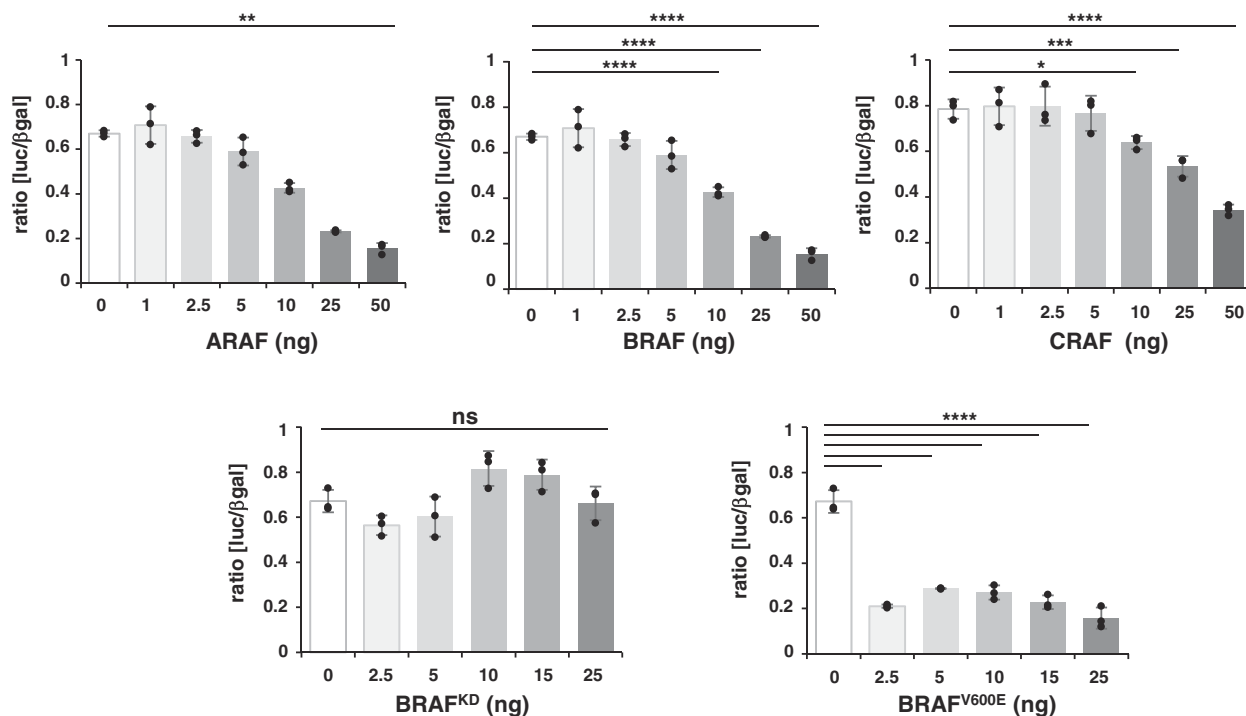


**Fig. 6 Effect of RAF proteins on MITF transcriptional activity.** HEK293T cells were cotransfected with 5 ng of MITF plasmid and increasing doses of either ARAF, CRAF, BRAF<sup>WT</sup>, BRAF<sup>V600E</sup> or BRAF<sup>KD</sup> constructs in the presence of a TYR-Luc luciferase reporter and a control  $\beta$ -galactosidase reporter. The ratio of luciferase to  $\beta$ -galactosidase activities is shown as the mean with standard deviations of three replicates ( $n = 3$ ). One-way ANOVA test was performed to compare all conditions and Dunnett's tests for the multiple comparisons to the no MITF condition (n.s., non-significant; \*  $p$  value < 0.05; \*\*  $p$  value < 0.01; \*\*\*  $p$  value < 0.001; \*\*\*\*  $p$  value < 0.0001).

metabolism, autophagy, etc)<sup>15,40–48</sup>. The contradictory observations regarding the role of MITF in proliferation lead to the establishment of the MITF rheostat model whereby MITF activity is linked to melanoma cell phenotype: in this model, high levels of MITF are associated with pro-proliferative phenotype whereas lower levels are correlated with invasiveness (Fig. 7, left part)<sup>15,42</sup>. Recently, the MITF rheostat model was refined by incorporating six phenotypic states ranging from hyper- to under-differentiated, and associated with different level of MITF activity<sup>49,50</sup>. The modulation of MITF activity in melanoma cells is highly complex and partly due to a dynamic regulation at transcriptional and post-translational levels<sup>11</sup>. Here, we revealed an unsuspected mechanism of MITF activity modulation by demonstrating a direct interaction between RAF kinases and MITF. Indeed, overexpression of ARAF, BRAF or CRAF kinases triggers a partial subcellular relocalization of MITF in the cytoplasm, thus enabling to reduce nuclear concentrations of MITF that could fine tune MITF activity and, thus impacting phenotype switching (Fig. 7). This mechanism of proliferation regulation could happen more particularly when the pro-proliferative ERK/MAPK pathway is highly activated. Nevertheless, BRAF activity inhibition by Vemurafenib did not prevent MITF binding. This suggests that MITF binding to RAF kinases is rather due to a specific conformation than to a high kinase activity, in agreement with MITF not being a direct RAF kinase substrate. This study clearly establishes a cytoplasmic and direct binding between MITF and RAF proteins. However, the MITF transcription factor and the RAS/RAF/MEK/ERK pathway are two tightly interconnected players in melanoma, the regulation of MITF activity also involving phosphorylation of MITF by ERK<sup>19,20,22,23</sup>. The specific contribution of the novel regulatory mechanism by RAF/MITF complexes uncovered in our study is difficult to decipher without specific tools, such as compounds or peptides that abrogate

complex formation without affecting MITF phosphorylation by ERK. Even if the biological significance of the interaction between MITF and RAF kinases deserves further investigations, our study reveals that the regulation of MITF activity by the MAPK/ERK pathway appears more complex than previously anticipated.

## Material and methods

**Cell lines.** Wild type, ARAF-only and control cells were obtained from previously described NRAS-mutated murine melanoma<sup>7</sup>. NRAS-mutated murine melanoma cells, named “wild type” cells in the manuscript, display normal levels of ARAF, BRAF and CRAF. ARAF-only cells and control cells are derived from these NRAS-mutated murine melanoma cells. ARAF-only cells are double knockout for BRAF and CRAF. Control cells display normal levels of BRAF and CRAF and stably express a shRNA against ARAF (TRCN0000294819, Mission shRNA library, Sigma)<sup>7</sup>. Cells were cultured in HAM F-12 Medium (Gibco) containing 10% fetal bovine serum (FBS), 100 mg/mL streptomycin, 100 U/mL penicillin and 2 mM L-glutamine (Invitrogen). Human embryonic kidney 293 T (HEK293T) cells were maintained in Dulbecco's modified Eagle's medium (DMEM, Gibco) supplemented with 10% FBS, 100 mg/mL streptomycin, 100 U/mL penicillin, and 1 mg/mL amphotericin B. The A375 and SK28 human melanoma cell lines were a gift from Nicolas Dumaz (Saint Louis Hospital, France) and MelR melanoma cells a gift from Caroline Robert (Gustave Roussy Hospital, France). A375 and MelR cell lines were cultured in DMEM and SK28 in RPMI medium (GIBCO) supplemented with 10% FBS, 100 U/mL penicillin and 100 mg/mL streptomycin. When indicated, cells were treated overnight with DMSO or Vemurafenib (PLX4032) (1  $\mu$ M, Selleckchem). Cells were tested for mycoplasma contamination and cultured at 37 °C and 5% CO<sub>2</sub>.

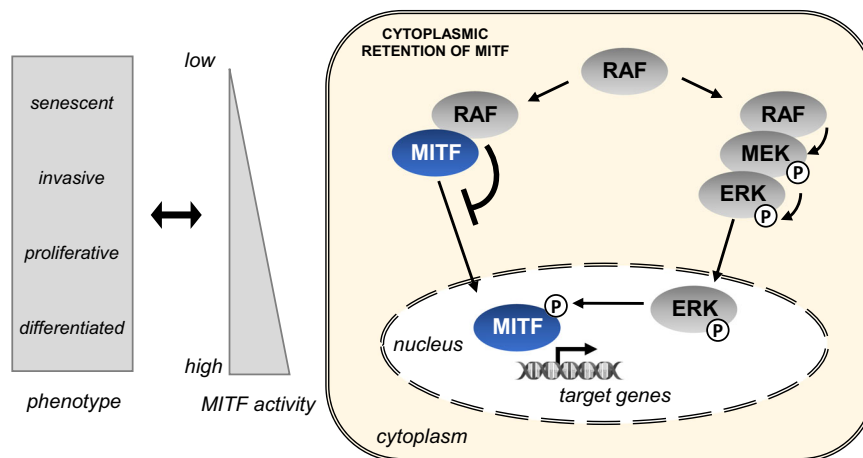


**Fig. 7 Hypothetical model. Scheme illustrating the regulation of MITF activity by direct binding with RAF kinases.** Model illustrating the regulation of MITF activity by direct binding with RAF kinases.

**Proteomics and mass spectrometry analysis.** ARAF-only or control cells were lysed in NP40 buffer (Tris pH7.5, 50 mM, NaCl, 150 mM, 0.5% NP40, protease and phosphatase inhibitors). Five or four biological replicates were prepared for each condition, respectively. Endogenous ARAF was immunoprecipitated with ARAF antibody (75804, Cell Signaling) and Pierce<sup>TM</sup> protein-A magnetic beads on 1 mg of total protein extracts. Immunoprecipitation was performed at 4 °C for 4 hours and pellets were washed 3 times in NP40 buffer and twice in 100  $\mu$ L of ABC buffer (25 mM  $\text{NH}_4\text{HCO}_3$ ). Beads were resuspended in ABC buffer and digested with 0.20  $\mu$ g of trypsin/LysC (Promega) for 1 hour at 37 °C. Samples were loaded onto homemade Tips packed with Empore<sup>TM</sup> C18 Extraction Disks (3 M<sup>TM</sup> Discs 2215) for desalting. Peptides were eluted using 40/60 MeCN/ $\text{H}_2\text{O}$  + 0.1% formic acid and vacuum concentrated to dryness. Liquid chromatography was performed with an RSLCnano system (Ultimate 3000, Thermo Scientific) coupled to a Q Exactive HF-X with a Nanospray Flex ion source (Thermo Scientific). Peptides were trapped on a C18 column (75  $\mu$ m inner diameter  $\times$  2 cm; nanoViper Acclaim PepMap<sup>TM</sup> 100, Thermo Scientific) with buffer A (2/98 MeCN/ $\text{H}_2\text{O}$  in 0.1% formic acid) at a flow rate of 2.5  $\mu$ L/min over 4 min. Separation was performed on a 50 cm $\times$ 75  $\mu$ m C18 column (nanoViper Acclaim PepMap<sup>TM</sup> RSLC, 2  $\mu$ m, 100  $\text{\AA}$ , Thermo Scientific) regulated at 50 °C with a linear gradient of 2–30% buffer B (100% MeCN in 0.1% formic acid) at a flow rate of 300 nL/min over 91 min. MS full scans were performed in the ultrahigh-field Orbitrap mass analyser in ranges  $m/z$  375–1,500 with a resolution of 120,000 at  $m/z$  200. The top 20 intense ions were subjected to Orbitrap *via* high energy collision dissociation (HCD) activation and a resolution of 15,000 with the AGC target set to  $10^5$  ions. We selected ions with charge state from 2+ to 6+ for screening. Normalized collision energy (NCE) was set at 27 and the dynamic exclusion of 40 s. For identification, the data were searched against the *Mus Musculus* UniProt canonical database (22082017 containing 16888 sequences) using Sequest-HT through proteome discoverer (version 2.0). Enzyme specificity was set to trypsin and a maximum of two-missed cleavage sites were allowed. Oxidized methionine carbamidomethyl cysteines and N-terminal acetylation were set as variable modifications. Maximum allowed mass deviation was set to 10 ppm for monoisotopic precursor ions and 0.02 Da for MS/MS peaks. The resulting files were further processed using

myProMS v3.5<sup>51</sup>. FDR calculation used Percolator<sup>52</sup> and was set to 1 % at the peptide level for the whole study. The label free quantification was performed by peptide Extracted Ion Chromatograms (XICs) computed with MassChroQ version 2.0.1<sup>53</sup>. For protein quantification, XICs from proteotypic peptides shared between compared conditions (TopN matching), missed cleavages and carbamidomethyl cysteine modified peptides were used. Global MAD normalization was applied on the total signal to correct the XICs for each biological replicate. To estimate the significance of the change in protein abundance, a linear model (adjusted on peptides and biological replicates) based on two-tailed *t* tests was performed and *p* values were adjusted with a Benjamini–Hochberg FDR. Protein with at least nine total peptides in all replicates, a twofold enrichment and an adjusted *p* value < 0.001 were considered significantly enriched in sample comparison. Unique proteins were considered with at least four total peptides in all replicates.

**Bioinformatics analyses.** A subset of 431 interactors (Supplementary Data 2), specifically enriched in ARAF only cells, was selected as follows: partners with a number of peptides  $\geq 9$ , ratio > 2 and adjusted *p* value < 0.001 and partners exclusively identified in ARAF-only cells (359 and 72 proteins, respectively). One protein (Iap, UniProt ID: P03975) has been lost during ID conversion, from UniProt to Entrez. ClusterProfiler (version 4.0.5)<sup>54</sup> and Pathview packages<sup>55</sup> (version 1.32.0) on R (version 4.1.1) were used to visualize the selected interactors involved in MAPK signaling. Process and pathway enrichment analysis and protein-protein interaction (PPI) enrichment analysis were performed by using the Metascape online tool<sup>25</sup> (<https://metascape.org>). For the process and pathway enrichment analysis, terms with a *p* value < 0.01, a minimum count of 3, and an enrichment factor > 1.5 were collected and grouped into clusters based on their membership similarities. For the PPI enrichment analysis, only physical interactions in STRING (physical score > 0.132) and BioGrid were used. The resultant network contains the subset of proteins that form physical interactions with at least one other member in the list. If the network contained between 3 and 500 proteins, the Molecular Complex Detection (MCODE) algorithm was applied to identify densely connected network components. Process and pathway enrichment analysis was then applied to

each MCODE component. PPI network was visualized by using Cytoscape (version 3.8.2).

**siRNA-based functional screen.** ARAF-only cells were seeded in 96-wells plate at  $8.10^3$  cells per well in HAM F-12 Medium without antibiotics. After 24 hours, cells were transfected with siRNA against the 99 putative partners of ARAF selected for the screen (mouse ON-TARGETplus siRNA, pool of 4 siRNA, Dharmacon) or siCTL (ON-TARGETplus non-targeting siRNA, pool of 4 siRNA, Dharmacon) by using DharmaFECT 3 transfection reagent. After 8 hours, medium was changed and the proliferation was followed for 72 hours by using IncuCyte<sup>®</sup>. SiRNA targeting ARAF was a pool of 4 siRNA (J-042948-05, J-042948-06, J-042948-07, J-042948-08, Dharmacon). Individual siRNA targeting MITF were from Dharmacon (si mitf#1 J-047441-05, si mitf#2 J-047441-07).

**Transfection and coimmunoprecipitation.** HEK293T were transfected with pcDNA3-MITF (HA-MITF or myc-MITF, gift from C.Bertolotto) and pcDNA3-RAF plasmids (HA-ARAF, HA-BRAF, HA-CRAF) or pmcef-RAF plasmids (myc-BRAF, myc-BRAF<sup>V600E</sup> or myc-BRAF<sup>KD</sup>) or empty vector using Lipofectamine reagent (Invitrogen). In cotransfection experiments with N-terminal or C-terminal part of BRAF, either pcDNA3-HA-Nter-BRAF and/or pcDNA3-flag-Cter-BRAF<sup>37</sup> were transfected with pcDNA3-myc-MITF or empty vectors. After 48 hours, cells were lysed in NP40 buffer and extracts were precipitated overnight at 4 °C either with anti-HA (3F10, Roche), anti-Flag (M2, Sigma) or anti-Myc (9E10, Santa Cruz) and Pierce<sup>™</sup> protein-G magnetic beads. Immunoprecipitates were washed with NP40 Buffer and boiled in Laemmli's sample buffer. They were then resolved by sodium dodecyl sulfate-polyacrylamide gel electrophoresis (SDS-PAGE) and transferred onto a polyvinylidene difluoride membrane (Millipore). For endogenous immunoprecipitation in mouse melanoma cells, cell lysates were incubated overnight at 4 °C with anti-ARAF antibody (4432, Cell Signaling) and Pierce<sup>™</sup> protein-A magnetic beads. For endogenous immunoprecipitation in human melanoma cells, 2 mg of protein from NP40 buffer cell lysates were incubated overnight at 4 °C with anti-BRAF antibody (sc5284, Santa Cruz) and Pierce<sup>™</sup> protein-G magnetic beads. For immunoprecipitation of recombinant proteins, 15 ng of human recombinant MITF protein (Origene) were incubated overnight at 4 °C in NP40 Buffer with 75 ng of human recombinant flag-ARAF (Origene) and anti-flag magnetic beads (M2, Sigma). Coimmunoprecipitations are representative of at least three independent experiments and were quantified using Image J software as indicated in figure legends.

**Cell fractionation.** HEK293T were transfected as previously described. After 48 h, fractionation was performed as described in Suzuki et al.<sup>56</sup>. Briefly,  $5.10^6$  cells were washed in cold PBS and resuspended in lysis buffer (PBS 1X, 1 mM orthovanadate, 0.01% Igepal). An aliquot was removed as total extract. After centrifugation, the cytoplasmic fraction was found in the supernatant and the nuclear part in the pellet. SDS at a final 1% concentration and benzonase (Sigma) were added to each fraction. The cytoplasmic MITF over total MITF ratio was obtained using Image J by dividing the ratio of cytoplasmic MITF over cytoplasmic MEK-1 by the ratio of total MITF over total MEK-1.

**Western blotting and antibodies.** For SDS-PAGE analysis, the membranes were blocked with 5 % milk in PBS Tween 20 (10 %) for 30 min at room temperature. Membranes were then probed overnight at 4 °C with the appropriated primary antibodies: anti-MITF (HPA003259, Sigma), anti-HA (3F10, Roche), anti-myc (9E10, Santa

Cruz), anti-flag (M2, Sigma), anti-ARAF (4432, Cell Signaling), anti-BRAF (sc5284, Santa Cruz), anti-CRAF (610151, BD Biosciences), anti-ERK (sc93, Santa Cruz), anti-pERK (M8159, Sigma), anti-laminA/C (10298-1-AP, Proteintech), anti-MEK1 (sc219, Santa Cruz) and anti- $\beta$ -actin (A1978, Sigma) antibodies. Antigen-antibody complexes were detected by horseradish peroxidase-coupled secondary antibodies followed by enhanced chemiluminescence. Signals were acquired using a cooled-CDD camera (Fusion FX Spectra, Vilber).

**Proximity ligation assay (PLA).** Cells were grown on glass coverslips, fixed and permeabilized. PLA (Duolink) was performed according to the manufacturer's instructions (Sigma) using antibodies against ARAF (cs4432, Cell Signaling) and MITF (ab12039, abcam), BRAF (F7, Santa Cruz) and MITF (HPA003259, Sigma), or CRAF (610151, BD Biosciences) and MITF (HPA003259, Sigma). Images were captured using a 3D Leica fluorescence microscope. The average number of dots per cell (identified by its nucleus stained with DAPI) was determined by analysing at least 148 different cells with Image J software.

**Immunofluorescence.** HEK293T cells were seeded at  $3.10^5$  cells per well in 6-wells slides (Millicell, Millipore) precoated with poly-L-lysine (Sigma) and transfected with pcDNA3-myc-MITF and pcDNA3-RAF plasmids (HA-ARAF, HA-BRAF or HA-CRAF) or empty vector as previously described. After 48 hours, cells were fixed in 4% paraformaldehyde, blocked (0.1% Triton X-100, 10% goat serum in PBS) and stained overnight at 4 °C with anti-myc antibody (Santa Cruz) and anti-ARAF (Cell Signaling) or anti-MITF (Sigma) and anti-BRAF (Santa Cruz) or anti-CRAF (BD Biosciences). Anti-mouse Alexa Fluor 594 and anti-rabbit Alexa Fluor 488 or anti-rabbit Alexa Fluor 594 and anti-mouse Alexa Fluor 488 were used for detection. Fluoroshield with DAPI (Sigma) was used as mounting medium. Images were captured using a 3D/optigrid Leica fluorescent microscope. For quantification by using Image J software, the nuclear and cytosolic compartments were selected by applying an automatic threshold (Li Dark method) to the DAPI and FITC images. The nucleus-cytoplasm ratio was then computed by dividing the mean intensity of TexasRed2 (MITF) fluorescence extracted from nucleus region by the mean intensity from cytosolic regions obtained by subtracting DAPI from the FITC surface. The background intensity was measured on each TexasRed2 image and subtracted from the mean intensities before calculating the ratio.

**Luciferase reporter assay.** HEK293T cells seeded at  $10^4$  cells per well in 96-wells plate were co-transfected by using 0.3  $\mu$ L of lipofectamine in a final volume of 100  $\mu$ L with 50 ng of the pTYR-Luc luciferase reporter plasmid (kindly provided by C.Bertolotto), 1.7 ng of p $\beta$ gal, 5 ng of pcDNA3-myc-MITF and from 0 to 25 ng of pcDNA3 expression vector, empty or containing the RAF coding sequences. Dual luciferase and  $\beta$ -galactosidase reporter assay was performed 48 hours after transfection, using Dual-Light<sup>™</sup> Luciferase &  $\beta$ -Galactosidase Reporter Gene Assay System (Invitrogen). Cells were washed with saline phosphate buffer and lysed with 15  $\mu$ L/well of Dual-Light<sup>™</sup> lysis solution. After 10 min incubation at room temperature, 25  $\mu$ L/well of Buffer A were added and the luciferase activity was measured for 1 second using luminometer (TriStar<sup>2</sup>, Berthold) after injection of 100  $\mu$ L/well of Galacton-Plus<sup>®</sup> diluted 1:100 in Buffer B. After 1 h incubation in the dark, the  $\beta$ -galactosidase activity was measured after injection of 100  $\mu$ L/well of Accelerator-II reagent for 0.5 s/well. For western blot analysis of luciferase assays, cells in 96-wells plate were lysed

in Tris pH7.5, 150 mM, NaCl, 150 mM, 0.5% NP40, 0.2%SDS, protease and phosphatase inhibitors.

**Statistics and reproducibility.** All statistical analyses were conducted using GraphPad Prism. Each assay was conducted in at least three biological replicates. The exact sample size is given in the legend of each figure. The mean  $\pm$  standard deviation (SD) is displayed. Statistical analysis of PLA and immunofluorescence experiments were performed by using two-tailed unpaired *t* tests with Welch's correction when variances were significantly different. One-way or two-way ANOVA with Dunnett's multiple comparisons test were used for IncuCyte® or luciferase assays respectively ( $\alpha = 0.05$ ). Statistics for change in protein abundance were based on two-tailed *t* tests with *p* values adjusted with a Benjamini–Hochberg FDR.

**Reporting summary.** Further information on research design is available in the Nature Research Reporting Summary linked to this article.

### Data availability

The datasets produced in this study are available in the PRIDE database<sup>57</sup> as detailed (PXD020155). The source data for the graphs and charts in the main figures are available in Supplementary Data 4, and uncropped WB images in Supplementary Fig. 7. Any remaining information can be obtained from the corresponding author upon reasonable request

Received: 9 April 2021; Accepted: 12 January 2022;

Published online: 28 January 2022

### References

- Miller, A. J. & Mihm, M. C. *Melanoma N. Engl. J. Med.* **355**, 51–65 (2006).
- Fedorenko, I. V., Gibney, G. T. & Smalley, K. S. M. NRAS mutant melanoma: biological behavior and future strategies for therapeutic management. *Oncogene* **32**, 3009–3018 (2013).
- Garnett, M. J. & Marais, R. Guilty as charged: B-RAF is a human oncogene. *Cancer Cell* **6**, 313–319 (2004).
- Buday, L. & Downward, J. Many faces of Ras activation. *Biochim. Biophys. Acta* **1786**, 178–187 (2008).
- Peyssonnaud, C. & Eychène, A. The Raf/MEK/ERK pathway: new concepts of activation. *Biol. Cell* **93**, 53–62 (2001).
- Guo, Y.-J. et al. ERK/MAPK signalling pathway and tumorigenesis. *Exp. Ther. Med.* **19**, 1997–2007 (2020).
- Dorard, C. et al. RAF proteins exert both specific and compensatory functions during tumour progression of NRAS-driven melanoma. *Nat. Commun.* **8**, 15262 (2017).
- Yen, I. et al. ARAF mutations confer resistance to the RAF inhibitor belvarafenib in melanoma. *Nature* **594**, 418–423 (2021).
- Marais, R., Light, Y., Paterson, H. F., Mason, C. S. & Marshall, C. J. Differential regulation of Raf-1, A-Raf, and B-Raf by oncogenic ras and tyrosine kinases. *J. Biol. Chem.* **272**, 4378–4383 (1997).
- Cheli, Y., Ohanna, M., Ballotti, R. & Bertolotto, C. Fifteen-year quest for microphthalmia-associated transcription factor target genes. *Pigment Cell Melanoma Res.* **23**, 27–40 (2010).
- Goding, C. R. & Arnheiter, H. MITF—the first 25 years. *Genes Dev.* **33**, 983–1007 (2019).
- Hemesath, T. J. et al. microphthalmia, a critical factor in melanocyte development, defines a discrete transcription factor family. *Genes Dev.* **8**, 2770–2780 (1994).
- King, R., Googe, P. B., Weilbaecher, K. N., Mihm, M. C. & Fisher, D. E. Microphthalmia transcription factor expression in cutaneous benign, malignant melanocytic, and nonmelanocytic tumors. *Am. J. Surg. Pathol.* **25**, 51–57 (2001).
- Wellbrock, C. & Arozarena, I. Microphthalmia-associated transcription factor in melanoma development and MAP-kinase pathway targeted therapy. *Pigment Cell Melanoma Res.* **28**, 390–406 (2015).
- Carreira, S. et al. Mitf regulation of Dia1 controls melanoma proliferation and invasiveness. *Genes Dev.* **20**, 3426–3439 (2006).
- Hoek, K. S. et al. Metastatic potential of melanomas defined by specific gene expression profiles with no BRAF signature. *Pigment Cell Res.* **19**, 290–302 (2006).
- Hoek, K. S. et al. In vivo switching of human melanoma cells between proliferative and invasive states. *Cancer Res.* **68**, 650–656 (2008).
- Tsoi, J. et al. Multi-stage differentiation defines melanoma subtypes with differential vulnerability to drug-induced iron-dependent oxidative stress. *Cancer Cell* **33**, 890–904.e5 (2018).
- Wu, M. et al. c-Kit triggers dual phosphorylations, which couple activation and degradation of the essential melanocyte factor Mi. *Genes Dev.* **14**, 301–312 (2000).
- Hemesath, T. J., Price, E. R., Takemoto, C., Badalian, T. & Fisher, D. E. MAP kinase links the transcription factor Microphthalmia to c-Kit signalling in melanocytes. *Nature* **391**, 298–301 (1998).
- Xu, W. et al. Regulation of microphthalmia-associated transcription factor MITF protein levels by association with the ubiquitin-conjugating enzyme hUBC9. *Exp. Cell Res.* **255**, 135–143 (2000).
- Price, E. R. et al. Lineage-specific signaling in melanocytes. C-kit stimulation recruits p300/CBP to microphthalmia. *J. Biol. Chem.* **273**, 17983–17986 (1998).
- Ngeow, K. C. et al. BRAF/MAPK and GSK3 signaling converges to control MITF nuclear export. *Proc. Natl Acad. Sci. U. S. A.* **115**, E8668–E8677 (2018).
- An, S. et al. A-Raf: A new star of the family of raf kinases. *Crit. Rev. Biochem. Mol. Biol.* **50**, 520–531 (2015).
- Zhou, Y. et al. Metascape provides a biologist-oriented resource for the analysis of systems-level datasets. *Nat. Commun.* **10**, 1523 (2019).
- Ehrenreiter, K. et al. Raf-1 regulates Rho signaling and cell migration. *J. Cell Biol.* **168**, 955–964 (2005).
- Niault, T. et al. From autoinhibition to inhibition in trans: the Raf-1 regulatory domain inhibits Rok-alpha kinase activity. *J. Cell Biol.* **187**, 335–342 (2009).
- Galmiche, A. & Fueller, J. RAF kinases and mitochondria. *Biochim. Biophys. Acta BBA - Mol. Cell Res.* **1773**, 1256–1262 (2007).
- Wang, H. G., Rapp, U. R. & Reed, J. C. Bcl-2 targets the protein kinase Raf-1 to mitochondria. *Cell* **87**, 629–638 (1996).
- O'Neill, E., Rushworth, L., Baccarini, M. & Kolch, W. Role of the kinase MST2 in suppression of apoptosis by the proto-oncogene product Raf-1. *Science* **306**, 2267–2270 (2004).
- Rauch, J. et al. Differential localization of A-Raf regulates MST2-mediated apoptosis during epithelial differentiation. *Cell Death Differ.* **23**, 1283–1295 (2016).
- Lee, M. H. et al. Mitochondrial localization and regulation of BRAFV600E in thyroid cancer: a clinically used RAF inhibitor is unable to block the mitochondrial activities of BRAFV600E. *J. Clin. Endocrinol. Metab.* **96**, E19–E30 (2011).
- Zhang, X.-Y. et al. Revealing A-Raf functions through its interactome. *Biochim. Biophys. Acta Proteins Proteom.* **1866**, 849–856 (2018).
- Zhang, X.-Y. et al. Comparative interactome analysis reveals distinct and overlapping properties of Raf family kinases. *Biochem. Biophys. Res. Commun.* **514**, 1217–1223 (2019).
- Laurette, P. et al. Transcription factor MITF and remodeler BRG1 define chromatin organisation at regulatory elements in melanoma cells. *eLife* **4**, e06857 (2015).
- Davies, H. et al. Mutations of the BRAF gene in human cancer. *Nature* **417**, 949–954 (2002).
- Hmitou, I., Druillennec, S., Valluet, A., Peyssonnaud, C. & Eychène, A. Differential regulation of B-raf isoforms by phosphorylation and autoinhibitory mechanisms. *Mol. Cell Biol.* **27**, 31–43 (2007).
- Cutler, R. E., Stephens, R. M., Saracino, M. R. & Morrison, D. K. Autoregulation of the Raf-1 serine/threonine kinase. *Proc. Natl Acad. Sci. USA.* **95**, 9214–9219 (1998).
- Chong, H. & Guan, K.-L. Regulation of Raf through phosphorylation and N terminus-C terminus interaction. *J. Biol. Chem.* **278**, 36269–36276 (2003).
- Garraway, L. A. et al. Integrative genomic analyses identify MITF as a lineage survival oncogene amplified in malignant melanoma. *Nature* **436**, 117–122 (2005).
- Carreira, S. et al. Mitf cooperates with Rb1 and activates p21Cip1 expression to regulate cell cycle progression. *Nature* **433**, 764–769 (2005).
- Cheli, Y. et al. Mitf is the key molecular switch between mouse or human melanoma initiating cells and their differentiated progeny. *Oncogene* **30**, 2307–2318 (2011).
- Cheli, Y. et al. Hypoxia and MITF control metastatic behaviour in mouse and human melanoma cells. *Oncogene* **31**, 2461–2470 (2012).
- Haq, R. et al. Oncogenic BRAF regulates oxidative metabolism via PGC1 $\alpha$  and MITF. *Cancer Cell* **23**, 302–315 (2013).
- McGill, G. G. et al. Bcl2 regulation by the melanocyte master regulator Mitf modulates lineage survival and melanoma cell viability. *Cell* **109**, 707–718 (2002).
- Möller, K. et al. MITF has a central role in regulating starvation-induced autophagy in melanoma. *Sci. Rep.* **9**, 1055 (2019).
- Strub, T. et al. Essential role of microphthalmia transcription factor for DNA replication, mitosis and genomic stability in melanoma. *Oncogene* **30**, 2319–2332 (2011).
- Giuliano, S. et al. Microphthalmia-associated transcription factor controls the DNA damage response and a lineage-specific senescence program in melanomas. *Cancer Res.* **70**, 3813–3822 (2010).

49. Rambow, F. et al. Toward minimal residual disease-directed therapy in melanoma. *Cell* **174**, 843–855.e19 (2018).
50. Rambow, F., Marine, J.-C. & Goding, C. R. Melanoma plasticity and phenotypic diversity: therapeutic barriers and opportunities. *Genes Dev.* **33**, 1295–1318 (2019).
51. Pouillet, P., Carpentier, S. & Barillot, E. myProMS, a web server for management and validation of mass spectrometry-based proteomic data. *Proteomics* **7**, 2553–2556 (2007).
52. Spivak, M., Weston, J., Bottou, L., Käll, L. & Noble, W. S. Improvements to the percolator algorithm for Peptide identification from shotgun proteomics data sets. *J. Proteome Res.* **8**, 3737–3745 (2009).
53. Valot, B., Langella, O., Nano, E. & Zivy, M. MassChroQ: a versatile tool for mass spectrometry quantification. *Proteomics* **11**, 3572–3577 (2011).
54. Yu, G., Wang, L.-G., Han, Y. & He, Q.-Y. clusterProfiler: an R package for comparing biological themes among gene clusters. *Omics J. Integr. Biol.* **16**, 284–287 (2012).
55. Luo, W. & Brouwer, C. Pathview: an R/Bioconductor package for pathway-based data integration and visualization. *Bioinforma. Oxf. Engl.* **29**, 1830–1831 (2013).
56. Suzuki, K., Bose, P., Leong-Quong, R. Y., Fujita, D. J. & Riabowol, K. REAP: A two minute cell fractionation method. *BMC Res. Notes* **3**, 294 (2010).
57. Perez-Riverol, Y. et al. The PRIDE database and related tools and resources in 2019: improving support for quantification data. *Nucleic Acids Res.* **47**, D442–D450 (2019).

### Acknowledgements

We thank Caroline Robert (Gustave Roussy Hospital, France) and Nicolas Dumaz (Saint Louis Hospital, France) for human melanoma cells. This work was funded by grants from the Ligue Nationale Contre le Cancer (Equipe labellisée), Fondation ARC, Gefluc and the Société Française de Dermatologie. C.E. and L.M.-O. were supported by a fellowship from the Ministère Français de l'Enseignement Supérieur, de la Recherche et de l'Innovation, and Fondation ARC. This work was also supported by "Région Ile-de-France" and Fondation pour la Recherche Médicale grants (to D.L.).

### Author contributions

C.E., A.E., C.P., and S.D. conceived the study and designed the experiments. C.E., L.M.-O., L.M., and S.D. performed and analysed the experiments. C.B. provided MITF plasmids and critically revised the manuscript. F.D. carried out the MS experimental work and D.L.

supervised MS and data analysis. L.B. and C.M. wrote software for immunofluorescence quantification. C.E., A.E., C.P., and S.D. wrote the manuscript. A.E., C.P., and S.D. supervised the research.

### Competing interests

The authors declare no competing interests.

### Additional information

**Supplementary information** The online version contains supplementary material available at <https://doi.org/10.1038/s42003-022-03049-w>.

**Correspondence** and requests for materials should be addressed to Sabine Druillennec.

**Peer review information** *Communications Biology* thanks David Vredevoogd and the other, anonymous, reviewers for their contribution to the peer review of this work. Primary Handling Editors: Toril Holein and Anam Akhtar. Peer reviewer reports are available.

**Reprints and permission information** is available at <http://www.nature.com/reprints>

**Publisher's note** Springer Nature remains neutral with regard to jurisdictional claims in published maps and institutional affiliations.



**Open Access** This article is licensed under a Creative Commons Attribution 4.0 International License, which permits use, sharing, adaptation, distribution and reproduction in any medium or format, as long as you give appropriate credit to the original author(s) and the source, provide a link to the Creative Commons license, and indicate if changes were made. The images or other third party material in this article are included in the article's Creative Commons license, unless indicated otherwise in a credit line to the material. If material is not included in the article's Creative Commons license and your intended use is not permitted by statutory regulation or exceeds the permitted use, you will need to obtain permission directly from the copyright holder. To view a copy of this license, visit <http://creativecommons.org/licenses/by/4.0/>.

© The Author(s) 2022

## 2. Appendix 2 Co-author paper 2

***Identification of a high-risk retinoblastoma subtype with stemness features, dedifferentiated cone states and neuronal/ganglion cell gene expression.*** J. Liu, D. Ottaviani, M. Sefta, C. Desbrouesses, E. Chapeaublanc, R. Aschero, N. Sirab, F. Lubieniecki, G. Lamas, L. Tonon, C. Dehainault, P. Fréneaux, S. Reichman, N. Karboul, A. Biton, **L. Mirabal-Ortega**, M. Larcher, C. B., S. Arrufat, A. Nicolas, N. Elarouci, T. Popova, F. Nemat, D. Decaudin, D. Gentien, S. Baulande, O. Mariani, F. Dufour, S. Guibert, C. Vallot, L. Lumbroso-Le Rouic, A. Matet, L. Desjardins, G. Pascual-Pasto, M. Suñol, J. mora, G. Correa Llano, J. Couturier, E. Barillot, P. Schaiquevich, M. Gauthier-Villars, D. Stoppa-Lyonnet, L. Golmard, C. Houdayer, H. Brisse, I. Bernard-Pierrot, E. Letouzé, A. Viari, S. Saule, X. Sastre-Garau, F. Doz, A. Carcaboso, N. Cassoux, C. Pouponnot, O. Goureau, G. Chantada, A. de Reyniès, I. Aerts and F. Radvanyi. (2021) Nature Communications (doi.org/10.1038/s41467-021-25792-0)

To established the dependency of Retinoblastoma cells on MYC/MYCN, I participated to the generation of cell lines MYC or MYCN knockdown using shRNAs. I also participated to the preparation of mARNs from these cells to be used for RNAseq analyses. These experiments contributed to demonstrate the activation of MYC/MYCN in the high-risk Subtype 2 of Retinoblastoma.



# A high-risk retinoblastoma subtype with stemness features, dedifferentiated cone states and neuronal/ganglion cell gene expression

Jing Liu <sup>1,2,3,34</sup>, Daniela Ottaviani <sup>1,2,4,34</sup>, Meriem Sefta<sup>1,2,34</sup>, Céline Desbrosses <sup>1,2</sup>, Elodie Chapeaublanc <sup>1,2</sup>, Rosario Aschero <sup>5</sup>, Nanor Sirab <sup>1,2</sup>, Fabiana Lubieniecki<sup>5</sup>, Gabriela Lamas<sup>5</sup>, Laurie Tonon<sup>6</sup>, Catherine Dehainault<sup>7,8</sup>, Clément Hua <sup>1,2</sup>, Paul Fréneaux<sup>7</sup>, Sacha Reichman <sup>9</sup>, Narjese Karboul<sup>1,2</sup>, Anne Biton <sup>1,2,10,11,30</sup>, Liliana Mirabal-Ortega <sup>12,13,14</sup>, Magalie Larcher<sup>12,13,14</sup>, Céline Brulard<sup>1,2,31</sup>, Sandrine Arrufat<sup>7</sup>, André Nicolas<sup>7</sup>, Nabila Elarouci<sup>3</sup>, Tatiana Popova<sup>15</sup>, Fariba Némati <sup>16</sup>, Didier Decaudin<sup>16</sup>, David Gentien<sup>16</sup>, Sylvain Baulande <sup>17</sup>, Odette Mariani<sup>7</sup>, Florent Dufour <sup>1,2</sup>, Sylvain Guibert<sup>18</sup>, Céline Vallot <sup>18</sup>, Livia Lumbroso-Le Rouic<sup>19</sup>, Alexandre Matet <sup>19,20</sup>, Laurence Desjardins<sup>19</sup>, Guillem Pascual-Pasto<sup>21,22</sup>, Mariona Suñol<sup>21,23</sup>, Jaume Catala-Mora <sup>21,24</sup>, Genoveva Correa Llano<sup>21,22</sup>, Jérôme Couturier<sup>7</sup>, Emmanuel Barillot <sup>10,11</sup>, Paula Schaiquevich <sup>5,25</sup>, Marion Gauthier-Villars<sup>7,8,15</sup>, Dominique Stoppa-Lyonnet <sup>7,8,20</sup>, Lisa Golmard<sup>7,8,15</sup>, Claude Houdayer<sup>7,8,15,32</sup>, Hervé Brisse <sup>26</sup>, Isabelle Bernard-Pierrot <sup>1,2</sup>, Eric Letouzé <sup>27,28</sup>, Alain Viari<sup>6</sup>, Simon Saule<sup>12,13,14</sup>, Xavier Sastre-Garau<sup>7,33</sup>, François Doz<sup>20,29</sup>, Angel M. Carcaboso <sup>21,22</sup>, Nathalie Cassoux<sup>19,20</sup>, Celio Pouponnot<sup>12,13,14</sup>, Olivier Goureau<sup>9</sup>, Guillermo Chantada <sup>4,21,22,25,35</sup>, Aurélien de Reyniès<sup>3,35</sup>, Isabelle Aerts<sup>1,2,29,35</sup> & François Radvanyi <sup>1,2,35</sup>✉

Retinoblastoma is the most frequent intraocular malignancy in children, originating from a maturing cone precursor in the developing retina. Little is known on the molecular basis underlying the biological and clinical behavior of this cancer. Here, using multi-omics data, we demonstrate the existence of two retinoblastoma subtypes. Subtype 1, of earlier onset, includes most of the heritable forms. It harbors few genetic alterations other than the initiating *RB1* inactivation and corresponds to differentiated tumors expressing mature cone markers. By contrast, subtype 2 tumors harbor frequent recurrent genetic alterations including *MYCN*-amplification. They express markers of less differentiated cone together with neuronal/ganglion cell markers with marked inter- and intra-tumor heterogeneity. The cone dedifferentiation in subtype 2 is associated with stemness features including low immune and interferon response, E2F and MYC/MYCN activation and a higher propensity for metastasis. The recognition of these two subtypes, one maintaining a cone-differentiated state, and the other, more aggressive, associated with cone dedifferentiation and expression of neuronal markers, opens up important biological and clinical perspectives for retinoblastomas.

**R**etinoblastoma is a rare childhood cancer of the developing retina with an incidence rate of about 1 in 17,000 live births<sup>1–3</sup>, but is the most frequent pediatric intraocular malignancy. The main therapeutic objective for retinoblastoma is first to save the child's life through early detection, treatment of the ocular tumor, and prevention of metastatic spread. Secondary goals are eye preservation and maximization of visual potential<sup>4</sup>. In low-income countries, retinoblastoma is associated with low patient survival due to delayed diagnosis, poor access to multi-disciplinary retinoblastoma-specific healthcare, and socio-economic factors. In high-income countries, tumor remission is achieved in more than 95% of cases, however some patients still develop metastases<sup>5</sup>. Metastases can be due to dissemination through the optic nerve into the central nervous system (CNS) and through the sclera to the orbit. Retinoblastoma can also give rise to systemic metastases<sup>6</sup>. Several histopathological features are considered high-risk factors for tumor progression and metastasis<sup>7</sup>.

Retinoblastoma is usually initiated by biallelic inactivation of the *RB1* tumor suppressor gene. A minority of non-hereditary retinoblastomas (<2%) are initiated by *MYCN*-amplification without *RB1* inactivation<sup>8</sup>. In most cases, hereditary retinoblastomas are bilateral, whereas non-hereditary cases are always unilateral.

The retina includes six types of neurons (rod and cone photoreceptors, bipolar, amacrine, horizontal, and ganglion cells) and Müller glia, all of which are generated from multipotent retinal progenitor cells<sup>9,10</sup>. Studies in human show that the cell-of-origin of retinoblastoma is a cone precursor<sup>11–15</sup>.

Three studies based on gene expression profiling reached conflicting conclusions concerning the possible existence of retinoblastoma molecular subtypes and the retinal cell type-specific markers expressed in retinoblastoma<sup>16–18</sup>. Beyond *RB1*, the only recurrently mutated gene in retinoblastoma (7–13% of cases) is the epigenetic modifier gene *BCOR*<sup>19–21</sup>. Recurrent genomic alterations have been identified: gains and amplifications on 1q, 2p (targeting *MYCN*), and 6p, losses on 13q (targeting *RB1*) and 16q<sup>22–25</sup>. Several studies have reported a positive correlation between high copy-number alterations, age at diagnosis, and other clinical and histopathological variables, including unilaterality, non-hereditary status, and low differentiation<sup>24,26–30</sup>. Despite this wealth of findings, a molecular framework for understanding the biology and clinical behavior of retinoblastoma is lacking.

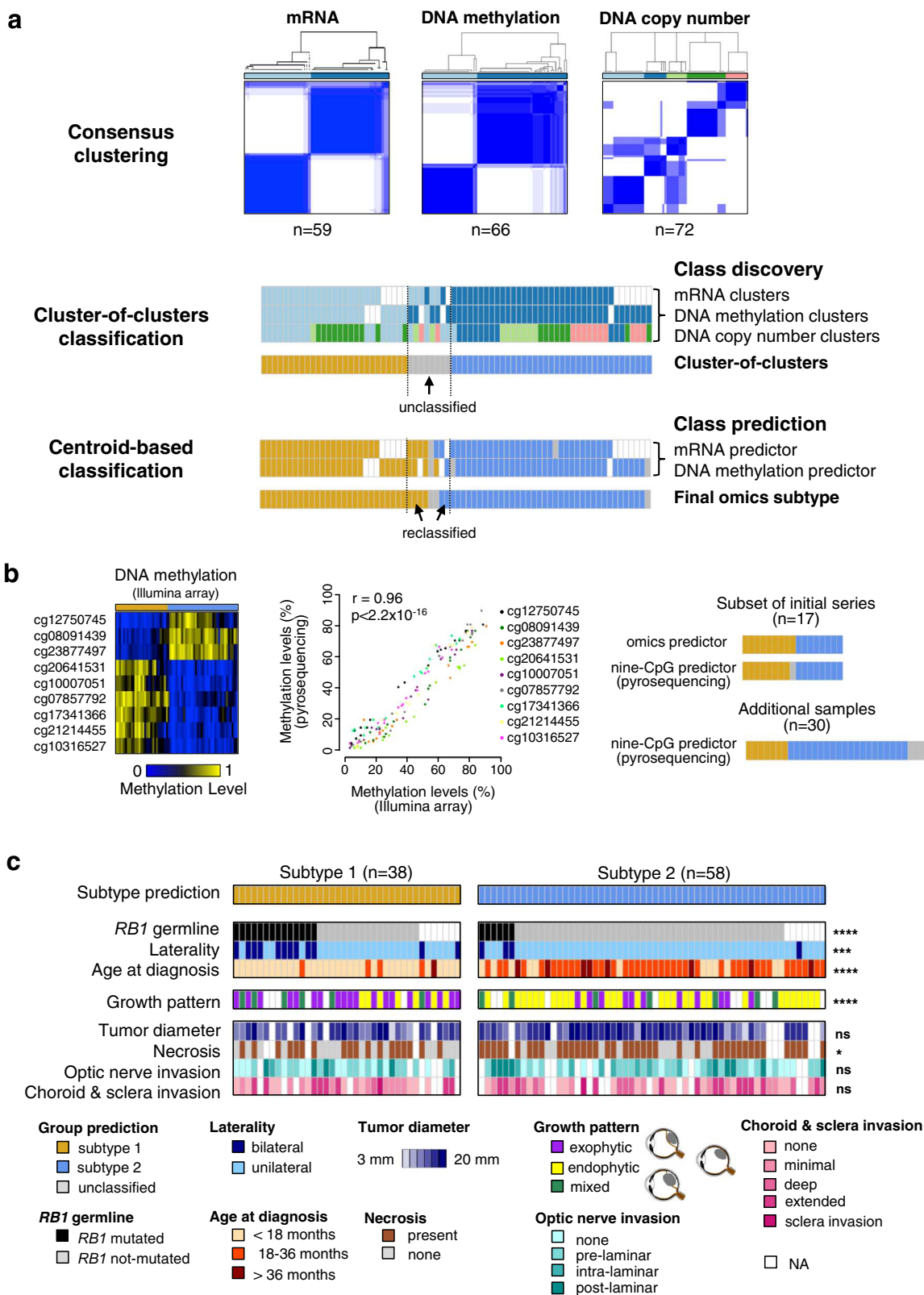
In this work, we identify two subtypes of retinoblastoma associated with different clinical and pathological features (age at diagnosis, laterality, heredity, and growth pattern) following integrative analysis of the transcriptome, methylome, and DNA copy-number alteration data from a series of 102 retinoblastomas. Further characterization provides evidence for the relevance of these two subtypes for understanding the biology of retinoblastoma, and for clinical management of this disease. Few genetic alterations other than *RB1* inactivation are associated with subtype 1 tumors. By contrast, in addition to *RB1* inactivation, almost all subtype 2 tumors harbor other recurrent genetic alterations, including *MYCN* amplifications. Consistent with a maturing cone precursor as the cell-of-origin of retinoblastoma, we find that both subtypes express cone markers. We show, by a detailed analysis of cone differentiation including the use of immunohistochemistry, retinal organoids, and single cells, that subtype 2 tumors are less differentiated than subtype 1 tumors and express neuronal/ganglion cell markers with marked inter- and intratumor heterogeneity. This lower cone differentiation in subtype 2 is associated with stemness features, including a higher propensity for metastasis, as shown by a study of an additional series of 112 retinoblastomas, including metastatic tumors.

## Results

**Identification of two retinoblastoma molecular subtypes with distinct clinical and pathological features.** We analyzed a series of 102 enucleated retinoblastomas (Supplementary Data 1). To investigate the existence of different retinoblastoma molecular subtypes, we combined three genomic approaches, mRNA expression, DNA methylation, and somatic copy-number alterations (SCNAs) in a subset of 72 of the 102 retinoblastomas. All three datasets were available for 53 of the 72 tumors, and at least two of the three datasets were available for all 72 tumors (Supplementary Data 1). Within each of these three omics datasets, we calculated several partitions of the samples in *k* clusters (*k*-partitions), for various values of *k*, through unsupervised hierarchical clustering, using varying numbers of features and different linkages (see “Methods” section). Then, for each omics and each value of *k*, we performed a consensus clustering analysis to derive a consensus *k*-partition. Doing so the transcriptome-based and methylome-based analyses both yielded stable consensus partitions in two clusters, while the SCNA-based analysis yielded a stable consensus partition in five clusters (Fig. 1a, upper panel and Supplementary Fig. 1a). Cluster memberships from each of the three partitions were analyzed by a cluster-of-clusters approach, briefly, a sample co-classification matrix was built and was then subjected to hierarchical clustering using complete linkage. It revealed the convergence of the three partitions around two molecular subtypes gathering 89% (64/72) of the cases (Fig. 1a, middle panel and Supplementary Fig. 1b). Nearest centroid classification attributed to the same subtypes 63 of the 64 classified samples. Moreover, six of the eight unclassified samples could be attributed to a subtype, yielding a final number of 69 classified samples (69/72, 96%): 31 belonging to subtype 1 and 38 to subtype 2 (Fig. 1a lower panel, and Supplementary Fig. 1c, Supplementary Data 1).

To assign to a subtype the 30 remaining tumors of our 102 tumor series, we then established a nine-CpG-based classifier, based on the genome-wide CpG methylation array profiling (see “Methods” section) (Fig. 1b, left panel and Supplementary Data 1). We verified that there was a high concordance in quantifying the level of CpG methylation between DNA methylation arrays and pyrosequencing assays (Fig. 1b, middle panel). This nine-CpG-based classifier attributed seven of the remaining 30 samples to subtype 1, and 20 to subtype 2, while three cases remained unclassified (Fig. 1b, right panel). Altogether the majority of the tumors (96/102, 94%) could be assigned to one of the two subtypes (38 to subtype 1, 58 to subtype 2).

We then compared the clinical and pathological features of these two subtypes (Fig. 1c, Table 1, Supplementary Data 1). Patients with subtype 1 tumors were significantly younger at diagnosis (median age = 11.0 vs 23.9 months; Wilcoxon rank-sum test,  $p = 8.9 \times 10^{-11}$ ). This subtype included 75% of the bilateral ( $p = 1.51 \times 10^{-3}$ ) and 70% of the hereditary cases ( $p = 7.68 \times 10^{-4}$ ). Unexpectedly, among patients with subtype 1 tumors, age at diagnosis did not differ significantly between hereditary forms (median = 10.2 months) and non-hereditary forms (median = 11.2 months) (Wilcoxon rank-sum test,  $p = 0.451$ ). Likewise, there was also no significant difference between the age at diagnosis for hereditary and non-hereditary forms of subtype 2 tumors (median = 19.8 and 24.7 months, respectively, Wilcoxon rank-sum test,  $p = 0.320$ ). Retinoblastomas generally display exophytic growth (into the subretinal space), endophytic growth (towards the vitreous), or, less frequently, a mixed growth pattern (both endophytic and exophytic). Subtype 1 tumors were significantly more likely to be exophytic, whereas most of the subtype 2 tumors were endophytic ( $p = 7.33 \times 10^{-4}$ ). Necrotic areas were more frequently observed in subtype 2 tumors than in subtype 1 tumors



( $p = 0.020$ ). Tumor diameter and histological risk features (optic nerve invasion, choroid, or sclera invasion) did not differ significantly between the two subtypes.

**Subtype 2 displayed more genetic alterations than subtype 1 and included the MYCN-amplified tumors.** We investigated the

genomic characteristics of the two tumor subtypes, by determining their SCNA profiles (Supplementary Data 2). Gains of 1q, 2p (*MYCN*), 6p, 13q, and losses/LOH of 13q (*RB1*), 16q were the most frequent alterations, consistent with reported findings for retinoblastoma<sup>22-25</sup>. 6p gains and 13q losses/LOH were equally distributed between tumor subtypes, whereas 1q gains, 2p gains, and 16q losses/LOH were significantly more frequent in the

**Fig. 1 Multi-omics-based molecular subtypes of retinoblastoma and clinical characteristics.** **a** Consensus clustering of retinoblastomas based on transcriptomic, DNA methylation, and copy-number alteration data (top panel). Unsupervised cluster-of-clusters analysis (middle panel). Supervised centroid-based classification (bottom panel). Final omics subtype: subtype 1,  $n = 31$  (gold); subtype 2,  $n = 38$  (blue); unclassified,  $n = 3$  (gray). **b** Heatmap showing methylation values (methylome arrays) for the nine-CpG-based classifier (left panel). Correlation between methylation values assessed by pyrosequencing and by methylome array, for 17 tumors (middle panel). A two-sided Pearson's correlation test was used. The nine-CpG-based classifier applied to a subset of 17 tumors of the initial series, led to the same classification as obtained by the -omics approach in 16 cases (one case being not classified by the nine-CpG-based classifier). Subtype assignment of 30 additional tumors based on the nine-CpG-based classifier (right panel). **c** Final molecular classification of 96 retinoblastomas and their key clinical and pathological characteristics.  $p \geq 0.05$  (ns),  $p < 0.05$  (\*),  $p < 0.01$  (\*\*),  $p < 0.001$  (\*\*\*),  $p < 0.0001$  (\*\*\*\*). For comparisons of *RB1* germline mutation, laterity, growth pattern, tumor diameter, and necrosis between two subtypes,  $\chi^2$  tests were used. For comparisons of age at diagnosis and tumor diameter between two subtypes, two-sided Kruskal–Wallis rank tests were used. For comparisons of optic nerve invasion and choroid and sclera invasion between two subtypes, two-sided Fisher's exact tests were used. Exact  $p$ -values are provided in Table 1.

subtype 2 samples ( $p = 5.5 \times 10^{-11}$ ,  $p = 0.0037$ , and  $p = 1.8 \times 10^{-7}$ , respectively) (Fig. 2a). *MYCN* amplifications varied from 14 to 246 copies (Supplementary Data 2) and were found only in subtype 2 tumors (10/58) ( $p = 0.013$ ).

The overall genomic instability score, estimated as the proportion of genome with copy-number alterations, was significantly higher ( $p = 3.3 \times 10^{-7}$ ) for subtype 2 than for subtype 1 tumors (Fig. 2b), and was also significantly higher when tumors with *MYCN* amplification were excluded from the analysis. By contrast, genomic instability scores did not differ between subtype 2 tumors with *MYCN* amplifications and subtype 1 tumors.

We then characterized the mutational landscape of the retinoblastoma subtypes. We performed whole-exome capture followed by paired-end massively parallel sequencing (WES) on genomic tumoral and matched normal DNA of 71 patients from the 102-retinoblastoma series (subtype 1,  $n = 25$ ; subtype 2,  $n = 41$ ; unclassified,  $n = 5$ ). We identified 242 somatic mutations in 186 genes (Supplementary Data 2). The tumors harbored a median of two mutations. The number of somatic mutations identified by WES was significantly higher ( $p = 1.2 \times 10^{-7}$ ) for subtype 2 than for subtype 1 tumors (Fig. 2c). Restricting subtype 2 tumors to either *MYCN*-amplified or *MYCN*-non-amplified tumors yielded the same result.

Three genes, *RB1*, *BCOR*, and *ARID1A*, were found to be recurrently mutated. We performed targeted sequencing for these three genes in 23 of the 31 samples lacking WES data. The distributions of *RB1*, *BCOR*, *ARID1A* mutations, *MYCN* amplifications, 1q gains, and 16q losses are shown by subtype in Fig. 2d. For *RB1* the germinal and somatic point mutations identified are shown, together with deletions, copy-neutral LOH, and promoter methylation. *RB1* mutations were found in most tumors, regardless of subtype, and no difference in the mutation type was observed between the two tumor subtypes. Of note, we found a tumor without *RB1* alteration, it belonged to subtype 2 and displayed a high level of *MYCN* amplification (141 copies). *BCOR* mutations ( $n = 9$ ) were found exclusively in subtype 2 ( $p = 0.02$ ), as were the two *ARID1A* mutations. Most of the subtype 2 tumors without *MYCN* amplification (46/48, 96%) presented gains of 1q and/or losses of 16q. By contrast, none of the *MYCN*-amplified tumors except one had a 1q gain or 16q loss ( $p = 0.005$ ) (Fig. 2d).

**Subtype 2 tumors harbored hypermethylation within CpG islands and hypomethylation outside CpG islands.** We compared the methylome of subtype 1 tumors ( $n = 27$ ) and subtype 2 tumors ( $n = 36$ , including 4 *MYCN*-amplified tumors). A heatmap representing the methylation levels of the 6607 CpGs significantly differentially methylated between the two subtypes (Supplementary Data 2) is shown in Fig. 2e. Subtype 2 tumors showed more frequent hypermethylation within CpG islands, and

a more frequent hypomethylation outside CpG islands, than subtype 1 tumors (Fig. 2f, g and Supplementary Fig. 2). The four *MYCN*-amplified subtype 2 tumors studied presented a hypomethylation outside CpG islands and did not present hypermethylation within CpG islands (Fig. 2g).

**The two subtypes exhibited differences in the expression of cone and ganglion/neuronal markers and in stemness.** We compared the transcriptome of the two subtypes. Almost one-third of the genes were found differentially expressed between the two subtypes (6207/20408, adjusted  $p$ -value  $< 0.05$ ) (Supplementary Data 3).

Cone markers (such as *GUCA1C*, *GNAT2*, *ARR3*, *GUCA1A*, *GUCA1B*, *GNGT2*, *PDE6C*, *PDE6H*, *OPN1SW*) and neuronal/ganglion markers (such as *EBF3*, *DCX*, *ROBO1*, *SOX11*, *GAP43*, *PCDHB10*, *STMN2*, *NEFM*, *POU4F2*, *EBF1*) were among the most differentially expressed genes. Cone markers were overexpressed in subtype 1 tumors, whereas neuronal/ganglion markers were overexpressed in subtype 2 tumors (Fig. 3a). Among the genes known to be involved in retinoblastoma<sup>1,31</sup>, several were found to be differentially expressed between the two subtypes (*KIF14*, *MDM4*, *MIR17HG*, *MYCN*, *SKP2* upregulated in subtype 2; *RBL2* downregulated in subtype 2) (Supplementary Data 3). Some of these genes were located in gained/amplified (*KIF14* and *MDM4* at 1q32.1 and *MYCN* at 2p24.3), or lost (*RBL2* at 16q12.2) chromosomal regions, whereas others were involved in the *MYC/MYCN* pathway (*MIR17HG*, *SKP2*). Hierarchical clustering of the 6207 genes identified three main gene clusters: two upregulated in subtype 1 (gene cluster 1.1 consisting of 1201 genes and gene cluster 1.2 consisting of 1788 genes) and one containing all the genes upregulated in subtype 2 (3112 genes; gene cluster 2) (Fig. 3b). We performed enrichment analysis using the gene sets from gene ontology biological processes (GOBP) and MSigDB hallmarks (HALLMARK) (Fig. 3c and Supplementary Data 3). Cluster 1.1 genes mainly upregulated in a subset of subtype 1 tumors, were associated with tumor microenvironment (immune response, inflammation, interferon response, complement, glial cells) and rod cells markers. Cluster 1.2 was enriched in genes related to fatty acid metabolism, oxidative phosphorylation, and photoreceptor/cone cells. Cluster 2 was enriched in genes associated with the cell cycle, E2F target genes, RNA processing, *MYC* pathway, and neuron morphogenesis.

The lack of an inflammation/immune signature and the enrichment in *MYC* and E2F target genes in subtype 2 was evocative of stemness features<sup>32,33</sup>. Moreover, *CD24*, one of the two most overexpressed genes in subtype 2 tumors (Fig. 3a and Supplementary Data 3), has been shown to be a neuronal stem cell marker and a cancer stem cell marker for several tumor types<sup>34</sup>. Stemness indices, based on transcriptomic data, allowed relative evaluation of the degree of stemness in tumor samples. We applied four different stemness signatures<sup>32,33,35,36</sup> to the 59

**Table 1 Clinical and histopathological characteristics of patients stratified by molecular subtype.**

	Subtype 1		Subtype 2		N	p-value <sup>a</sup>
	n (%)	n (%)	n (%)	n (%)		
Patients	38 (40)	58 (60)	96			
Clinical Center						
Institut Curie	31 (42)	43 (58)	74	0.655 <sup>b</sup>		
Hospital Garrahan	6 (33)	12 (66)	18			
Hospital Sant Joan de Déu	1 (25)	3 (75)	4			
Sex						
Female	17 (35)	31 (65)	48	0.403 <sup>c</sup>		
Male	21 (44)	27 (56)	48			
<i>RB1</i> germline mutation						
Yes	14 (70)	6 (30)	20	7.681 × 10 <sup>-4</sup> c		
No	17 (28)	44 (72)	61			
NA	7 (47)	8 (53)	15			
Laterality						
Bilateral	12 (75)	4 (25)	16	1.506 × 10 <sup>-3</sup> c		
Unilateral	26 (33)	54 (66)	80			
Age at diagnosis						
<18 months	33 (73)	12 (27)	45	2.132 × 10 <sup>-9</sup> d		
18–36 months	4 (10)	38 (90)	42			
>36 months	1 (11)	8 (89)	9			
Growth pattern						
Endophytic	7 (18)	31 (82)	38	7.332 × 10 <sup>-4</sup> c		
Exophytic	19 (63)	11 (37)	30			
Mixed	6 (46)	7 (54)	13			
NA	6 (40)	9 (60)	15			
Tumor diameter (mm)						
(3.98–6.67]	1 (50)	1 (50)	2	0.2094 <sup>d</sup>		
(6.67–9.33]	1 (25)	3 (75)	4			
(9.33–12]	7 (50)	7 (50)	14			
(12–14.7]	9 (64)	5 (36)	14			
(14.7–17.3]	9 (27)	24 (73)	33			
(17.3–20]	5 (31)	11 (69)	16			
NA	6 (46)	7 (54)	13			
Necrosis						
Yes	18 (31)	40 (69)	58	0.0203 <sup>c</sup>		
None	16 (57)	12 (43)	28			
NA	4 (40)	6 (60)	10			
Optic nerve invasion						
None	12 (48)	13 (52)	25	0.7467 <sup>b</sup>		
Prelaminar	12 (39)	19 (61)	31			
Intralaminar	4 (33)	8 (66)	12			
Post-laminar	4 (31)	9 (69)	13			
NA	6 (40)	9 (60)	15			
Choroid and sclera invasion						
None	10 (40)	15 (60)	25	0.6468 <sup>b</sup>		
Minimal	10 (48)	11 (52)	21			
Deep	1 (14)	6 (86)	7			
Extended	8 (38)	13 (62)	21			
Sclera invasion	1 (50)	1 (50)	2			
NA	8 (40)	12 (60)	20			

NA not available, n number in each subtype, N total number.

<sup>a</sup>Significant p-value < 0.05.<sup>b</sup>Two-sided Fisher's exact test.<sup>c</sup>Chi<sup>2</sup> test.<sup>d</sup>Two-sided Kruskal-Wallis rank test.

retinoblastoma samples for which transcriptomic data were available. The stemness indices assessed by these signatures were significantly higher in subtype 2 than in subtype 1 (Fig. 3d, upper panel and Supplementary Fig. 3a). In addition, the stemness indices obtained with the different signatures were highly correlated (Supplementary Fig. 3b). We searched for hallmark gene sets associated with stemness (Supplementary Data 3). The hallmarks positively correlated with stemness included E2F

targets, MYC targets V2, MYC targets V1 and G2/M checkpoint (Fig. 3d, lower panel and Supplementary Data 3). These hallmarks were the same as those identified in cluster 2 (cluster of genes overexpressed in subtype 2). The hallmarks negatively correlated with stemness included interferon-alpha response, interferon-gamma response, and complement (Fig. 3d, lower panel and Supplementary Data 3), and were the same as those identified in cluster 1.1 (cluster of genes overexpressed in subtype 1 and associated with the tumor microenvironment). We also assessed the relationship between stemness and the abundance of the various immune cells, as estimated with the Microenvironment Cell Population (MCP)—counter score<sup>37</sup>. Stemness indices were negatively correlated with the MCP scores of monocytic lineage, B lineage, and cytotoxic lymphocytes (Fig. 3d, lower panel and Supplementary Data 3). Altogether, we showed that subtype 2 was associated with high stemness.

The upregulation of cone-related genes in subtype 1 and of neuronal/ganglion cell-related genes in subtype 2 (Fig. 3a) led us to analyze in detail the expression of genes associated with the different retinal cell types (rod and cone photoreceptors, ganglion, amacrine, bipolar, and horizontal cells, and Müller glia). The list of retinal cell type markers was selected from a systematic literature search and from single-cell RNA-seq (scRNA-seq) data obtained at different time points during human retinal development<sup>38</sup>. From the annotated cell types defined by Lu et al.<sup>38</sup>, we identified lists of candidate markers associated with each retinal cell type (Supplementary Data 3). In order to choose the most specific markers, we developed a tool for visualizing gene expression profiles in the different retinal cell types (see “Methods” section) (<https://retinoblastoma-retina-markers.curie.fr/>). Based on an analysis of the expression profiles of the candidate markers obtained from Lu et al.'s data and of markers found in the literature we proposed markers for the different retinal cell types (given in Supplementary Data 3).

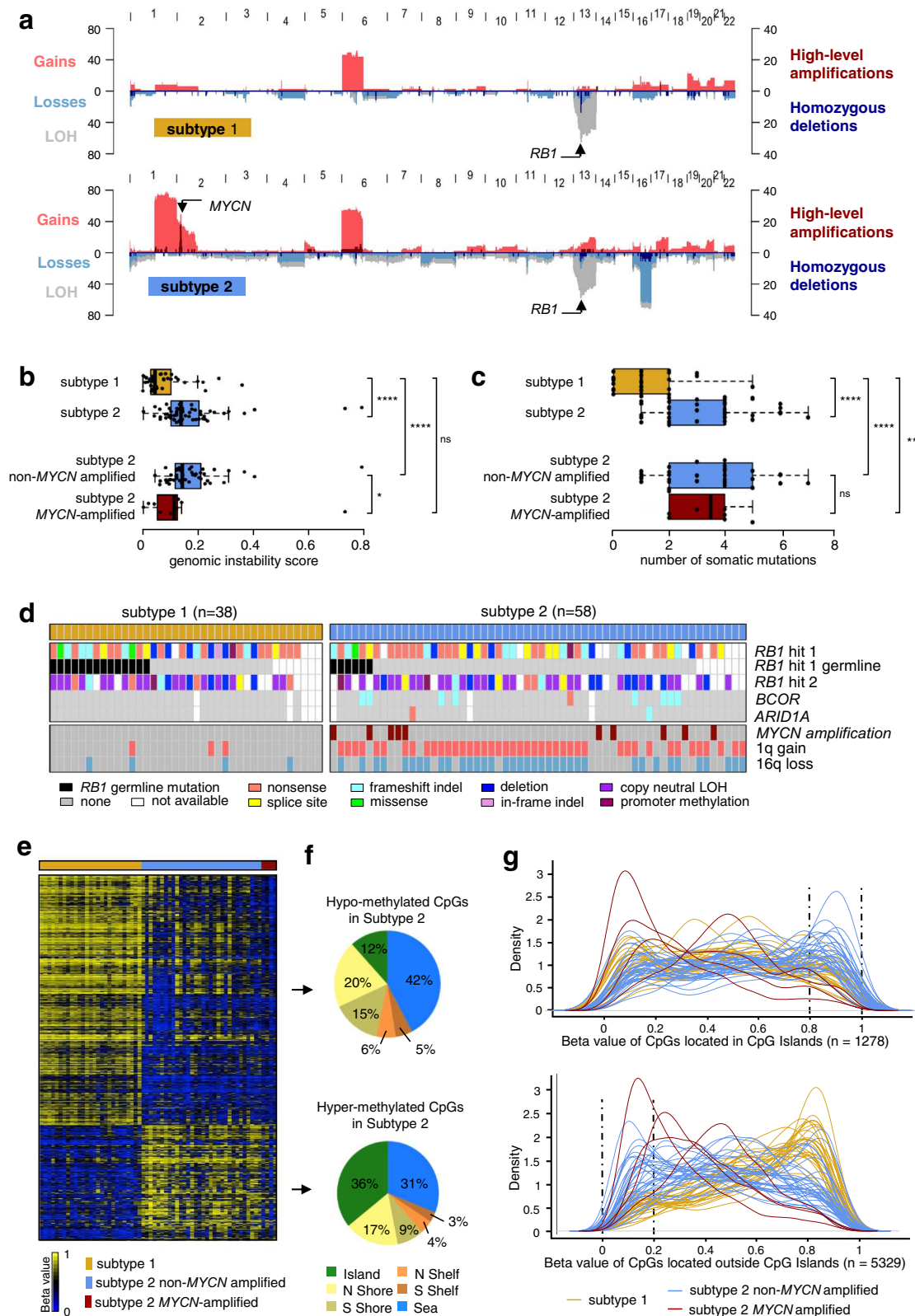
Cone markers were overall expressed in both subtype 1 and 2 retinoblastomas, with different expression levels between subtypes depending on the markers (Fig. 3e, upper panel). Among the 24 ganglion cell markers analyzed, a small subset (*EBF3*, *EBF1*, *GAP43*, *POU4F2*, *NEFM*, *ALCAM*, *NRN1*, *CNTN2*) were consistently overexpressed in subtype 2 tumors (Supplementary Fig. 4a and Fig. 3e, lower panel).

Using the lists of candidate markers associated with each retinal cell type obtained from Lu et al.'s data<sup>38</sup>, we provided further evidence for an enrichment of markers associated with ganglion cells in subtype 2 tumors (Supplementary Data 3). These genes overexpressed in subtype 2 tumors can be considered both as ganglion and neuronal genes. Indeed, although specific to ganglion cells in the context of the retina (Supplementary Fig. 4b), all displayed expression in the brain and played different functions in the central nervous system<sup>39–47</sup>.

Most of the markers of other retinal cell types (rods, amacrine, bipolar, horizontal, and Müller glia cells) were not expressed in retinoblastomas or were only expressed in a subset of tumors (Supplementary Fig. 4a). The expression of these markers was likely due to the presence of normal retinal cells in some retinoblastomas. Indeed non-neoplastic rods and Müller glial cells have been shown to be present in some retinoblastomas<sup>13</sup>.

### State of cone differentiation and expression of neuronal/ganglion cell markers distinguished the two subtypes.

The expression of cone markers observed in both subtypes of retinoblastoma is consistent with the retinoblastoma cell-of-origin being a committed cone cell. Differences in cone marker expression were observed between the two subtypes, raising the question of whether these differences could correspond to



different stages of cone differentiation. Retinal organoids are three-dimensional structures derived from human induced pluripotent stem (iPS) cells that recapitulate the spatial and temporal differentiation of the retina providing powerful in vitro models of human retinal development<sup>48,49</sup>. We measured the level of expression of early and late cone markers in retinal organoids at various time points (d35, d49, d56, d84, d112, d175) after the

differentiation of human iPS cells into the retina, and in subtype 1 (n = 23) and subtype 2 (n = 44) retinoblastomas, using the NanoString technology (Fig. 4a and Supplementary Data 4). As expected, in iPS cell-derived retinal organoids, the expression of early photoreceptor/cone markers (*OTX2*, *CRX*, *THRB*, *RXRG*) appeared at earlier time points than late cone markers (*PDE6H*, *GNAT2*, *ARR3*, *GUCA1C*). *GUCA1C* was the last marker to be

**Fig. 2 Genomic characterization, somatic mutational landscape, and DNA methylation profiles of the two retinoblastoma subtypes.** **a** Pattern of somatic copy-number alterations in subtype 1 (top,  $n = 38$ ) and subtype 2 (bottom,  $n = 58$ ) retinoblastomas. **b** Boxplots comparing genomic instability between subtype 1 tumors ( $n = 38$ ) and subtype 2 tumors ( $n = 58$ ). Among the subtype 2 tumors, non-*MYCN*-amplified ( $n = 48$ ) and *MYCN*-amplified ( $n = 10$ ) tumors are also shown. Significant differences were tested by two-sided Wilcoxon tests for Subtype 1 vs Subtype 2:  $p = 3.3 \times 10^{-7}$ ; Subtype 1 vs Subtype 2 non-*MYCN*:  $p = 1.2 \times 10^{-7}$ ; Subtype 1 vs Subtype 2 *MYCN*-amplified:  $p = 0.147$ ; and Subtype 2 non-*MYCN*-amplified vs Subtype 2 *MYCN*-amplified:  $p = 0.014$ . **c** Boxplots comparing the number of somatic mutations between subtype 1 tumors ( $n = 25$ ) and subtype 2 tumors ( $n = 41$ ). Among the subtype 2 tumors, non-*MYCN*-amplified ( $n = 33$ ) and *MYCN*-amplified ( $n = 8$ ) tumors are also shown. Significance differences were tested by two-sided Wilcoxon tests for Subtype 1 vs Subtype 2:  $p = 8.1 \times 10^{-7}$ ; Subtype 1 vs Subtype 2 non-*MYCN*-amplified:  $p = 3.5 \times 10^{-6}$ ; Subtype 1 vs Subtype 2 *MYCN*-amplified:  $p = 0.001$ ; and Subtype 2 non-*MYCN*-amplified vs Subtype 2 *MYCN*-amplified:  $p = 0.775$ . **b, c** In the boxplots, the central mark indicates the median and the bottom and top edges of the box the 25th and 75th percentiles. The whiskers are the smaller of 1.5 times the interquartile range or the length of the 25th percentiles to the smallest data point or the 75th percentiles to the largest data point. Data points outside the whiskers are outliers. Note:  $p \geq 0.05$  (ns),  $p < 0.05$  (\*),  $p < 0.01$  (\*\*),  $p < 0.001$  (\*\*\*),  $p < 0.0001$  (\*\*\*\*). **d** Somatic mutations of the three genes recurrently altered by tumor subtype. For *RB1* are indicated the germline mutations. *MYCN* amplifications, 1q gains, and 16q losses are also shown. **e** Heatmap of the 6607 differentially methylated CpGs (difference of methylation level  $>0.2$ , adjusted  $p < 0.05$ , two-sided Wilcoxon test and BH correction) between subtype 1 and subtype 2. **f** Distribution, in subtype 2 as compared to subtype 1, of hypomethylated CpGs (upper panel) and hypermethylated CpGs (lower panel), by CpG content and neighborhood context. **g** Density plots showing the distribution of methylation levels of the differentially methylated CpGs located in CpG islands (upper panel) and outside CpG islands (lower panel).

expressed, consistent with previous *in vitro* and *in vivo* observations<sup>50,51</sup>. Early cone markers were expressed in both tumor subtypes, at very similar levels. By contrast, late cone markers were expressed, on average, at lower levels in subtype 2 tumors, the most downregulated marker *GUCA1C* being the latest cone marker expressed. These results indicated that subtype 1 tumors corresponded to a more differentiated stage of cone development than subtype 2 tumors.

As several neuronal/ganglion cell lineage-related genes were shown to be differentially expressed between tumor subtypes (Fig. 3), we also compared their levels of expression in retinal organoids and in tumor samples of the two subtypes (Fig. 4a and Supplementary Data 4). Ganglion-cell markers were expressed at early time points of retinal differentiation (from d49), and their expression levels decreased after d84, consistent with the loss of ganglion cells in retinal organoids at late time points<sup>52</sup>. These ganglion markers were upregulated in subtype 2 compared to subtype 1 tumors (Fig. 4a). Two of them, *EBF3* and *GAP43*, were expressed in subtype 2 tumors with levels comparable to those observed in retinal organoids between d49 and d84.

To more precisely determine the cone development stage corresponding to subtype 1 and subtype 2 tumor cells, we calculated, for each time point after the induction of retinal differentiation, the correlation coefficient between the centroid of each tumor subtype and those of the organoids using cone marker expression (Fig. 4b). Subtype 1 tumors were closest to later cone differentiation (highest correlation observed at d173), whereas subtype 2 tumors were closest to earlier cone differentiation (highest correlation observed between d84 and d112).

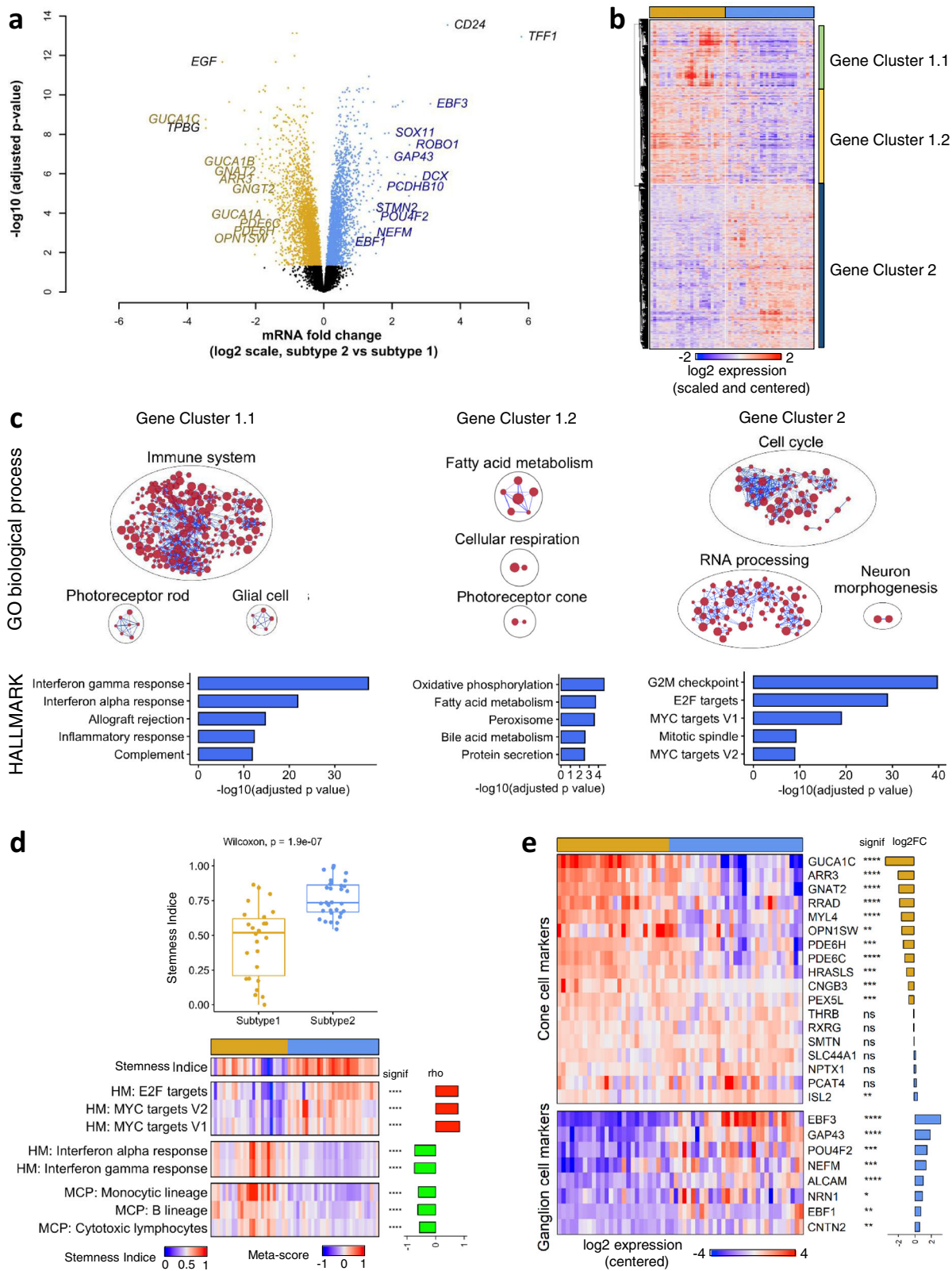
To illustrate the degree of cone differentiation achieved by individual retinoblastoma cases of each subtype, we generated a phylogenetic tree using photoreceptor/cone marker expression, incorporating retinal organoid samples at various time points after the induction of differentiation, and retinoblastoma samples (Fig. 4c). All subtype 1 tumors were close to iPSC cell-derived retinal organoids at a late time point of differentiation (d173). Subtype 2 tumors were spread out from d84 to d173 retinal organoids.

To explore further the heterogeneity in terms of cone differentiation in retinoblastoma, we studied by immunohistochemistry the distribution of an early photoreceptor marker (CRX), and a later marker specific to the cone lineage (ARR3). We also assessed the expression of one ganglion cell marker (EBF3). Immunohistochemical staining was performed on paraffin-embedded samples of subtype 1 ( $n = 9$ ) and subtype 2

( $n = 25$ ) retinoblastomas (Supplementary Data 4). Two examples of each tumor subtype are presented in Fig. 4d. As expected, in the peritumoral normal retina, the transcription factor CRX was expressed in all cells of the outer nuclear layer (ONL), whereas ARR3 was expressed in a subset of cells in the ONL. EBF3 was expressed in ganglion cells, but also in some amacrine cells in the inner nuclear layer, as previously reported<sup>51,53–55</sup>. All tumors, regardless of the subtype, expressed the photoreceptor marker CRX in agreement with retinoblastoma being derived from cone-committed cells. The ARR3<sup>+</sup>/EBF3<sup>-</sup> pattern was the only pattern observed in subtype 1 tumors (Fig. 4d, e and Supplementary Data 4). These tumors were positive for the proliferation marker Ki-67 (Fig. 4d, and Supplementary Data 4). Two types of expression patterns were observed for ARR3 and EBF3 in subtype 2 tumors (Fig. 4d). Most subtype 2 tumors (16/25, 64%) coexpressed ARR3 and EBF3 (ARR3<sup>+</sup>/EBF3<sup>+</sup>), as illustrated by tumor RB659 in Fig. 4d. Other subtype 2 tumors (8/25, 32%) displayed mutually exclusive expression of ARR3 and EBF3 (ARR3<sup>-</sup>/EBF3<sup>+</sup> or ARR3<sup>+</sup>/EBF3<sup>-</sup> areas), as illustrated by tumor RB617 in Fig. 4d. One tumor (1/25) expressed EBF3 but not ARR3. Tumors of subtype 2 coexpressing ARR3 and EBF3 (ARR3<sup>+</sup>/EBF3<sup>+</sup>) were always positive for Ki-67. In subtype 2 tumors with a mutually exclusive expression of ARR3 and EBF3, the ARR3<sup>-</sup>/EBF3<sup>+</sup> areas were always positive for Ki-67, whereas the ARR3<sup>+</sup>/EBF3<sup>-</sup> areas were mostly negative for Ki-67 (6 of 7 cases tested) (Fig. 4d and Supplementary Data 4). Histological examination of these Ki-67-negative ARR3<sup>+</sup>/EBF3<sup>-</sup> areas showed the presence of fleurettes (foci of photoreceptor differentiation) and an absence of mitoses in three of these six cases. The presence of these different areas within the tumor could reflect a range of tumor cell type stages, from stem, to progenitor to differentiating to terminally differentiated, with many of the latter being post-mitotic. Alternatively, the Ki-67-negative ARR3<sup>+</sup>/EBF3<sup>-</sup> areas could correspond to retinoma, a benign non-proliferative lesion observed adjacent to retinoblastoma<sup>56–58</sup>.

**Single-cell analysis of intratumoral heterogeneity in a subtype 2 tumor.** To further explore the intratumoral heterogeneity of subtype 2 tumors, we performed droplet-based single-cell RNA sequencing on a subtype 2 tumor (RBSC11). Immunohistochemical analysis of this tumor showed a mutually exclusive expression of ARR3 and EBF3, defining two types of areas (CRX<sup>+</sup>/ARR3<sup>+</sup>/EBF3<sup>-</sup> and CRX<sup>+</sup>/ARR3<sup>-</sup>/EBF3<sup>+</sup>) (Supplementary Fig. 5a), as observed in about 30% of subtype 2 tumors.

We retained transcriptomes of 1198 cells after initial quality controls (Supplementary Fig. 5b). To identify the different cell



populations present in the tumor, we performed shared nearest neighbor (SNN) clustering and identified seven clusters (Fig. 5a).

To characterize the different clusters, we used (1) known cell type-specific markers, (2) cluster markers (the most upregulated genes in the cluster compared to all other clusters), (3) pathway analysis of cluster markers, (4) correlation to bulk mRNA expression profiles of purified cell types (Fig. 5b, c and

Supplementary Fig. 5c, d, Supplementary Data 5). Clusters 0–4, accounting for 89.2% of all cells analyzed, expressed early photoreceptor/cone markers (e.g., *OTX2*, *CRX*, *THRB*, and *RXRG*). Clusters 0 and 2 expressed neuronal/ganglion cell markers (e.g., *GAP43*, *SOX11*, *UCHL1*, *DCX*, *EBF3*), whereas clusters 1 and 4 expressed late cone markers (e.g., *ARR3* and *GUCA1C*). Clusters 2 and 4 expressed proliferation markers, such

**Fig. 3 Transcriptomic differences between the two retinoblastoma subtypes.** **a** Volcano plot with genes significantly upregulated in subtype 1 ( $n = 26$ ) (gold) and subtype 2 ( $n = 31$ ) (blue). The genes related to cone-cell and neuronal/ganglion-cell differentiation are indicated (in gold and blue, respectively), together with the most highly differentially expressed genes in each subtype. **b** Hierarchical clustering of the significantly differentially expressed genes identified three main gene clusters. **c** Upper panels: Gene sets from the GOBP collection enriched in clusters 1.1, 1.2, 2 in hypergeometric tests. Results are presented as networks of enriched gene sets (nodes) connected based on their overlapping genes (edges). Node size is proportional to the total number of genes in the gene set concerned. The names of the various GOBP terms are given in Supplementary Data 3. Bottom panels: Top 5 Gene sets from the HALLMARK collection enriched in clusters 1.1, 1.2, 2. **d** Upper panel: Boxplots of stemness indices, determined as in Malta et al.<sup>32</sup>, in the two subtypes of retinoblastoma (subtype 1 tumors:  $n = 26$ , subtype 2 tumors:  $n = 31$ ). In the boxplots, the central mark indicates the median and the bottom and top edges of the box the 25th and 75th percentiles. Whiskers are the smaller of 1.5 times the interquartile range or the length of the 25th percentiles to the smallest data point or the 75th percentiles to the largest data point. Data points outside the whiskers are outliers. Significance was tested by a two-sided Wilcoxon test,  $p = 1.9 \times 10^{-7}$ . Bottom panel: Heatmap of stemness indices and meta-score of the most correlated and anti-correlated HALLMARK (HM) pathways and MCP-score of the most anti-correlated immune cells. Spearman's rho and  $p$ -value are shown in the figure.  $p < 0.0001$  (\*\*\*\*). **e** Heatmap representing expression pattern of cone- and ganglion-associated genes in the two subtypes of retinoblastoma. Statistical significance and log<sub>2</sub> fold-change in expression between subtype 2 and subtype 1 are also shown. Adjusted  $p \geq 0.05$  (ns), adjusted  $p < 0.05$  (\*), adjusted  $p < 0.01$  (\*\*), adjusted  $p < 0.001$  (\*\*\*), adjusted  $p < 0.0001$  (\*\*\*\*). Limma moderated two-sided  $t$ -tests and BH correction were used. Exact  $p$ -values are provided in Supplementary Data 3.

as *MKI67*. Cluster 3 presented a hypoxic gene expression program, including expression of the pro-apoptotic gene *BNIP3*. Clusters 5 and 6, accounting for 10.8% (129/1198) of all cells analyzed expressed hematopoietic markers, probably corresponding to stromal cell populations. Cluster 5 expressed monocyte/microglia markers (e.g., *CD14* and *AIF1*), whereas cluster 6 expressed T-lymphocyte markers, including markers of T-cell activation (e.g., *CD3D* and *TRAC*). A visualization of the expression of markers of each cluster is shown in Supplementary Fig. 5e, together with the expression of these markers in the normal developing retina.

To analyze the genomic heterogeneity in this tumor, we inferred copy-number variations (CNVs) in each single cell from the single-cell transcriptome data (see “Methods” section) (Fig. 5d). This analysis revealed that clusters 0–4 corresponded to tumor cells (presence of genomic alterations), whereas clusters 5 and 6 corresponded to normal cells (absence of genomic alterations). Genomic alteration patterns subdivided malignant cells into three distinct cell populations: cells with multiple genomic alterations (gains of 1q, 2q, 9p, 13q, loss of 8q), cells with 2p and 10q gains, and cells with 10q gains only. All cells from clusters 0 and 2 (*CRX*<sup>+</sup>/*EBF3*<sup>+</sup>/*GAP43*<sup>+</sup> tumor cells), and some cluster 3 cells, corresponded to the first profile (multiple alterations). Cells from clusters 1 and 4 (*CRX*<sup>+</sup>/*ARR3*<sup>+</sup>/*GUCA1C*<sup>+</sup> tumor cells) corresponded to the last two profiles (10q gain  $\pm$  2p gain). Lastly, some cluster 3 cells corresponded to the second profile (2p and 10q gains).

The phenotypic analysis and the inferred copy-number alterations from single-cell RNA-seq data led us to conclude that the malignant cells of the subtype 2 tumor analyzed consisted of two populations, one expressing early photoreceptor/cone markers and neuronal/ganglion cell markers (clusters 0 and 2), and the other expressing early photoreceptor/cone markers and late cone markers (clusters 1 and 4). These two cell populations existed in three states, G1/S (clusters 0 and 1), G2/M (clusters 2 and 4), and hypoxic (cluster 3). A schema summarizing the interpretation of the different clusters is shown in Fig. 5e (upper panel). The *CRX*<sup>+</sup>/*EBF3*<sup>+</sup>/*GAP43*<sup>+</sup> tumor population (clusters 0 and 2), presenting numerous genomic alterations, appeared to be genomically homogeneous. The *CRX*<sup>+</sup>/*ARR3*<sup>+</sup>/*GUCA1C*<sup>+</sup> tumor population (clusters 1 and 4) was less unstable and consisted of two genomically different subpopulations. A tumor progression tree constructed from the genomic alterations found in the different cell populations of this tumor is proposed in Fig. 5e (bottom panel). The co-expression of *CRX*/*EBF3*/*GAP43* (early photoreceptor/cone marker and neuronal/ganglion cell markers)

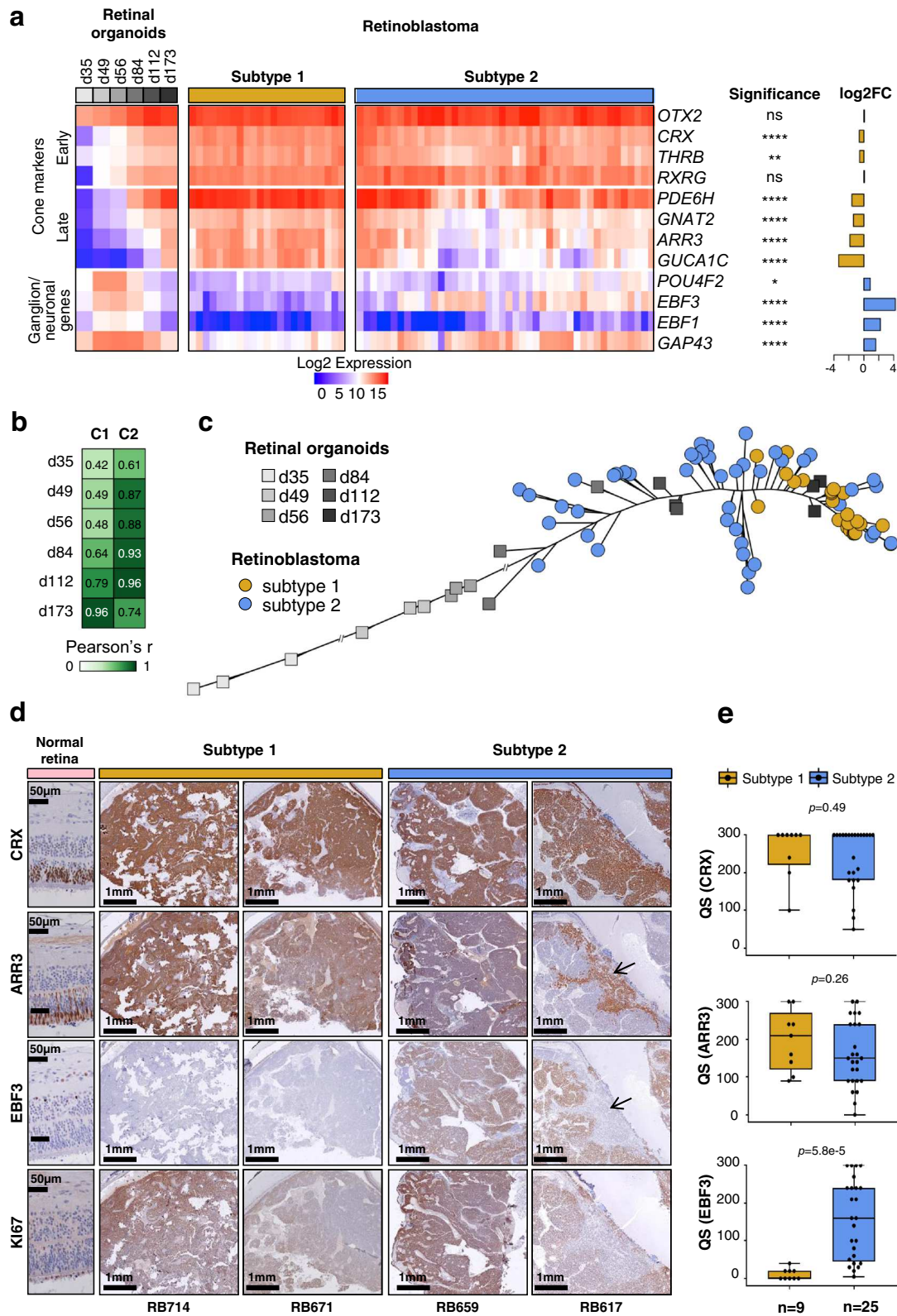
was unique to tumor cells as it was absent or very rare during normal retinal development (Supplementary Fig. 5f).

The single-cell RNA-seq analysis was performed on only one retinoblastoma. Single-cell analysis of additional tumors of both subtypes are necessary to further assess retinoblastoma heterogeneity and to investigate the relationship between retinal development and tumorigenesis using trajectory inference methods such as the ones estimating RNA velocity<sup>59,60</sup>.

**Subtype 2 tumors are associated with a higher risk of metastasis.** We then investigated whether the retinoblastomas developing metastases belonged to a specific molecular subtype. No patients in our initial series of 102 retinoblastomas cases developed metastases. We, therefore, studied an additional series of 112 primary tumors presenting high-risk pathological features (HRPFs) at diagnosis, among which 19 tumors subsequently developed metastasis. All these patients were treated at the Garrahan Hospital (Buenos Aires, Argentina). Their clinicopathological characteristics, including HRPFs, are provided in Supplementary Data 6 and summarized in Table 2.

TFF1 belongs to a family of small secretory molecules involved in the protection and repair of the gastrointestinal tract<sup>61</sup>. *TFF1* is not expressed in the normal developing retina (Supplementary Fig. 6a). It was the top upregulated gene in subtype 2 tumors compared to subtype 1 tumors (fold-change = 55, adjusted  $p$ -value  $< 10^{-12}$ , Fig. 3a, Supplementary Data 3), with expression in most subtype 2 tumors but little or no expression in subtype 1 tumors (Supplementary Fig. 6b, c). These results were confirmed based on the transcriptome of two additional tumor series<sup>16,18</sup> (Supplementary Figs. 6b, c and 7).

We assessed TFF1 protein expression by immunohistochemistry, in 55 of the tumors from our initial series of 102 classified retinoblastomas (18 subtype 1 and 37 subtype 2 tumors). Expression of TFF1, *CRX*, and *ARR3* are shown for representative tumors of subtypes 1 and 2 in Fig. 6a. Subtype 1 tumors displayed little or no TFF1 expression (QS  $\leq 50$ ; QS, quick score), whereas most subtype 2 tumors displayed high levels of expression (QS  $> 50$ ; Fig. 6a, b, Supplementary Data 6). We then analyzed TFF1 expression in the additional series of 112 primary tumors with HRPFs including 19 metastatic cases (Garrahan series). TFF1 expression could be evaluated in 18 of the 19 primary tumors that subsequently developed metastasis. All 18 cases were positive for TFF1 (QS  $> 50$ ), in contrast to the non-metastatic cases ( $p = 0.00033$ ) (Fig. 6b and Supplementary Data 6),



suggesting that they belonged to subtype 2. Consistent with this, 15 of the 16 metastatic cases analyzed were also positive for EBF3 (QS > 270) (Supplementary Data 6), a ganglion marker specifically associated with subtype 2 (Figs. 3a, 4d, e and Supplementary Fig. 6). In seven of the 19 metastatic cases, tissues were available from both the primary tumor and the metastasis. In all but one of these cases, the metastatic sites were also positive for TFF1 (QS

range of 90–300). For EBF3, the six metastatic sites analyzed were positive (QS > 255), including the one negative for TFF1 (Fig. 6c and Supplementary Data 6). All these results suggested that subtype 2 tumors are more aggressive than subtype 1 tumors. These findings require validation by additional evidence for subtype 2 assignment, and by studies on additional series of metastatic cases.

**Fig. 4 Expression of cone and neuronal/ganglion cell markers in retinoblastoma and retinal organoids.** **a** Heatmap showing the expression of cone and ganglion markers in retinal organoids at different differentiation time points, and in subtype 1 and subtype 2 tumors assessed by NanoString technology. Differences in gene expression between the two subtypes were assessed by two-sided t-tests with BH correction. Exact *p*-values are provided in Supplementary Data 4. **b** Pearson's correlation of the expression of 8 cone markers, between the centroids of the 2 retinoblastoma subtypes and retinal organoids at different time points in differentiation. C1: centroid of subtype 1; C2: centroid of subtype 2. **c** Phylogenetic tree based on cone marker expression, for retinal organoids at different differentiation time points and for retinoblastoma samples. **d** Immunohistochemical staining of CRX, ARR3, EBF3, and Ki-67 in normal retina and retinoblastoma. For RB617, the black arrows indicate the mutually exclusive patterns for ARR3 and EBF3. Immunohistochemistry experiments were performed on 34 samples (subtype 1, *n* = 9; subtype 2, *n* = 25). Two representative images are shown for each subtype. **e** Boxplots showing the quick score (QS) for the differentiation markers used in the immunohistochemical analysis: CRX, ARR3, and EBF3. In the boxplots, the central mark indicates the median and the bottom and top edges of the box the 25th and 75th percentiles. The whiskers are the smaller of 1.5 times the interquartile range or the length of the 25th percentiles to the smallest data point or the 75th percentiles to the largest data point. Data points outside the whiskers are outliers. Two-sided Wilcoxon tests were used.

## Discussion

The use of a multi-omics approach led us to the reliable identification of two main retinoblastoma molecular subtypes. The different molecular, pathological and clinical features of these two subtypes highlighted the relevance of this classification. In support of this, we could validate the transcriptomic signatures that distinguished the two subtypes in two independent series of retinoblastoma<sup>16,18</sup> (Supplementary Fig. 7). The features of these two subtypes provide explanations for previous biological and clinical observations, with potential implications for retinoblastoma research and treatment.

Both subtypes expressed cone markers, consistent with the cone origin of human retinoblastoma<sup>11–15</sup>. There are several possible non-exclusive explanations for the existence of two subtypes of retinoblastoma. The two subtypes may be derived from cone precursors located at different retinal positions. Several studies have reported a central-to-peripheral progression of retinoblastoma location with increasing age at diagnosis<sup>62</sup>. As subtype 2 tumors are diagnosed significantly later than subtype 1 tumors (median age = 23.9 vs 11 months), they are therefore likely to be more peripherally located than subtype 1 tumors. The two subtypes may be derived from different cone precursors. They may also be derived from cone precursors at different stages of maturation. Arguing against this last explanation, it has been shown that *RB1*<sup>-/-</sup> retinoblastoma derived from an ARR3<sup>+</sup> maturing cone precursor<sup>15</sup>.

We showed that subtype 1 tumors presented later markers of differentiated cones (ARR3<sup>+</sup>, GUCA1C<sup>+</sup>) and that subtype 2 tumors presented markers of earlier differentiation with an important heterogeneity between and within tumors. This is in agreement with the lower differentiation and the heterogeneity reported in older retinoblastoma patients<sup>58</sup>. As both subtypes are likely derived from an ARR3<sup>+</sup> maturing cone precursor, the lower differentiation and the heterogeneity of subtype 2 tumors with *RB1* inactivation probably result from a dedifferentiation process.

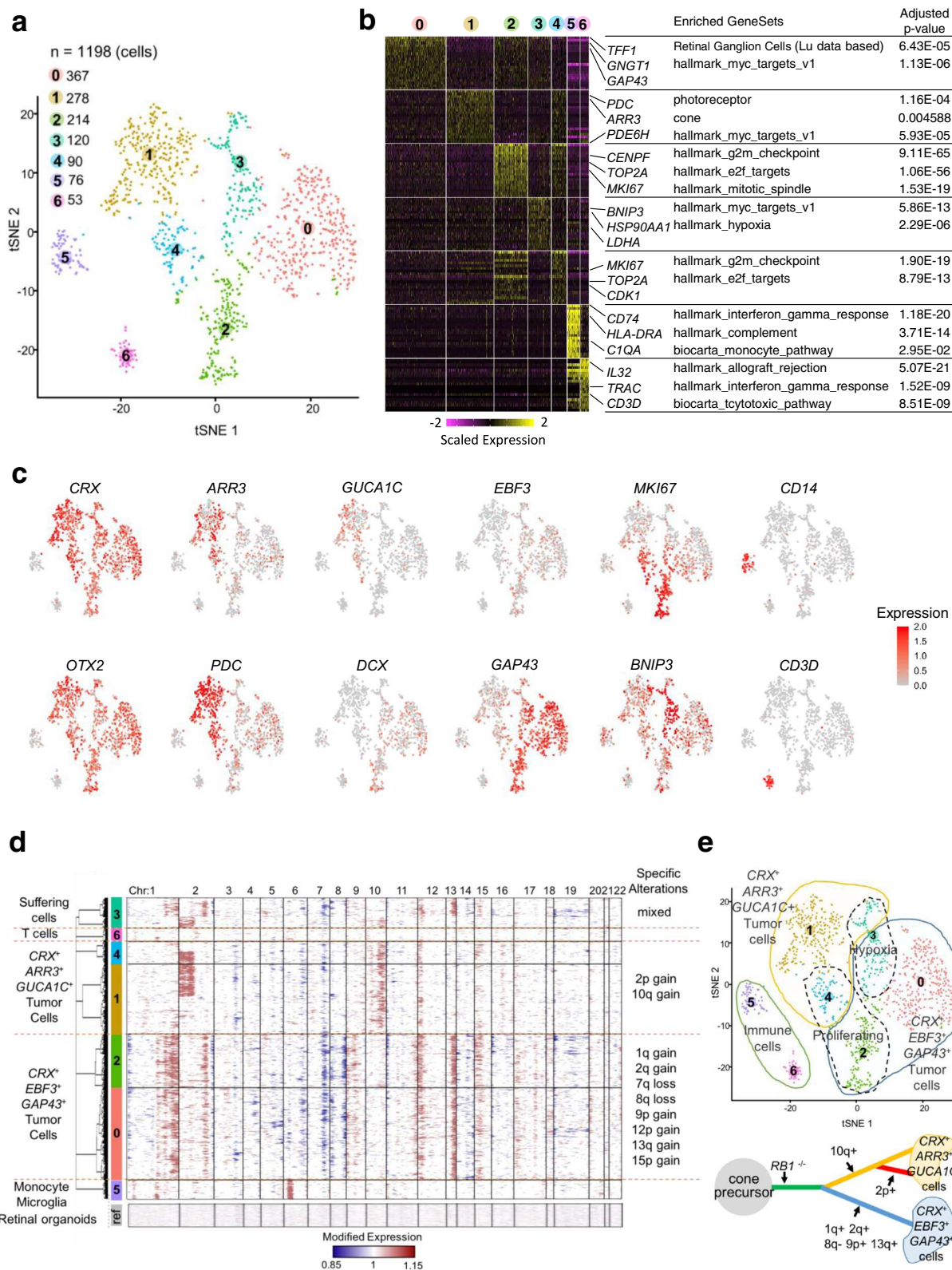
We found that subtype 2 was associated with low immune and interferon response, E2F and MYC/MYCIN activation, and a higher propensity for metastasis, corresponding to stemness features recently reported<sup>32,33,35,36</sup>. Genetic alterations and losses of function of *RB1* and *TP53* have also been shown to be associated with stemness in various cancers<sup>32,36</sup>. *RB1* inactivation was present in most of the tumors of both retinoblastoma subtypes, but, nevertheless, a difference in stemness was observed between the two subtypes. The higher stemness in subtype 2 could be related to a decreased expression of another gene from the *RB* family, *RBL2*, located on 16q, which was lost in the majority of subtype 2 tumors. The higher stemness in subtype 2 tumors could be also related to an increased expression of *MDM4*, an inhibitor of *TP53* located on 1q which was gained/amplified in 74% of subtype 2 tumors. It has been proposed that both *MDM4* and

*MDM2* abrogate p53-mediated tumor surveillance in retinoblastoma<sup>63,64</sup>. Our results indicate that *MDM4* could be involved in subtype 2 tumors. In addition to the expression of cone markers, subtype 2 tumors overexpressed markers attributed to ganglion cell markers in the context of the retina. However, all these markers can also be viewed as neuronal markers (they correspond to genes expressed and involved in the central nervous system). Moreover, among the genes overexpressed in subtype 2 tumors, we identified neuronal genes expressed during the development of retinal ganglion cells but also of other retinal cell types (like *SOX11*, *DCX*, *STMN2*). These observations suggest that subtype 2 may be considered as a cone-neuronal subtype.

Expression of neuronal genes has now been found not only in the brain and neuroendocrine tumors, but also in some cancers of epithelial origin (breast, ovary, colon)<sup>65</sup>. In recent years, it has become clear that tumor cells exploit neuronal and neurodevelopmental pathways to proliferate, migrate, and interact with normal cells, including endothelial cells and neurons<sup>65,66</sup>. Therefore, the overexpression of neuronal genes that we found in subtype 2 tumors may contribute to the aggressiveness of these tumors.

The overexpression of *MYCN*/*MYC* target genes in subtype 2 tumors, and the assignment of 10 out of 11 *MYCN*-amplified tumors to subtype 2 tumors (the remaining *MYCN*-amplified tumor being unclassified) suggest that *MYCN*/*MYC* play an important role in this subtype. *MYC* and *MYCN* have been implicated in other pediatric tumors, including neuroblastoma and medulloblastoma, often in subsets of high-risk tumors. In neuroblastoma, *MYCN* amplification is found in approximately 20% of cases and is associated with high-risk disease and poor prognosis<sup>67</sup>. It has recently been shown that *MYC* could also be a driver in another subset of high-risk neuroblastomas<sup>68,69</sup>. Group 3 medulloblastoma are associated with *MYC* amplification (10–17%) and the worst overall survival<sup>70,71</sup>. The activation of *MYC*/*MYCN* in subtype 2 tumors might be exploited for specific treatments of these tumors. Indeed *MYC*/*MYCN* can be inhibited indirectly by targeting their transcription with drugs such as *JQ1* and *OTX015*<sup>72</sup>, or directly, by targeting *MYC*/*MAX* interaction<sup>73</sup>.

In the series of 102 retinoblastomas, tumors with *MYCN* amplification accounted for 17% of subtype 2 tumors. *MYCN*-amplified tumors did not cluster separately from other subtype 2 tumors on transcriptome analyses, but they nevertheless had specific features. Clinically, tumors with *MYCN* amplification were diagnosed at an earlier age than other subtype 2 tumors (median age at diagnosis: 15.9 vs 26.9 months). Molecularly, the tumors with *MYCN* amplification could be distinguished from subtype 2 tumors without *MYCN* amplification on the basis of uncommon 1q gains and 16q losses. Moreover, the tumors with *MYCN* amplification were hypomethylated outside CpG islands, as in other subtype 2 tumors, but they did not display



hypermethylation within CpG islands, by contrast to other subtype 2 tumors.

In high- and middle-income countries, the frequency of enucleation for retinoblastoma is decreasing, due to early diagnosis and the development of new conservative treatments. Techniques for analyzing tumor DNA methylation and copy-number changes in aqueous humor samples and blood from cell-free DNA have

recently been developed<sup>74,75</sup>. The molecular characterization of retinoblastoma has, to date, been performed on tumor samples obtained from enucleation. The analyses of retinoblastoma through the use of liquid biopsy should provide a more comprehensive picture of the disease. Moreover, aqueous humor and blood samples could potentially be used to optimize retinoblastoma treatment through stratification by subtype.

**Fig. 5 Intratumor heterogeneity at the single-cell level of a subtype 2 retinoblastoma (RBSC11).** **a** 2D t-SNE plot of 1198 single retinoblastoma cells from one patient. Each dot represents one cell. **b** Heatmap of top cluster markers (top 20 most upregulated genes per cluster according to fold-change). Representative cluster markers and enriched gene sets are shown. Cluster marker *p*-values were calculated by hypergeometric tests with BH correction. **c** Expression of selected genes shown in 2D t-SNE plot (early photoreceptor markers: *CRX*, *OTX2*; late cone markers: *ARR3*, *GUCAT1C*; neuronal/ganglion markers: *EBF3*, *GAP43*, *DCX*; proliferation marker: *MKI67*; pro-apoptotic marker: *BNIP3*; macrophage marker: *CD14*; T-cell marker: *CD3D*). **d** CNV profiles inferred from single-cell gene expression. Each row represents the profile of one individual cell. The genes on chromosome 6p overexpressed in the non-malignant cells monocyte/microglia correspond to HLA complex genes and should not be interpreted as CNV in cluster 5. **e** Upper panel: Diagram summarizing the interpretation of the different clusters of the 2D t-SNE plot. Lower panel: A progression model for this retinoblastoma case based on genomic alterations.

**Table 2 Clinical and pathological characteristics of an additional series of 112 primary tumors presenting HRPFs.**

Characteristics	Metastatic (n = 19)	Non-metastatic (n = 93)	p-value
Laterality n (%)			
Unilateral	14 (73.7%)	70 (75.3%)	0.8844 <sup>a</sup>
Bilateral	5 (26.3%)	23 (24.7%)	
Age at diagnosis (months)			
Median (range)	31 (10–88)	31 (1–168)	0.9166 <sup>b</sup>
Initial treatment n (%)			
Enucleation	15 (78.9%)	91 (97.8%)	0.007394 <sup>c</sup>
Pre-enucleation chemotherapy	4 (21.1%)	2 (2.2%)	
IRSS Stage I HRPF			
Isolated massive choroidal invasion (+ scleral invasion)	4 (1) (21%)	7 (6) (7.5%)	0.0312 <sup>c</sup>
Post-laminar optic nerve invasion (+ massive choroidal and/or scleral invasion)	9 (3) (47.4%)	83 (49) (89.3%)	
IRSS Stage II			
Tumor at the resection margin of the optic nerve	5 (26.3%)	3 (3.2%)	0.003428 <sup>c</sup>
IRSS not classified			
Complete necrosis	1 (5.3%)	0	
Site of metastatic relapse			
Isolated orbit	3 (15.8%)		
CNS	6 (31.6%)		
Systemic	1 (5.3%)	N/A	
Orbit and lymph node	1 (5.3%)		
Orbit and systemic relapse	3 (15.8%)		
Orbit and CNS	5 (26.3%)		

<sup>a</sup>Chi<sup>2</sup> test.  
<sup>b</sup>Two-sided Wilcoxon rank-sum test.  
<sup>c</sup>Two-sided Fisher's exact test.

In conclusion, the identification of two molecular subtypes—cone-like and cone/neuronal—represents a major advance in the understanding of retinoblastoma. It should redefine further studies of this pediatric cancer, including the development of models, improvement of diagnosis and prognosis, and identification of more specific treatments. The high stemness and neuronal features associated with subtype 2 tumors connect retinoblastoma with emerging fields of cancer research, and open up new opportunities for treatment.

## Methods

### Patient samples

**Initial series of 102 retinoblastomas.** We included 102 tumors from 50 male patients and 52 female patients in this study. These patients came from three different hospitals: Institut Curie in Paris, France (78 patients), the Garrahan Hospital in Buenos Aires, Argentina (19 patients), and the Sant Joan de Déu Hospital in Barcelona, Spain (5 patients). The median age at diagnosis was 19.9 months (minimum: 27 days, maximum: 9.65 years). Six patients had received chemotherapy and/or radiotherapy prior to enucleation.

**Series of 112 retinoblastomas with HRPFs.** We included an independent series of 112 patients with high-risk pathological features (HRPFs)<sup>7</sup> from the Garrahan Hospital in this study (61 females and 51 males). The median age at diagnosis was 31 months (range: 1–168 months). Among the 112 patients, 19 subsequently developed the metastatic disease (9 females and 10 males). The median time from retinoblastoma diagnosis to metastasis was nine months (range: 4–65 months). Additional clinical characteristics are included in Table 2 and Supplementary Data 6.

Formalin-fixed paraffin-embedded tissues from the 112 tumors were analyzed. For seven metastatic patients, the metastatic sites were also available.

**Additional retinoblastoma sample for single-cell RNA sequencing.** One additional sample (RBSC11) was studied by single-cell RNA-seq. The sample was obtained from an enucleated patient >18 months of age with a unilateral non-hereditary form of retinoblastoma who did not receive treatment prior to enucleation.

**Fetal retina.** Fetal retinas were obtained from medical abortions. They were provided by the Fetal Pathology Unit of Antoine-Béclère Hospital in Paris (France). Three fetal retinas—RET215 (from a 20-week-old fetus), RET2 (23-week-old fetus), and RET1 (27-week-old fetus) were included in this study.

**Ethics statement.** All experiments were performed retrospectively and in accordance with the Declaration of Helsinki and the legislation of each participating country—France, Argentina, and Spain. The study was approved by the Institut Curie Review Board, the institutional review board of the Hospital de Pediatria Juan P Garrahan, and the Clinical Research Ethics Committee of Sant Joan de Déu Hospital. Written informed consent was obtained from parents or legal guardians of retinoblastoma patients, in accordance with current guidelines and legislation of each participating country.

Human fetuses (20, 23, 27 GW) were obtained from legally-induced terminations of pregnancy performed at the Antoine-Béclère Hospital in France. Fetal tissues were collected with the women's written consent, in accordance with the legal procedure agreed by the French National Agency for Biomedical Research (Agence de Biomédecine) and the approval of the local ethics committee of Antoine-Béclère Hospital.

**Human iPSC maintenance and retinal organoid generation.** Human-induced pluripotent stem cells (iPSCs) derived from dermal fibroblasts (hiPSC-2 clone)<sup>52</sup>

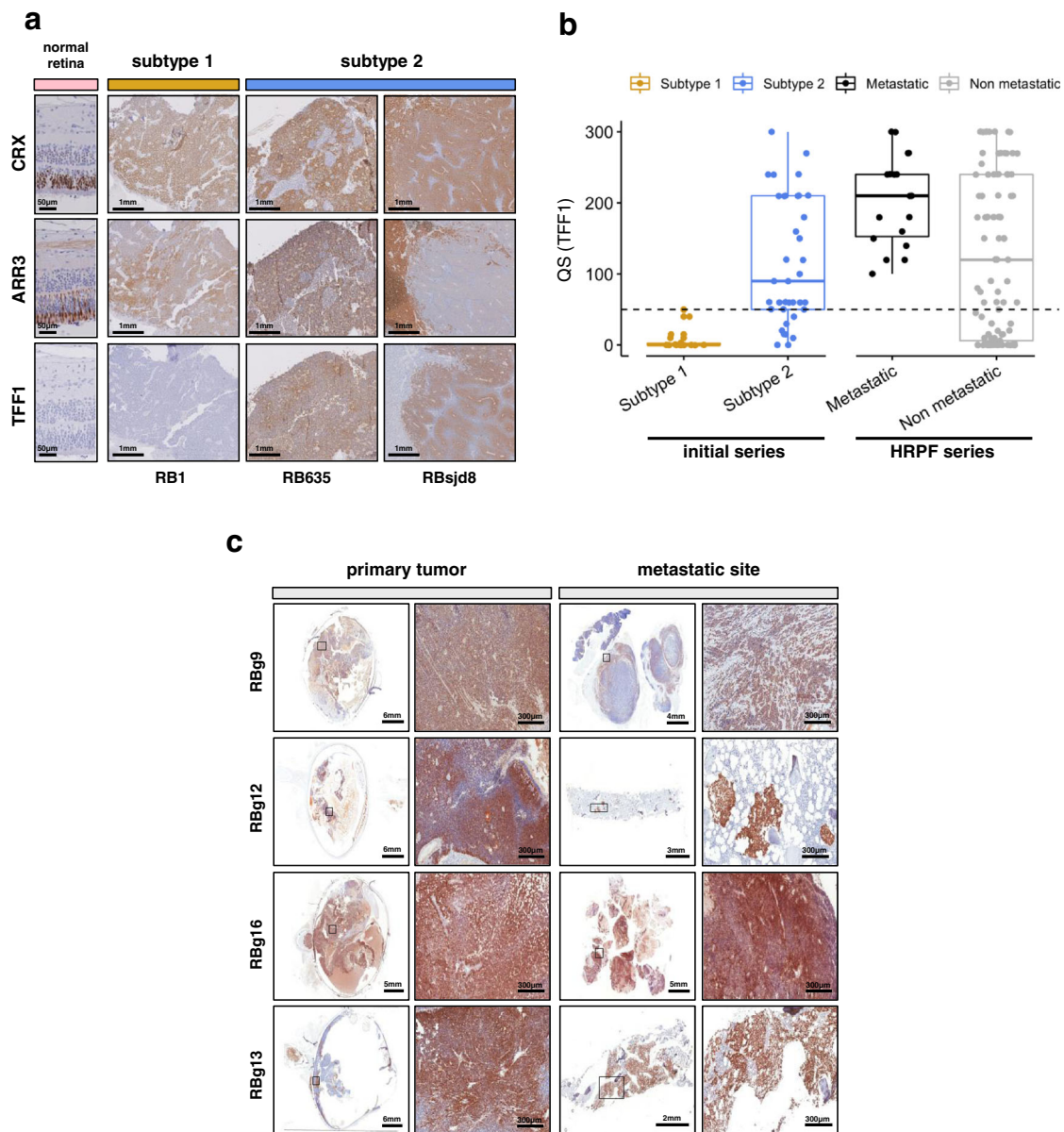


**Fig. 6 Subtype 2 tumors are associated with a higher risk of metastasis. a** Immunostaining of CRX, ARR3, and TFF1 in normal retina and retinoblastoma. Immunohistochemistry experiments were performed on 55 samples (subtype 1,  $n = 18$ ; subtype 2,  $n = 37$ ) from the initial series of 102 retinoblastomas. Representative images are shown: one subtype 1 tumor (RB1) and two subtype 2 tumors (RB635, RBsjd8). The subtype 2 tumors presented either a co-staining (RB635) or a mirror pattern (RBsjd8) for ARR3 and TFF1. **b** Boxplots showing the quick score (QS) for TFF1 in 55 tumors of the initial series (subtype 1,  $n = 18$ ; subtype 2,  $n = 37$ ), and in 112 tumors of the HRPF series. In the boxplots, the central mark indicates the median and the bottom and top edges of the box the 25th and 75th percentiles. The whiskers are the smaller of 1.5 times the interquartile range or the length of the 25th percentiles to the smallest data point or the 75th percentiles to the largest data point. Data points outside the whiskers are outliers. Two-sided Wilcoxon tests were used to assess the difference of the QS for Subtype 1 vs Subtype 2,  $p = 1.1 \times 10^{-7}$ , and metastatic vs non-metastatic,  $p = 0.007$ . **c** Immunostaining of TFF1 for primary tumors of metastatic retinoblastoma (left) and their metastatic sites (right), at low and high magnification. TFF1 expression could be assessed by immunohistochemistry for 6 of 7 available primary-metastasis tumor pairs. Representative images of four are shown.

were cultured on truncated recombinant human vitronectin-coated dishes in a humidified 37 °C incubator with 5% CO<sub>2</sub> in Essential 8™ medium (ThermoFisher Scientific) with daily medium change and weekly passage (2 ml enzyme-free Gentle cell dissociation reagent for 7 min at room temperature)<sup>48</sup>. For retinal differentiation, adherent iPSCs were expanded to 70–80% and cultured in Essential 6™ medium (ThermoFisher Scientific) for 2 days, followed by replacing each 2–3 days Essential 6™ medium supplemented with 1% N-2 Supplement, 10 units/ml Penicillin and 10 µg/ml Streptomycin (ThermoFisher Scientific). At around day 28, retinal organoids were isolated with a needle and cultured as floating structures in ProB27 medium (DMEM:Nutrient Mixture F-12 1:1, L-glutamine, 1% MEM non-essential amino acids, 2% B27 supplement (ThermoFisher Scientific), 10 units/ml Penicillin, and 10 µg/ml Streptomycin) supplemented with recombinant human FGF2 (PeproTech) for a week and then in ProB27 medium for the next several weeks allowing retinal differentiation and maturation<sup>48,76</sup>. By RT-qPCR and

immunofluorescence analysis, we previously showed that the different iPSC lines (hiPSC-2 clone<sup>52</sup>, AAVS1:CrxP\_H2BmCherry hiPSC line<sup>77</sup>) we used, are able to produce the whole repertoire of retinal cells, in an identical way and following the same chronological order with first the appearance of ganglion cells, then the amacrine and horizontal cells and finally the mature photoreceptors, the bipolar cells, and the Müller glial cells. The use of different markers of photoreceptor lineage (CRX, RCVRN, NRL, NR2E3, ARR3, RHO, OPSINS...) showed that the genesis of cones and rods is identical in the different iPSC lines used.

#### Sample collection and processing

**Tumor samples. Institut Curie.** Immediately after enucleation, a needle was inserted through the anterior chamber of the eye to extract a tumor sample by aspiration. The tumor specimen was placed in an RPMI medium on ice. The cells were

resuspended, counted and the suspension was split in two (for DNA and RNA preparation). The tubes were then centrifuged to remove the medium and the pellet was snap-frozen for later extraction. The remainder of the ocular globe was paraffin-embedded. For tumor DNA extraction, samples were first incubated in lysis buffer with recombinant proteinase K (Roche, Boulogne-Billancourt, France). They were next incubated with RNase A (Roche). DNA was then extracted using a standard phenol–chloroform protocol. Tumor RNA was extracted using the miRNeasy Mini Kit, according to the manufacturer's instructions (Qiagen, Courtabouef, France).

**Garrahan Hospital and Sant Joan de Déu Hospital.** Immediately after enucleation, a needle was inserted through the anterior chamber of the eye to extract a tumor sample by aspiration. The tumor specimen was either placed in guanidine thiocyanate or snap-frozen for later extraction. For tumor samples preserved in guanidine thiocyanate, alkaline phenol/chloroform/isoamyl alcohol (24:1:25) extraction was used for tumor DNA extraction. For snap-frozen tumor samples, commercial affinity columns (QIAamp DNA Mini Kit, Qiagen) or a standard phenol–chloroform protocol were used for tumor DNA extraction.

**Single-cell RNA-seq sample.** Tumor sample was processed immediately following needle aspiration through the anterior chamber of the eye. The sample was placed in an ice-cold CO<sub>2</sub>-independent medium. Density gradient centrifugation by Histopaque-1077 (Sigma-Aldrich) was used to remove debris, dead cells, and erythrocytes. The isolated viable cells were mechanically dissociated, washed, and resuspended in phosphate-buffered saline supplemented with 0.04% bovine serum. Cell count and viability were determined by trypan blue exclusion on a Vi-CELL XR (Beckman Coulter Life Sciences).

**Blood samples.** For Curie hospital samples, normal DNA was extracted with a perchlorate/chloroform protocol or FujiFilm QuickGene technology (Kurabo Biomedical, Osaka, Japan). For Garrahan Hospital samples, normal DNA was extracted with a phenol/chloroform/isoamyl alcohol (24:1:25) protocol or with commercial affinity columns (QIAamp DNA Mini Kit, Qiagen). For Sant Joan de Déu Hospital samples, a standard isopropanol precipitation protocol was used.

**Fetal retina.** Fetal tissues were maintained in ice-cold Hanks balanced salt solution (HBSS) after medical abortions. For the isolation of neural retinal tissue, eyes were transferred onto a sterile Petri dish containing ice-cold PBS and maintaining a cornea side-up position with fine forceps. A small incision was made in the corneoscleral junction using a small scalpel. The tip of the curved microscissors was inserted into the small incision. Eyes were carefully rotated of 360 degrees, and small incisions were made all the way around the eye, parallel to the corneoscleral junction, allowing dissociation of the anterior eyecup and lens from the posterior eyecup. The posterior eyecup was passed onto a small Petri dish containing ice-cold PBS. The neural retina was carefully isolated from the underlying retinal pigmented epithelium by blunt dissection using fine forceps. RNA was extracted using the miRNeasy Mini Kit, according to the manufacturer's instructions (Qiagen, Courtabouef, France).

**Human iPSCs.** Total RNA was extracted from human iPSCs using the Nucleospin RNA II kit (Macherey-Nagel), according to the manufacturer's instructions.

**Gene expression arrays.** RNA of 59 samples (see Supplementary Data 1) were hybridized, in two batches, to Affymetrix Human Genome U133 plus 2.0 Array Plates (Santa Clara, CA) according to Affymetrix standard protocols. Raw CEL files were RMA<sup>78</sup> normalized using R package *affy* 1.60.0. Batch effects were corrected with the help of the Bioconductor package *SVA* 3.30.1. The arrays were mapped to genes with a Brainarray Custom CDF (EntrezG version 23)<sup>79</sup>. Independent component analysis in  $k = 3$  independent components (IC) was performed using R package *MineICA* 1.24.0 (JADE method)<sup>80,81</sup>. The genes with high negative ( $< -2.5$ ) or positive contributions ( $> 2.5$ ) to IC were analyzed through pathway enrichment analysis (hypergeometric tests), seeking specifically signatures related to potential contamination by stromal cells. Genes with high positive contributions to IC #1 were found highly enriched in markers of stromal cells, and were discarded from clustering analyses.

**DNA methylation arrays.** Sixty-six DNA samples (Supplementary Data 1) were hybridized on Infinium HumanMethylation450 BeadChip arrays (Illumina, San Diego, CA). Four microliters of bisulfite-converted DNA were used for hybridization, following the Illumina Infinium HD Methylation protocol<sup>82</sup>. Data were processed using *preprocessIllumina* and *getBeta* functions in R package *Minfi* 1.28.4<sup>83</sup>. Probes were annotated using the R package *IlluminaHumanMethylation450kmanifest* 0.4. Probes located in Chromosome X and Chromosome Y were discarded from subsequent analyses.

**SNP arrays and BAC-CGH arrays.** Ninety-five retinoblastomas were analyzed using SNP arrays or BAC-CGH arrays (Supplementary Data 1). Seventy tumor samples were analyzed on high-density SNP arrays. The B allele frequency and log-ratio signals were smoothed and analyzed using the Genome Alteration Print (GAP) algorithm ([http://bioinfo-out.curie.fr/projects/snp\\_gap/](http://bioinfo-out.curie.fr/projects/snp_gap/))<sup>84</sup>. Twenty-five

tumor samples were analyzed on BAC-CGH microarrays. These arrays consisted of 3510 or 5323 clones covering the human genome with an average resolution of 850Kb or 560Kb; they were designed by the CIT-CGH Consortium (INSERM U830, Institut Curie, Paris) and IntegragenTM<sup>85</sup>. Hybridized slides were scanned and the scan data was pre-processed using R package *MANOR* 1.36.0<sup>86</sup> to correct for local spatial bias and continuous spatial gradient. Each array-CGH profile was centered on the median log<sub>2</sub> ratio and then analyzed to extrapolate copy-number profiles using the *GLAD* algorithm 2.28.1<sup>87</sup>.

**Whole-exome sequencing.** Whole-exome sequencing was performed for 71 retinoblastomas and matched normal (blood) samples (Supplementary Data 2). For 32 tumor/normal sample pairs, sequence capture and exome sequencing were performed by the Sequencing Platform of Institut Curie. The Nextera exome enrichment kit (Illumina) was used for DNA library preparation. The eluted fraction was amplified by PCR and sequenced on an Illumina HiSeq 2500 sequencer as paired-end 100 × 100 bp or 150 × 150 bp reads. For the remaining 39 tumors/normal sample pairs, sequence capture and exome sequencing were performed by Integragen. The protocol followed by Integragen has been described elsewhere<sup>88</sup>. In brief, Agilent in-solution enrichment (SureSelect Human All Exon Kit v4 + UTR) was used for DNA library preparation. The eluted fraction was amplified by PCR and sequenced on an Illumina HiSeq 2000 sequencer as paired-end 75 bp reads.

**Single-cell library preparation and sequencing.** Six thousand cells were loaded onto the Chromium System using the single-cell 3' reagent kits v2, in accordance with the manufacturer's protocol (10× Genomics), where single cells are partitioned in droplets. Following capture and lysis, cDNA incorporating UMI (unique molecular identifier) and cell barcode was synthesized and amplified. Amplified cDNA was fragmented and the Illumina sequencing library was constructed as per the manufacturer's protocol (Illumina). Libraries were loaded at 400pM and pair-end sequenced on NovaSeq 6000 using NovaSeq 6000 S1 Reagent Kit (Illumina). Cells were sequenced at a mean depth of 100000. For quality control and quantification of cDNA and library, BioAnalyzer (Agilent BioAnalyzer High Sensitivity chip) was used.

#### Additional RNA quantification, DNA methylation, and mutation analyses

**NanoString® codeset design and mRNA quantification.** A codeset of 22 target genes was custom-designed and manufactured by NanoString® (Supplementary Data 4). One hundred nanograms of total RNA extracted from each sample was assessed on the Gen2 nCounter Analysis System from NanoString® Technologies at the Genomics Platform of the Curie Institute following the manufacturer's instructions. Samples were hybridized with multiplexed NanoString® probes containing a biotinylated capture probe and a reporter probe attached to a fluorescent barcode specific for each transcript, according to the nCounter codeset design (NanoString, Seattle, WA, USA). Hybridized samples were then purified and immobilized in a sample cartridge on the nCounter Prep Station for data collection, followed by quantification of the target mRNA in each sample using the nCounter Digital Analyzer (NanoString®). Data were normalized according to NanoString guidelines with nSolver 4.0. Briefly, the background was subtracted using the geometric mean of negative controls provided by NanoString®. The matrix was log-transformed (base 2) for further analysis.

**Pyrosequencing.** Forty-seven retinoblastoma samples were analyzed by performing pyrosequencing of the 9 selected CpGs (Supplementary Data 1 and Data Analysis section (Array-based methylation signature)).

Bisulfite treatment of genomic DNA (500 ng) was performed using the EZ DNA Methylation kit (Zymo Research). Primer design for each CpG target was performed using the PyroMark Assay Design software 2.0.2 (Qiagen) and pyrosequencing reaction was performed using PyroMark Q24 instrument (Qiagen). Primers used are provided in Supplementary Data 7. Pyrograms obtained were analyzed using the PyroMark Q24 software 2.0.6.20 (Qiagen) and methylation status was calculated at each CpG of interest.

**Targeted sequencing.** Targeted sequencing of the exonic regions of *RBI*, *BCOR*, and *ARID1A* was performed by IntegraGen SA (Evry, France) on 23 samples from the series of 102 retinoblastomas not subjected to whole-exome sequencing (Supplementary Data 2). The Fluidigm Access Array microfluidic system was used. PCR products were barcoded, pooled, and subjected to Illumina sequencing on a MiSeq instrument as paired-end 150-bp reads.

**Sanger sequencing.** Primer design was performed using Primer3 plus software<sup>89</sup>. Their sequences are provided in Supplementary Data 7. PCR amplification was performed with the HotStarTaq plus DNA Polymerase (Qiagen). PCR products were purified and sequenced at the Genomics Platform of the Institut Curie, using an ABI 3730 XL (Applied Biosystems, Life Technologies). Sequence analysis was carried out using Sequencher® version 5.4.1 sequence analysis software (Gene Codes Corporation, Ann Arbor, MI USA). One hundred nonsynonymous variants were identified by whole-exome sequencing and all variants identified by targeted sequencing were verified using Sanger dye-terminator sequencing. We validated 92

nonsynonymous mutations identified by whole-exome sequencing (of 100 variants tested, 92%) and all the mutations identified by targeted sequencing.

**Immunohistochemistry.** Immunohistochemical staining was performed on 3  $\mu\text{m}$ -thick sections.

For the cohort of 102 retinoblastomas included in this study, automated immunostaining for CRX, ARR3, EBF3, Ki-67 (Supplementary Data 4), and TFF1 (Supplementary Data 6) was performed on the available paraffin-embedded samples with Autostainer 480 (Lab Vision) at Institut Curie. The following antibodies were used: anti-CRX (Abcam, ab140603; 1:300 for AFA/Bouin fixed tissue and 1:500 for formalin-fixed tissues), anti-ARR3 (Proteintech Group, 11100-2-AP; 1/300 for AFA/Bouin fixed tissue and 1/500 for formalin-fixed tissues), anti-EBF3 (Abnova Corporation, H00253738-M05; 1/800), anti-Ki-67 (Abcam, ab1558; 1/2500), and anti-TFF1 (Sigma-Aldrich, HPA003425; 1/1000). Additional information about the conditions used is described in Supplementary Data 4. For each slide, staining was assessed by eyeballing independently by two specialists (authors: NS and PF) blind to molecular subtype classification, taking into account the intensity (I) as null (0), mild (1), moderate (2), and strong (3), and the percentage (P) of tumor cells with stained nuclei for CRX and EBF3 and stained cytoplasm for ARR3 and TFF1. The quick score (QS) was then calculated as  $I * P$  (from 0 to 300).

For the independent series of 112 retinoblastomas with high-risk pathological features from Garrahan Hospital, immunostaining of TFF1 was performed manually in the Pathology Department of the Garrahan Hospital according to the procedure used at Institut Curie. For each slide, staining was assessed independently by three specialists (authors: R.A., F.L., and G.L.).

### Bioinformatics and data analysis

**GISTIC analysis.** The copy-number alteration data for the 72 retinoblastomas studied by consensus clustering were first analyzed using GISTIC2.0 2.0.22<sup>90</sup>. Twelve significant recurrent copy-number alteration regions were identified. The average copy number for each sample across these regions was then used for consensus clustering of the copy-number alteration data.

**Consensus clustering.** Consensus clustering was performed independently on the transcriptomic, methylomic, and GISTIC-processed copy-number alteration data of 72 retinoblastoma samples ( $n = 59$  transcriptomes,  $n = 66$  methylomes,  $n = 72$  copy-number alteration profiles) (Supplementary Data 1). mRNA expression was assessed through Affymetrix U133plus2.0 arrays, genome methylation through Illumina Infinium Human Methylation 450 BeadChip arrays, and somatic copy-number alterations through SNP arrays or CGH-BAC arrays.

For the transcriptomic data, consensus hierarchical clustering was derived from a series of 24 dendrograms, which were obtained on all 59 retinoblastoma samples (columns) by analyzing 8 data subsets related to various numbers of genes (rows), through hierarchical clustering using 3 different linkage methods (average, complete, and Ward) and one distance metric ( $1 - \text{Pearson correlation coefficient}$ ). To construct the 8 data subsets, various number of genes (rows) (spanning between 100 and 4709 genes) were selected based on 2 criteria: minimal robust coefficient of variation (rCV) thresholds spanning the 99.5th to the 60th percentiles, and  $p$ -value lower than 0.01 for a test of variance (we test whether the variance for a gene is higher or not than the median variance across all genes).

Having obtained these 24 dendrograms, we cut each dendrogram in  $k$  clusters, and get a series of partitions in  $k$  groups, for  $k$  ranging from 2 to 8 (NB: a partition in  $k$  groups is called a  $k$ -partition). For each value of  $k$ , we then derived a consensus  $k$ -partition from the 24  $k$ -partitions obtained from the 24 dendrograms. To do so, we first calculated the (samples  $\times$  samples) co-classification matrix from these 24  $k$ -partitions (NB: in the co-classification matrix, the cell ( $i, j$ ) reports the number of partitions where samples  $i$  and  $j$  belong to the same group). The co-classification matrix is a similarity matrix and can be transformed into a dissimilarity matrix by replacing the value  $x$  in each cell ( $i, j$ ) by  $\text{MAX\_VALUE} - x$  (Here  $\text{MAX\_VALUE} = 24$ ). Then this dissimilarity matrix can be used to perform the hierarchical clustering of the related samples, using the complete linkage. Finally, the obtained dendrogram is cut in  $k$  clusters to yield the consensus  $k$ -partition.

Of note, before calculating the consensus  $k$ -partitions ( $k$  from 2 to 8), we assessed the intrinsic stability of the underlying  $k$ -partitions, as compared to  $k$ -partitions obtained using the same linkage and the same set of genes, but based on “noisy” data. “Noisy” data were generated for each of the 8 data subsets (200 iterations for each) by addition of random Gaussian noise ( $\mu = 0$ ,  $\sigma = 1.5 \times$  median variance calculated from the data set). The stability of each initial  $k$ -partition was then assessed using a stability score corresponding to the mean symmetric difference distance between an initial  $k$ -partition and the corresponding  $k$ -partitions derived from “noisy” data. The symmetric difference distance compares two partitions and gives the proportion of retention of the pairs of samples that are in the same group. It brings values ranging from 0 to 1: comparing two equal partitions yields a value of 1.

Consensus clustering of the methylomic data ( $n = 66$  retinoblastomas) was performed in a similar manner, this time with between 2086 and 87937 CpGs selected (rCV thresholds spanning the 99.5th to the 60th percentiles and a  $p$ -value lower than 0.01 for the test of variance). Consensus clustering of the GISTIC-processed copy-number alteration data ( $n = 72$  retinoblastomas) was also performed in a similar manner, this time with 3 or 4 significant copy-number

regions selected (rCV thresholds spanning the 80th to the 50th percentiles and a  $p$ -value lower than 0.01 for the test of variance). We observed both for transcriptome and methylome that the (intra-omics) consensus partition with  $k = 2$  clusters was more stable than solutions with  $k > 2$  clusters. We thus selected  $k = 2$  clusters for these two omics. The DNA copy-number data yielded 5 clusters.

**Cluster-of-clusters and centroid classification.** To identify a common samples’ partition across all three genomic platforms (transcriptome, methylome, copy number), we used a cluster-of-cluster approach. Based on the three unsupervised consensus partitions previously obtained from the three omics datasets (one consensus partition per omics data set), we first built a (samples  $\times$  samples) co-classification matrix, with values ranging from 0 to 1, with 0 corresponding to a pair of samples that never co-classify in any genomic data set, and 1 corresponding to a pair of samples that always co-classify in all three genomic datasets. This matrix was then subjected to hierarchical clustering using complete linkage. Three clusters of clusters were thus identified ( $n = 27$ ,  $n = 37$ , and  $n = 8$ ). The two larger cluster-of-clusters corresponded to two core molecular subtypes, subtype 1 and subtype 2. The smallest cluster-of-clusters ( $n = 8$ ) corresponded to ambiguous samples whose cluster assignments were not consistent across all three genomic platforms.

To classify these remaining samples according to either subtype 1 or subtype 2, we built two supervised centroid-based predictors, one transcriptomic and the other methylomic. The two core clusters of clusters defining subtype 1 and 2 were used to train these classifiers. For the transcriptomic data, the centroids of subtype 1 and subtype 2 were calculated as the intra-cluster median expression of the 800 genes most significantly differentially expressed between the two clusters (taking the 400 most upregulated genes in each subtype); similarly, for the methylomic data, the centroids of subtypes 1 and 2 were based on the median beta value of the 10,000 CpGs most significantly differentially methylated between the two clusters (5000 most methylated in each subtype). Each sample was assigned to the class whose centroid was closest to its profile, based on a Pearson’s correlation coefficient of at least 0.1 (we let unclassified samples yielding a Pearson’s correlation coefficient less than 0.1 to any of the two centroids/classes). Following this centroid-based step, we could classify 6 of the 8 samples without initial cluster-of-cluster attribution (four were assigned to cluster 1, two to cluster 2). This step also identified 3 outlier samples: two were already unclassified after the first cluster-of-clusters step, one was attributed initially to cluster 2.

**Copy-number analysis.** Copy-number alterations (CNAs) were analyzed using whole-exome sequencing (WES) data ( $n = 63$ ), SNP arrays (Illumina HumanCNV370 quad,  $n = 15$ ; Illumina Human610 quad,  $n = 6$ ; Affymetrix Cytoscan,  $n = 3$ ), and BAC arrays (3510 markers,  $n = 12$ ; 5323 markers,  $n = 3$ ). BAC arrays were analyzed using GLAD algorithm 2.28.1<sup>87</sup> to smooth log-ratio profiles into homogeneous segments and assign a discrete status to each segment (homozygous deletion, deletion, normal, gain, amplification). SNP arrays were analyzed using the Genome Alteration Print method<sup>84</sup>, which takes into account both the log ratio and B allele frequency signals to determine normal cell contamination, tumor ploidy, and the absolute copy-number of each segment. The median absolute copy-number was considered to be the zero level of each sample. Segments with an absolute copy number  $> \text{zero} + 0.5$  or  $< \text{zero} - 0.5$  were considered to have gains and deletions, respectively. Segments with an absolute copy-number  $\geq 5$  or  $\leq 0.5$  were considered to have high-level amplifications and homozygous deletions, respectively. To identify CNAs using WES data, we calculated the log ratio of the coverage in each tumor and its matched normal sample for each bait of the exome capture kit with a coverage  $\geq 30\times$  in the normal sample. Log-ratio profiles were then smoothed using the circular binary segmentation algorithm, as implemented in the Bioconductor package DNACopy 1.50.1<sup>91</sup> (default parameters except  $\text{min.width} = 4$ ,  $\text{undo.splits} = \text{sdundo}$ ,  $\text{undo.SD} = 1.5$ ). The most frequent smoothed value was considered to be the zero level of each sample. Segments with a smoothed log ratio  $> \text{zero} + 0.15$  or  $< \text{zero} - 0.15$  were considered to have gains and deletions, respectively. High-level amplification and homozygous deletion thresholds were defined as the mean  $\pm 5$  s.d. of log ratios in regions of normal copy number. Visual inspection of the profiles allowed to validate recurrent focal amplifications and homozygous deletions.

For a given sample, the GNL (Gain = 1/Normal = 0/Loss = -1) copy-number data are aggregated by chromosome, as the proportion of features with an aberration (i.e., gain or loss). The overall genomic instability score corresponds to the mean score across all chromosomes.

**Whole-exome sequencing analysis pipeline and mutation annotation.** Sample reads were aligned using Burrows–Wheeler Aligner (BWA 0.7.4)<sup>92</sup>. Targeted regions were sequenced to an average depth of 82 $\times$ , with 99% of the regions covered by  $\geq 1\times$ , 97.0% covered by  $\geq 4\times$ , and 87% covered by  $\geq 20\times$ .

For detection of somatic single-nucleotide variants (SNVs) and base insertions or deletions (indels), we used two separate variant-calling pipelines, the results of which were then merged. The first pipeline used MuTect 1.1.5<sup>93</sup> for SNV calling and the GATK SomaticIndelDetector 2.1–8 for indel calling<sup>94–96</sup>. The second pipeline used VarScan 2.3.7 somatic and VarScan somatic filter for both SNV and indel calling (<http://varscan.sourceforge.net>)<sup>97</sup>. After the variants called by both pipelines were merged, they were annotated using Annovar v2014Mar10<sup>98</sup>. Custom

filters and manual curation using the Integrative Genomics Viewer (IGV 2.3.34)<sup>99</sup> were then used to maximize the number of true positive calls and to minimize the number of false positives.

### Methylation analysis

**Array-based methylation signature.** From the methylome array data ( $n = 66$ ), we selected the most differentially methylated CpGs between the two retinoblastoma subtypes (clusters of clusters) based on statistics of the Wilcoxon test. Out of the top 50 hypermethylated CpGs and top 30 hypomethylated CpGs of subtype 2 retinoblastoma (by  $p$ -value), top 7 hypermethylated and top 7 hypomethylated CpGs by the difference of beta value were selected for pyrosequencing. 5 of them did not perform well in pyrosequencing. This method led to the selection of 9 CpGs significantly differentially methylated that have been analyzed by pyrosequencing for sample classification. Seventeen samples from the initial series were analyzed by pyrosequencing for validation of the nine-CpG-based classifier (9 subtype 1, 8 subtype 2); from these samples, we derived subtype 1 and subtype 2 centroids based on these 9 CpGs. The nearest-centroid approach (with Pearson's metric and a minimal threshold of 0.3) correctly assigned 16 of these 17 samples to their known subtype and left unassigned the remaining sample. Additional samples analyzed by pyrosequencing for these 9 CpGs were then classified using the nearest-centroid approach (Pearson's metric) at a minimal threshold of 0.3.

**Differential methylation analysis.** Differential methylation analysis was performed by two-sided Wilcoxon rank-sum test and BH correction to compare methylation level of 473,864 probes between 27 subtype 1 and 36 subtype 2 retinoblastomas. 94,101 probes were found differentially methylated between the two subtypes (69,901 probes higher in subtype 1, 24,200 probes higher in subtype 2). 6607 probes had a difference of beta value of more than 0.2 (4520 higher in subtype 1, 2087 higher in subtype 2) (Supplementary Data 2).

**Differential gene expression and pathway enrichment analysis.** Differential gene expression analysis was performed by Limma R package 3.40.6<sup>100</sup> to compare the expression of 20,408 genes between 26 subtype 1 and 31 subtype 2 tumors. 6207 genes were found differentially expressed (adjusted  $p$ -value < 0.05) (Supplementary Data 3). Three main gene clusters were identified by hierarchical cluster analysis (mean centering of genes,  $1 -$  Pearson's correlation coefficient as distance and average linkage). Visualization using heatmaps was performed with the R package ComplexHeatmap 2.1.1. Pathway enrichment analysis was performed by R clusterProfiler package 3.12.0<sup>101</sup>. Enriched gene sets from GOBP (Gene Ontology Biological Process) with adjusted  $p$ -value < 0.01 were selected for Cytoscape (3.7) EnrichmentMap (2.1.1) analysis<sup>102</sup>. Gene sets tested (GOBP and HALLMARK) were from the Molecular Signatures Database (MSigDB, version 6.2)<sup>103</sup>.

**Evaluation of stemness by transcriptome.** Stemness indices in retinoblastoma were evaluated as described in Malta et al.<sup>32</sup>. Briefly, the weight vectors of 12,955 genes were obtained by Malta et al. as a stemness signature to identify pluripotent stem cells from progenitor cells in PCBC (Progenitor Cell Biology Consortium) transcriptomic data set. 12,364 genes were available in our data set. After mean-centering, the expression matrix, Spearman's correlation with the stemness signature vectors were calculated for each sample of retinoblastoma and then scaled to the range of 0 to 1 as the stemness indices. The other three stemness indices were estimated using three stemness gene signatures (Miranda et al., Shats et al., Smith et al. of 109, 80, and 49 genes, respectively)<sup>33,35,36</sup> by *ssgsea* function of R package *gsva* 1.30.0. Boxplots were generated using R package *ggpubr* 0.2.0.

**Pathway meta-score.** Pathway meta-scores were calculated as the average expression of the genes involved in one selected pathway and then centered and scaled.

**Analysis of two independent transcriptomic datasets.** We applied the nearest-centroid approach (with Pearson's metric and a minimal threshold of 0.1) using the transcriptomic centroids calculated from our datasets to classify two publicly available transcriptomic datasets (GSE59983 and GSE29683).

In the Kooi et al.'s series<sup>18</sup> ( $n = 76$ ), 46 subtype 1 samples and 28 subtype 2 samples were identified, 2 samples were unable to be assigned a subtype. In the McEvoy et al.'s series<sup>16</sup> ( $n = 55$ ), 24 subtype 1 samples and 22 subtype 2 samples were identified among the 48 samples, 2 samples were unable to be assigned a subtype. Some samples ( $n = 7$ ) were excluded from clustering analysis due to the high contamination of retinal pigmented epithelial (RPE) cells. We examined the average expression of an RPE gene signature (from Liao et al.<sup>104</sup>,  $n = 83/87$  genes present in the data) and removed the suspected outlier samples ( $n = 7$ ) by Interquartile rule (suspected outliers are the samples when their average expression of RPE signature >  $Q3 + 1.5$  IQR or <  $Q1 - 1.5$  IQR).

**Phylogenetic analysis of retinoblastoma and retinal organoids.** Gene expression data of 8 genes related to cone-cell differentiation (*OTX2*, *CRX*, *THRB*, *RXRG*, *PDE6H*, *GNAT2*, *ARR3*, *GUCA1C*) were assessed by NanoString in 67 retinoblastomas (23 subtype 1 and 44 subtype 2) and 18 retinal organoids at 6 time

points after induction from iPSCs were used in phylogenetic analysis. Phylogenies were inferred by the minimal evolution algorithm<sup>105</sup> using *fastme.bal* function in R ape package 5.3 applied to Euclidean distance matrix based on these 8 gene expressions.

### Single-cell transcriptome analysis

**RBSC11 retinoblastoma.** Sample demultiplexing, alignment to the reference genome (GRCh38, Ensembl 84, pre-built Cell Ranger reference version 1.2.0), quantification and initial quality control (QC) were performed using the Cell Ranger software (version 2.1.1, 10x Genomics).

Genes that were expressed in more than 3 cells and cells that expressed more than 500 genes and less than 5% of mitochondria genes were retained ( $n = 1198$ ). The median numbers of genes and UMI counts per cell were 2911 and 7749, respectively. Normalization and clustering were performed using Seurat package version 2.3.4. UMI counts were normalized by *NormalizeData* function with *logNormalize* method, by a scaling factor of the median UMI count. UMI counts were then scaled to regress out the effect of UMI counts. Variable genes were found with *FindVariableGenes* function with *logVIM* function. Genes with an average expression more than 0.0125 and < 8 and with dispersion more than 0.5 were considered as variable genes for principal component analysis (PCA). Cell clusters were identified by *FindClusters* function with shared nearest neighbor (SNN) method modularity optimization-based clustering algorithm<sup>106</sup>, using the first 20 principal components. The parameter Resolution in the *FindClusters* was set between 0.4 and 1.4 and finally set to 0.6 for it provided a better biological interpretation.

Cluster markers were identified by *FindAllMarkers* function. Briefly, the expression of genes that expressed in more than 10% of cells in one cluster were compared with the expression of these genes in all other clusters, using Wilcoxon rank-sum test and corrected with BH correction. The procedure was repeated for all clusters. Genes upregulated in each cluster with more than 0.2 fold were considered as cluster markers. Pathway analysis of cluster markers was performed by R *clusterProfiler* package<sup>101</sup>. Gene sets tested were from the Molecular Signatures Database<sup>103</sup> (HALLMARK and BioCarta) and from Supplementary Data 3 (Cell type markers\_Lu data and Selected cell type markers).

Correlation to bulk mRNA expression profiles of purified cell types was performed by R *SingleR* package 1.0.1<sup>107</sup>. The expression profile of each cell was compared with the expression profiles of a data set that contains 713 microarray samples classified to 38 main cell types and further annotated to 169 subtypes<sup>108</sup>.

Copy-number variations (CNVs) were inferred from the single-cell gene expression by *InferCNV* package 0.8.2, using normal retinal organoids derived from hiPSCs as reference.

**Normal developing retina (Lu et al.<sup>38</sup>, data).** Normal retina scRNA-seq data from Lu et al.<sup>38</sup> were retrieved from GEO Omnibus database GSE138002. We retrieved the final filtered count matrix (GSE138002\_Final\_matrix.mtx.gz), gene annotations (GSE138002\_genes.csv.gz), and cell annotations (GSE138002\_Final\_barcode.csv.gz). The latest includes, for each cell, the UMAP coordinates and the retinal cell type annotation computed by Lu et al. that was used for our analysis. Normalization of the UMI counts and identification of markers for each cell type was done with Seurat as described for the retinoblastoma sample. We also looked for pan-photoreceptor markers (markers of both cones and rods). Among the markers of Cones or Rods, genes that were found overexpressed in Cones against all other types except Rods and in Rods against all other types except Cones were assigned to pan-photoreceptor. Values indicated in Supplementary Data 3 for pan-photoreceptor markers have been computed using the *FindAllMarkers* function comparing photoreceptor cells against all other cells.

**Visualization tool.** A R-Shiny web-app [<https://retinoblastoma-retina-markers.curie.fr>], based on the shiny (v.1.6.0) and shinydashboard (v.0.7.1) R-packages, was developed to visualize the expression of markers of the retina cell populations, of the two subtypes of retinoblastoma and other genes of interest cited across the manuscript in the two single-cell RNA-seq datasets (from normal human developing retina<sup>38</sup> and from a subtype 2 retinoblastoma, RBSC11 (this report)). The different plots and tables are made based on the R packages *cowplot* (v.1.1.1) and the ones included in *tidyverse* (v.1.3.0).

**Reporting summary.** Further information on research design is available in the Nature Research Reporting Summary linked to this article.

### Data availability

The raw array data are deposited in the Gene Expression Omnibus (GEO) database under accession code GSE58785. The raw whole-exome sequencing data are deposited in the European Genome-Phenome Archive (EGA) database under accession code EGAS00001005248. The raw targeted sequencing data are deposited in the EGA database under accession code EGAS00001005550. The raw single-cell RNA sequencing data are deposited in the EGA database under accession code EGAS00001005178. Data in EGA is available under restricted access, access can be obtained by contacting Retinoblastoma Data Access Committee - Institut Curie (data.office@curie.fr). The public retinoblastoma

transcriptomic data used in this study are available in the GEO database under accession codes [GSE29683](#) and [GSE59983](#). The public human developing retina scRNA-seq data used in this study are available in the GEO database under accession code [GSE138002](#). The remaining data are available within the Article, Supplementary Information, or Source Data file. Additional data inquiry can be addressed to the Lead contact: francois.radvanyi@curie.fr. Source data are provided with this paper.

### Code availability

Codes used to generate the analysis, figures and visualization app (<https://retinoblastoma-retina-markers.curie.fr>) are available at Github repositories (DOI: 10.5281/zenodo.5164167, DOI: 10.5281/zenodo.5163255)<sup>109,110</sup>.

Received: 14 November 2020; Accepted: 26 August 2021;

Published online: 22 September 2021

### References

- Dimaras, H. et al. Retinoblastoma. *Nat. Rev. Dis. Primers* **1**, 15021 (2015).
- Dyer, M. A. Lessons from retinoblastoma: implications for cancer, development, evolution, and regenerative medicine. *Trends Mol. Med.* **22**, 863–876 (2016).
- Munier, F. L. et al. Conservative management of retinoblastoma: challenging orthodoxy without compromising the state of metastatic grace. ‘Alive, with good vision and no comorbidity’. *Prog. Retin. Eye Res.* **73**, 100764 (2019).
- AlAli, A., Kletke, S., Gallie, B. & Lam, W.-C. Retinoblastoma for pediatric ophthalmologists. *Asia-Pac. J. Ophthalmol.* **7**, 160–168 (2018).
- Lu, J. E. et al. Metastases and death rates after primary enucleation of unilateral retinoblastoma in the USA 2007–2017. *Br. J. Ophthalmol.* **103**, 1272–1277 (2019).
- Dunkel, I. J. & Chantada, G. L. in *Clinical Ophthalmic Oncology* (ed. Saunders, W. B.) 484–486 (Saunders, 2007).
- Sastre, X. et al. Proceedings of the consensus meetings from the International Retinoblastoma Staging Working Group on the pathology guidelines for the examination of enucleated eyes and evaluation of prognostic risk factors in retinoblastoma. *Arch. Pathol. Lab. Med.* **133**, 1199–1202 (2009).
- Rushlow, D. E. et al. Characterisation of retinoblastomas without RB1 mutations: genomic, gene expression, and clinical studies. *Lancet Oncol.* **14**, 327–334 (2013).
- Turner, D. L., Snyder, E. Y. & Cepko, C. L. Lineage-independent determination of cell type in the embryonic mouse retina. *Neuron* **4**, 833–845 (1990).
- Cepko, C. Intrinsically different retinal progenitor cells produce specific types of progeny. *Nat. Rev. Neurosci.* **15**, 615–627 (2014).
- Bogenmann, E., Lochrie, M. A. & Simon, M. I. Cone cell-specific genes expressed in retinoblastoma. *Science* **240**, 76–78 (1988).
- Munier, F. L., Balmer, A., van Melle, G. & Gailloud, C. Radial asymmetry in the topography of retinoblastoma. *Clues Cell Orig. Ophthalmic Genet.* **15**, 101–106 (1994).
- Xu, X. L. et al. Retinoblastoma has properties of a cone precursor tumor and depends upon cone-specific MDM2 signaling. *Cell* **137**, 1018–1031 (2009).
- Xu, X. L. et al. Rb suppresses human cone-precursor-derived retinoblastoma tumours. *Nature* **514**, 385–388 (2014).
- Singh, H. P. et al. Developmental stage-specific proliferation and retinoblastoma genesis in RB-deficient human but not mouse cone precursors. *Proc. Natl Acad. Sci. USA* **115**, E9391LP–E9399400 (2018).
- McEvoy, J. et al. Coexpression of normally incompatible developmental pathways in retinoblastoma genesis. *Cancer Cell* **20**, 260–275 (2011).
- Kapatai, G. et al. Gene expression profiling identifies different sub-types of retinoblastoma. *Br. J. Cancer* **109**, 512–525 (2013).
- Kooi, I. E. et al. Loss of photoreceptor and gain of genomic alterations in retinoblastoma reveal tumor progression. *EBioMedicine* **2**, 660–670 (2015).
- Zhang, J. et al. A novel retinoblastoma therapy from genomic and epigenetic analyses. *Nature* **481**, 329–334 (2012).
- McEvoy, J. et al. RB1 gene inactivation by chromothripsis in human retinoblastoma. *Oncotarget* **5**, 438–450 (2014).
- Kooi, I. E. et al. Somatic genomic alterations in retinoblastoma beyond RB1 are rare and limited to copy number changes. *Sci. Rep.* **6**, 25264 (2016).
- Kooi, I. E. et al. A meta-analysis of retinoblastoma copy numbers refines the list of possible driver genes involved in tumor progression. *PLoS ONE* **11**, e0153323 (2016).
- Mairal, A. et al. Detection of chromosome imbalances in retinoblastoma by parallel karyotype and CGH analyses. *Genes. Chromosomes Cancer* **28**, 370–379 (2000).
- Herzog, S. et al. Marked differences in unilateral isolated retinoblastomas from young and older children studied by comparative genomic hybridization. *Hum. Genet.* **108**, 98–104 (2001).
- Bowles, E. et al. Profiling genomic copy number changes in retinoblastoma beyond loss of RB1. *Genes. Chromosomes Cancer* **46**, 118–129 (2007).
- van der Wal, J. E. et al. Comparative genomic hybridisation divides retinoblastomas into a high and a low level chromosomal instability group. *J. Clin. Pathol.* **56**, 26–30 (2003).
- Zielinski, B. et al. Detection of chromosomal imbalances in retinoblastoma by matrix-based comparative genomic hybridization. *Genes. Chromosomes Cancer* **43**, 294–301 (2005).
- Sampieri, K. et al. Array comparative genomic hybridization in retinoma and retinoblastoma tissues. *Cancer Sci.* **100**, 465–471 (2009).
- Mol, B. M. et al. High resolution SNP array profiling identifies variability in retinoblastoma genome stability. *Genes. Chromosomes Cancer* **53**, 1–14 (2014).
- Polski, A. et al. Variability in retinoblastoma genome stability is driven by age and not heritability. *Genes. Chromosomes Cancer* **59**, 584–590 (2020).
- Priya, K., Jada, S. R., Quah, B. L., Quah, T. C. & Lai, P. S. High incidence of allelic loss at 16q12.2 region spanning RBL2/p130 gene in retinoblastoma. *Cancer Biol. Ther.* **8**, 714–717 (2009).
- Malta, T. M. et al. Machine learning identifies stemness features associated with oncogenic dedifferentiation. *Cell* **173**, 338–354.e15 (2018).
- Miranda, A. et al. Cancer stemness, intratumoral heterogeneity, and immune response across cancers. *Proc. Natl Acad. Sci. USA* **116**, 9020–9029 (2019).
- Gilliam, D. T., Menon, V., Bretz, N. P. & Pruzsak, J. The CD24 surface antigen in neural development and disease. *Neurobiol. Dis.* **99**, 133–144 (2017).
- Shats, I. et al. Using a stem cell-based signature to guide therapeutic selection in cancer. *Cancer Res.* **71**, 1772–1780 (2011).
- Smith, B. A. et al. A human adult stem cell signature marks aggressive variants across epithelial cancers. *Cell Rep.* **24**, 3353–3366.e5 (2018).
- Becht, E. et al. Estimating the population abundance of tissue-infiltrating immune and stromal cell populations using gene expression. *Genome Biol.* **17**, 218 (2016).
- Lu, Y. et al. Single-cell analysis of human retina identifies evolutionarily conserved and species-specific mechanisms controlling development. *Dev. Cell* **53**, 473–491.e9 (2020).
- Sleven, H. et al. De novo mutations in EBF3 cause a neurodevelopmental syndrome. *Am. J. Hum. Genet.* **100**, 138–150 (2017).
- Tinterri, A. et al. Active intermixing of indirect and direct neurons builds the striatal mosaic. *Nat. Commun.* **9**, 4725 (2018).
- Gauthier-Campbell, C., Bredt, D. S., Murphy, T. H. & El-Husseini, A. E.-D. Regulation of dendritic branching and filopodia formation in hippocampal neurons by specific acylated protein motifs. *Mol. Biol. Cell* **15**, 2205–2217 (2004).
- Miller, J. A. et al. Transcriptional landscape of the prenatal human brain. *Nature* **508**, 199–206 (2014).
- Benzing, K., Flunkert, S., Schedl, A. & Engelkamp, D. A novel approach to selectively target neuronal subpopulations reveals genetic pathways that regulate tangential migration in the vertebrate hindbrain. *PLoS Genet.* **7**, e1002099 (2011).
- Wingo, A. P. et al. Large-scale proteomic analysis of human brain identifies proteins associated with cognitive trajectory in advanced age. *Nat. Commun.* **10**, 1619 (2019).
- Bye, C. R., Rytova, V., Alsanie, W. F., Parish, C. L. & Thompson, L. H. Axonal growth of midbrain dopamine neurons is modulated by the cell adhesion molecule ALCAM through trans-heterophilic interactions with L1cam, Chl1, and semaphorins. *J. Neurosci.* **39**, 6656–6667 (2019).
- Piras, I. S. et al. Association of AEBP1 and NRN1 RNA expression with Alzheimer’s disease and neurofibrillary tangle density in middle temporal gyrus. *Brain Res.* **1719**, 217–224 (2019).
- Masuda, T. Contactin-2/TAG-1, active on the front line for three decades. *Cell Adh. Migr.* **11**, 524–531 (2017).
- Reichman, S. et al. Generation of storable retinal organoids and retinal pigmented epithelium from adherent human iPSC cells in xeno-free and feeder-free conditions. *Stem Cells* **35**, 1176–1188 (2017).
- Kruczek, K. & Swaroop, A. Pluripotent stem cell-derived retinal organoids for disease modeling and development of therapies. *Stem Cells* **38**, 1206–1215 (2020).
- Kaewkhaw, R. et al. Transcriptome dynamics of developing photoreceptors in three-dimensional retina cultures recapitulates temporal sequence of human cone and rod differentiation revealing cell surface markers and gene networks. *Stem Cells* **33**, 3504–3518 (2015).
- Hoshino, A. et al. Molecular anatomy of the developing human retina. *Dev. Cell* **43**, 763–779.e4 (2017).
- Reichman, S. et al. From confluent human iPSC cells to self-forming neural retina and retinal pigmented epithelium. *Proc. Natl Acad. Sci. USA* **111**, 8518–8523 (2014).
- Gill, K. P. et al. Enriched retinal ganglion cells derived from human embryonic stem cells. *Sci. Rep.* **6**, 30552 (2016).

54. Aparicio, J. G. et al. Temporal expression of CD184(CXCR4) and CD171(LICAM) identifies distinct early developmental stages of human retinal ganglion cells in embryonic stem cell derived retina. *Exp. Eye Res.* **154**, 177–189 (2017).
55. Chuang, J.-H. et al. Expression profiling of cell-intrinsic regulators in the process of differentiation of human iPSCs into retinal lineages. *Stem Cell Res. Ther.* **9**, 140 (2018).
56. Gallie, B. L. et al. Loss of RB1 induces non-proliferative retinoma: increasing genomic instability correlates with progression to retinoblastoma. *Hum. Mol. Genet.* **17**, 1363–1372 (2008).
57. Sampieri, K. et al. Genomic differences between retinoma and retinoblastoma. *Acta Oncol.* **47**, 1483–1492 (2008).
58. Eagle, R. C. J. High-risk features and tumor differentiation in retinoblastoma: a retrospective histopathologic study. *Arch. Pathol. Lab. Med.* **133**, 1203–1209 (2009).
59. La Manno, G. et al. RNA velocity of single cells. *Nature* **560**, 494–498 (2018).
60. Kester, L. & van Oudenaarden, A. Single-cell transcriptomics meets lineage tracing. *Cell Stem Cell* **23**, 166–179 (2018).
61. Jahan, R. et al. Odyssey of trefoil factors in cancer: diagnostic and therapeutic implications. *Biochim. Biophys. Acta Rev. cancer* **1873**, 188362 (2020).
62. King, B. A. et al. Spatiotemporal patterns of tumor occurrence in children with intraocular retinoblastoma. *PLoS ONE* **10**, e0132932 (2015).
63. Laurie, N. A. et al. Inactivation of the p53 pathway in retinoblastoma. *Nature* **444**, 61–66 (2006).
64. Qi, D.-L. & Cobrinik, D. MDM2 but not MDM4 promotes retinoblastoma cell proliferation through p53-independent regulation of MYCN translation. *Oncogene* **36**, 1760–1769 (2017).
65. Jung, E., Alfonso, J., Monyer, H., Wick, W. & Winkler, F. Neuronal signatures in cancer. *Int. J. Cancer* <https://doi.org/10.1002/ijc.33138> (2020).
66. Monje, M. Synaptic communication in brain cancer. *Cancer Res.* **80**, 2979–2982 (2020).
67. Matthay, K. K. et al. Neuroblastoma. *Nat. Rev. Dis. Primers* **2**, 16078 (2016).
68. Wang, L. L. et al. Augmented expression of MYC and/or MYCN protein defines highly aggressive MYC-driven neuroblastoma: a Children’s Oncology Group study. *Br. J. Cancer* **113**, 57–63 (2015).
69. Zimmerman, M. W. et al. MYC drives a subset of high-risk pediatric neuroblastomas and is activated through mechanisms including enhancer hijacking and focal enhancer amplification. *Cancer Discov.* **8**, 320–335 (2018).
70. Northcott, P. A. et al. Subgroup-specific structural variation across 1,000 medulloblastoma genomes. *Nature* **488**, 49–56 (2012).
71. Roussel, M. F. & Robinson, G. W. Role of MYC in medulloblastoma. *Cold Spring Harb. Perspect. Med.* **3**, a014308 (2013).
72. Puissant, A. et al. Targeting MYCN in neuroblastoma by BET bromodomain inhibition. *Cancer Discov.* **3**, 308–323 (2013).
73. Han, H. et al. Small-molecule MYC inhibitors suppress tumor growth and enhance immunotherapy. *Cancer Cell* **36**, 483–497.e15 (2019).
74. Berry, J. L. et al. Potential of aqueous humor as a surrogate tumor biopsy for retinoblastoma. *JAMA Ophthalmol.* **135**, 1221–1230 (2017).
75. Jung, M. et al. Cell-free SHOX2 DNA methylation in blood as a molecular staging parameter for risk stratification in renal cell carcinoma patients: a Prospective Observational Cohort study. *Clin. Chem.* **65**, 559–568 (2019).
76. Slembrouck-Brec, A., Nanteau, C., Sahel, J.-A., Goureau, O. & Reichman, S. Defined xeno-free and feeder-free culture conditions for the generation of human iPSC-derived retinal cell models. *J. Vis. Exp.* **139**, 57795 (2018).
77. Gagliardi, G. et al. Characterization and transplantation of CD73-positive photoreceptors isolated from human iPSC-derived retinal organoids. *Stem Cell Rep.* **11**, 665–680 (2018).
78. Irizarry, R. A. et al. Exploration, normalization, and summaries of high density oligonucleotide array probe level data. *Biostatistics* **4**, 249–264 (2003).
79. Dai, M. et al. Evolving gene/transcript definitions significantly alter the interpretation of GeneChip data. *Nucleic Acids Res.* **33**, e175 (2005).
80. Biton, A., Zinoviyev, A., Barillot, E. & Radvanyi, F. *MineICA: Independent Component Analysis of Transcriptomic Data* (2013).
81. Nordhausen, K., Gutch, H. W., Oja, H. & Theis, F. J. in *Latent Variable Analysis and Signal Separation* (eds Theis, F., Cichocki, A., Yeredor, A. & Zibulevsky, M.) 172–179 (Springer Berlin Heidelberg, 2012).
82. Bibikova, M. et al. High density DNA methylation array with single CpG site resolution. *Genomics* **98**, 288–295 (2011).
83. Aryee, M. J. et al. Minfi: a flexible and comprehensive Bioconductor package for the analysis of Infinium DNA methylation microarrays. *Bioinformatics* **30**, 1363–1369 (2014).
84. Popova, T. et al. Genome Alteration Print (GAP): a tool to visualize and mine complex cancer genomic profiles obtained by SNP arrays. *Genome Biol.* **10**, R128 (2009).
85. Idbaih, A. et al. Two types of chromosome 1p losses with opposite significance in gliomas. *Ann. Neurol.* **58**, 483–487 (2005).
86. Neuvial, P. et al. Spatial normalization of array-CGH data. *BMC Bioinformatics* **7**, 1–20 (2006).
87. Hupé, P., Stransky, N., Thiery, J.-P., Radvanyi, F. & Barillot, E. Analysis of array CGH data: from signal ratio to gain and loss of DNA regions. *Bioinformatics* **20**, 3413–3422 (2004).
88. Guichard, C. et al. Integrated analysis of somatic mutations and focal copy-number changes identifies key genes and pathways in hepatocellular carcinoma. *Nat. Genet.* **44**, 694–698 (2012).
89. Untergasser, A. et al. Primer3Plus, an enhanced web interface to Primer3. *Nucleic Acids Res.* **35**, W71–W74 (2007).
90. Mermel, C. H. et al. GISTIC2.0 facilitates sensitive and confident localization of the targets of focal somatic copy-number alteration in human cancers. *Genome Biol.* **12**, R41 (2011).
91. Venkatraman, E. S. & Olshen, A. B. A faster circular binary segmentation algorithm for the analysis of array CGH data. *Bioinformatics* **23**, 657–663 (2007).
92. Li, H. & Durbin, R. Fast and accurate short read alignment with Burrows-Wheeler transform. *Bioinformatics* **25**, 1754–1760 (2009).
93. Cibulskis, K. et al. Sensitive detection of somatic point mutations in impure and heterogeneous cancer samples. *Nat. Biotechnol.* **31**, 213–219 (2013).
94. Van der Auwera, G. A. et al. From FastQ data to high confidence variant calls: the Genome Analysis Toolkit best practices pipeline. *Curr. Protoc. Bioinformatics* **43**, 11.10.1–11.10.33 (2013).
95. DePristo, M. A. et al. A framework for variation discovery and genotyping using next-generation DNA sequencing data. *Nat. Genet.* **43**, 491–498 (2011).
96. McKenna, A. et al. The Genome Analysis Toolkit: a MapReduce framework for analyzing next-generation DNA sequencing data. *Genome Res.* **20**, 1297–1303 (2010).
97. Koboldt, D. C. et al. VarScan 2: somatic mutation and copy number alteration discovery in cancer by exome sequencing. *Genome Res.* **22**, 568–576 (2012).
98. Yang, H. & Wang, K. Genomic variant annotation and prioritization with ANNOVAR and wANNOVAR. *Nat. Protoc.* **10**, 1556–1566 (2015).
99. Thorvaldsdóttir, H., Robinson, J. T. & Mesirov, J. P. Integrative Genomics Viewer (IGV): high-performance genomics data visualization and exploration. *Brief. Bioinformatics* **14**, 178–192 (2013).
100. Smyth, G. K. *limma: Linear Models for Microarray Data. Bioinformatics and Computational Biology Solutions Using R and Bioconductor* 397–420 (Springer, New York, 2005).
101. Yu, G., Wang, L.-G., Han, Y. & He, Q.-Y. clusterProfiler: an R package for comparing biological themes among gene clusters. *OMICS* **16**, 284–287 (2012).
102. Merico, D., Isserlin, R., Stueker, O., Emili, A. & Bader, G. D. Enrichment map: a network-based method for gene-set enrichment visualization and interpretation. *PLoS ONE* **5**, e13984 (2010).
103. Subramanian, A. et al. Gene set enrichment analysis: a knowledge-based approach for interpreting genome-wide expression profiles. *Proc. Natl Acad. Sci. USA* **102**, 15545–15550 (2005).
104. Liao, J.-L. et al. Molecular signature of primary retinal pigment epithelium and stem-cell-derived RPE cells. *Hum. Mol. Genet.* **19**, 4229–4238 (2010).
105. Desper, R. & Gascuel, O. Fast and accurate phylogeny reconstruction algorithms based on the minimum-evolution principle. *J. Comput. Biol.* **9**, 687–705 (2002).
106. Waltman, L. & van Eck, N. J. A smart local moving algorithm for large-scale modularity-based community detection. *Eur. Phys. J. B* **86**, 471 (2013).
107. Aran, D. et al. Reference-based analysis of lung single-cell sequencing reveals a transitional profibrotic macrophage. *Nat. Immunol.* **20**, 163–172 (2019).
108. Mabbott, N. A., Baillie, J. K., Brown, H., Freeman, T. C. & Hume, D. A. An expression atlas of human primary cells: inference of gene function from coexpression networks. *BMC Genomics* **14**, 632 (2013).
109. Liu, J. et al. Source codes for “A high-risk retinoblastoma subtype with stemness features, dedifferentiated cone states and neuronal/ganglion cell gene expression”. *GitHub* <https://doi.org/10.5281/zenodo.5164167> (2021).
110. Liu, J. et al. Source codes of visualisation tool for “A high-risk retinoblastoma subtype with stemness features, dedifferentiated cone states and neuronal/ganglion cell gene expression”. *GitHub* <https://doi.org/10.5281/zenodo.5163255> (2021).

## Acknowledgements

We thank Cécile Reyes and Aude Vieillefon from the Genomics platform, Benoît Albaud from the NGS platform at the Institut Curie (IC), Emmanuel Martin from Integragen for sequencing, and Nadège Gruel (IC) for her help in the single-cell experiments. We thank Dr. Jelena Martinovic and Prof. Alexandra Benachi from Béclère Hospital, Dr. M. Eugenia Riveiro from OTD Oncology, and Pr. Daniel Louvard from IC for their help with this work. M.E.S. was supported by fellowships from the French MESRI and the IC, D.O. by the SFCE, the IC, and the AMCC, J.L. by the Fondation ARC, C.D. by the Barletta Foundation, Clé.H. by La Ligue Contre le Cancer. A.M.C. was funded by ISCii-FEDER (CP13/00189). This work was supported by the Retinostop Association, the Barletta Foundation, the INCa, and the INSERM in the framework of an ICGC project

(<https://icgc.org/icgc/cgp/62/355/1002881>), the IC, the ICGex Equipex program, the INCa/UNADEV, the SFCE, the FES, the Association l'Etoile de Martin, the ANR in the framework of LabEx LIFESENSES (ANR-10-LABX-65), and IHU FOReSIGHT (ANR-18-IAHU-01), the XBTC sponsored by Pla Director d'Oncologia de Catalunya.

### Author contributions

Resources: L.L.L.-R., A.M., L.D., J.C.-M., H.S., H.B., F.r.D., A.M.C., N.C., G.C. and I.A. (clinical data); F.L., G.L., P.F., Ma.S., X.S.G., A.M.C. and G.C. (pathological data); Ca.D., J.C., M.G.-V., D.S.-L., L.G. and Cla.H. (genetic data); R.A., F.L., G.L., O.M. and G.P.-P. (RNA, DNA preparation). Investigation: A.N., Céd., C.P., D.D., D.G., D.O., I.B.-P., J.C., J.G., J.L., L.M.O., F.I.D., F.N., M.L., N.K., N.S., O.G., P.S., R.A., S.A., S.B. and S.R. Methodology: E.C., Clé.H. and C.B. (development of visualization tools). Formal analysis (bioinformatics and statistical analyses): J.L., Me.S., E.C., L.T., Clé.H., A.B., C.B., T.P., S.G., C.V., E.B., E.L., A.V. and A.d.R. Data curation: E.C. and N.E. Conceptualization: J.L., D.O., Me.S., I.B.P., S.S., X.S.-G., Fr.D., N.C., C.P., O.G., G.C., A.d.R., I.A. and F.R. Visualization: J.L., D.O., Me.S., E.C., R.A., N.S., Clé.H., F.N., E.L., C.P., G.C., A.d.R. and F.R. Writing—original draft: J.L., D.O., Me.S., G.C., A.d.R. and F.R. Writing—review and editing: all authors. Funding acquisition: Me.S., Fr.D., O.G., G.C. and F.R. Supervision: A.M.C., G.C., A.d.R., I.A. and F.R. We thank the patients and their families for participating in this study.

### Competing interests

The authors declare no competing interests.

### Additional information

**Supplementary information** The online version contains supplementary material available at <https://doi.org/10.1038/s41467-021-25792-0>.

**Correspondence** and requests for materials should be addressed to François Radvanyi.

**Peer review information** *Nature Communications* thanks Quan Nguyen and the other, anonymous, reviewer(s) for their contribution to the peer review of this work. Peer reviewer reports are available.

**Reprints and permission information** is available at <http://www.nature.com/reprints>

**Publisher's note** Springer Nature remains neutral with regard to jurisdictional claims in published maps and institutional affiliations.



**Open Access** This article is licensed under a Creative Commons Attribution 4.0 International License, which permits use, sharing, adaptation, distribution and reproduction in any medium or format, as long as you give appropriate credit to the original author(s) and the source, provide a link to the Creative Commons license, and indicate if changes were made. The images or other third party material in this article are included in the article's Creative Commons license, unless indicated otherwise in a credit line to the material. If material is not included in the article's Creative Commons license and your intended use is not permitted by statutory regulation or exceeds the permitted use, you will need to obtain permission directly from the copyright holder. To view a copy of this license, visit <http://creativecommons.org/licenses/by/4.0/>.

© The Author(s) 2021

<sup>1</sup>Institut Curie, CNRS, UMR144, Equipe Labellisée Ligue contre le Cancer, PSL Research University, 75005 Paris, France. <sup>2</sup>Sorbonne Universités, UPMC Université Paris 06, CNRS, UMR144, 75005 Paris, France. <sup>3</sup>Programme Cartes d'Identité des Tumeurs, Ligue Nationale Contre le Cancer, 75013 Paris, France. <sup>4</sup>Precision Medicine, Hospital J.P. Garrahan, Buenos Aires, Argentina. <sup>5</sup>Pathology Service, Hospital J.P. Garrahan, Buenos Aires, Argentina. <sup>6</sup>Synergie Lyon Cancer, Plateforme de Bioinformatique "Gilles Thomas", Centre Léon Bérard, 69008 Lyon, France. <sup>7</sup>Département de Biologie des Tumeurs, Institut Curie, 75005 Paris, France. <sup>8</sup>Service de Génétique, Institut Curie, 75005 Paris, France. <sup>9</sup>Institut de la Vision, Sorbonne Université, INSERM, CNRS, 75012 Paris, France. <sup>10</sup>Institut Curie, PSL Research University, INSERM, U900, 75005 Paris, France. <sup>11</sup>École des Mines ParisTech, 77305 Fontainebleau, France. <sup>12</sup>Institut Curie, CNRS, UMR3347, PSL Research University, 91405 Orsay, France. <sup>13</sup>Institut Curie, PSL Research University, INSERM, U1021, 91405 Orsay, France. <sup>14</sup>Université Paris-Saclay, 91405 Orsay, France. <sup>15</sup>Institut Curie, PSL Research University, INSERM U830, 75005 Paris, France. <sup>16</sup>Département de Recherche Translationnelle, Institut Curie, 75005 Paris, France. <sup>17</sup>Institut Curie, PSL Research University, NGS Platform, 75005 Paris, France. <sup>18</sup>GeCo Genomics Consulting, Integrigen, 91000 Evry, France. <sup>19</sup>Département de Chirurgie, Service d'Ophtalmologie, Institut Curie, 75005 Paris, France. <sup>20</sup>Université de Paris, Paris, France. <sup>21</sup>Institut de Recerca Sant Joan de Déu, 08950 Barcelona, Spain. <sup>22</sup>Pediatric Hematology and Oncology, Hospital Sant Joan de Déu, 08950 Barcelona, Spain. <sup>23</sup>Department of Pathology, Hospital Sant Joan de Déu, 08950 Barcelona, Spain. <sup>24</sup>Department of Ophthalmology, Hospital Sant Joan de Déu, 08950 Barcelona, Spain. <sup>25</sup>National Scientific and Technical Research Council, CONICET, Buenos Aires, Argentina. <sup>26</sup>Département d'Imagerie Médicale, Institut Curie, 75005 Paris, France. <sup>27</sup>Centre de Recherche des Cordeliers, Sorbonne Universités, INSERM, 75006 Paris, France. <sup>28</sup>Functional Genomics of Solid Tumors, équipe labellisée Ligue Contre le Cancer, Université de Paris, Université Paris 13, Paris, France. <sup>29</sup>SIREDO Center (Care, Innovation and Research in Pediatric Adolescent and Young Adult Oncology), Institut Curie, 75005 Paris, France. <sup>30</sup>Present address: Institut Pasteur - Hub Bioinformatique et Biostatistique - C3BI, USR 3756 IP CNRS, 75015 Paris, France. <sup>31</sup>Present address: INSERM U930, CHU Bretonneau, 37000 Tours, France. <sup>32</sup>Present address: Department of Genetics, Rouen University Hospital, 76000 Rouen, France. <sup>33</sup>Present address: Department of Pathology, Centre Hospitalier Intercommunal de Créteil, 94000 Créteil, France. <sup>34</sup>These authors contributed equally: Jing Liu, Daniela Ottaviani, Meriem Sefta. <sup>35</sup>These authors jointly supervised this work: Guillermo Chantada, Aurélien de Reyniès, Isabelle Aerts, François Radvanyi. ✉email: [francois.radvanyi@curie.fr](mailto:francois.radvanyi@curie.fr)

### 3. Appendix 3 First author Book Chapter

***In Vivo Medulloblastoma Modeling.*** Mirabal-Ortega L., Larcher M., Morabito M., Foray C., Duvillié B., Eychène A., Pouponnot C. (2021) In: Seano G. (eds) Brain Tumors. Neuromethods, vol 158. Springer, New York (doi.org/10.1007/978-1-0716-0856-2\_2)

In this chapter of the Brain Tumors, Neuromethods book, I participated at the writing and reviewing process, to provide the readers with tools and information that allow MB tumors modeling *in vivo*. Here, we described how MB patient derived xenografts (PDXs) are cultured *in vitro* to allow genetic manipulation in these interesting models. We also provided information about the culture and genetic modification of granule cell progenitors (GCPs) isolated from the cerebellum. There is also a description of the protocols we used for retroviral production and infection of PDXs and GCPs. Last, we described the orthotopic grafting of either MB cell lines and PDXs or GCPs.



Neuromethods 158

Springer Protocols

Giorgio Seano *Editor*

# Brain Tumors

 Humana Press



## In Vivo Medulloblastoma Modeling

Liliana Mirabal-Ortega, Magalie Larcher, Morgane Morabito, Chloé Foray, Bertrand Duvillié, Alain Eychène, and Celio Pouponnot

### Abstract

Medulloblastoma (MB), the most frequent malignant brain tumor in children, is localized in the cerebellum. The standard care includes surgery, radiotherapy, and chemotherapy leading to an overall survival (OS) of 70–80%, but survivors suffer from severe side effects. Based on gene expression, MB is divided in four different molecular subgroups—WNT, SHH, Group 3 (G3), and Group 4 (G4)—which differ in terms of clinics, prognosis, genetic alterations, and cell of origin. The WNT group is characterized by the activation of the WNT/ $\beta$ -catenin signaling pathway and displays the best prognosis. The SHH group is driven by deregulation of the SHH signaling pathway and has an intermediate prognosis. G3 and G4 are less characterized. Contrary to the SHH and WNT groups, no specific alteration of a given signaling pathway has been described. G3 is the group with the worse prognosis. Few recurrent genetic alterations have been characterized including MYC amplification in less than 20% of G3 tumors. Nevertheless, all G3-MBs overexpress MYC through mechanisms not completely understood. G3-MBs also express an abnormal photoreceptor differentiation program found in the retina but not in the cerebellum during normal development. It has been shown that NRL and CRX, two master transcription factors (TF) of the photoreceptor lineage, are required for the establishment of this program as well as for G3 tumor maintenance. G4 has an intermediate prognosis, and the most frequent alteration is the overexpression of PRDM6. It has been recently proposed that this group could be driven by activation of an ERBB4-SRC signaling.

Established cell lines and patient-derived xenografts (PDXs) are available to study MB. The different groups of MB have also been modeled in vivo using either genetically engineered mouse models (GEMMs) or orthotopic transplantation of mouse cerebellar progenitors modified to overexpress oncogenes and/or to inactivate tumor suppressors. Here, we provide the readers with tools and information that allow MB modeling in vivo. We describe how to purify granular cell cerebellar progenitors or PDXs and to culture them in vitro in order to modulate gene expression by lentiviral infection. We provide protocols for the retrovirus production and infection. We also describe the experimental procedures for orthotopic grafting in the cerebellum, which is used to assess how genetic modifications alter in vivo tumor formation of reinjected modified PDX cells or GCPs.

**Key words** Medulloblastoma, Animal models, Patient-derived xenograft (PDX), Cerebellar progenitors, Cerebellum, Orthotopic grafting

## 1 Introduction

In developing countries, pediatric tumors are the second most frequent cause of death in children older than 1. Among childhood cancers, leukemia is the most prevalent, representing about 30% of the cases, while tumors of the central nervous system (CNS) are the most common solid tumors (20%) [1].

Medulloblastoma (MB) is a pediatric CNS tumor originating in the cerebellum. Although rare, it represents the most malignant brain tumor in childhood. It arises at a median age of 7, with more than 70% of patients that are below the age of 10, but it can be also diagnosed in adolescents and adults. Patients with MB present symptoms such as intracranial pressure, hydrocephalus, nausea, vomiting, and balance or motor coordination problems [2]. Different histological variants have been described including classic, desmoplastic, and large cells/anaplastic (LC/A) MB [3]. Metastases are found in ~30% of patients at diagnosis and are associated with a bad prognosis. They are mainly found in leptomeninges, although systemic metastases can be observed in very rare patients with advanced and highly treated disease [3].

The current standard care for MB patients is composed of surgery, followed by radiotherapy of the entire cranio-spinal axis and association of different chemotherapies. This treatment scheme is applied to all patients except infants below the age of 3, who are spared of radiotherapy due to the high toxicity on the developing brain. This heavy multimodal treatment has allowed reaching an overall survival (OS) of 80% but at the cost of severe side effects including neurological and cognitive deficits, endocrine disorders, hearing loss, and, possibly, secondary cancers [3]. When relapse is observed, very few therapeutic options remain and the outcome is almost always fatal [3].

### 1.1 The MB Groups

To better understand the disease and stratify patients, molecular analyses have established a novel classification of the disease. As expected and observed in many different cancers, inter-tumor heterogeneity has been uncovered. MB does not represent a single entity but gathers at least four distinct groups differing in their molecular and clinical characteristics, prognosis, and cell of origin [3, 4]. These four groups—WNT, SHH, Group 3 (G3), and Group 4 (G4)—have first been identified through transcriptomic analyses [5–8] and further validated by DNA methylation profiling [9] and proteomic analyses [10–12] (Table 2.1). Recently, three different studies have shown that each group could be further subdivided into subtypes providing a better prognostic value. However, the number and nature of these subtypes are variable between these studies, and no consensus has yet been reached [13–15].

**Table 2.1**

Main clinical and molecular features of medulloblastoma subgroups

	<b>WNT</b>	<b>SHH</b>	<b>G3</b>	<b>G4</b>
Age at diagnosis	Children and adults	Infants, children, and adults	Infants and children	Children and adults
Incidence	10–15%	25–30%	20–25%	35–40%
Metastasis at diagnosis	5–10%	20%	40–50%	35–40%
Overall survival (5 years)	Very good/95%	Intermediate/75%	Poor/50%	Intermediate/75%
Histology	Classic	Classic, desmoplastic, LC/A	Classic, LC/A	Classic, LC/A
Proposed cell of origin	Lower rhombic lip progenitors	Granule cell progenitors	Neural stem cells or Granule cell progenitors	Not yet determined
Main molecular drivers	<i>CTNNB1</i>	<i>PTCH1</i>	<i>MYC, GFII and GFIB</i>	PRDM6, SRC
Expression signature	WNT signaling	SHH signaling	Photoreceptor/GABAergic	Neuronal/glutamergic

### 1.1.1 The WNT Group

The WNT group, as highlighted by its name, is driven by the activation of the WNT/ $\beta$ -catenin signaling pathway. It represents 10–15% of all MBs and is usually found in older patients, adolescents and adults. WNT group displays the most favorable outcome with an OS at 5 years over 95%. It is in most cases of classic histology and is very rarely metastatic at diagnosis. Clinical trials are ongoing to evaluate whether treatment de-escalation could be an option in order to decrease side effects. It should be noticed that adult WNT-MBs have a less favorable outcome [3, 16]. Different pieces of evidence, including a genetically engineered mouse model (GEMM) based on the concurrent conditional expression of a mutant *Ctnnb1* (stabilized form of  $\beta$ -catenin) and inactivation of TP53, led to propose that the cell of origin of the WNT group is a lower rhombic lip progenitor residing in the brainstem outside the cerebellum [17].

### 1.1.2 The SHH Group

The SHH-MBs represent 25–30% of MB cases and are driven by deregulation of the cognate SHH signaling pathway. Metastases are found in 20% of SHH-MB at diagnosis. It is associated with the three main types of histology: desmoplastic, classic, and LC/A [3].

It should be emphasized that desmoplastic histology is mainly found in SHH-MBs and virtually absent in other groups and presents a better prognosis. This group is the most prevalent in infants below the age of 3 and in adults. It is less frequent in children and adolescents. Overall, it has an intermediate prognosis around 75% of survival. Within this group, OS can be refined according to the different subtypes recently described [13, 15]. Some SHH subtypes display an extremely bad prognosis, while others have a predictive very good outcome. The granule cell progenitors (GCPs), which are highly proliferative during postnatal cerebellar development, have been clearly demonstrated to be the cell of origin of SHH-MB [18, 19], and several mouse models have been generated by targeting genetic alterations in this cell type (see below).

While SHH and WNT groups are driven by the deregulation of specific signaling pathways, alterations that specifically drive G3 and G4 are much less characterized. Moreover, much less mutations and recurrent alterations are found in these two latter groups.

### 1.1.3 Group 3

G3 represents 20–25% of all MB cases and has the worse prognosis with a 5-year OS of 60%. These tumors usually occur in infants or young children. They display mainly a classic or LC/A histology and are highly metastatic at diagnosis (40–50%). Tumor recurrence is usually not found at the primary tumor bed but rather at metastatic sites [3]. While MYC amplification is found in less than 20% of G3, all G3-MBs express high levels of MYC through unknown mechanisms. Accordingly, G3 tumors are characterized by a MYC target gene signature with high expression of ribosomal genes, genes involved in mRNA processing, transcription, and translation [5, 6, 10, 11]. MYCN is also amplified in 5% of cases. Beside MYC amplification, GFII transcription factors (GFII and GFII B) are overexpressed in 15% of patients, mostly through enhancer hijacking mechanisms [20]. Their role as a codriver together with MYC has been validated using animal models [20, 21]. Moreover, G3 tumors display very surprising characteristics. They express a set of genes usually turned on specifically in the photoreceptor cells of the retina but never in the cerebellum [5, 6, 22]. Thus, G3 shows an aberrant identity unrelated to its tissue of origin, the cerebellum. We recently showed that NRL and CRX, two master transcription factors (TF) of the photoreceptor lineage, establish this aberrant identity. Importantly, they are also required for MB growth [22]. This challenges the widely accepted concept of lineage addiction, which postulates that cancer cells depend on the identity of a given cell lineage from which cancer grows. This work shows that cancer cells can be driven by an abnormal identity unrelated to its tissue of origin. As the SHH-MB, G3 have been further divided into subtypes with different clinical outcomes. Indeed, it has been shown that one subtype characterized by high MYC expression, including MYC amplified tumors, shows the worse prognosis [13]. The cell of origin of G3 tumors remains a

matter of debate. It has been suggested that G3 cells could arise either from CD133<sup>+</sup> cerebellar neural stem cells [23] or from the GCPs (see below).

#### 1.1.4 Group 4

G4 is the most prevalent MB group found in 35–40% of patients. Its histology is most frequently classic, but LC/A histology is also encountered at lower frequency. It is found in older patients, mainly older children, adolescents, and adults. It is of intermediate prognosis with an OS at 5 years around 75%. It is also frequently metastatic at diagnosis (35–40%), and, as in G3-MB, relapses are more frequent at metastatic sites [3]. The most frequent alteration, found in around 20% of cases, is an enhancer hijacking mechanism that leads to strong overexpression of PRDM6, a putative lysine-methyl transferase. PRDM6 alteration is considered as a putative driver event in G4, but its exact role has not been clearly demonstrated yet [14]. Recently, proteomic and phospho-proteomic studies have proposed that G4 could be driven by activation of an ERBB4-SRC signaling. The relevance of SRC activation has been further validated with the development of an animal model based on in utero electroporation and that displays some characteristics of G4 tumors [11].

## 1.2 MB Models

As in other cancers, established cell lines and patient-derived xenografts (PDX) are frequently used in the MB field. The different groups of MB have been modeled in vivo either by genetically engineered mouse models (GEMMs) or by orthotopic transplantation of modified mouse cerebellar progenitors manipulated to overexpress oncogenes and/or to inactivate tumor suppressors. In contrast, no patient-derived organoid has been established for MB so far, and, in contrast to glioblastoma, primary cultures from patient samples can be maintained for only very short term in MB and are not commonly used.

Interestingly, the stable expression of a Luciferase gene in all these models allowed a longitudinal follow-up of tumor growth upon orthotopic transplantation into the cerebellum of immunodeficient mice by bioluminescence quantification. This allows assessing the impact of gene overexpression, gene extinction, or drug treatment on tumor growth. We have used this system on cell lines or MB-PDX to demonstrate the role of the transcription factor NRL, a master regulator of photoreceptor development, on Group 3-MB growth [22].

In the following section, we will give a brief overview of some in vivo models used in the MB field. We do not attempt to provide an exhaustive description of them.

#### 1.2.1 Patient-Derived Xenografts

Patient-derived xenografts (PDX) have become a widely used model in cancer research since they are presumed to faithfully recapitulate the original tumors from which they derived. PDXs are established from fresh surgical MB material that is grafted subcuta-

neously or orthotopically directly into the cerebellum of immunocompromised mice (Nod Scid Gamma mice for the establishment). The PDXs are maintained *in vivo* by serial passages in immunodeficient mice either subcutaneously or in the cerebellum. It has been demonstrated that PDXs can be established from the different MB groups and remain stable across serial sub-transplantations [24] although some subclonal selection can occur [25]. Very recently, a biobank has been established allowing the availability of 15 MB PDXs including 1 WNT-MB, 4 SHH-MBs, 7 G3-MBs, and 3 G4-MBs [25]. Five out of the seven G3 PDXs harbor MYC amplification. The establishment rate for MB was around 35%. It should be noticed that PDXs have been mostly established from high-risk MBs indicating that aggressive tumors are more favorable to grow as PDXs. When compared to subcutaneous grafting, initial grafting in the cerebellum may be more efficient and might allow a better grafting efficiency for less aggressive tumors. Important information is provided on these PDXs including transcriptomic and whole-exome sequencing data: <https://research.fhcr.org/olson/en/btrl.html> and [https://hgserver1.amc.nl/cgi-bin/r2/main.cgi?&dscope=PDX\\_OLSON&option=about\\_dscope](https://hgserver1.amc.nl/cgi-bin/r2/main.cgi?&dscope=PDX_OLSON&option=about_dscope). PDX models have been used, for example, to validate important players in MB biology [22] or to investigate different potential therapies such as smoothed inhibitors in the SHH group [26], the CDK4/CDK6 Palbociclib inhibitor for SHH and G3 groups [27], or anti-BCL therapy in the G3 [22]. In Sect. 2.1, we provide the experimental procedure to short-term culture these PDXs in order to overexpress or downregulate gene expression by retroviral infection and to investigate how this genetic manipulation can affect tumor growth orthotopically.

### 1.2.2 Genetically Engineered Mouse Models (GEMMs)

Although highly time-consuming, laborious, and expensive, genetically engineered mouse models (GEMMs) have proven to be one of the most valuable tools in cancer research. Such models are based on the editing of the mouse genome, including gene deletion (knockout mice), gene mutation (knock-in mice), or gene overexpression (transgenic mice). In contrast to other models, GEMMs develop *de novo* tumors in their natural and immune proficient environment allowing to carefully study the different steps in tumorigenesis, from initiation to advanced cancer states [28]. GEMMs have allowed to validate different genetic drivers in MB as well as to identify the cell of origin of different groups, especially for the SHH and WNT groups.

These models have been widely used to study the SHH group. The first MB GEMM was described in 1997. It consists of PTCH1<sup>-/+</sup> mice that develop medulloblastoma at low frequency, in about 20% of cases. Noteworthy, these MBs have lost the second allele of PTCH1 [29]. This and other ubiquitous or conditional knockout mouse models have been widely used to validate differ-

ent cooperating oncogenic events in this group. Moreover, different conditional GEMMs have allowed to firmly establish that SHH-MB originates from GCPs and that a GCP identity is crucial for tumor formation [18, 19].

A unique GEMM has been described for the WNT tumors. Several observations support the fact that WNT-MB might arise outside the cerebellum, from cells in the dorsal brainstem, which originate from the lower rhombic lip [17]. Accordingly, a knock-in mice, in which the expression of an activated mutated form of  $\beta$ -catenin can be conditionally induced in different cell progenitors, have shown that activated  $\beta$ -catenin has no effect on cerebellar progenitors but induces abnormal accumulation of cells in the dorsal brainstem.

Using transgenic mice, it has been shown that NMYC overexpression in the cerebellum induces different types of MBs including G3, G4, and SHH [30, 31].

### 1.2.3 Orthotopic Transplantation of Modified/Transformed Cerebellar Progenitors

To get insights into the cell of origin of the G3 group, a model originally developed for SHH-MB by Dr. Roussel's laboratory has been used. This model relies on the modification of murine cerebellar progenitors that are then orthotopically grafted in animals. For the original SHH model, GCPs were purified from  $p53^{-/-}::Ink4C^{-/-}$  mice at early postnatal stages between p2 and p8, when these progenitors are still proliferating. Oncogenic hits such as overexpression of NMYC were introduced by retroviral infection. The resulting modified GCPs, when grafted into the cerebellum of immunocompromised mice, led to the formation of SHH-MB [32]. A modified experimental procedure allowed G3 tumor formation when other oncogenic combinations were used. For instance, the loss of p53 together with MYC (c-MYC) overexpression in GCPs forms G3-MB when transplanted into the cerebellum of nude mice. These results led to propose that GCPs may be the cell of origin of G3 [33].

Another model described for G3 is based on the retroviral transduction of another cerebellar cell population that expresses the neural stem cell (NSC) marker CD133 (prominin-1) [23]. It has been subsequently demonstrated that G3 tumors can be modeled when these cerebellar stem cells are engineered to overexpress a stabilized form of MYC together with a dominant negative form of p53 (DN-p53) and are subsequently transplanted in the cerebellum of NSG mice [23]. This model supports the idea that G3 may arise from CD133<sup>+</sup> cerebellar NSCs.

Noticeably, while these two types of modified progenitors could be in principle transplanted back into syngeneic mice, only immunodeficient animals were used as recipients in published reports. Indeed, our own data tend to indicate that transplantation in syngeneic animals is much less efficient for unknown reasons.

Moreover, since G3 can be modeled from different cerebellar progenitors or NSC, its cell of origin remains elusive. Even more provokingly, using in utero electroporation leading to overexpression of MYC and a dominant negative form of TP53, it has been shown that G3-MB can arise from different cerebellar progenitors. Thus, it has been proposed that G3-MB is mainly driven by specific oncogenic hits, in particular MYC overexpression, rather than its deregulation in a specific cell of origin [34].

It is important to mention that while all the above models indeed display G3 characteristics, they all combine MYC overexpression with p53 inactivation. However, neither p53 loss nor its mutation is found in G3 at diagnosis [3], questioning the relevance of these models. Nevertheless, these models were used to validate the driving role of GFI-1 TF in G3 tumors (see above). It has been shown that retroviral mediated overexpression of MYC together with GFI-1 both in CD133<sup>+</sup> cerebellar NSC [20] and in GCP [21] can induce G3-MB when transplanted. These models based on the in vitro transformation of GCPs by MYC and GFI1 are described in the following section.

---

## 2 Experimental Tools to Model and Study the Biology of MB In Vivo

In the following sections, we describe the short-term in vitro culture of PDXs that allows gene expression manipulation by retroviral infection. We next provide information on MB modeling using the modified GCP culture. We provide protocols for the purification of these cells and their culture conditions. We also describe retroviral production and infection allowing gene expression manipulation in PDXs and GCPs. Finally, we provide a description of the experimental procedure to perform orthotopic grafting in the cerebellum, which is used to reinject both PDXs cells and GCPs.

### 2.1 Patient-Derived Xenografts (PDXs)

Patient-derived xenograft (PDX) model constitutes an essential tool to study MB. It better recapitulates heterogeneity and molecular features of patient tumors compared to in vitro models. For PDX establishment, tumor tissues freshly isolated from untreated patients are inoculated into immunodeficient mice, usually NSG mice, where they can be maintained and serially passaged either subcutaneously or orthotopically in the cerebellum. Cells from these PDXs, when cultured in vitro, can be engineered to knock down (KD) or overexpress a given gene, whose role in MB can be subsequently studied. Once these modified cells are grafted either subcutaneously or orthotopically into the cerebellum of nude mice, it is possible to evaluate the effect of the expression of this specific gene in MB tumor biology. As an example of such an approach, we have shown that NRL, a master transcription factor

of the photoreceptor lineage in the retina, is critical for G3-MB maintenance [22]. To this end, cultures of different G3 PDXs were established, and cells from PDXs were manipulated using retroviruses to induce either NRL KD or overexpression. The effect of these modifications on MB tumor growth was then evaluated *in vivo*, by performing orthotopic grafting of PDX cells in nude mice, allowing us to establish NRL requirement for MB growth.

### 2.1.1 Short-Term *In Vitro* Cultures from PDXs

PDXs extracted from animals are processed to be short-term cultured to allow genetic modifications of the cells. PDXs are first grown in the fat pad neck of mice (NMRI nude mice, Janvier Labs) until they reach a volume of around 1.5 cm<sup>3</sup>. PDXs are extracted from freshly euthanized animals using sterile forceps, scalpels, and scissors. Once extracted, the PDX is placed in a Petri dish and any adjacent non-tumor or necrotic tissue should be removed. Using a scalpel, the tumor is cut in small pieces (around 3–4 mm<sup>3</sup>) that are then disaggregated by enzymatic digestion. To that end, pieces of tumor are covered by the dissociation buffer (2.5 mL of buffer containing Neurobasal medium (Gibco) supplemented with 1 mg/mL DNase (Worthington), 2.5 mg/mL Collagenase P (Roche), 2.5 mg/mL Collagenase/Dispase (Roche) and B27 supplement without vitamin A (Gibco)) and incubated at 37 °C for 30 min<sup>1</sup>. The suspension is filtered using a 40 µm cell strainer (Sigma) to remove debris. The cell strainer is then rinsed with 10 mL of Neurobasal medium and the filtrate is centrifuged at 520 g for 5 min. After centrifugation, the cell pellet is resuspended in a buffer containing 1 mL of Neurobasal medium supplemented with 0.5 mg/mL DNase, 0.35% D-Glucose (Sigma), and 2 mL of CMF-PBS pH 7.4 buffer (NaCl 0.14 M, KCl 4 mM, glucose 11.1 mM, NaH<sub>2</sub>PO<sub>4</sub> H<sub>2</sub>O 3.2 mM, KH<sub>2</sub>PO<sub>4</sub> 3.2 mM, NaHCO<sub>3</sub> 0.004%). The different cell populations are separated using discontinuous Percoll gradient (Sigma), constituted of two phases, Percoll 35% and Percoll 60%. Percoll dilutions are prepared in CMF-PBS-EDTA (2.5 mM final) buffer. Trypan blue solution 0.4% (Gibco) is added to the Percoll 60% solution to better visualize the cells. The 3 mL cell suspension is deposited on the top of the Percoll gradient and centrifuged at 1800 g for 13 min with minimal acceleration and break (Eppendorf Centrifuge 5810R). At the end of centrifugation, cells at the interface of Percoll 60–35% are collected and transferred into a 15 mL tube filled with CMF-PBS to obtain a final volume of 15 mL. Cells are then centrifuged at 520 g for 5 min to remove the remaining Percoll solution. Finally, cells are seeded at a concentration of  $2 \times 10^6$  cells/mL in low attachment Corning® flasks or plates to prevent adhesion since PDX cells are grown in neurosphere conditions. PDX MB primary cultures are maintained in Neurobasal medium (Gibco) supplemented with B27 supplement without vitamin A (Gibco), 0.012% BSA (Sigma), 1% penicillin/streptomycin, 1% L-glutamine

(Invitrogen), 12.5 ng/mL of human bFGF (Peprotech), and 12.5 ng/mL of human EGF (Peprotech)<sup>2</sup>. This culture can be subjected to retroviral infection after 2 h of incubation at 37 °C (see below for the description of the protocol).

## **2.2 Culture of Granular Cell Progenitors (GCPs)**

MYC is overexpressed in all G3 tumors, but, although necessary, it is not sufficient to give rise to G3-MB and therefore requires additional oncogenic hits. This was shown using the G3-MB mouse models based on orthotopic grafting of modified GCPs or cerebellar stem cells. Indeed, overexpression of MYC itself in these cells does not induce MB formation, while its combination with p53 inactivation or GFI-1 overexpression does [20, 21, 23, 33]. As described for the GFI-1 TFs, these models are particularly suited to validate novel G3 driver genes by testing their ability to cooperate with MYC to induce MB. For these models, GCPs need to be isolated, shortly cultured in vitro, and genetically manipulated to be then grafted into the cerebellum of mice. Here, we described how to perform these different steps.

### **2.2.1 Cerebella Dissection and GCP Isolation**

For cerebella dissection, pups (aged between P5 and P8) are decapitated, and the skin from the dorsal part of the head is removed using sterile scissors and forceps. The brain along the skull is dissociated from the rest of the head using forceps. The skull is then carefully removed by pulling it out from the front to the cerebellum, and the brain is transferred into a plate containing cold CMF-PBS. Meninges are scratched using very thin forceps under binocular loupes, paying attention not to damage the cerebellum, which is then separated from the rest of the brain. It is important to fully remove the meninges to avoid contamination of the GCP culture. All the manipulations should be performed at 4 °C.

After dissection, cerebella are transferred into polypropylene conical tubes (15 mL) (two or three cerebella per tube) containing 1 mL of a Trypsin/DNase solution (10 mg/mL Trypsin (Gibco), 1 mg/mL DNase, 0.006 M NaOH, 1.5 mg/mL MgSO<sub>4</sub> 7H<sub>2</sub>O) and incubated at 37 °C for 5 min. Then, the Trypsin/DNase solution is carefully removed, and the cerebella are resuspended in 1 mL of DNase solution (Neurobasal medium supplemented with 0.5 mg/mL DNase and 0.35% D-Glucose), and the tissue is mechanically dissociated by successively pipetting up and down with a 1000 µl micropipette and then with a syringe with 20G and, then, 23G needles. Each step is done approximately 15 times. The suspension is then centrifuged at 720 g for 5 min at 4 °C, the cell pellet is resuspended in 1 mL of the DNase solution described above, and 2 mL of CMF-PBS pH 7.4 buffer is then added. To separate the different cell types, the 3 mL cell suspension is centrifuged through a 35–60% Percoll gradient as described above (Sect. 2.1.1). The cell pellet is resuspended in 50 µL of DNase solution,

and then GCP culture medium (Neurobasal medium supplemented with B27 supplement, 1% penicillin/streptomycin, 0.2% Fungizone, 1% L-glutamine (Invitrogen), SPITE medium supplement (Sigma), 0.1 mM N-acetyl cysteine (Sigma), 0.45% D-glucose, oleic acid albumin/linoleic acid (Sigma)) is added. Cells are then plated in a 35-mm-diameter culture dish and incubated at 37 °C during a period of time between 45 min and 2 h. This step allows eliminating adherent cells, such as astrocytes, microglia, etc. Then, plates are gently flushed with a 1000  $\mu$ L micropipette in order to recover cells that are in suspension and slightly adherent. Cells are plated at  $2 \times 10^6$  GCPs/mL in culture medium containing 0.2  $\mu$ g/mL Sonic hedgehog (R&D Systems). Of note, GCPs in culture are quite fragile, making it difficult to keep viable cultures for several days<sup>3</sup>.

### **2.3 Retroviral Production**

PDX cells or GCP cultures can be subjected to lentiviral infection in order to overexpress or KD (shRNA-mediated gene silencing) genes as previously described [22]. The use of lentiviral systems for modifying cells involves the production of retroviral particles that encode the gene of interest. We use retroviral defective systems that allow gene overexpression (pMIGR (also named MIGR1) (addgene, <https://www.addgene.org/27490/>) or pMSCV vectors (addgene, <https://www.addgene.org/86537/>) or shRNA-mediated gene knockdown (pLKO vector (a shRNA library is available at SIGMA <https://www.sigmaaldrich.com/life-science/functional-genomics-and-rnai/shrna/library-information/vector-map.html>), a packaging vector (encoding the gag/pol gene) and a plasmid encoding the envelope gene. The pMIGR or pMSCV vectors contain an IRES that allows the translation of the gene of interest and the GFP gene from the same cistron. Infected cells can be FACS-sorted using this marker. Other derivatives of these vectors can be found with different markers including the luciferase gene allowing a noninvasive follow-up of tumor growth by bioluminescence imaging and quantification. This tracer is particularly useful when cells are orthotopically grafted in the brain or the cerebellum (see below). On the other hand, to induce stable KD of genes of interest, lentiviral particles are produced using the pLKO.1-TRC vector, commonly used for the expression of shRNAs. pLKO-based vectors contain a selectable marker, the puromycin resistance gene (other resistant genes being also available), making possible the selection of infected cells by adding the antibiotic to the culture media. The choice of the packaging vector and of the envelope encoding plasmid depends on the backbone vector and the species of the cells to be infected, respectively. For example, when using the pLKO vector to infect human PDXs, we used the psPAX and pMD2/VSVG plasmids. The latter allows producing amphotropic retroviral particles that can infect both human and rodent cells. For murine GCP culture, the pMIGR (or MIGR1)

together with the pCMV-Gag/Pol [35] and the pSV-E-MLV plasmids [36] is used. The latest plasmid encodes an ecotropic envelope allowing infection of mouse and rat cells. To produce retroviruses, HEK293T cells seeded at a density of  $1 \times 10^5$  cells/cm<sup>2</sup> are co-transfected with the three plasmids at a concentration of 0.066 µg/cm<sup>2</sup> (retroviral backbone vector), 0.09 µg/cm<sup>2</sup> (packaging vector), and 0.044 µg/cm<sup>2</sup> (env plasmid) using Invitrogen™ Lipofectamine™ 2000 Transfection Reagent, following manufacturer indications. Twenty-four hour post transfection, the media is replaced by a fresh harvest media that is normally used to cultivate the cells that will be infected. Viral particles are harvested at 48, 60, and 72 h after transfection by collecting the medium followed by filtration.

#### **2.4 Retroviral Infection of PDX Cells and GCPs**

To infect PDXs, 9 mL of a cell suspension is prepared at  $4 \times 10^6$  cells/mL and plated in T75 low-attaching flasks. Then, 1 mL of viral particles is added to cell culture.

For GCP infection, a cell suspension at  $2 \times 10^6$  cells/mL is plated at 500 µL/well in a 12-well plate and incubated 30 min at 37 °C. Then, 250 µL of viral suspension/well is added and plates are incubated 1 h and 30 min at 37 °C, followed by the addition of another 250 µL of viral suspension/well and an incubation for 1 h and 30 min at 37 °C. Then, 500 µL of media is removed and 250 µL of viral suspension/well is again added. SHH is added to cells at a final concentration of 0.2 µg/mL, and plates are incubated overnight at 37 °C. GCP media are then removed and replaced by fresh media. Cells can be further processed for transplantation in mice.

#### **2.5 Preparing Culture of PDX Cells and GCPs for Orthotopic Grafting**

Cells to be orthotopically grafted are flushed and harvested. They are washed twice by centrifugation and resuspended in CMF-PBS at an adequate concentration to be injected. For GCP,  $1 \times 10^6$  cells/5 µL/mice are used. For each PDX, adequate concentration shall be determined for reproducible tumor growth. We usually use  $3 \times 10^5$  cells/5 µL/mice for the G3 PDXs available in our lab.

#### **2.6 Orthotopic Grafting**

##### **2.6.1 Animal Preparation**

Orthotopic transplants are performed in 7–8-weeks-old NMRI nude female mice (Janvier Labs). Mice are acclimated to the animal facility at least 1 week before surgery. The grafting of tumor cells is performed under anesthesia. First, animals are anesthetized in an induction chamber (Anesthesia workstation AST-00, Anestéo) supplied with isoflurane (5%), compressed air (1 L/min), and O<sub>2</sub> (0.8 L/min). For surgery, mice are placed in a stereotaxic frame supplied with a microinjection system (PHYMED), while they are kept in inhalation masks (isoflurane 3–5%) (Fig. 2.1). Local anesthetic and analgesic are supplied before surgery such as bupivacaine (5 mg/mL, Aguettant) and Buprecare (0.3 mg/mL,

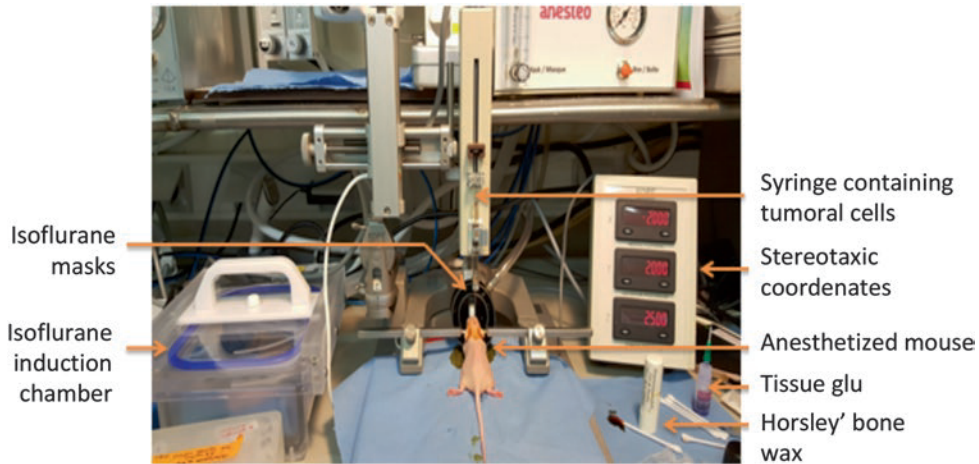


**Fig. 2.1** Stereotaxic surgery area and animal preparation. For anesthesia, mice are placed in an induction chamber supplied with isoflurane (5%), compressed air (1 L/min), and  $O_2$  (0.8 L/min). For the surgery, anesthetized animals are placed in a stereotaxic frame while kept in inhalation masks (isoflurane 3–5%), and the exact coordinates of injection are determined

Axiencie), respectively. During anesthesia, an adequate body temperature of animals is maintained using heated pads (Anestéo), while heated lamps (Anestéo) are used during the awakening phase.

### 2.6.2 Stereotaxic Surgery

As part of the preoperative care, mice receive an intraperitoneal injection of 50  $\mu\text{L}$  of Buprecare. The animal is positioned by hooking its incisors in the frame hold using ears bars. Once the animal is well fixed, additional local anesthetic is supplied: two injections of 30  $\mu\text{L}$  of bupivacaine is performed subcutaneously at the level of the skull around the site of incision. The skin of this area is disinfected with a Betadine solution (10%, MEDA Pharma), and then, using surgical sterile scissors, an incision is performed along the midline to expose the skull. The pericranial transparent tissues are scraped with the help of a sterile cotton tip. Then, the exact area of injection is determined using stereotaxic referent coordinates: a small hole in the skull is made using a 25G needle at 2 mm lateral and 2 mm posterior to the Lambda (Fig. 2.2). Then, a Hamilton syringe 1700 (10  $\mu\text{L}$ , 26 G) coupled to an automate injector is inserted in this emplacement, first to a depth of 3 mm and then raised to 2.5 mm to proceed with the injection of 5  $\mu\text{L}$  of cell suspension at a rate of 2.5  $\mu\text{L}/\text{min}$ . The syringe should remain in place for two additional minutes following injection and, then, gently removed<sup>4</sup>. The scission is closed using Horsley bone wax (SMI) and the skin is closed with tissue glu (Surgibond)<sup>5</sup>.

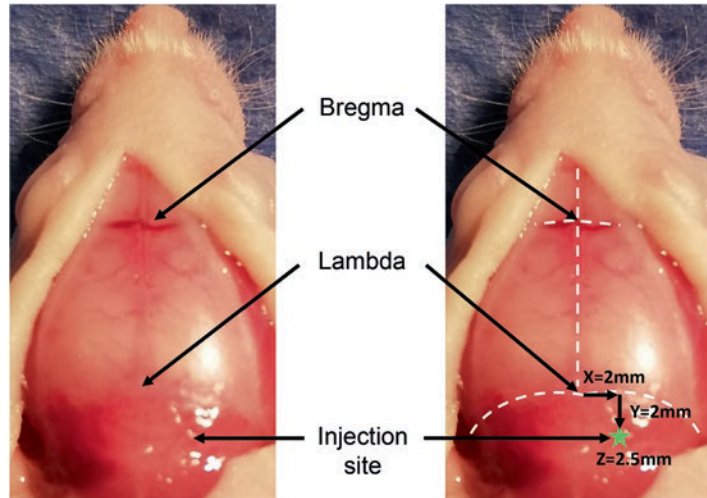


**Fig. 2.2** Site of injection for orthotopic grafting in the cerebellum. The site of injection is determined using the Lambda point as a reference. From here, stereotaxic coordinates are determined and cells are injected at 2 mm lateral (X) and 2 mm posterior (Y) to the Lambda and at a depth of 2.5 mm (Z)

## 2.7 *In Vivo* Bioluminescence Imaging Using IVIS

Cells orthotopically grafted in mice are engineered to express the luciferase gene, following infection with retrovirus encoding this gene (see above). This allows to follow tumor growth in a noninvasive manner using bioluminescence. Animals bearing tumor cells expressing the luciferase gene are injected with luciferin, the substrate of the luciferase enzyme. During oxidation of luciferin catalyzed by Luciferase, light is emitted. The photons are captured using an IVIS spectrum in vivo imaging system (Perkin Elmer), and images are subsequently analyzed using the Living Image software. The intensity of the signal is a direct measure of tumor size since Luciferase concentration (number of cells expressing the reporter gene) is linearly correlated to photon emission. Bioluminescence imaging and quantification are performed at different time points to follow tumor growth in a noninvasive manner. IVIS imaging of animals is performed under isoflurane anesthesia (2%), 15 min after an IP administration of luciferin (30 mg/mL 50  $\mu$ L, Perkin Elmer).

As mentioned above, genetic modifications of GCPs have been used in the field to investigate the different oncogenic hits cooperating with MYC to promote G3-MB formation. As an example, we present here the results obtained when GCPs overexpressing a stabilized form of MYC and GF11 using two pMIGR constructs are orthotopically grafted in the cerebellum of immunodeficient mice. One of the pMIGR construct coexpresses the Luciferase gene, allowing noninvasive follow-up of tumor growth by bioluminescence imaging (Fig. 2.3). Thus, grafted mice develop tumors that are detectable by bioluminescence from day 20 after surgery with

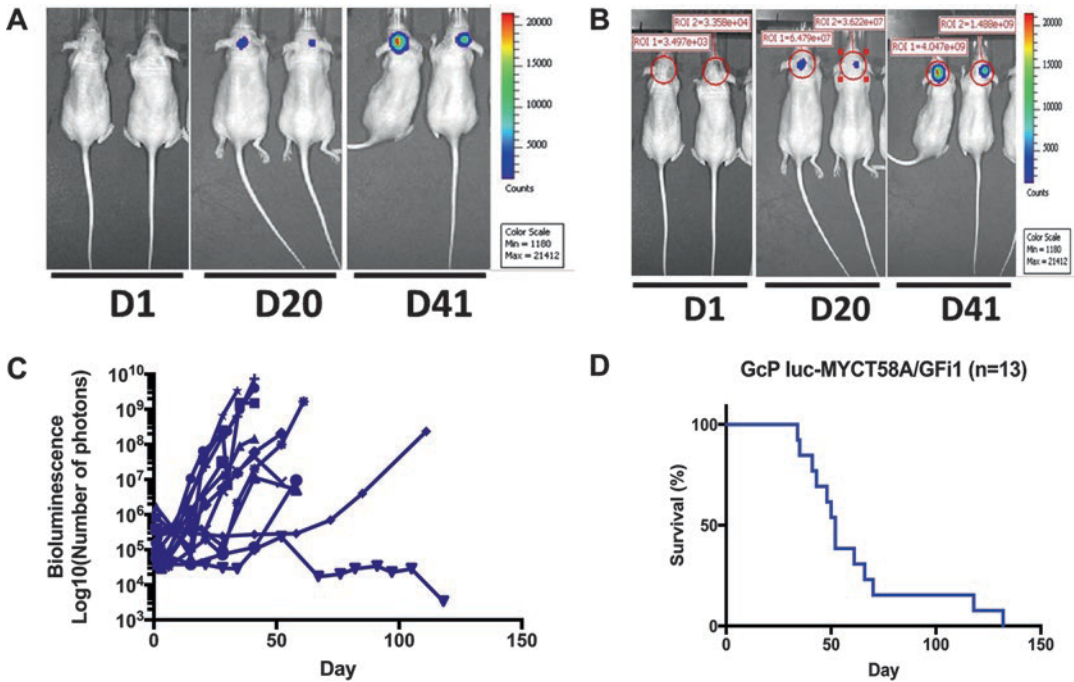


**Fig. 2.3** Orthotopic grafting of GCPs overexpressing MYC and GF11 leads to medulloblastoma formation in immunodeficient mice. (**a**, **b**) Tumor growth was followed by IVIS bioluminescence imaging. **A**. Images of luciferase signal in representative animals at the indicated days. (**b**) Representative images shown in **A** with the selected area of photon measurement (region of interest, ROI). (**c**) Number of photons measured as indicated in **B** for all the animals in the experiment ( $n = 12$ ) during time. (**d**) Kaplan-Meier survival curves of these animals

a signal increasing in time (Fig. 2.3a). Quantification of bioluminescent signal is performed using the Living Image software. All images obtained from each animal at the different time points are analyzed by measuring the amount of photons emitted. To that end, an area of quantification (red circle—region of interest (ROI)—Fig. 2.3b) is similarly applied to all mice in all images. This allows to measure the amount of photons emitted (Fig. 2.3b).

Photon emission is then plotted at given time points, to obtain the variation of the bioluminescence signal, indicating the size of the developing tumors (Fig. 2.3c). These types of experiments allow the follow-up of tumor growth without animal euthanasia. Animals are spared until they show clinical endpoints requiring euthanasia (Fig. 2.3d).

### 3 Troubleshooting

1. If tissue disaggregation is not satisfying after this step, the time of incubation could be increased and, in any case, should be optimized for each PDX.

2. PDX MB primary cultures can be maintained in culture for a limited period of time; any experimental procedure with these cultures should be planned taking into account this feature.
3. In order to obtain an adequate number of GCPs, the exact number of processed cerebella should be determined and optimized considering that cell yield depends on the mouse strain and pup age. In our conditions, the best results are obtained at P7. The dissection part could also be optimized to improve the final result.
4. Animal respiration should be monitored all along the surgery. If respiration seems laborious, with an inefficient rhythm or if it stops completely, remove the animal rapidly from the stereotaxic frame and install it in a warm surface. A tail massage, from the end of the tail to the body, can be performed in order to help blood circulation. The thorax can be also compressed repeatedly.
5. After surgery, recovery from anesthesia should be carefully monitored to detect any sign of suffering/distress. Possible symptoms after brain stereotaxic surgery could involve bowed head, reduced locomotion, or distress behaviors such as mice running in circle. In this case, animals should be isolated with minimal disturbance. If signs of pain are still detected the day after surgery, additional analgesic could be provided. If the mouse does not recover from these symptoms, euthanasia is required.

---

## 4 Conclusion

In conclusion, the experimental procedures presented here allow to study the role of different players in MB biology *in vivo*. For example, potential oncogenic hits that are susceptible to cooperate with MYC to induce MB can be validated and, more generally, specific groups of MB can be modeled.

---

## Acknowledgment

We thank members of our laboratory for helpful advice and comments. This work was supported by grants from Ligue Nationale Contre le Cancer (Val d'Oise 2019 - Oise-Yvelines #M18759, #M16649 and Legs Chovet), Institut National du Cancer (INCa, Pair Pédiatrie, Mr. ROBOT), the IRS "NanoTheRad" of University U-PSUD (Paris-Saclay), and Gefluc Ile de France, Association AIDA. LMO and MM were supported by a fellowship from the Ministère Français de l'Enseignement Supérieur, de la Recherche et de l'Innovation and Fondation ARC (fourth-year PhD fellowship).

## References

1. Ward E, DeSantis C, Robbins A, Kohler B, Jemal A (2014) Childhood and adolescent cancer statistics, 2014. *CA Cancer J Clin* 64:83–103. <https://doi.org/10.3322/caac.21219>
2. Dörner L, Fritsch MJ, Stark AM, Mehdorn HM (2007) Posterior fossa tumors in children: how long does it take to establish the diagnosis? *Childs Nerv Syst* 23:887–890. <https://doi.org/10.1007/s00381-007-0323-8>
3. Northcott PA, Robinson GW, Kratz CP, Mabbott DJ, Pomeroy SL, Clifford SC, Rutkowski S, Ellison DW, Malkin D, Taylor MD, Gajjar A, Pfister SM (2019) Medulloblastoma. *Nat Rev Dis Primers* 5:11. <https://doi.org/10.1038/s41572-019-0063-6>
4. Taylor MD, Northcott PA, Korshunov A, Remke M, Cho YJ, Clifford SC, Eberhart CG, Parsons DW, Rutkowski S, Gajjar A, Ellison DW, Lichter P, Gilbertson RJ, Pomeroy SL, Kool M, Pfister SM (2011) Molecular subgroups of medulloblastoma: the current consensus. *Acta Neuropathol* 123:465–472. <https://doi.org/10.1007/s00401-011-0922-z>
5. Cho YJ, Tsherniak A, Tamayo P, Santagata S, Ligon A, Greulich H, Berhoukim R, Amani V, Goumnerova L, Eberhart CG, Lau CC, Olson JM, Gilbertson RJ, Gajjar A, Delattre O, Kool M, Ligon K, Meyerson M, Mesirov JP, Pomeroy SL (2010) Integrative genomic analysis of medulloblastoma identifies a molecular subgroup that drives poor clinical outcome. *J Clin Oncol* 29:1424–1430. <https://doi.org/10.1200/JCO.2010.28.5148>
6. Kool M, Koster J, Bunt J, Hasselt NE, Lakeman A, van Sluis P, Troost D, Meeteren NS, Caron HN, Cloos J, Mrcic A, Ylstra B, Grajkowska W, Hartmann W, Pietsch T, Ellison D, Clifford SC, Versteeg R (2008) Integrated genomics identifies five medulloblastoma subtypes with distinct genetic profiles, pathway signatures and clinicopathological features. *PLoS One* 3:e3088. <https://doi.org/10.1371/journal.pone.0003088>
7. Northcott PA, Korshunov A, Witt H, Hielscher T, Eberhart CG, Mack S, Bouffet E, Clifford SC, Hawkins CE, French P, Rutka JT, Pfister S, Taylor MD (2010) Medulloblastoma comprises four distinct molecular variants. *J Clin Oncol* 29:1408–1414. <https://doi.org/10.1200/JCO.2009.27.4324>
8. Thompson MC, Fuller C, Hogg TL, Dalton J, Finkelstein D, Lau CC, Chintagumpala M, Adesina A, Ashley DM, Kellie SJ, Taylor MD, Curran T, Gajjar A, Gilbertson RJ (2006) Genomics identifies medulloblastoma subgroups that are enriched for specific genetic alterations. *J Clin Oncol* 24:1924–1931. <https://doi.org/10.1200/JCO.2005.04.4974>
9. Schwalbe EC, Williamson D, Lindsey JC, Hamilton D, Ryan SL, Megahed H, Garami M, Hauser P, Dembowska-Baginska B, Perek D, Northcott PA, Taylor MD, Taylor RE, Ellison DW, Bailey S, Clifford SC (2013) DNA methylation profiling of medulloblastoma allows robust subclassification and improved outcome prediction using formalin-fixed biopsies. *Acta Neuropathol (Berl)* 125:359–371. <https://doi.org/10.1007/s00401-012-1077-2>
10. Archer TC, Ehrenberger T, Mundt F, Gold MP, Krug K, Mah CK, Mahoney EL, Daniel CJ, LeNail A, Ramamoorthy D, Mertins P, Mani DR, Zhang H, Gillette MA, Clauser K, Noble M, Tang LC, Pierre-François J, Silterra J, Jensen J, Tamayo P, Korshunov A, Pfister SM, Kool M, Northcott PA, Sears RC, Lipton JO, Carr SA, Mesirov JP, Pomeroy SL, Fraenkel E (2018) Proteomics, post-translational modifications, and integrative analyses reveal molecular heterogeneity within medulloblastoma subgroups. *Cancer Cell* 34:396–410.e8. <https://doi.org/10.1016/j.ccell.2018.08.004>
11. Forget A, Martignetti L, Puget S, Calzone L, Brabetz S, Picard D, Montagud A, Liva S, Sta A, Dingli F, Arras G, Rivera J, Loew D, Besnard A, Lacombe J, Pagès M, Varlet P, Dufour C, Yu H, Mercier AL, Indersie E, Chivet A, Leboucher S, Sieber L, Beccaria K, Gombert M, Meyer FD, Qin N, Bartl J, Chavez L, Okonechnikov K, Sharma T, Thatikonda V, Bourdeaut F, Pouponnot C, Ramaswamy V, Korshunov A, Borkhardt A, Reifenberger G, Pouillet P, Taylor MD, Kool M, Pfister SM, Kawauchi D, Barillot E, Remke M, Ayrault O (2018) Aberrant ERBB4-SRC signaling as a hallmark of group 4 medulloblastoma revealed by integrative phosphoproteomic profiling. *Cancer Cell* 34:379–395.e7. <https://doi.org/10.1016/j.ccell.2018.08.002>
12. Rivero-Hinojosa S, Lau LS, Stampar M, Staal J, Zhang H, Gordish-Dressman H, Northcott PA, Pfister SM, Taylor MD, Brown KJ, Rood BR (2018) Proteomic analysis of medulloblastoma reveals functional biology with translational potential. *Acta Neuropathol Commun* 6:48. <https://doi.org/10.1186/s40478-018-0548-7>
13. Cavalli FMG, Remke M, Rampasek L, Peacock J, Shih DJH, Luu B, Garzia L, Torchia J, Nor C, Morrissy AS, Agnihotri S, Thompson YY, Kuzan-Fischer CM, Farooq H, Isaev K, Daniels

- C, Cho B-K, Kim S-K, Wang K-C, Lee JY, Grajkowska WA, Perek-Polnik M, Vasiljevic A, Faure-Conter C, Jouvett A, Giannini C, Nageswara Rao AA, Li KKW, Ng H-K, Eberhart CG, Pollack IF, Hamilton RL, Gillespie GY, Olson JM, Leary S, Weiss WA, Lach B, Chambless LB, Thompson RC, Cooper MK, Vibhakar R, Hauser P, van Veelen M-LC, Kros JM, French PJ, Ra YS, Kumabe T, López-Aguilar E, Zitterbart K, Sterba J, Finocchiaro G, Massimino M, Van Meir EG, Osuka S, Shofuda T, Klekner A, Zollo M, Leonard JR, Rubin JB, Jabado N, Albrecht S, Mora J, Van Meter TE, Jung S, Moore AS, Hallahan AR, Chan JA, Tirapelli DPC, Carlotti CG, Fouladi M, Pimentel J, Faria CC, Saad AG, Massimi L, Liau LM, Wheeler H, Nakamura H, Elbabaa SK, Perezpeña-Diazconti M, Chico Ponce de León F, Robinson S, Zapotocky M, Lassaletta A, Huang A, Hawkins CE, Tabori U, Bouffet E, Bartels U, Dirks PB, Rutka JT, Bader GD, Reimand J, Goldenberg A, Ramaswamy V, Taylor MD (2017) Intertumoral heterogeneity within medulloblastoma subgroups. *Cancer Cell* 31:737–754.e6. <https://doi.org/10.1016/j.ccell.2017.05.005>
14. Northcott PA, Buchhalter I, Morrissy AS, Hovestadt V, Weischenfeldt J, Ehrenberger T, Gröbner S, Segura-Wang M, Zichner T, Rudneva VA, Warnatz H-J, Sidiropoulos N, Phillips AH, Schumacher S, Kleinheinz K, Waszak SM, Erkek S, Jones DTW, Worst BC, Kool M, Zapatka M, Jäger N, Chavez L, Hutter B, Bieg M, Paramasivam N, Heinold M, Gu Z, Ishaque N, Jäger-Schmidt C, Imbusch CD, Jugold A, Hübschmann D, Risch T, Amstislavskiy V, Gonzalez FGR, Weber UD, Wolf S, Robinson GW, Zhou X, Wu G, Finkelstein D, Liu Y, Cavalli FMG, Luu B, Ramaswamy V, Wu X, Koster J, Ryzhova M, Cho Y-J, Pomeroy SL, Herold-Mende C, Schuhmann M, Ebinger M, Liau LM, Mora J, McLendon RE, Jabado N, Kumabe T, Chuah E, Ma Y, Moore RA, Mungall AJ, Mungall KL, Thiessen N, Tse K, Wong T, Jones SJM, Witt O, Milde T, Von Deimling A, Capper D, Korshunov A, Yaspo M-L, Kriwacki R, Gajjar A, Zhang J, Beroukheim R, Fraenkel E, Korbelt JO, Brors B, Schlesner M, Eils R, Marra MA, Pfister SM, Taylor MD, Lichter P (2017) The whole-genome landscape of medulloblastoma subtypes. *Nature* 547:311–317. <https://doi.org/10.1038/nature22973>
15. Schwalbe EC, Lindsey JC, Nakjang S, Crosier S, Smith AJ, Hicks D, Rafiee G, Hill RM, Iliasova A, Stone T, Pizer B, Michalski A, Joshi A, Wharton SB, Jacques TS, Bailey S, Williamson D, Clifford SC (2017) Novel molecular subgroups for clinical classification and outcome prediction in childhood medulloblastoma: a cohort study. *Lancet Oncol* 18:958–971. [https://doi.org/10.1016/S1470-2045\(17\)30243-7](https://doi.org/10.1016/S1470-2045(17)30243-7)
16. Wang J, Garancher A, Ramaswamy V, Wechsler-Reya RJ (2018) Medulloblastoma: from molecular subgroups to molecular targeted therapies. *Annu Rev Neurosci* 41:207–232. <https://doi.org/10.1146/annurev-neuro-070815-013838>
17. Gibson P, Tong Y, Robinson G, Thompson MC, Currle DS, Eden C, Kranenburg TA, Hogg T, Poppleton H, Martin J, Finkelstein D, Pounds S, Weiss A, Patay Z, Scoggins M, Ogg R, Pei Y, Yang ZJ, Brun S, Lee Y, Zindy F, Lindsey JC, Takeito MM, Boop FA, Sanford RA, Gajjar A, Clifford SC, Roussel MF, McKinnon PJ, Gutmann DH, Ellison DW, Wechsler-Reya RJ, Gilbertson RJ (2010) Subtypes of medulloblastoma have distinct developmental origins. *Nature* 468:1095–1099. <https://doi.org/10.1038/nature09587>
18. Schuller U, Heine VM, Mao J, Kho AT, Dillon AK, Han YG, Huillard E, Sun T, Ligon AH, Qian Y, Ma Q, Alvarez-Buylla A, McMahon AP, Rowitch DH, Ligon KL (2008) Acquisition of granule neuron precursor identity is a critical determinant of progenitor cell competence to form Shh-induced medulloblastoma. *Cancer Cell* 14:123–134. <https://doi.org/10.1016/j.ccr.2008.07.005>
19. Yang ZJ, Ellis T, Markant SL, Read TA, Kessler JD, Bourbonoulas M, Schuller U, Machold R, Fishell G, Rowitch DH, Wainwright BJ, Wechsler-Reya RJ (2008) Medulloblastoma can be initiated by deletion of patched in lineage-restricted progenitors or stem cells. *Cancer Cell* 14:135–145. <https://doi.org/10.1016/j.ccr.2008.07.003>
20. Northcott PA, Lee C, Zichner T, Stütz AM, Erkek S, Kawauchi D, Shih DJH, Hovestadt V, Zapatka M, Sturm D, Jones DTW, Kool M, Remke M, Cavalli FMG, Zuyderduyn S, Bader GD, VandenBerg S, Esparza LA, Ryzhova M, Wang W, Wittmann A, Stark S, Sieber L, Seker-Cin H, Linke L, Kratochwil F, Jäger N, Buchhalter I, Imbusch CD, Zipprich G, Raeder B, Schmidt S, Diessl N, Wolf S, Wiemann S, Brors B, Lawerenz C, Eils J, Warnatz H-J, Risch T, Yaspo M-L, Weber UD, Bartholomae CC, von Kalle C, Turányi E, Hauser P, Sanden E, Darabi A, Siesjö P, Sterba J, Zitterbart K, Sumerauer D, van Sluis P, Versteeg R, Volckmann R, Koster J, Schuhmann MU, Ebinger M, Grimes HL, Robinson GW, Gajjar A, Mynarek M, von Hoff K, Rutkowski S, Pietsch T, Scheurlen W, Felsberg J, Reifenberger G, Kulozik AE, von Deimling A, Witt O, Eils R, Gilbertson RJ, Korshunov A, Taylor MD,

- Lichter P, Korbel JO, Wechsler-Reya RJ, Pfister SM (2014) Enhancer hijacking activates GF11 family oncogenes in medulloblastoma. *Nature* 511:428–434. <https://doi.org/10.1038/nature13379>
21. Vo BT, Li C, Morgan MA, Theurillat J, Finkelstein D, Wright S, Hyle J, Smith SMC, Fan Y, Wang Y-D, Wu G, Orr BA, Northcott PA, Shilatifard A, Sherr CJ, Roussel MF (2017) Inactivation of Ezh2 upregulates Gfi1 and drives aggressive Myc-driven group 3 medulloblastoma. *Cell Rep* 18:2907–2917. <https://doi.org/10.1016/j.celrep.2017.02.073>
  22. Garancher A, Lin CY, Morabito M, Richer W, Rocques N, Larcher M, Bihannic L, Smith K, Miquel C, Leboucher S, Herath NI, Dupuy F, Varlet P, Haberler C, Walczak C, El Tayara N, Volk A, Puget S, Doz F, Delattre O, Druillennec S, Ayrault O, Wechsler-Reya RJ, Eychène A, Bourdeaut F, Northcott PA, Pouponnot C (2018) NRL and CRX define photoreceptor identity and reveal subgroup-specific dependencies in Medulloblastoma. *Cancer Cell* 33:435–449.e6. <https://doi.org/10.1016/j.ccell.2018.02.006>
  23. Pei Y, Moore CE, Wang J, Tewari AK, Eroshkin A, Cho YJ, Witt H, Korshunov A, Read TA, Sun JL, Schmitt EM, Miller CR, Buckley AF, McLendon RE, Westbrook TE, Northcott PA, Taylor MD, Pfister SM, Febbo PG, Wechsler-Reya RJ (2012) An animal model of MYC-driven medulloblastoma. *Cancer Cell* 21:155–167. <https://doi.org/10.1016/j.ccr.2011.12.021>
  24. Zhao X, Liu Z, Yu L, Zhang Y, Baxter P, Voicu H, Gurusiddappa S, Luan J, Su JM, Leung HE, Li X-N (2012) Global gene expression profiling confirms the molecular fidelity of primary tumor-based orthotopic xenograft mouse models of medulloblastoma. *Neuro Oncol* 14:574–583. <https://doi.org/10.1093/neuroonc/nos061>
  25. Brabetz S, Leary SES, Gröbner SN, Nakamoto MW, Şeker-Cin H, Girard EJ, Cole B, Strand AD, Bloom KL, Hovestadt V, Mack NL, Pakiam F, Schwalm B, Korshunov A, Balasubramanian GP, Northcott PA, Pedro KD, Dey J, Hansen S, Ditzler S, Lichter P, Chavez L, Jones DTW, Koster J, Pfister SM, Kool M, Olson JM (2018) A biobank of patient-derived pediatric brain tumor models. *Nat Med* 24:1752–1761. <https://doi.org/10.1038/s41591-018-0207-3>
  26. Kool M, Jones DTW, Jäger N, Northcott PA, Pugh TJ, Hovestadt V, Piro RM, Esparza LA, Markant SL, Remke M, Milde T, Bourdeaut F, Ryzhova M, Sturm D, Pfaff E, Stark S, Hutter S, Seker-Cin H, Johann P, Bender S, Schmidt C, Rausch T, Shih D, Reimand J, Sieber L, Wittmann A, Linke L, Witt H, Weber UD, Zapatka M, König R, Beroukhi R, Bergthold G, van Sluis P, Volckmann R, Koster J, Versteeg R, Schmidt S, Wolf S, Lawerenz C, Bartholomae CC, von Kalle C, Unterberg A, Herold-Mende C, Hofer S, Kulozik AE, von Deimling A, Scheurlen W, Felsberg J, Reifenberger G, Hasselblatt M, Crawford JR, Grant GA, Jabado N, Perry A, Cowdrey C, Croul S, Zadeh G, Korbel JO, Doz F, Delattre O, Bader GD, McCabe MG, Collins VP, Kieran MW, Cho Y-J, Pomeroy SL, Witt O, Brors B, Taylor MD, Schüller U, Korshunov A, Eils R, Wechsler-Reya RJ, Lichter P, Pfister SM, PedBrain Tumor Project ICGC (2014) Genome sequencing of SHH medulloblastoma predicts genotype-related response to smoothened inhibition. *Cancer Cell* 25:393–405. <https://doi.org/10.1016/j.ccr.2014.02.004>
  27. Cook Sangar ML, Genovesi LA, Nakamoto MW, Davis MJ, Knobluagh SE, Ji P, Millar A, Wainwright BJ, Olson JM (2017) Inhibition of CDK4/6 by Palbociclib significantly extends survival in medulloblastoma patient-derived Xenograft mouse models. *Clin Cancer Res* 23:5802–5813. <https://doi.org/10.1158/1078-0432.CCR-16-2943>
  28. Kersten K, de Visser KE, van Miltenburg MH, Jonkers J (2017) Genetically engineered mouse models in oncology research and cancer medicine. *EMBO Mol Med* 9:137–153. <https://doi.org/10.15252/emmm.201606857>
  29. Goodrich LV, Milenković L, Higgins KM, Scott MP (1997) Altered neural cell fates and medulloblastoma in mouse patched mutants. *Science* 277:1109–1113. <https://doi.org/10.1126/science.277.5329.1109>
  30. Swartling FJ, Grimmer MR, Hackett CS, Northcott PA, Fan QW, Goldenberg DD, Lau J, Masic S, Nguyen K, Yakovenko S, Zhe XN, Gilmer HC, Collins R, Nagaoka M, Phillips JJ, Jenkins RB, Tihan T, Vandenberg SR, James CD, Tanaka K, Taylor MD, Weiss WA, Chesler L (2010) Pleiotropic role for MYCN in medulloblastoma. *Genes Dev* 24:1059–1072. <https://doi.org/10.1101/gad.1907510>
  31. Swartling FJ, Savov V, Persson AI, Chen J, Hackett CS, Northcott PA, Grimmer MR, Lau J, Chesler L, Perry A, Phillips JJ, Taylor MD, Weiss WA (2012) Distinct neural stem cell populations give rise to disparate brain tumors in response to N-MYC. *Cancer Cell* 21:601–613. <https://doi.org/10.1016/j.ccr.2012.04.012>
  32. Zindy F, Uziel T, Ayrault O, Calabrese C, Valentine M, Rehg JE, Gilbertson RJ, Sherr CJ, Roussel MF (2007) Genetic alterations in mouse medulloblastomas and generation of tumors de novo from primary cerebellar gran-

- ule neuron precursors. *Cancer Res* 67:2676–2684. <https://doi.org/10.1158/0008-5472.CAN-06-3418>
33. Kawauchi D, Robinson G, Uziel T, Gibson P, Rehg J, Gao C, Finkelstein D, Qu C, Pounds S, Ellison DW, Gilbertson RJ, Roussel MF (2012) A mouse model of the most aggressive subgroup of human medulloblastoma. *Cancer Cell* 21:168–180. <https://doi.org/10.1016/j.ccr.2011.12.023>
34. Kawauchi D, Ogg RJ, Liu L, Shih DJH, Finkelstein D, Murphy BL, Rehg JE, Korshunov A, Calabrese C, Zindy F, Phoenix T, Kawaguchi Y, Gronych J, Gilbertson RJ, Lichter P, Gajjar A, Kool M, Northcott PA, Pfister SM, Roussel MF (2017) Novel MYC-driven medulloblastoma models from multiple embryonic cerebellar cells. *Oncogene* 36:5231–5242. <https://doi.org/10.1038/onc.2017.110>
35. Reya T, Duncan AW, Ailles L, Domen J, Scherer DC, Willert K, Hintz L, Nusse R, Weissman IL (2003) A role for Wnt signalling in self-renewal of haematopoietic stem cells. *Nature* 423:409–414. <https://doi.org/10.1038/nature01593>
36. Landau NR, Littman DR (1992) Packaging system for rapid production of murine leukemia virus vectors with variable tropism. *J Virol* 66:5110–5113

#### 4. Appendix 4 Co-author paper 3

***An autocrine ActivinB mechanism drives TGFb/Activin signaling in Group 3 medulloblastoma.*** Morabito M., Larcher M., Cavalli F., Foray C., Forget A., **Mirabal-Ortega L.**, Andrianteranagna M., Druillennec S., Garancher A., Masliah-Planchon J., Leboucher S., Debalkew A., Raso A., Delattre O., Puget S., Doz F., Taylor MD., Ayrault O., Bourdeaut F., Eychène A., Pouponnot C. (2019) EMBO Molecular Medecine (DOI 10.15252/emmm.201809830)

During the first year of my PhD I participated to the reviewing process of the work of a previous PhD student in the lab. Specifically, I was involved in the demonstration *in vitro* of the autocrine stimulation by Activin B in G3 and non-G3 cell lines and PDXs as well as the activation of PMEMPA1, a direct target of this pathway. I also participated to the experiments to evaluate the effect of Galunisertib, an inhibitor of this pathway, on G3 MB tumor growth *in vivo*.





# An autocrine ActivinB mechanism drives TGF $\beta$ /Activin signaling in Group 3 medulloblastoma

Morgane Morabito<sup>1,2,3,4,5</sup>, Magalie Larcher<sup>1,2,3,4,5</sup>, Florence MG Cavalli<sup>6,7</sup>, Chloé Foray<sup>1,2,3,4,5</sup>, Antoine Forget<sup>1,2,3,4,5</sup>, Liliana Mirabal-Ortega<sup>1,2,3,4,5</sup>, Mamy Andrianteranagna<sup>5,8,9,10,11,12,13</sup>, Sabine Druillennec<sup>1,2,3,4,5</sup>, Alexandra Garancher<sup>1,2,3,4,5</sup>, Julien Masliah-Planchon<sup>5,8,9,11</sup>, Sophie Leboucher<sup>1,4</sup>, Abel Debalkew<sup>6,7</sup>, Alessandro Raso<sup>14</sup>, Olivier Delattre<sup>5,8,9,11</sup>, Stéphanie Puget<sup>15,16</sup>, François Doz<sup>8,11,15</sup>, Michael D Taylor<sup>6,7,17,18</sup>, Olivier Ayrault<sup>1,2,3,4,5</sup>, Franck Bourdeaut<sup>5,8,9,10,11</sup>, Alain Eychène<sup>1,2,3,4,5</sup>  & Celio Pouponnot<sup>1,2,3,4,5,\*</sup> 

## Abstract

Medulloblastoma (MB) is a pediatric tumor of the cerebellum divided into four groups. Group 3 is of bad prognosis and remains poorly characterized. While the current treatment involving surgery, radiotherapy, and chemotherapy often fails, no alternative therapy is yet available. Few recurrent genomic alterations that can be therapeutically targeted have been identified. Amplifications of receptors of the TGF $\beta$ /Activin pathway occur at very low frequency in Group 3 MB. However, neither their functional relevance nor activation of the downstream signaling pathway has been studied. We showed that this pathway is activated in Group 3 MB with some samples showing a very strong activation. Beside genetic alterations, we demonstrated that an ActivinB autocrine stimulation is responsible for pathway activation in a subset of Group 3 MB characterized by high PMEPA1 levels. Importantly, Galunisertib, a kinase inhibitor of the cognate receptors currently tested in clinical trials for Glioblastoma patients, showed efficacy on orthotopically grafted MB-PDX. Our data demonstrate that the TGF $\beta$ /Activin pathway is active in a subset of Group 3 MB and can be therapeutically targeted.

**Keywords** activin; medulloblastoma; Smad2; Smad3; TGFbeta

**Subject Category** Cancer

**DOI** 10.15252/emmm.201809830 | Received 19 September 2018 | Revised 28

June 2019 | Accepted 2 July 2019 | Published online 22 July 2019

**EMBO Mol Med (2019) 11: e9830**

## Introduction

Medulloblastoma (MB), a cerebellar tumor, is one of the most common malignant brain tumors in children (Holgado *et al*, 2017; Wang *et al*, 2018). Current therapy associates surgery, chemotherapy, and radiotherapy. This aggressive regimen allowed an increase in the overall survival rate up to 70–80% but induces dramatic long-term side effects (Martin *et al*, 2014). In addition, the overall survival rate of high-risk patients is far below (Holgado *et al*, 2017; Wang *et al*, 2018). It is therefore crucial to identify new treatments that decrease side effects and improve efficacy.

Genomic and transcriptomic approaches allowed the stratification of MB patients into 4 different molecular groups: WNT (Wingless), SHH (Sonic Hedgehog), Group 3, and Group 4 (Northcott *et al*, 2012a; Taylor *et al*, 2012). These groups display differences in

1 Institut Curie, Orsay, France

2 INSERM U1021, Centre Universitaire, Orsay, France

3 CNRS UMR 3347, Centre Universitaire, Orsay, France

4 University Paris Sud – Paris-Saclay, Orsay, France

5 PSL Research University, Paris, France

6 The Arthur and Sonia Labatt Brain Tumour Research Center, The Hospital for Sick Children, Toronto, ON, Canada

7 Developmental and Stem Cell Biology Program, The Hospital for Sick Children, Toronto, ON, Canada

8 Institut Curie, Paris, France

9 INSERM U830, Paris, France

10 Translational Research in Pediatric Oncology, Institut Curie SiRIC, Paris, France

11 SIREDO Center (Care, innovation, Research in pediatric, adolescent and young adult oncology), Institut Curie, Paris, France

12 INSERM, U900, Paris, France

13 MINES ParisTech, CBIO-Centre for Computational Biology, Paris, France

14 Department of Patology, ASL 3 Genovese, SC Laboratorio d'Analisi, Genova, Italy

15 Université Paris Descartes, Sorbonne Paris Cité, Paris, France

16 Département Neurochirurgie Pédiatrique, AP-HP, Hôpital Necker-Enfants Malades, Paris, France

17 Department of Laboratory Medicine and Pathobiology, University of Toronto, Toronto, ON, Canada

18 Division of Neurosurgery, The Hospital for Sick Children, Toronto, ON, Canada

\*Corresponding author. Tel: +33 1 69 86 30 79; Fax: +33 1 69 86 30 51; E-mail: celio.pouponnot@curie.fr

terms of cell of origin, transcriptional, epigenetic, and mutational signatures. They also differ in their clinical characteristics such as histology, overall survival rate, and presence of metastases. Recently, intragroup heterogeneity has been further uncovered, allowing their division into subtypes with some specific clinical parameters as well as genomic alterations (Cavalli *et al*, 2017a; Northcott *et al*, 2017; Schwalbe *et al*, 2017). Although the existence of subdivisions within the different groups is clear, the outlines of the different subtypes have not completely reached a consensus so far. The WNT group represents 10% of all MBs and is driven by constitutive activation of the WNT/ $\beta$ -catenin pathway with patients showing the best prognosis. The SHH group accounts for 20–25% of MB and is characterized by mutations involving different mediators of the SHH pathway. It is considered of intermediate prognosis. However, recent sub-classifications identified SHH subtypes with poorer outcomes (Cavalli *et al*, 2017a; Schwalbe *et al*, 2017). On the other side, Group 3 and Group 4 are far less characterized due to their genetic and clinical heterogeneity. They display some degrees of overlap with a few samples (~10%) being difficult to specifically assign to either Group. They share some clinical characteristics, such as a high propensity to metastasis and genetic alterations such as *OTX2* amplifications or *KBTBD4* mutations (Northcott *et al*, 2017). In contrast to SHH and WNT groups, no deregulation of a given signaling pathway has been yet reported. Group 4 represents 35–40% of all MB patients and shows, in few cases, *MYCN* and *CDK6* amplifications and *KDM6A* mutations. Recently, it has been shown that genomic alterations involving enhancer hijacking induce *PRDM6* overexpression in 15–20% of Group 4 (Northcott *et al*, 2017). Group 3 represents 20–25% of MB patients and is associated with bad prognosis. This group is highly metastatic and characterized by *MYC* overexpression, which can be explained in 15–20% of cases by its amplification. However, *MYC* overexpression is not sufficient to induce Group 3 MB and requires additional cooperating oncogenic events (Kawauchi *et al*, 2012; Pei *et al*, 2012). Some of them have been identified, such as *GFI1* and *GFI1B* that are highly expressed in a subset of Group 3 through enhancer hijacking (Northcott *et al*, 2014). These transcription factors have been demonstrated to drive Group 3 MB tumorigenesis in animal models when associated with *MYC* overexpression (Northcott *et al*, 2014). At the transcriptomic level, Group 3 is characterized by the expression of a photoreceptor program defined by genes whose expression is highly restricted to the retina (Kool *et al*, 2008; Cho *et al*, 2011). We recently uncovered that this program defines a subtype within Group 3 tumors, which exhibits a functional dependency to this ectopic program through its two main drivers, the retina-specific transcription factors *NRL* and *CRX* (Garancher *et al*, 2018). Thus, Group 3 can be subdivided into 2–3 different subtypes according to the different studies (Cavalli *et al*, 2017a; Northcott *et al*, 2017; Schwalbe *et al*, 2017). Cavalli *et al* (2017a) have identified 3 subtypes, one is composed of tumors with high *MYC* expression including those with amplification of this gene, named G3 $\gamma$ . This subtype has the worse prognosis. The second subtype, G3 $\beta$ , is over-represented by tumors with *GFI1* alterations, and the last one G3 $\alpha$ , by tumors expressing photoreceptor genes in which few amplifications of mediators of the TGF $\beta$ /Activin pathway can be found (Cavalli *et al*, 2017a). Since Group 3 displays the worse prognosis, targeted therapies are actively searched. Different actionable targets have been proposed mainly based on genomic data, including the

TGF $\beta$  signaling, which has been suggested to be deregulated in few Group 3 MB, although no functional data have been reported so far. A study on structural genomic variations across over 1,000 MB has first described few amplifications of different mediators of the TGF $\beta$ /Activin pathway in Group 3 MB (Northcott *et al*, 2012b). They include *ACVR2A* and *ACVR2B*, two type II receptors for Activin, as well as *TGFBR1*, a type I receptor for TGF $\beta$ , highlighting a potential deregulation of Smad2/3 signaling (see below). Additionally, since *OTX2* has been demonstrated to be a target gene of this signaling pathway (Jia *et al*, 2009), it has been proposed that *OTX2* amplifications could represent a mechanism by which the pathway is also deregulated downstream (Northcott *et al*, 2012b). The putative significance of this signaling pathway in Group 3 was reinforced by two subsequent studies, one involving sequencing in a large cohort of MB (Northcott *et al*, 2017) and the other showing that several components of this signaling pathway could also be deregulated at their expression level, through Group 3-specific enhancers (Lin *et al*, 2016). Although these studies might indicate a potential deregulation of the Smad2/3 signaling pathway, this could account for only a modest proportion of Group 3 tumors.

The TGF $\beta$  superfamily is a large family of cytokines divided into two distinct groups of ligands: the TGF $\beta$ s/Activins and the BMPs. TGF $\beta$ /Activin ligands signal through Smad2/3. These ligands bring together two types of serine/threonine kinase receptors, the type I and the type II, which are specific for a set of ligands. The TGF $\beta$ s (TGF $\beta$ 1, TGF $\beta$ 2, and TGF $\beta$ 3) signal through the TGFBR1 type I and TGFBR2 type II receptors. Activin, encoded by 4 different genes, *INHBA*, *INHBB*, *INHBC*, and *INHBE*, can activate different couples of receptors including the *ACVR2A* and *ACVR2B* type II and *ACVR1A* (ALK4) and *ACVR1C* (ALK7) type I receptors. *INHA*, encoding inhibin- $\alpha$ , is an inhibitor of the Activin ligands. Activin and TGF $\beta$  ligands lead to the phosphorylation and activation of the same intracellular mediators, Smad2 and Smad3, which then associate with the co-Smad, Smad4. The hetero-complex translocates to the nucleus, where it activates the transcription of target genes with the help of DNA binding partners (Levy & Hill, 2006; Ross & Hill, 2008).

TGF $\beta$ /Activin signaling displays pleiotropic functions depending on the cellular and environmental context. Its implication in cancer has been well documented, mainly through TGF $\beta$  ligands, although BMPs and Activins ligands can be also involved (Seoane & Gomis, 2017). The role of the TGF $\beta$  signaling pathway in cancer is complex, acting either as a tumor suppressor pathway in some instances or as a tumor promoter in others (Massagué, 2008; Seoane & Gomis, 2017). Its oncogenic role is mainly associated with an autocrine (or paracrine) stimulation, due to the strong expression of TGF $\beta$  ligands. The TGF $\beta$  pathway has been shown to promote cell proliferation in specific context such as in Glioblastoma (Bruna *et al*, 2007) and cancer stem cell maintenance (Peñuelas *et al*, 2009; Anido *et al*, 2010; Lonardo *et al*, 2011). Studies on the role of Activin ligands in cancer are much more scarce (Wakefield & Hill, 2013). By activating the same mediators Smad2/3, a parallel can be drawn between TGF $\beta$  and Activin. Indeed, Activins act both as tumor suppressors and tumor promoters (Chen *et al*, 2002; Antsiferova & Werner, 2012; Marino *et al*, 2013; Wakefield & Hill, 2013). Their pro-tumorigenic role has been validated in animal models in which deletion of the activin inhibitor, *INHA*, led to gonadal tumors in mice as well as cachexia-like syndrome (Matzuk *et al*, 1994; Vassalli *et al*, 1994). ActivinB has also been shown to play a role in

cancer stem cell maintenance (Lonardo *et al*, 2011) and in cell dedifferentiation in an insulinoma mouse model and deletion of *INHBB* encoding ActivinB increases survival (Ripoche *et al*, 2015).

Several observations pinpoint to a potential role of the Smad2/3 signaling pathway in Group 3 MB but no published data have confirmed the deregulation of this signaling pathway, nor its functional involvement in Group 3 biology. In this study, we investigated these aspects to bring the proof of principle that this signaling pathway represents an interesting therapeutic target in MB and to identify patients that could be eligible to such therapy.

## Results

### TGF $\beta$ /ActivinB signaling pathway is active in Group 3 MB

Since different genomic alterations in the TGF $\beta$ /Activin pathway have been previously described in Group 3 MB (Northcott *et al*, 2012b, 2017; Lin *et al*, 2016), we first investigated whether the pathway is activated in patient samples. We performed WB analysis on 38 medulloblastomas: 7 WNT, 12 SHH, 10 Group 3, and 9 Group 4 tumors. Activation of the pathway, monitored by the level of Smad2 phosphorylation (P-Smad2), was observed in some patient samples from all MB groups (Fig 1A). An inter-tumor heterogeneity was observed in each group, with some samples with high P-Smad2. However, an overall higher level of Smad2 phosphorylation was observed in Group 3 when normalized to  $\beta$ -actin (Fig EV1A, left panel). This was not evidenced when normalized to total Smad2 (Fig EV1A, right panel) since an important variation of Smad2 level was observed (Fig 1A). This is in line with the modification of Smad2 stability by auto-regulatory mechanisms (Yan *et al*, 2018). Thus, the overall level of P-Smad2/ $\beta$ -actin, which formally reflects the level of nuclear and active Smad2, led us to conclude that TGF $\beta$ /Activin pathway is activated in some Group 3 patients.

Considering that amplifications of receptors of the pathway have been described in less than 10% of Group 3 tumors (Northcott *et al*, 2012b), we hypothesized that other mechanisms may account for pathway activation in several G3 samples. Activation of the Smad2/3 pathway in cancer is frequently due to autocrine/paracrine activation by TGF $\beta$  ligands (Rodón *et al*, 2014). Therefore, we analyzed the expression of major mediators of the TGF $\beta$ /Activin pathway, including ligands and receptors in previously published MB dataset at the mRNA (Data ref: Cavalli *et al*, 2017b) and protein (Data ref: Archer *et al*, 2018b) levels. No major difference in the expression of the different receptors was observed between the different groups (Fig EV1B and C). In contrast, striking differences were observed for the ligands. For example, *TGF $\beta$ 2* was found highly expressed in SHH tumors (Fig EV1B and C and Appendix Table S1). We observed higher expression levels of *TGF $\beta$ 1*, *TGF $\beta$ 3*, and *INHBB* (encoding ActivinB) in Group 3 in comparison with the other ones although expression of *TGF $\beta$ 3* is similar between Group 3 and Group 4 (Fig 1B). These results were confirmed at the protein level (Fig EV1C). These data were compatible with an autocrine activation of the pathway by one of those ligands listed above in Group 3 MB.

We next investigated the activation of TGF $\beta$ /Activin pathway in MB cell lines. We analyzed the level of P-Smad2 in four well-established Group 3 MB cell lines (HDMB03, D458, 1603MED, and D283)

as well as in three cell lines classified as non-Group 3 (DAOY, ONS76, and UW228). Western Blot (WB) analyses showed higher basal intensity of P-Smad2 signal in Group 3 cell lines (Fig 1C), confirming that the pathway is activated in this group. As in patient samples, we observed heterogeneity in the activation of the pathway, with a very strong basal level of pathway activation being observed in the 1603MED cell line while in some cell lines its level was modest.

To understand what drives the basal activation of the pathway in Group 3 cell lines, we investigated the expression level of different ligands and receptors of the pathway by RT-qPCR (Figs 1D and EV1D). No marked difference in the expression of the receptors was found between Group 3 and non-Group 3 cell lines, except a higher expression of *ACVR1B*, *ACVR2A*, and *ACVR2B* (Fig EV1D and Appendix Table S2) and a lower expression of *TGFBR2*, an obligatory partner for *TGFBR1*, in Group 3 cell lines. We did not observe any direct correspondence between the expression of the different receptors and the level of activation of the pathway in the different Group 3 cell lines (i.e., level of P-Smad2 in Fig 1C), suggesting that pathway activation is not directly linked to the deregulation of receptors expression. We investigated the expression of different ligands (Figs 1D and EV1D) and found a higher expression of *INHBB* in the 1603MED and D283 Group 3 cell lines as compared to the others (Fig 1D and Appendix Table S2). Interestingly, this level of expression directly corresponded to that of P-Smad2 levels, strong in 1603MED to intermediate in D283. This suggested that the ActivinB, encoded by *INHBB*, could be the major driver of Smad2/Smad3 phosphorylation in this group. The same observation could be drawn for *TGF $\beta$ 3* in 1603MED and to a lesser extent in D283, while genes encoding the other ligands were not overexpressed in the cell lines showing a high level of P-Smad2 (Fig EV1D). Taken together, these results suggested the potential existence of an autocrine mechanism involving either *TGF $\beta$ 3* or *INHBB* that could be responsible for TGF $\beta$ /Activin signaling activation in Group 3 MB.

### An autocrine stimulation involving ActivinB

To further investigate the presence of a potential autocrine mechanism, we first analyzed the ability of cell lines to respond to exogenous stimulation by either TGF $\beta$  or Activin ligands, each requiring different sets of receptors. Non-Group 3 cell lines showed an increase in P-Smad2 signals in response to TGF $\beta$  stimulation, while no modulation was observed upon Activin stimulation (Fig 2A, left in blue). Strikingly, Group 3 MB cell lines showed the complete opposite profile: P-Smad2 signal was increased upon Activin stimulation, while it remained unchanged upon TGF $\beta$  stimulation (Fig 2A, right in yellow). Noteworthy, 1603MED displayed a very high basal level of P-Smad2 which is constitutive. The reason for which G3 cell lines respond to Activin but not to TGF $\beta$  is currently unknown. However, we noticed a lower level of *TGFBR2* in these cells, a receptor required for TGF $\beta$  response (Fig EV1D). This was also observed in G3 tumor samples at the RNA and protein level (Fig EV1B and C). These opposite responses suggested a ligand-specific response between MB subgroups with Group 3 MB cell lines being able to respond to Activin but not to TGF $\beta$ , thereby excluding TGF $\beta$  ligands as a potential autocrine source for Smad2 activation. Since Group 3 cell lines displayed concomitant pathway activation and *INHBB* expression, these results strongly suggested that an

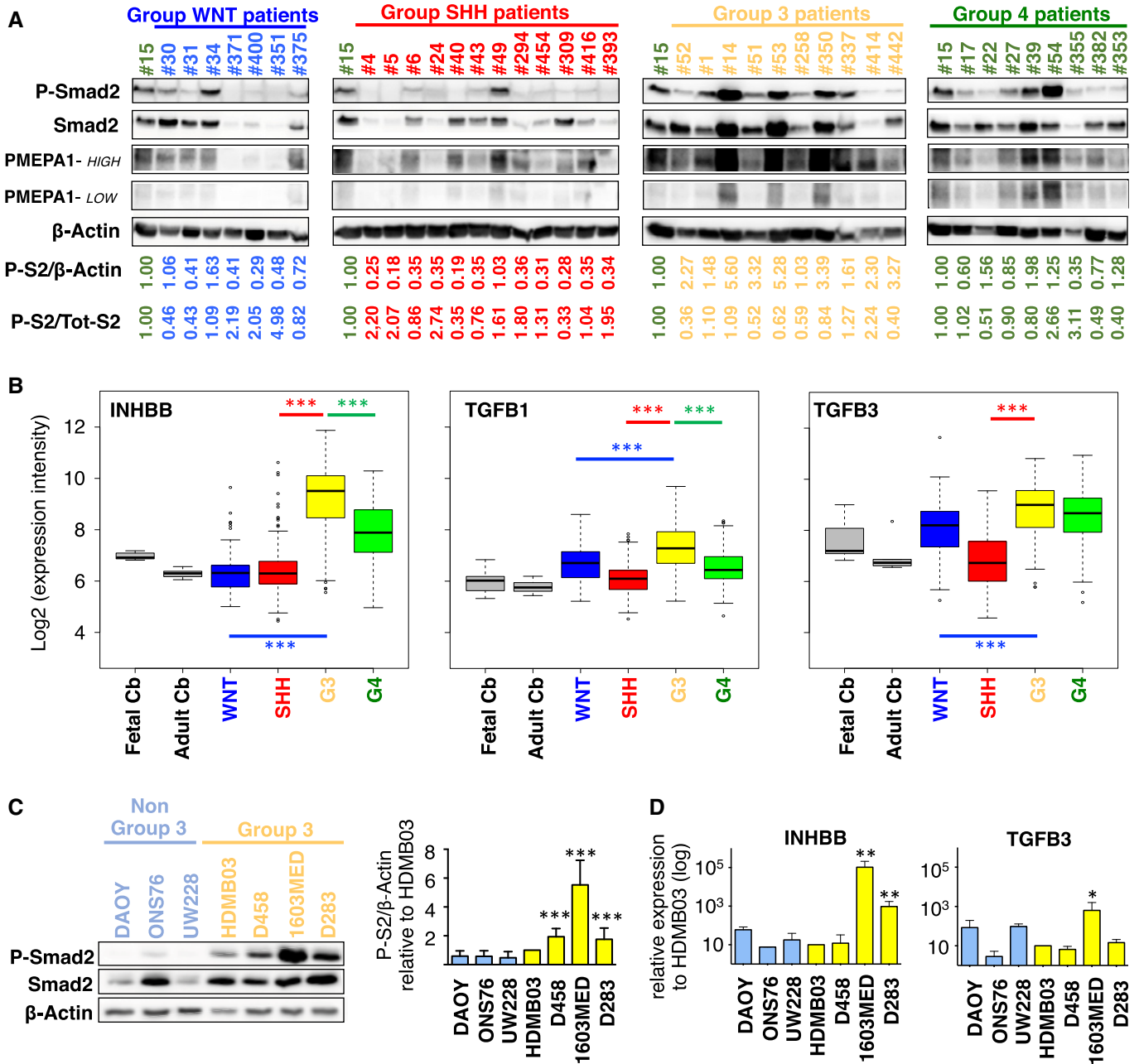


**Figure 1. TGFβ/ActivinB pathway is activated in Group 3 MB patients and cell lines.**

**A** Immunoblot analysis of phosphorylated Smad2 (P-Smad2) and PMEPA1 (high and low exposures displayed) in MB patient sample lysates from different groups: WNT (blue), SHH (red), Group 3 (yellow), or Group 4 (green). β-Actin was used as a loading control. Relative quantification of P-Smad2 signal to β-actin (P-S2/β-Actin) and total Smad2 (P-S2/Tot-S2) are indicated below the blots.

**B** Boxplots summarizing the expression of *INHBB*, *TGFB1*, and *TGFB3* ligands of the TGFβ/Activin pathway in the different groups of MB (blue WNT, red SHH, yellow Group 3, and green Group 4) and in fetal and adult cerebellum (gray) in the dataset of Cavalli et al (Data ref: Cavalli et al, 2017b).

**C** Immunoblot analysis of phosphorylated Smad2 (P-Smad2) in non-Group 3 (blue) and Group 3 (yellow) MB cell lines on the left panel. The level of total Smad2 (Smad2) was assessed, and β-actin was used as a loading control. On the right panel, relative level of P-Smad2 (P-S2) was quantified to total β-actin. P-Smad2 to total Smad2 normalization is also provided on Appendix Fig S5.

**D** RT-qPCR was performed on RNA extracted from non-Group 3 (blue) and Group 3 (yellow) MB cell lines to compare expression levels of *INHBB* (left) and *TGFB3* (right).

Data information: Wilcoxon rank-sum tests were performed to determine P-values for panel (B). Boxplot center lines show data median; box limits indicate the 25<sup>th</sup> and 75<sup>th</sup> percentiles; lower and upper whiskers extend 1.5 times the interquartile range (IQR) from the 25<sup>th</sup> and 75<sup>th</sup> percentiles, respectively. Outliers are represented by individual points (B). The remaining P-values were determined by unpaired t-test. \*P < 0.05, \*\*P < 0.01, \*\*\*P < 0.001, \*\*\*\*P < 0.0001. Bars represent the mean ± SD. Number of replicates is n ≥ 3. The exact P-values and number of replicates are indicated in Appendix Table S5. Detailed statistics are presented in Appendix Table S1 for panel (B) and Appendix Table S2 for panel (D).

Source data are available online for this figure.

ActivinB (encoded by *INHBB*) autocrine stimulation could be responsible for the activation of the pathway in the 1603MED and D283 Group 3 cell lines. To further investigate the potential role of ActivinB in the basal Smad2 activation in these cell lines, we focused on the 1603MED cell line, which shows the strongest basal activation. Treatment of 1603MED cells with an ActivinB blocking antibody induced a decrease in P-Smad2 level (Fig 2B). Importantly, the specificity of this antibody toward ActivinB was verified by showing that it does not block TGF $\beta$  stimulation (Appendix Fig S1). These experiments supported that an autocrine ActivinB production induced, at least partially, a strong activation of the pathway in 1603MED. This was further supported by P-Smad2 inhibition upon treatment with follistatin, a ligand trap for Activins (Fig 2B). We next sought to directly demonstrate that 1603MED cells secrete ActivinB. HDMB03 cells were used as receiving cells to conditioned media, since they showed the lowest basal activation of the pathway among G3 cell lines (Fig 1C) but efficiently responded to exogenous ActivinB and not to TGF $\beta$  stimulation (Fig 2A). Three culture media were tested as follows: a non-conditioned media that had never been in contact with any cells, an HDMB03-conditioned media, both of them being used as negative controls, and a 1603MED conditioned media. HDMB03 cells were treated with these different media for 1 h, and the effect on the Smad2 pathway was tested by WB (Fig 2C). 1603MED conditioned media induced a strong P-Smad2 signal as compared to the two control media. This induction was prevented by incubation with an ActivinB blocking antibody (Fig 2C), strongly supporting that 1603MED secreted active ActivinB ligand. To further substantiate this hypothesis, we targeted *INHBB* expression by siRNA in 1603MED. Although expression of *INHBB* was reduced to only 40% (Fig 2D), we nonetheless observed a decrease in P-Smad2 level (Fig 2E) resulting in decreased cell growth (Fig 2F). All these effects were rescued by exogenous addition of ActivinB (Fig EV2). Altogether, these results strongly support an autocrine secretion of ActivinB by 1603MED cells leading to P-Smad2 activation and promoting 1603MED cell proliferation.

### ActivinB stimulation promotes proliferation

We next investigated the role of Activin pathway activation in Group 3 MB cell lines. D458 (Fig 3A–D) and D283 (Fig 3E–H) cells, which showed intermediate basal activation of the pathway (Fig 1C), were stimulated with ActivinB (Fig 3). Activation of the pathway was validated by monitoring P-Smad2 levels (Fig 3A and E). Incucyte Proliferation Assay revealed an increase in cell proliferation upon ActivinB stimulation in both cell lines (Fig 3B and F). It remains to be determined why ActivinB did not promote cell growth while activating the pathway in HDMB03 (Appendix Fig S2). An increase in cell proliferation can result from faster cell cycle progression, a reduction in cell death, or both. We analyzed the cell cycle profile by BrdU incorporation and 7AAD labeling and observed an increase in the number of cells in S phase following ActivinB stimulation, concomitant with a decrease in G0/G1 (Fig 3C and G). Apoptosis was monitored by FACS analysis of cleaved caspase-3 staining. We did not detect consistent effects on apoptosis, with a slight decrease in D458 cell line following stimulation after 2 days (Fig 3D), while no changes were detected in D283 (Fig 3H). These results indicated that ActivinB stimulates cell proliferation in Group 3 cell lines mainly by promoting cell cycle progression.

### Inhibition of the pathway decreases proliferation

We next investigated the consequences of pharmacological inhibition of the pathway in Group 3 MB cell lines (Fig 4). One Group 3 cell line that exhibits a very high basal activation of the pathway (1603MED, Fig 4A–D) and one with an intermediate level (D283, Fig 4E–H) were treated with LY364947 or SB431542. These compounds prevent the phosphorylation of Smad2/3 by the TGF $\beta$  and Activin type I receptors. Indeed, we verified that they prevent TGF $\beta$ - as well as ActivinB-induced P-Smad2 (Appendix Fig S1). After 24 h of treatment, the level of P-Smad2 was decreased in 1603MED and D283 cell lines (Fig 4A and E, respectively). This pathway inactivation was accompanied by a decrease in cell proliferation (Fig 4B and F). FACS analyses were performed to measure BrdU incorporation and 7AAD labeling. Treatment with inhibitors induced a decrease in the percentage of cells in S phase concomitant with an increase in G0/G1 (Fig 4C and G). A very slight increase in the percentage of cells positive for cleaved caspase-3 staining was also observed (Fig 4D and H), showing that the inhibition of the pathway mainly impacted on cell cycle and to a much lesser extent on apoptosis.

### PMEPA1 is implicated in ActivinB promotion of cell growth

To identify relevant genes downstream of Activin signaling in Group 3 MB, we sorted the top 10 genes, whose expression was correlated with *INHBB* in Group 3 patient samples (Fig 5A). *PMEPA1*, which scored as the top gene, is a well-established Smad2/3 target gene in different cell types including P19 cells stimulated by Activin (Coda et al, 2017). Accordingly, we found that *PMEPA1* expression level was enriched in Group 3 MB (Fig 5B) and correlated with *INHBB* expression in MB (Fig 5C). This correlation is highest in G3 as compared to the other groups (Appendix Fig S3A). Accordingly, we observed a good correspondence between P-Smad2 overall level and *PMEPA1* protein expression in patient samples by Western blot analysis (Figs 1A and 5D and E, Appendix Fig S3B). We next tested whether *PMEPA1* is also a target of the Smad2 signaling in MB by modulating pathway activation (Fig 5F). Activation of the pathway by ActivinB induced an increase in *PMEPA1* mRNA and protein levels, while its inhibition by LY364947, SB431542, blocking ActivinB antibody, or follistatin had the opposite effect in G3 cell lines (Fig 5F and Appendix Fig S3C and D). *MYC* and *OTX2* are key players in Group 3 MB and are also known as Smad2/3 target genes in other cell types (Jia et al, 2009; Brown et al, 2011; Coda et al, 2017). Therefore, we investigated whether their expression could be modulated by this pathway in Group 3 MB cell lines. In contrast to *PMEPA1*, no major change was observed at the mRNA (Appendix Fig S3C) and protein (Fig 5F and Appendix Fig S3D) levels upon pathway inhibition regarding *OTX2*, while a slight decrease could be observed for *MYC*. However, no significant increase in *MYC* expression was observed upon ActivinB treatment (Appendix Fig S3C). Interestingly siRNA-mediated *INHBB* knockdown decreased *PMEPA1* expression that could be rescued upon ActivinB treatment (Fig EV3A). These results suggested that *PMEPA1* is a target gene of the Activin pathway in Group 3 MB but that neither *MYC* nor *OTX2*, two important players of this group, appears to be consistently regulated by this signaling pathway although minor effects are observed on *MYC*. The role of *PMEPA1* in cancer remains unclear and is likely to be cell type specific. It has been shown to either promote or

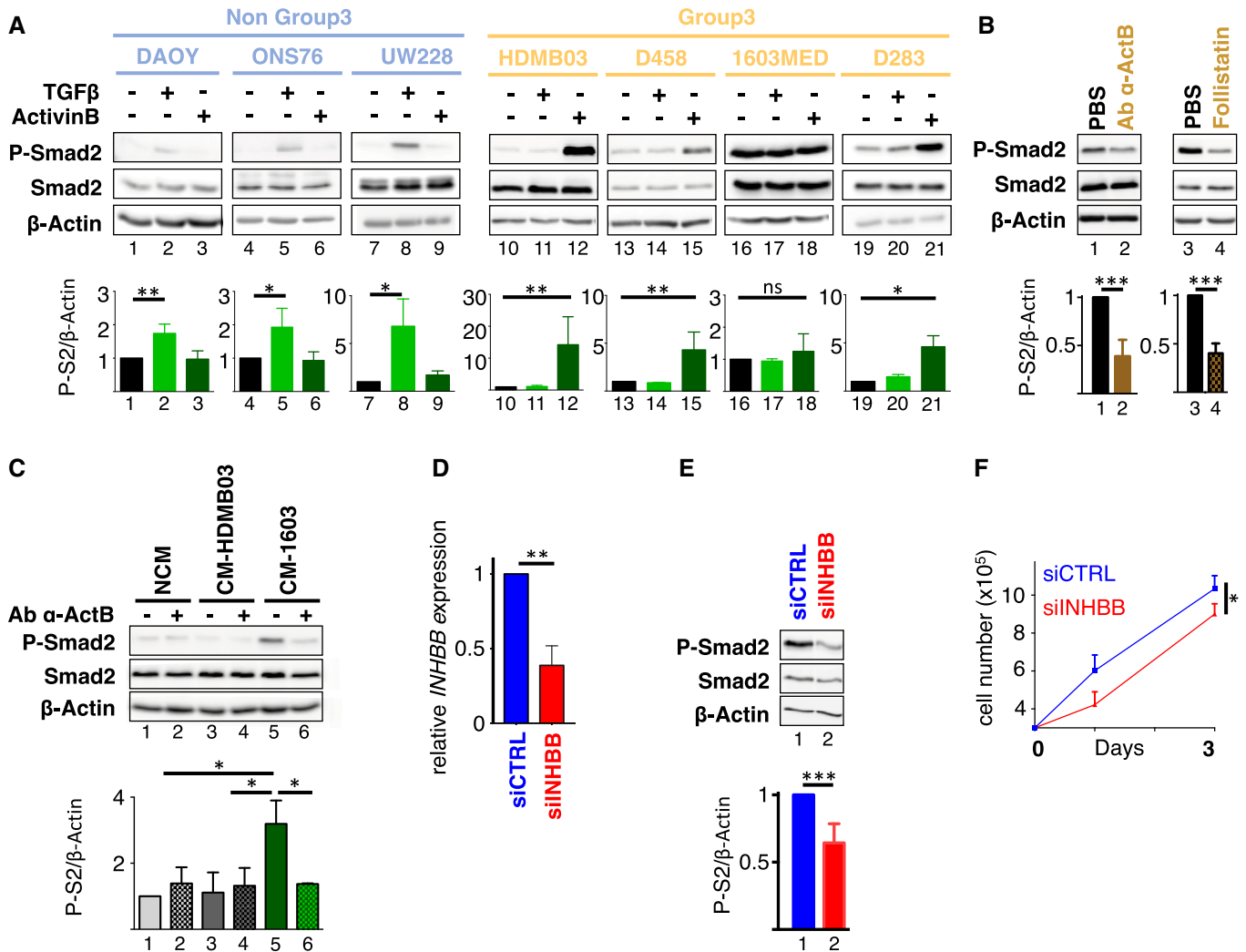


**Figure 2. An autocrine stimulation by ActivinB in the 1603MED cell line.**

A–C The level of phosphorylated Smad2 (P-Smad2) and total Smad2 (Smad2) was assessed by immunoblotting, and  $\beta$ -actin was used as a loading control. Lower bar graphs show WB quantification of P-Smad2 (P-S2) normalized to  $\beta$ -actin. (A) Activation of the pathway was assessed in non-Group 3 (blue) and Group 3 (yellow) MB cell lines in response to TGF $\beta$  or ActivinB stimulation for 1 h. (B) 1603MED cells were treated with PBS (vehicle) or a blocking antibody targeting ActivinB (Ab  $\alpha$ -ActB) or follistatin. (C) Conditioned media experiments were performed on the HDMB03 MB cell line. Phosphorylation of Smad2 was analyzed by immunoblot upon treatment with either non-conditioned media (NCM), media conditioned with HDMB03 cells (CM-HDMB03), or media conditioned with 1603MED cells (CM-1603). Pre-incubation with blocking antibody against ActivinB (Ab  $\alpha$ -ActB) or vehicle (PBS) was performed before HDMB03 cell-line treatment as indicated. Relative level of P-Smad2 (P-S2) was quantified to  $\beta$ -actin (below).

D RT-qPCR was performed on total RNA extracted from 1603MED cells 48 h after transfection with siRNA targeting INHBB. Relative *INHBB* expression was assessed. siCTRL condition was set at 1.

E 1603MED cells were transfected with the indicated control siRNA (siCTRL, blue) or targeting INHBB (siINHBB, red). Lysates were prepared 48 h after transfection. The level of phosphorylated Smad2 (P-Smad2) and total Smad2 (Smad2) was assessed by immunoblotting, and  $\beta$ -actin was used as a loading control. Lower bar graphs represent the quantification of the relative level of P-Smad2 (P-S2) to  $\beta$ -actin.

F Growth curve of 1603MED cells after transfection with either siCTRL (blue) or siINHBB (red).

Data information: P-Smad2 to total Smad normalization is provided on Appendix Fig S5. The *P*-values were determined by unpaired *t*-test. \**P* < 0.05, \*\**P* < 0.01, \*\*\**P* < 0.001. Bars represent the mean  $\pm$  SD. Number of replicates is *n*  $\geq$  3. The exact *P*-values and number of replicates are indicated in Appendix Table S5. Source data are available online for this figure.

restrain cancer progression (Liu *et al*, 2011; Fournier *et al*, 2015; Nie *et al*, 2016). Therefore, we investigated its role in Group 3 MB. siRNA-mediated PMEPA1 knockdown resulted in cell growth inhibition in both 1603MED and D283 cell lines (Figs 5G–J and EV3B–E), suggesting that PMEPA1 is an important mediator of Activin signaling-mediated proliferation in Group 3 MB.

### TGF $\beta$ /ActivinB signaling pathway in Group 3 MB Patient Derived Xenografts (PDXs)

We further validated the importance of the pathway in patient derived xenograft (PDX) models, known to remain close to the original tumor (Fig 6). As observed in Group 3 patient samples and cell

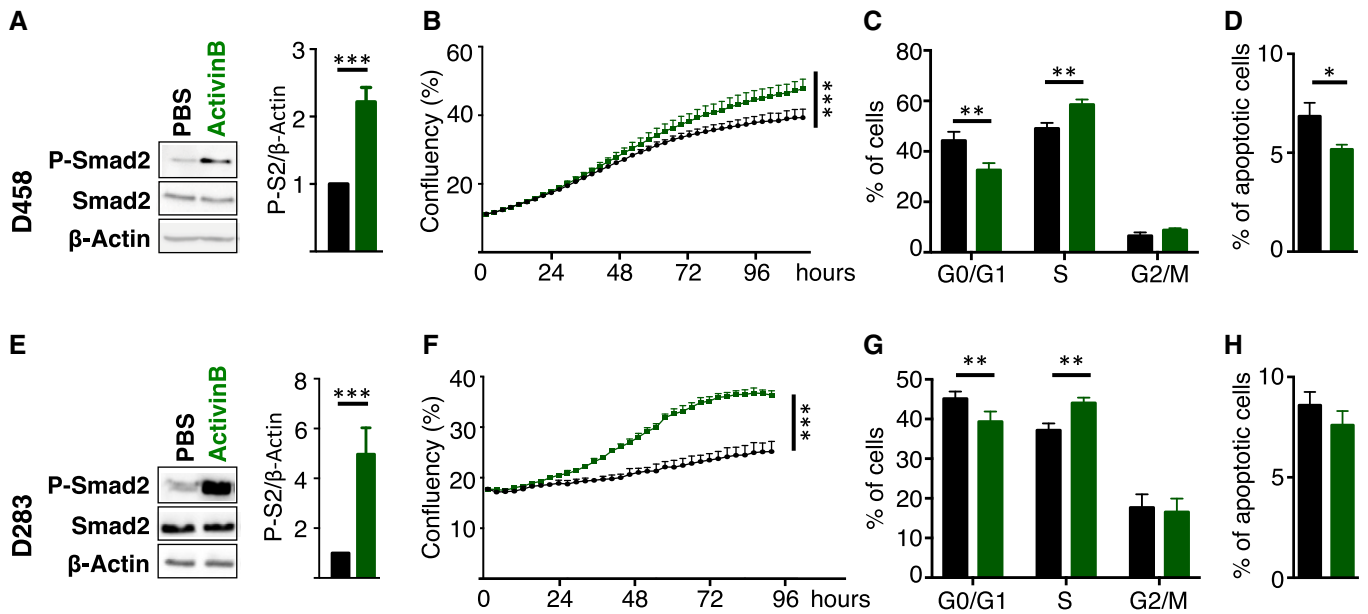


**Figure 3. ActivinB promotes cell proliferation in Group 3 MB cell lines.**

A–H D458 (A–D) or D283 (E–H) cell lines were treated with PBS (vehicle, black) or with ActivinB (green). (A and E) Immunoblot of phosphorylated Smad2 (P-Smad2), total Smad2, and  $\beta$ -actin in response to ActivinB stimulation for 24 h. Quantification of P-Smad2 (P-S2) to  $\beta$ -actin is shown on right panels. (B and F) P-Smad2 to total Smad normalization is provided on Appendix Fig S5. Growth curve experiments showing cell proliferation upon ActivinB treatment. (C and G) Cell cycle analysis by FACS measuring BrdU incorporation and 7AAD labeling at 48 h upon ActivinB stimulation. The percentage of cells in the different phases of the cell cycle is represented (G0/G1, S, and G2/M phases). (D and H) Percentage of apoptotic cells measured by FACS analysis of cleaved caspase-3 48 h after treatment with ActivinB. The *P*-values were determined by unpaired *t*-test and two-way ANOVA for (B and F). \**P* < 0.05, \*\**P* < 0.01, \*\*\**P* < 0.001. Bars represent the mean  $\pm$  SD. Number of replicates is *n*  $\geq$  3. The exact *P*-values and number of replicates are indicated in Appendix Table S5.

Source data are available online for this figure.

lines, we found heterogeneous levels of P-Smad2, from high to moderate, in the three Group 3 PDXs tested (Fig 6A). PDX4 displayed a very strong activation of the pathway, similar to that observed in the 1603MED cell line. We investigated the expression level of different mediators of the pathway by RT-qPCR (Fig 6B, Appendix Fig S4A). This analysis showed heterogeneous expression levels of *INHBB* in the 3 PDXs (Fig 6B), which tightly corresponded to the level of P-Smad2. PDX4, which showed the highest level of expression of *INHBB*, also displayed the highest P-Smad2 signal (see level of P-Smad2 in Fig 6A and *INHBB* expression in 6B). As in cell lines, Group 3 PDXs responded to Activin but not to TGF $\beta$  stimulation (Fig 6C). This result supported the observations in MB cell lines, suggesting a ligand specificity toward Activin in Group 3 MB. To further investigate the possibility of an autocrine mechanism involving ActivinB, we performed conditioned media experiments as described in Fig 2C. Conditioned media from PDX4, which displays a strong activation of the pathway, markedly increased P-Smad2 phosphorylation in the receiving HDMB03 cells (Fig 6D). This induction could be partially prevented when the media was pre-incubated with an ActivinB blocking antibody (Fig 6D). Moreover, PDX4 treated with the same antibody also showed a decrease in P-Smad2 (Fig 6E, Appendix Fig S4C). P-Smad2 signal could also be inhibited following treatment with inhibitors of type I receptors and follistatin (Fig 6E). We next assessed if this signaling pathway controls *PMEPA1* expression. As in cell lines, a decrease in *PMEPA1* expression was observed in PDXs after treatment with inhibitors and increased by ActivinB treatment. The expression of *MYC* and

*OTX2* remained mostly unchanged (Fig 6E, Appendix Fig S4B and C). Altogether, these results confirmed those obtained in cell lines, highlighting the presence of an autocrine stimulation involving ActivinB in Group 3 MB and identified *PMEPA1* as a gene, whose expression is controlled by this signaling pathway. We next investigated if inhibition of this pathway could be of therapeutic interest *in vivo*. The human PDX4, which displays a very high level of activation of the pathway, was orthotopically grafted into the cerebellum of nude mice. Animals were then treated 7 days per week twice a day with Galunisertib, a pharmacological inhibitor currently in clinical trial for Glioblastoma, Cisplatin as described in Niklison-Chirou *et al* (2017), or a combination. Galunisertib is described as a TGF $\beta$  type I inhibitor but, since TGF $\beta$  and Activin type I receptors are very similar, it also inhibits very efficiently ActivinB-induced Smad2 activation (Appendix Fig S1). Accordingly, we verified that Galunisertib recapitulated the main *in vitro* data obtained with LY364947 and SB431542 (Fig EV4A–C). Galunisertib-treated mice survived longer as compared to controls (Fig 7A), demonstrating the benefit of such treatment in tumors displaying high level of activation of the pathway. Accordingly, Galunisertib-treated mice displayed smaller tumors with less P-Smad2 (Fig 7B and C). No major difference was observed for Ki67 and cleaved caspase-3 staining (Fig EV4D and E). Although we did not observe any benefit from the combination of Galunisertib with Cisplatin (Figs 7A–C and EV4D and E), we cannot not exclude that different treatment kinetics could be more efficient. In this respect, other combinations with different drugs or radiotherapy remain to be evaluated.

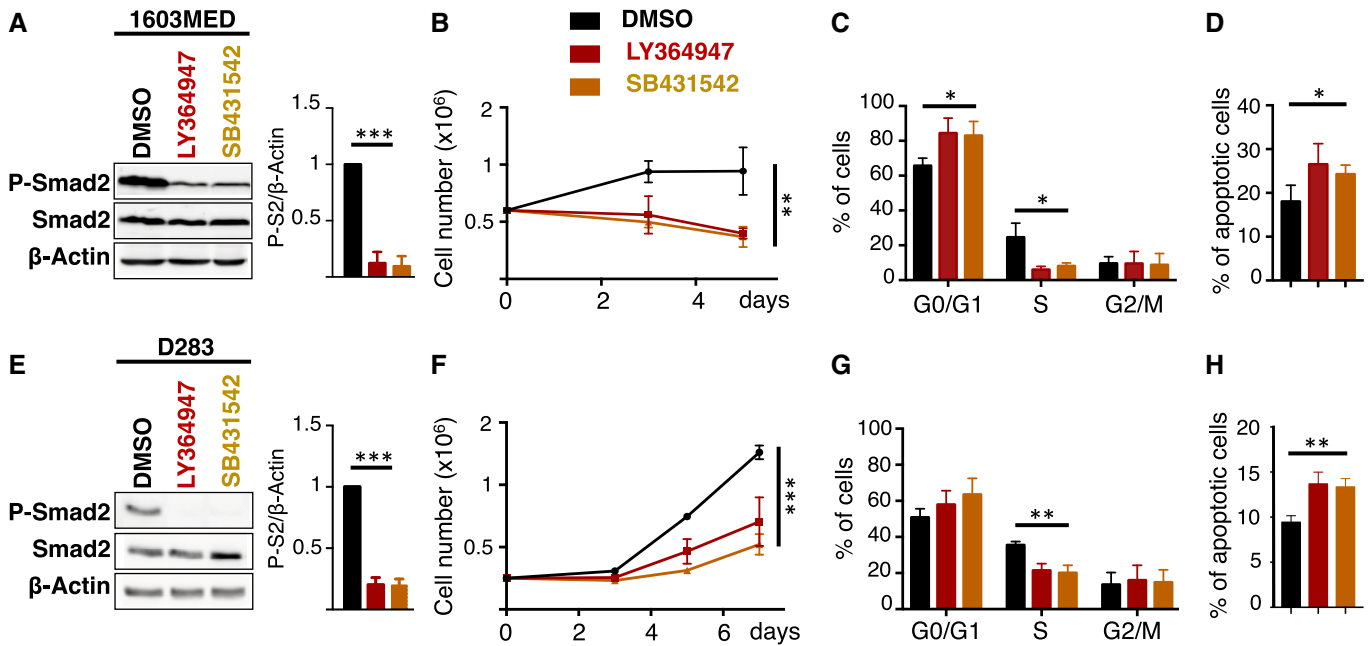


**Figure 4. TGF $\beta$ /ActivinB signaling promotes cell proliferation in Group 3 MB cell lines.**

A–H 1603MED (A–D) or D283 (E–H) cells were treated with DMSO (vehicle, black), with LY364947 (red), or with SB431542 (orange). (A and E) Immunoblot of phosphorylated Smad2 (P-Smad2), total Smad2, and  $\beta$ -actin upon inhibition of TGF $\beta$ /Activin signaling using LY364947 and SB431542 inhibitors for 24 h. Bar graphs on the right panel represent the quantification of the relative level of P-Smad2 (P-S2) to  $\beta$ -actin. (B and F) P-Smad2 to total Smad normalization is provided on Appendix Fig S5. Growth curve experiments showing cell proliferation upon TGF $\beta$ /Activin signaling inhibition. (C and G) Cell cycle analysis by FACS measuring BrdU incorporation and 7AAD labeling at 48 h upon inhibition. The percentage of cells in the different phases of the cell cycle is represented (G0/G1, S, and G2/M phases). (D and H) Percentage of apoptotic cells measured by FACS analysis of cleaved caspase-3 48 h after TGF $\beta$ /Activin signaling inhibition. The *P*-values were determined by unpaired *t*-test and two-way ANOVA for (B and F). \**P* < 0.05, \*\**P* < 0.01, \*\*\**P* < 0.001. Bars represent the mean  $\pm$  SD. Number of replicates is *n*  $\geq$  3. The exact *P*-values and number of replicates are indicated in Appendix Table S5.

Source data are available online for this figure.

### TGF $\beta$ /ActivinB signaling pathway in Group 3 $\alpha$ subtype of MB

As mentioned above, tumor samples, PDXs, and cell lines from Group 3 displayed an inter-tumoral heterogeneity regarding the level of

pathway activation, some of them showing a very strong P-Smad2 basal level. Recently, intragroup heterogeneity has been described in MB (Cavalli *et al*, 2017a; Northcott *et al*, 2017; Schwalbe *et al*, 2017) with the definition of new subtypes within Group 3 tumors. We

**Figure 5. PMEPA1 is a target gene involved in the response to Activin signaling.**

- A Ranking of top genes whose expression is correlated with *INHBB* in Group 3 MB patient samples. Spearman's rank correlation coefficient  $\rho$  and *P*-value are indicated.
- B Boxplots representing *PMEPA1* expression levels in the different MB groups (WNT in blue, SHH in red, Group 3 in yellow, and Group 4 in green) and in fetal and adult cerebellum (gray) in the dataset of Cavalli *et al* (Data ref: Cavalli *et al*, 2017b). Only *P*-values corresponding to comparisons between Group 3 and the other groups are indicated. Full statistics can be found in Appendix Table S1.
- C Scatter plot of *INHBB* and *PMEPA1* gene expression levels in all MB groups. Colored dots represent each patient samples, and colors represent the MB groups (WNT in blue, SHH in red, Group 3 in yellow, and Group 4 in green).
- D Boxplot represents the quantification of *PMEPA1* protein level normalized to  $\beta$ -actin levels across groups.
- E Scatter plot represents log<sub>2</sub> relative protein level of P-Smad2 (x-axis) and *PMEPA1* (Y-axis) normalized to  $\beta$ -actin in each individual samples.
- F Immunoblots of phosphorylated Smad2 (P-Smad2), total Smad2, MYC, *PMEPA1*, OTX2, and  $\beta$ -actin were performed on extracts from 1603MED or D283 or D458 cells treated with either DMSO (vehicle), LY364947, SB431542, blocking antibody against ActivinB (Ab  $\alpha$ -ActB), follistatin, PBS, or ActivinB (ActB) for 24 h. Blot quantification to  $\beta$ -actin is presented in Appendix Fig S3D.
- G Immunoblot analysis of *PMEPA1* levels 48 h after transfection with either siCTRL (blue) or siPMEPA1 (red). Bar graphs on the right represent the quantification of the relative level of *PMEPA1* protein level normalized to  $\beta$ -actin. P-Smad2 to total Smad normalization is provided on Appendix Fig S5.
- H Growth curves of 1603MED cells after transfection with either siCTRL (blue) or siPMEPA1 (red).
- I Immunoblot analysis of *PMEPA1* levels in D283 cells 48 h after transfection with either siCTRL (blue) or siPMEPA1 (red). Bar graphs on the right represent the quantification of the relative level of *PMEPA1* protein level normalized to  $\beta$ -actin. P-Smad2 to total Smad normalization is provided on Appendix Fig S5.
- J Growth curves of D283 cells after transfection with either siCTRL (blue) or siPMEPA1 (red).

Data information: The color code is the same as for (B, C, and E). Boxplot center lines show data median; box limits indicate the 25<sup>th</sup> and 75<sup>th</sup> percentiles; lower and upper whiskers extend 1.5 times the interquartile range (IQR) from the 25<sup>th</sup> and 75<sup>th</sup> percentiles, respectively (B and D). Outliers are represented by individual points (B). The *P*-values were determined by Spearman rank correlation test for (A and C), by unpaired *t*-test for (D, G and I), by two-way ANOVA for (H and J), and by Wilcoxon rank-sum test for panel (B and E). \**P* < 0.05, \*\**P* < 0.01, \*\*\**P* < 0.001. Bars represent the mean  $\pm$  SD. Number of replicates is *n*  $\geq$  3. The exact *P*-values and number of replicates are indicated in Appendix Table S5.

Source data are available online for this figure.

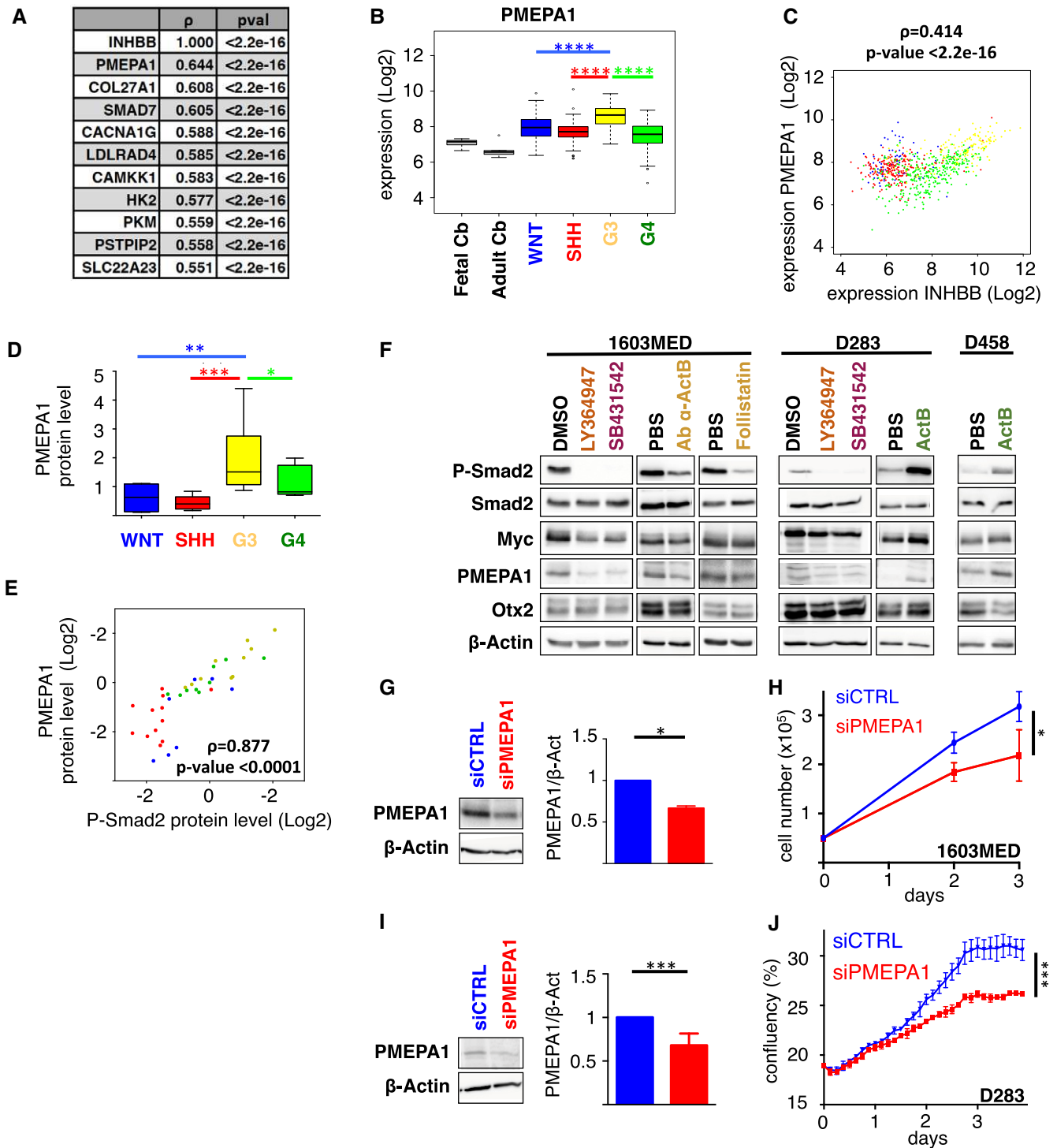


Figure 5.

wondered if this intragroup heterogeneity could explain our results. Since we showed that this strong activation was linked to an autocrine mechanism involving ActivinB, we investigated *INHBB* expression in these newly described subtypes of Group 3 tumors (Fig 7D). We found that *INHBB* displayed a significantly higher expression level in the Group 3 $\alpha$  subtype as compared to Group 3 $\beta$  and Group 3 $\gamma$  according to Cavalli *et al* (2017a) subtyping. Interestingly, *PMEPA1* displayed the same profile, and consequently, *INHBB* and

*PMEPA1* expression was tightly correlated in Group 3 (Fig 7E). In contrast, *MYC* expression showed an opposite expression pattern as compared to *INHBB* (Fig 7D): Group 3 $\gamma$  subtype, which is characterized by an enrichment of *MYC* amplifications, displayed the highest *MYC* expression levels, whereas the  $\alpha$  subtype showed the lowest (Cavalli *et al*, 2017a). We recently reported that *NRL* and *CRX* control photoreceptor genes expression and define a subset of Group 3 tumors (Garancher *et al*, 2018). We found that alike *INHBB*, *NRL* is highly

expressed in the G3 $\alpha$  subtype (Fig 7D and Appendix Table S3). This identifies Group 3 $\alpha$  as the subtype that expresses high level of *INHBB* and high photoreceptor genes.

### Discussion

Group 3 is the most aggressive MB group with patients showing the poorest prognosis. Several genomic alterations have been identified,

including those targeting the TGF $\beta$ /Activin pathway at very low frequency. Indeed, SCNA analyses have identified uncommon gains and/or amplifications of genes encoding receptors of the TGF $\beta$ /Activin pathway. Activation of the cognate Smad2/3 pathway in Group 3 tumors has never been investigated, neither its potential biological consequences nor its potential therapeutic targeting. Using patient samples, PDXs, and cell lines, we showed that, beside these infrequent genomic alterations, the TGF $\beta$ /Activin pathway is also activated in a specific subtype of Group 3, through an autocrine

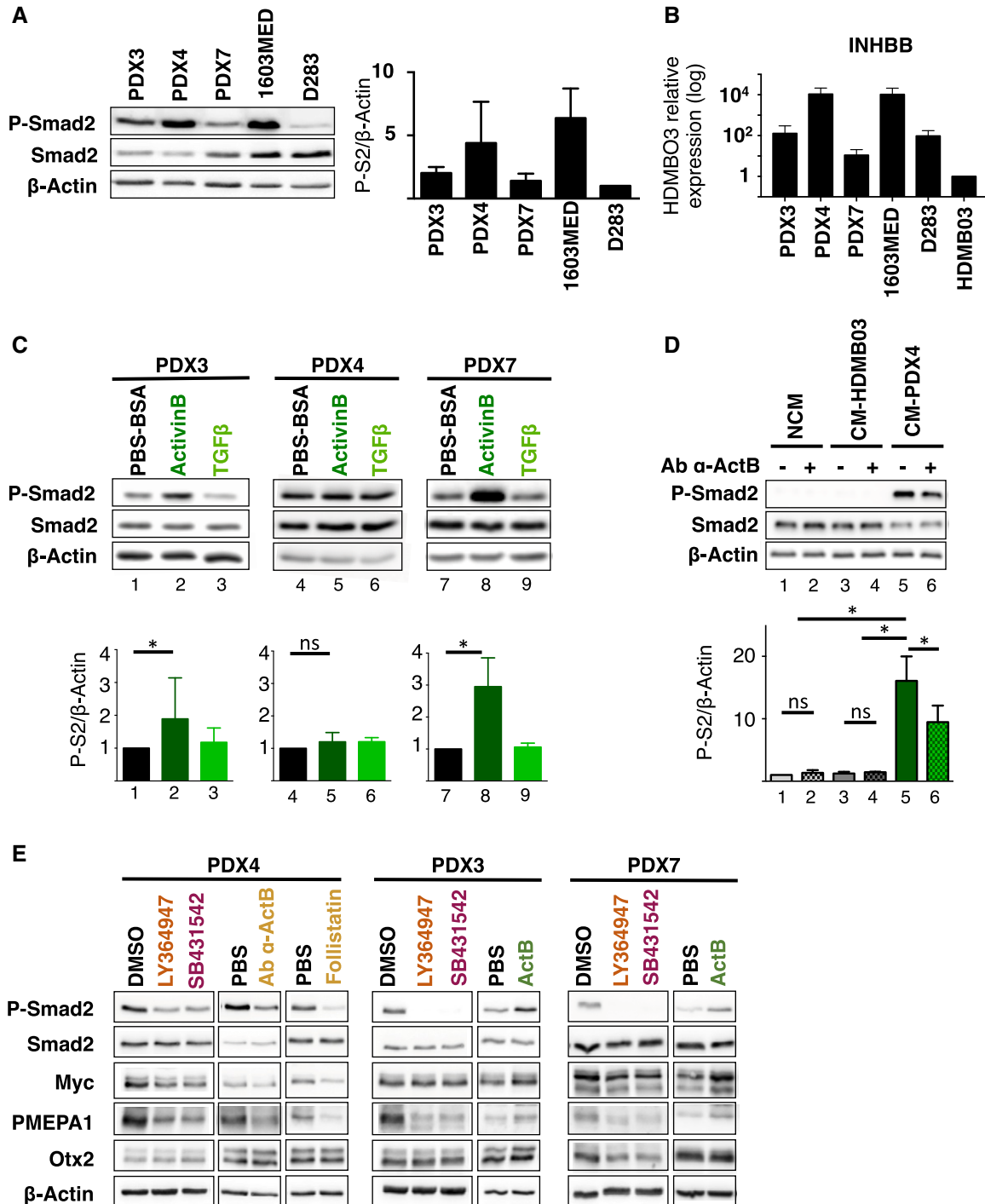


Figure 6.

**Figure 6. Activated TGF $\beta$ /ActivinB signaling in group 3 MB-PDXs.**

- A Immunoblot analysis of phosphorylated Smad2 (P-Smad2) in Group 3 MB cell lines and PDXs. The level of total Smad2 (Smad2) was assessed, and  $\beta$ -actin was used as a loading control. Quantification of P-Smad2 (P-S2) to  $\beta$ -actin is shown on right panel.
- B Expression of *INHBB* in Group 3 MB cell lines and PDXs relative to HDMB03 (set at 1) by RT-qPCR.
- C Immunoblot of phosphorylated Smad2 (P-Smad2), total Smad2, and  $\beta$ -actin upon ActivinB or TGF $\beta$  stimulation for 1 h. Quantification of P-Smad2 (P-S2) to  $\beta$ -actin is shown below.
- D Conditioned media experiments were performed on HDMB03 MB cell line. Phosphorylation of Smad2 (P-Smad2) was analyzed by immunoblot upon treatment with either non-conditioned media (NCM), media conditioned with HDMB03 cells (CM-HDMB03), or media conditioned on PDX4 cells (CM-PDX4). Pre-incubation with blocking antibody against ActivinB (Ab  $\alpha$ -ActB) or with vehicle was performed before HDMB03 cell-line treatment as indicated. Quantification of P-Smad2 (P-S2) to  $\beta$ -actin is shown below.
- E Immunoblots of phosphorylated Smad2 (P-Smad2), total Smad2, MYC, PMEPA1, OTX2, and  $\beta$ -actin were performed on extracts from cell cultures of PDX4, PDX3, and PDX7 treated with either DMSO (vehicle), LY364947, SB431542, blocking antibody against ActivinB (Ab  $\alpha$ -ActB), follistatin, PBS, or ActivinB for 24 h. WB quantification is depicted in Appendix Fig S4C.

Data information: P-Smad2 to total Smad normalization is provided on Appendix Fig S5. The *P*-values were determined by unpaired *t*-test. \**P* < 0.05. Detailed statistics are presented in Appendix Table S2 for panel (B). Bars represent the mean  $\pm$  SD. Number of replicates is *n*  $\geq$  3. The exact *P*-values and number of replicates are indicated in Appendix Table S5.

Source data are available online for this figure.

mechanism involving ActivinB. This pathway is involved in MB growth and represents an interesting therapeutic target.

**ActivinB mediates Smad2/3 signaling in Group 3 MB**

While activation of the TGF $\beta$ /Activin pathway has been described in SHH group, no data are currently available regarding its activation in Group 3. A recent report showed that Prune-1 may activate the TGF $\beta$  pathway in Group 3 MB but the level of pathway activation in Group 3 was not investigated nor its functional relevance (Ferrucci *et al*, 2018). It has also been suggested that TGF $\beta$  ligands determine the promigratory potential of bFGF signaling in MB but this study was performed in non-Group 3 cell lines and in atypical MB-PDX (Santhana Kumar *et al*, 2018). Using patient samples, we showed here that the TGF $\beta$ /Activin pathway is activated in a subset of Group 3. We confirmed these results using PDXs as well as MB cell lines. In many different cancers, TGF $\beta$  pathway activation involves autocrine loops, due to the high expression of genes encoding the different TGF $\beta$  ligands (Rodón *et al*, 2014). We investigated the potential mechanism of activation of the pathway in Group 3. As in other cancers, we observed high expression of *TGFB1* and *TGFB3* in Group 3 MB. In addition, we also observed very high expression of *INHBB*, which encodes ActivinB, suggesting that TGF $\beta$ 1, TGF $\beta$ 3, and ActivinB ligands could be potentially responsible for pathway activation. Unexpectedly, our data clearly showed that Group 3 cells do not respond to TGF $\beta$  stimulation, while they are highly sensitive to Activin, excluding *de facto* TGF $\beta$ 1 and TGF $\beta$ 3 as potential ligands that would activate the pathway in an autocrine manner. The mechanism underlying the lack of TGF $\beta$  responsiveness in G3 models is currently unknown. However, we noticed a significant decrease in RNA and protein *TGFB2* levels in G3 samples. Since *TGFB2* is absolutely required for signal transduction by TGF $\beta$  ligands, this observation may provide a plausible explanation to this lack of response. In any case, our experiments based on conditioned medium, blocking antibody, follistatin treatment, and siRNA on cell lines clearly pointed out on ActivinB as an important determinant of pathway activation in Group 3. Importantly, these observations were confirmed on PDXs. According to transcriptomic data showing that *INHBB* expression is found in a large number of Group 3 MB, this autocrine mechanism is very likely the main mechanism leading to pathway activation in this group. Additional mechanisms, such as amplifications of receptors or *Prune-1* expression (see above), could

also contribute to this activation, either by cooperating with ActivinB or by being involved in a more restricted number of Group 3 MBs that do not exhibit this autocrine mechanism. Interestingly, while TGF $\beta$ s and Activins activate the same Smad pathway (Smad2/3), TGF $\beta$ s autocrine mechanisms have been much more frequently described to be implicated in cancer progression than Activins (Chen *et al*, 2002; Wakefield & Hill, 2013), highlighting a singularity of Group 3 MBs. Since Activin is involved in developmental processes (Wu & Hill, 2009), its implication in Group 3 MB instead of TGF $\beta$  may relate to the pediatric nature of these tumors or to their cell of origin. In support of the latter and according to brain atlas data ([http://developingmouse.brain-map.org/search/show?page\\_num=0&page\\_size=5&no\\_paging=false&exact\\_match=true&search\\_term=Inhbb&search\\_type=gene](http://developingmouse.brain-map.org/search/show?page_num=0&page_size=5&no_paging=false&exact_match=true&search_term=Inhbb&search_type=gene)), *INHBB* displays a very cell-specific and dynamic profile during cerebellar development.

**ActivinB induces PMEPA1 expression and promotes cell cycle progression**

The TGF $\beta$ /Activin pathway is highly pleiotropic and sometimes displays antagonistic functions during carcinogenic processes. For example, it can promote either cell cycle arrest or proliferation, depending on the context. This opposite role has been well illustrated in Glioblastoma in which the epigenetic status of the cells, in particular its DNA methylation profile, is responsible for this duality (Bruna *et al*, 2007). In agreement with this pro-mitogenic activity, we found that pathway inhibition decreased cell proliferation in Group 3 MB, while ActivinB stimulation increased it by consistently promoting cell cycle progression. *MYC* and *OTX2*, two genes known to promote cell proliferation in Group 3 MB, are target genes of the Smad2/3 pathway in other contexts (Jia *et al*, 2009; Brown *et al*, 2011; Coda *et al*, 2017). In general, this signaling pathway reduces *MYC* expression (Warner *et al*, 1999; Seoane *et al*, 2001), although it can be induced in human embryonic stem cells (Brown *et al*, 2011). Since *OTX2* has been demonstrated to be a major Smad2/3 target gene in the nervous system (Jia *et al*, 2009), it has been proposed to be a Smad2/3 inducible gene in Group 3 MB (Ferrucci *et al*, 2018) and considered as part of this signaling pathway in MB (Northcott *et al*, 2012b). We did not detect any consistent changes in *MYC* and *OTX2* expression upon modulation of the Activin pathway, suggesting that this signaling pathway does not regulate these two genes in Group 3 tumors and promotes tumor growth through other

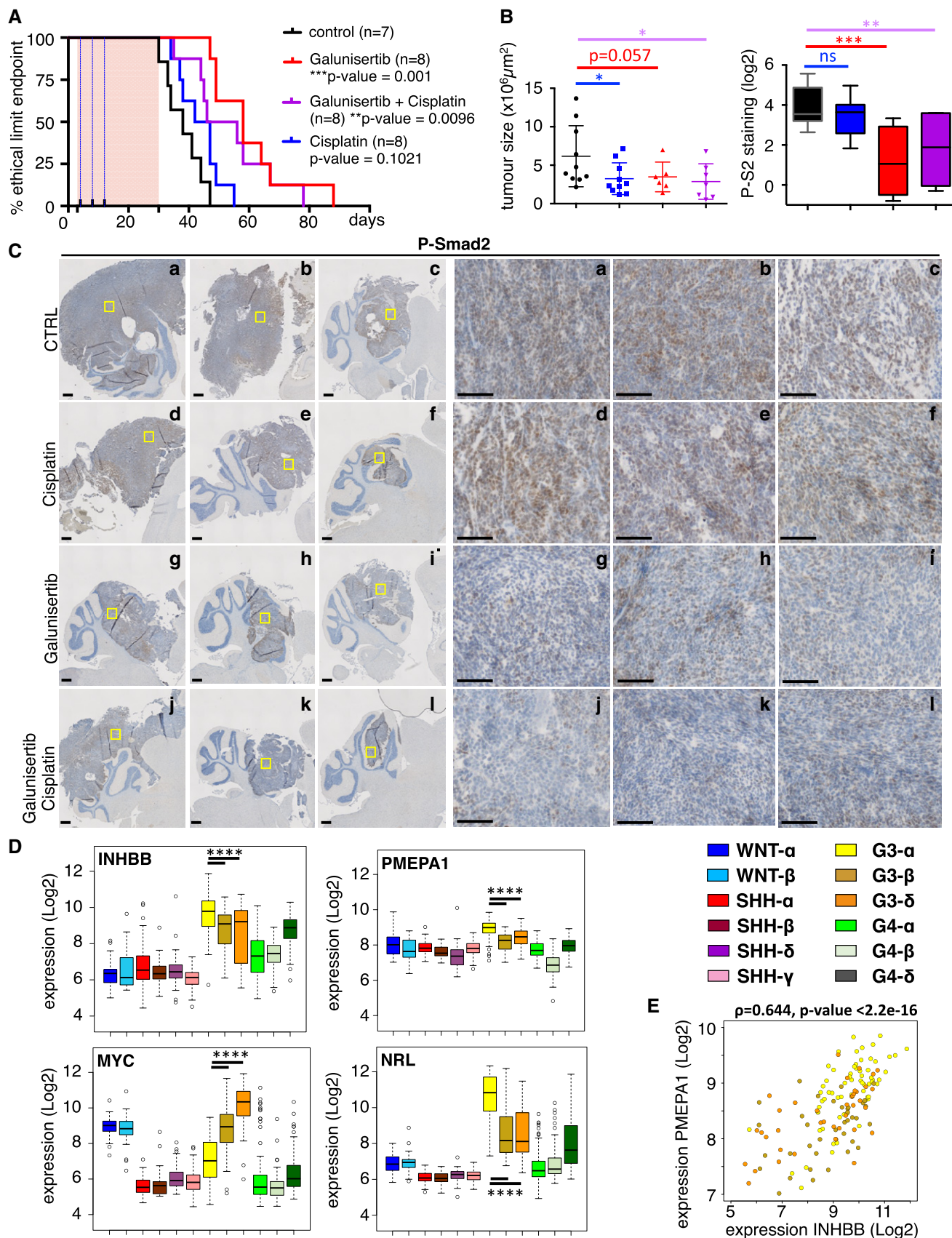


Figure 7.

**Figure 7. ActivinB signaling is a potential therapeutic target for patients of group 3 MB.**

- A Kaplan–Meier representing survival of mice treated with either vehicle (black) or Galunisertib (LY2157299, red) or Cisplatin (blue) or a combination of Galunisertib and Cisplatin (purple) after orthotopic grafting of PDX4 cells into the cerebellum. The pink rectangle represents Galunisertib treatment duration, while the blue dotted lines represent the 3 Cisplatin administrations.
- B Boxplot of tumor area after 25 days of treatment. On the right, boxplots represent quantification of P-Smad2 staining on tumor (IHC). The code color is similar to panel (A).
- C P-Smad2 staining by IHC in 3 representative tumors per group after 25 days of treatment. The scale bars represent 500 and 100  $\mu\text{m}$  on the left and right panels, respectively.
- D Boxplots representing the expression level of *INHBB*, *PMEPA1*, *MYC*, and *NRL* in the different MB subtypes, as defined in Cavalli et al (2017a). Only *P*-values corresponding to comparisons between Group 3 subtypes are indicated. Detailed statistics are presented in Appendix Table S3. Patient samples are colored by subtypes as indicated.
- E Scatter plot of *INHBB* and *PMEPA1*, expression levels in Group 3 patient samples. Colored dots represent each patient sample, and colors represent the group 3 MB subtypes ( $\alpha$  in yellow,  $\beta$  in brown, and  $\delta$  in orange). Note that this panel is identical to that shown in Appendix Fig S3A (yellow) except for the color code.

Data information: Center lines show data median; box limits indicate the 25<sup>th</sup> and 75<sup>th</sup> percentiles; lower and upper whiskers extend 1.5 times the interquartile range (IQR) from the 25<sup>th</sup> and 75<sup>th</sup> percentiles, respectively (B and D). Squares represents individual tumor (B). Outliers are represented by individual points (D). The *P*-values were determined by log-rank (Mantel-Cox) test on panel (A) and unpaired *t*-test on panel (B). Wilcoxon rank-sum tests were performed for panel (D). Spearman's rank correlation coefficient  $\rho$  and *P*-value are indicated on panel E. \**P* < 0.05, \*\**P* < 0.01, \*\*\**P* < 0.001, and \*\*\*\**P* < 0.0001. Bars represent the mean  $\pm$  SD. Number of replicates is *n*  $\geq$  3. The exact *P*-values and number of replicates are indicated in Appendix Table S5.

mechanisms. In contrast, we showed that *PMEPA1*, whose expression is induced by TGF $\beta$  or Activin signaling in many different contexts (Coda et al, 2017), is also an Activin-regulated gene in Group 3 MB. Indeed, inhibition or activation of the Activin signaling pathway modulated *PMEPA1* expression accordingly. This regulation is likely to be relevant in patients since *INHBB* and *PMEPA1* expression is correlated in human MB samples. *PMEPA1* is the top correlated gene with *INHBB* within Group 3 MB, showing that their expression is strongly linked in this group. In all MB samples, the correlation is lower than within Group 3 samples. Indeed, *PMEPA1* expression is higher in Group 3 but reaches an intermediate level in WNT and SHH groups that do not express *INHBB*. In WNT and SHH groups, *PMEPA1* expression is likely due to TGF $\beta$ /Activin pathway activation, as highlighted by the high level of P-Smad2 found in patient samples in those two groups, although pathway activation is independent on ActivinB autocrine stimulation. Thus, *PMEPA1* expression likely constitutes a relevant and general readout of Smad2/3 activation, which is due to an ActivinB autocrine stimulation in Group 3 and to other mechanisms in SHH and WNT groups. The role of *PMEPA1* in cancer appears to be quite complex. It has been shown to act as negative auto-regulatory loop by limiting Smad2/3 activation (Watanabe et al, 2010) although this appears to be isoform dependent (Fournier et al, 2015). Other reports suggested that *PMEPA1* could promote cell proliferation in cancer cells (Vo Nguyen et al, 2014; Nie et al, 2016) and convert TGF $\beta$ /Activin signaling from a tumor suppressor to tumor promoting pathway (Singha et al, 2010). Although not excluding that *PMEPA1* may limit Smad2/3 activation in Group 3 MB without abolishing it, our results are in line with those latter reports. Indeed, siRNA-mediated *PMEPA1* downregulation decreased Group 3 cell proliferation showing that it is an important mediator of ActivinB promoting Group 3 MB growth.

#### Targeting the TGF $\beta$ /Activin pathway in Group 3 as a therapeutic perspective

We observed an activation of the Smad2 pathway in Group 3 cell lines, PDXs, and patient samples. However, this activation appears to be heterogeneous. For example, some cell lines and PDXs displayed a very high basal level of Smad2 activation, while others a much more moderate and this held true on patient samples. Since

different Group 3 subtypes have been described recently (Cavalli et al, 2017a; Northcott et al, 2017; Schwalbe et al, 2017), we investigated whether *INHBB* expression could be enriched in a given subtype. We observed that *INHBB* expression is higher in subtype Group 3 $\alpha$  according to the classification of Cavalli et al (2017a). This subtype is characterized by the lack of *MYC* amplification and, as shown in this study, an overall moderate to low *MYC* expression level. This subtype displays high photoreceptor gene expression (Cavalli et al, 2017a), including those of the two master regulators of this program, *NRL* and *CRX*. Accordingly, we recently showed that their expression defines a specific subtype within Group 3 (Garancher et al, 2018). Our data may suggest that the expression of *INHBB* could lead to Smad2/3 activation in this subtype. Indeed, we found that *PMEPA1*, whose expression can be considered as a readout of Smad2/3 activation (see above), is significantly higher in Group 3 $\alpha$  subtype as compared to other Group 3 subtypes. Moreover, its expression is tightly correlated to that of *INHBB* in the Group 3 tumors, suggesting that *INHBB* expression leads to productive pathway activation. In support to this, PDX4, which expresses very high level of *INHBB*, also displays very strong Smad2 activation. This PDX is not *MYC* amplified and highly expresses the photoreceptor genes (Garancher et al, 2018). It should be nevertheless mentioned that the 1603MED cell line is also characterized by high *INHBB* expression and high Smad2 activation but is *MYC* amplified and does not express high level of photoreceptor genes (Raso et al, 2008). Thus, we proposed that activation of the Smad2/3 pathway involving an Activin B autocrine stimulation is enriched in subtype Group 3 $\alpha$ , although not limited to this subtype. Interestingly, treatment with Galunisertib, whose toxicity and efficacy is currently tested in clinical trials for Glioblastoma patients, increased the survival of mice orthotopically grafted with PDX4. This suggests that Group 3 $\alpha$  patients may be particularly sensitive to pathway inhibition.

In conclusion, the TGF $\beta$ /Activin signaling is activated through an ActivinB autocrine mechanism in a subset of Group 3 MB subtype. Not only this pathway is activated, but it also plays a growth-promoting role and constitutes an important driver of therapeutic interest in these tumors. We propose that high levels of *INHBB*, *PMEPA1* expression, and Smad2 phosphorylation might constitute biomarkers for potential Group 3 patients to be eligible to Galunisertib treatment.

## Materials and Methods

### Bioinformatics analyses

Normalized primary medulloblastoma gene expression data (763 samples) and samples affiliation published in Cavalli *et al* (2017a) were used to generate scatter plots and gene expression boxplots per subgroup and subtype for the genes of interest. Normalized primary medulloblastoma protein levels data (45 samples) and samples affiliation published in Archer *et al* (2018a) were used to generate protein levels boxplots per subgroup and subtype for the proteins of interest. Wilcoxon rank-sum tests were performed between subgroups and subtypes. Spearman rank correlation coefficients were computed between the *INHBB* gene expression values and all other genes for Group 3 samples. The gene pairs were ranked according to the Spearman correlation values.

### Patient samples

All MB samples were collected following written informed consent, and study approval was obtained by internal review boards from the following institutions: the Necker Hospital for Sick Children (Paris, France) and the Hospital for Sick Children (Toronto, Canada) (Forget *et al*, 2018).

### Cell culture conditions and treatments

HD-MB03 (named HDMB03) obtained from Dr. Milde (Milde *et al*, 2012), D458MED (named D458) obtained from Dr. Bigner (He *et al*, 1991), UW228 (Keles *et al*, 1995), ONS-76, and DAOY MB cell lines (ATCC) were cultured as described in Garancher *et al* (2018). 1603MED obtained from Dr. Raso (Raso *et al*, 2008) and D283MED (ATCC) (named D283) cell lines were maintained in DMEM condition supplemented with 12% fetal bovine serum (GIBCO), 50 units/ml penicillin and streptomycin (Invitrogen) and 0.1 mM non-essential amino acids and sodium pyruvate. 1603MED cell lines were also supplemented with 2 mM L-glutamine. All cells were cultured at 37°C in a humidified atmosphere containing 5% CO<sub>2</sub>. LY363947 and SB431532 resuspended in DMSO (selleckchem) were used at a final concentration of 5 μM for 24 h. Stimulations with TGFB1 and ActivinB were performed for 1 or 24 h at 10 ng/ml. Inhibitions with a recombinant blocking antibody against ActivinB (R&D systems) or recombinant follistatin (R&D systems) were performed for 24 h at 5 and 0.2 μg/ml, respectively.

### Growth curves and proliferation assays

For growth curve analyses, 1603MED cells were plated at  $8 \times 10^5$  cells/ml, and D283 and D458 at  $2.5 \times 10^5$  cells/ml. Cell were treated once at day 0. Number of viable cells was assessed as indicated in each figure. For D283 and D458, proliferation was monitored using Incucyte Proliferation Assay (Essen bioscience) by analyzing the surface occupied by cells (% confluence).

### Conditioned media experiments

Receiving cells (HDMB03) were plated at  $1.5 \times 10^5$  cells/well in 6-wells plates. 1603MED and HDMB03 conditioned media were

obtained by 18 h of incubation at  $1 \times 10^6$  cells/ml. Non-conditioned media was obtained in the same conditions in absence of cells. Media were collected, filtered, and incubated with PBS as control or blocking antibody against ActivinB (5 μg/ml) for 2 h at 4°C with rotation. Cells were treated with 1 ml of media for 1 h, and cell extracts were collected for WB analysis.

### Western Blotting and antibodies

Cell extracts were obtained and WB analyses performed as described in Rocques *et al* (2007). Membranes were incubated at 4°C overnight with anti-Smad2 (CST, CS86F7, 1/1,000), anti-PhosphoSmad2 (CST, CS138D4, 1/1,000), anti-OTX2 (MerckMillipore, #AB9566, 1/10,000), anti-MYC (CST, CSD3N8F, 1/1,000), anti-PMEPA1 (proteintech, 1/500), and anti-β-Actin (Sigma A1978, 1/5,000). Signals were acquired with a CCD camera (G/BOX, Syngene). All the P-Smad2/Total Smad2 normalizations for the relevant blots are provided in Appendix Fig S5.

### Real time RT-PCR

All experiments were performed according to the protocols described in Garancher *et al* (2018). Oligonucleotides used in this study are described in Appendix Table S4.

### siRNA and transfection assays

Transfection assays were performed in either 96- or 6-well plates. siRNA transfection was performed according to the manufacturer's instructions (Dharmacon). DharmaFECT 3 transfection reagent was used at 0.15 and 4 μl/100 μl of transfection medium for D283 and 1603MED cell lines, respectively. D283 cells were plated at  $5 \times 10^5$  cells/ml and siRNA were used at a final concentration of 25 nM. 1603MED cells were plated at a concentration of  $1 \times 10^6$  cells/ml with 10 μM final of siRNA. Transfection assay efficiency was assessed using siGlo (D001630-01-05). siRNA smartpool CTRL (D-001810-00-1005), smartpool INHBB (L-011702-00-0010), smartpool PMEPA1 (L-010501-00-0020), ON-TARGETplus individual siRNA PMEPA1#1 (L-010501-05), and PMEPA1#2 (L-010501-08) were purchased from Dharmacon. For rescue experiments, cells were stimulated 10 h after transfection with ActivinB at 10 ng/ml.

### Apoptosis and cell cycle analyses by flow cytometry

1603MED and D283 cell lines were plated at  $8 \times 10^5$  and  $2.5 \times 10^5$  cell/ml, respectively. Apoptosis was assessed at day 2 using cleaved caspase-3 staining with Apoptosis Kit, APC (BD Bioscience). Cell cycle was analyzed at day 2 using APC BrdU flow Kit (BD Bioscience). Experiments were performed using FACS Kanto (BD Bioscience) and analyzed with FlowJo software (Tree Star).

### Patient derived xenografts and PDX cultures

PDXs were obtained, maintained, dissociated, and cultured as described in Garancher *et al* (2018). PDX3, PDX4, and PDX7 correspond to ICN-MB-PDX-3, ICN-MB-PDX-4, and ICN-MB-PDX-7, respectively. All *in vitro* treatments were performed as described for cell lines.

## Animal experimentation

NMRI-nu immunodeficient mice were obtained from Janvier Laboratory. Experiments were performed on 7–8 weeks old female mice after 1 week of acclimation in animal facility of Curie Institute. Mice were housed under a controlled temperature and 12 h/12 h light–dark cycle with access to food and water *ad libitum* in conventional animal facility. For the animal welfare, mice are maintained in social groups with enrichment. Animal care and use for this study were performed in accordance with the recommendations of the European Community (2010/63/UE) for the care and use of laboratory animals. Experimental procedures were specifically approved by the ethics committee of the Institut Curie CEEA-IC #118 (Authorization 02383.02 given by National Authority) in compliance with the international guidelines.

## Orthotopic transplantation and pharmacological inhibitor treatments

NMRI Nude female mice (Janvier labs) were orthotopically grafted directly in the cerebellum at 7 weeks with  $3 \times 10^5$  cells/5  $\mu$ l of ICN-MB-PDX-4 cells as described in Garancher *et al* (2018). After 3 days, mice were administrated 300  $\mu$ l of LY2157299 (Galunisertib, AbMole Bioscience) orally at a dose of 75 mg/kg in 12% DMSO, 30% PEG, and water. Mice were treated 7 days a week twice a day until day 30. Mice were injected with Cisplatin (Sigma) in saline solution at a dose of 2 mg/kg intraperitoneally at days 4, 8, and 12 post-grafting. Mice were euthanized when scientific and clinical end points were reached and brains were collected and fixed.

## Tissue processing and immunohistochemistry (IHC)

After 25 days of treatment, 6 mice per group received ice-cold PBS and 4% formaldehyde/PBS via intracardiac perfusions. Brains were collected and fixed overnight in 4% formaldehyde/PBS at 4°C. IHC was performed on 12- $\mu$ m-thick sections with the following primary antibodies: anti-PhosphoSmad2 (CST, CS138D4, 1/300), Ki67 (CST, CS9161, 1/500), and cleaved caspase-3 (eBioscience, #14-5698-82, 1/500). Image acquisitions were performed on a Zeiss microscope. Tumor size and IHC staining were assessed using ImageJ software.

## Quantification and statistical analyses

Western blot was quantified from digital data acquisition (CCD camera) using ImageJ software. Statistical details can be found in both figures and figure legends. A  $P \leq 0.05$  is considered as significant. IHC quantifications were assessed using ImageJ software. All experiments were performed, at least, in three independent triplicates. Statistical analyses are provided in Appendix Table S1 (Statistics related to Figs 1B and 5B and C, and EV1B), Appendix Table S2 (Statistics related to Figs 1D and 6B, and EV1D and Appendix Fig S4A), and Appendix Table S3 (Statistics related to Figs 7D and E, and 6B, and Appendix Fig S3A). The exact  $P$ -values and number of replicates for each experiment are indicated in Appendix Table S5.

**Expanded View** for this article is available online.

## The paper explained

### Problem

Medulloblastoma (MB) is a pediatric tumor of the cerebellum arising at a median age of 7 years. The current treatment associates surgery, radiotherapy, and chemotherapy and has allowed reaching an overall survival of 70–80%. MB is a heterogeneous disease classified in four groups, with the poorly characterized Group 3 showing the worst prognosis. Few recurrent genomic alterations have been identified at low frequency, and at the transcriptional level, Group 3 is known to express MYC and photoreceptor genes. While highly problematic at the clinical level, neither specific nor targeted therapy has been identified for this specific Group.

### Results

We show that a subset of Group 3 MBs displays activation of the TGF $\beta$ /Activin pathway. In contrast to carcinomas where TGF $\beta$ s are the main driver of activation of this pathway, our data established that this activation is mainly due to an autocrine stimulation involving ActivinB. We identify a subset of Group 3 tumors in which this mechanism is at play. These tumors express high levels of *INHBB* (encoding ActivinB) and display high expression of *PMEPA1*, a well-known target gene of this signaling pathway. Functionally, the pathway sustains cell proliferation by inducing the expression of *PMEPA1*. Importantly, treatment with Galunisertib, an inhibitor of this pathway currently tested in clinical trials for Glioblastoma patients, increases the survival of mice orthotopically grafted with Group 3 MB-PDX.

### Impact

TGF $\beta$ /Activin signaling plays a driving role in a subset of Group 3 MBs. We propose that high level of Smad2 phosphorylation, high *INHBB*, and high expression of *PMEPA1* could represent valuable biomarkers for identifying patients who will be particularly eligible to Galunisertib treatment.

## Acknowledgements

We thank members of our laboratory for helpful advice and comments, C. Lasgi for her assistance in FACS analyses, C. Alberti and E. Belloir at the Institut Curie mouse facilities. The authors greatly acknowledge Cédric Messaoudi from Institut Curie UMR9187/UJ1196 and Laetitia Besse from the PICT-IBISA Imaging Facility for useful advices on image processing. We also thank Drs. D. Bigner, J.R. Silber, and T. Milde for providing us with materials. This work was funded by grants from Ligue Nationale Contre le Cancer (Essonne-Oise-Yvelines #M18759, #M16649, and Legs Choivet), Institut National du Cancer (INCa, Pair Pédiatrie, Mr ROBOT), the IRS “NanoTheRad” of University U-PSUD (Paris-Saclay), and ADAM-Cancer (Association D'enfants Atteints de Médulloblastome). AG, LMO, and MM were supported by a fellowship from the Ministère Français de l'Enseignement Supérieur, de la Recherche et de l'Innovation, and Fondation ARC (4th year PhD fellowship).

## Author contributions

Conceptualization: CP and MM. Methodology: CP, MM, FMGC, AF, SD, AG, FB, and AE. Investigation: MM, ML, FMGC, CF, MA, AF, LM-O, SD, AG, AD, and SL. Supervision: CP, FB, and AE. Resources: CP, FD, MDT, SP, OA, FB, JM-P, OD, AR, and AE. Writing—Original draft: CP, AE, and MM. Writing—Review & Editing: CP, AE, MM, and SD. Funding acquisition: CP, FB, and AE.

## Conflict of interest

The authors declare that they have no conflict of interest.

## For more information

Website team:

(i) <https://science.institut-curie.org/research/biology-chemistry-of-radiations-cell-signaling-and-cancer-axis/umr-3347-normal-and-pathological-signaling/team-eychene-pouponnot/>

*In situ* Hybridization data on the mouse developing brain can be found:

(i) <http://developingmouse.brain-map.org/>

Public Transcriptomic analysis of MB samples (R2):

(i) [https://hgserver1.amc.nl/cgi-bin/r2/main.cgi?&dscope=MB500&option=ab\\_out\\_dscope](https://hgserver1.amc.nl/cgi-bin/r2/main.cgi?&dscope=MB500&option=ab_out_dscope)

(ii) <https://hgserver1.amc.nl/cgi-bin/r2/main.cgi>

Public Proteomic analysis of MB samples:

(i) <https://medullo.shinyapps.io/archer2018/>

## References

- Anido J, Sáez-Borderías A, González-Juncà A, Rodón L, Folch G, Carmona MA, Prieto-Sánchez RM, Barba I, Martínez-Sáez E, Prudkin L *et al* (2010) TGF- $\beta$  receptor inhibitors target the CD44(high)/Id1(high) glioma-initiating cell population in human glioblastoma. *Cancer Cell* 18: 655–668
- Antsiferova M, Werner S (2012) The bright and the dark sides of activin in wound healing and cancer. *J Cell Sci* 125: 3929–3937
- Archer TC, Ehrenberger T, Mundt F, Gold MP, Krug K, Mah CK, Mahoney EL, Daniel CJ, LeNail A, Ramamoorthy D *et al* (2018a) Proteomics, post-translational modifications, and integrative analyses reveal molecular heterogeneity within medulloblastoma subgroups. *Cancer Cell* 34: 396–410.e8
- Archer TC, Ehrenberger T, Mundt F, Gold MP, Krug K, Mah CK, Mahoney EL, Daniel CJ, LeNail A, Ramamoorthy D *et al* (2018b). MassIVE: MSV000082644 (<https://massive.ucsd.edu/ProteoSAFe/dataset.jsp?accession=MSV000082644>) [DATASET]
- Brown S, Teo A, Pauklin S, Hannan N, Cho CH-H, Lim B, Vardy L, Dunn NR, Trotter M, Pedersen R *et al* (2011) Activin/Nodal signaling controls divergent transcriptional networks in human embryonic stem cells and in endoderm progenitors. *Stem Cells* 29: 1176–1185
- Bruna A, Darken RS, Rojo F, Ocaña A, Peñuelas S, Arias A, Paris R, Tortosa A, Mora J, Baselga J *et al* (2007) High TGF $\beta$ -Smad activity confers poor prognosis in glioma patients and promotes cell proliferation depending on the methylation of the PDGF-B gene. *Cancer Cell* 11: 147–160
- Cavalli FMG, Remke M, Rampasek L, Peacock J, Shih DJH, Luu B, Garzia L, Torchia J, Nor C, Morrissy AS *et al* (2017a) Intertumoral heterogeneity within medulloblastoma subgroups. *Cancer Cell* 31: 737–754.e6
- Cavalli FMG, Remke M, Rampasek L, Peacock J, Shih DJH, Luu B, Garzia L, Torchia J, Nor C, Morrissy AS *et al* (2017b). Gene Expression Omnibus GSE85218 (<https://www.ncbi.nlm.nih.gov/geo/query/acc.cgi?acc=GSE85218>). [DATASET]
- Chen Y-G, Lui HM, Lin S-L, Lee JM, Ying S-Y (2002) Regulation of cell proliferation, apoptosis, and carcinogenesis by activin. *Exp Biol Med* 227: 75–87
- Cho Y-J, Tsherniak A, Tamayo P, Santagata S, Ligon A, Greulich H, Berhoukim R, Amani V, Goumnerova L, Eberhart CG *et al* (2011) Integrative genomic analysis of medulloblastoma identifies a molecular subgroup that drives poor clinical outcome. *J Clin Oncol Off J Am Soc Clin Oncol* 29: 1424–1430
- Coda DM, Gaarenstroom T, East P, Patel H, Miller DSJ, Lobley A, Matthews N, Stewart A, Hill CS (2017) Distinct modes of SMAD2 chromatin binding and remodeling shape the transcriptional response to NODAL/Activin signaling. *Elife* 6: e22474
- Ferrucci V, de Antonellis P, Pennino FP, Asadzadeh F, Virgilio A, Montanaro D, Galeone A, Boffa I, Pisano I, Scognamiglio I *et al* (2018) Metastatic group 3 medulloblastoma is driven by PRUNE1 targeting NME1-TGF- $\beta$ -OTX2-SNAI1 via PTEN inhibition. *Brain J Neurol* 141: 1300–1319
- Forget A, Martignetti L, Puget S, Calzone L, Brabetz S, Picard D, Montagud A, Liva S, Sta A, Dingli F *et al* (2018) Aberrant ERBB4-SRC signaling as a hallmark of group 4 medulloblastoma revealed by integrative phosphoproteomic profiling. *Cancer Cell* 34: 379–395.e7
- Fournier PGJ, Juárez P, Jiang G, Clines GA, Niewolna M, Kim HS, Walton HW, Peng XH, Liu Y, Mohammad KS *et al* (2015) The TGF- $\beta$  signaling regulator PMEPA1 suppresses prostate cancer metastases to bone. *Cancer Cell* 27: 809–821
- Garancher A, Lin CY, Morabito M, Richer W, Rocques N, Larcher M, Bihannic L, Smith K, Miquel C, Leboucher S *et al* (2018) NRL and CRX define photoreceptor identity and reveal subgroup-specific dependencies in medulloblastoma. *Cancer Cell* 33: 435–449.e6
- He XM, Wikstrand CJ, Friedman HS, Bigner SH, Pleasure S, Trojanowski JQ, Bigner DD (1991) Differentiation characteristics of newly established medulloblastoma cell lines (D384 Med, D425 Med, and D458 Med) and their transplantable xenografts. *Lab Invest J Tech Methods Pathol* 64: 833–843
- Holgado BL, Guerreiro Stucklin A, Garzia L, Daniels C, Taylor MD (2017) Tailoring medulloblastoma treatment through genomics: making a change, one subgroup at a time. *Annu Rev Genomics Hum Genet* 18: 143–166
- Jia S, Wu D, Xing C, Meng A (2009) Smad2/3 activities are required for induction and patterning of the neuroectoderm in zebrafish. *Dev Biol* 333: 273–284
- Kawauchi D, Robinson G, Uziel T, Gibson P, Rehg J, Gao C, Finkelstein D, Qu C, Pounds S, Ellison DW *et al* (2012) A mouse model of the most aggressive subgroup of human medulloblastoma. *Cancer Cell* 21: 168–180
- Keles GE, Berger MS, Srinivasan J, Kolstoe DD, Bobola MS, Silber JR (1995) Establishment and characterization of four human medulloblastoma-derived cell lines. *Oncol Res* 7: 493–503
- Kool M, Koster J, Bunt J, Hasselt NE, Lakeman A, van Sluis P, Troost D, Meeteren NS, Caron HN, Cloos J *et al* (2008) Integrated genomics identifies five medulloblastoma subtypes with distinct genetic profiles, pathway signatures and clinicopathological features. *PLoS ONE* 3: e3088
- Levy L, Hill CS (2006) Alterations in components of the TGF- $\beta$  superfamily signaling pathways in human cancer. *Cytokine Growth Factor Rev* 17: 41–58
- Lin CY, Erkek S, Tong Y, Yin L, Federation AJ, Zapatka M, Haldipur P, Kawauchi D, Risch T, Warnatz H-J *et al* (2016) Active medulloblastoma enhancers reveal subgroup-specific cellular origins. *Nature* 530: 57–62
- Liu R, Zhou Z, Huang J, Chen C (2011) PMEPA1 promotes androgen receptor-negative prostate cell proliferation through suppressing the Smad3/4-c-Myc-p21 Cip1 signaling pathway. *J Pathol* 223: 683–694
- Lonardo E, Hermann PC, Mueller M-T, Huber S, Balic A, Miranda-Lorenzo I, Zagorac S, Alcalá S, Rodríguez-Arabaola I, Ramirez JC *et al* (2011) Nodal/Activin signaling drives self-renewal and tumorigenicity of pancreatic cancer stem cells and provides a target for combined drug therapy. *Cell Stem Cell* 9: 433–446
- Marino FE, Risbridger G, Gold E (2013) The therapeutic potential of blocking the activin signalling pathway. *Cytokine Growth Factor Rev* 24: 477–484
- Martin AM, Raabe E, Eberhart C, Cohen KJ (2014) Management of pediatric and adult patients with medulloblastoma. *Curr Treat Options Oncol* 15: 581–594
- Massagué J (2008) TGF $\beta$  in cancer. *Cell* 134: 215–230

- Matzuk MM, Finegold MJ, Mather JP, Krummen L, Lu H, Bradley A (1994) Development of cancer cachexia-like syndrome and adrenal tumors in inhibin-deficient mice. *Proc Natl Acad Sci USA* 91: 8817–8821
- Milde T, Lodrini M, Savellyeva L, Korshunov A, Kool M, Brueckner LM, Antunes ASLM, Oehme I, Pekrun A, Pfister SM et al (2012) HD-MB03 is a novel Group 3 medulloblastoma model demonstrating sensitivity to histone deacetylase inhibitor treatment. *J Neurooncol* 110: 335–348
- Nie Z, Wang C, Zhou Z, Chen C, Liu R, Wang D (2016) Transforming growth factor-beta increases breast cancer stem cell population partially through upregulating PMEPA1 expression. *Acta Biochim Biophys Sin* 48: 194–201
- Niklison-Chirou MV, Erngren I, Engskog M, Haglöf J, Picard D, Remke M, McPolin PHR, Selby M, Williamson D, Clifford SC et al (2017) TAp73 is a marker of glutamine addiction in medulloblastoma. *Genes Dev* 31: 1738–1753
- Northcott PA, Korshunov A, Pfister SM, Taylor MD (2012a) The clinical implications of medulloblastoma subgroups. *Nat Rev Neurol* 8: 340–351
- Northcott PA, Shih DJH, Peacock J, Garzia L, Morrissy AS, Zichner T, Stütz AM, Korshunov A, Reimand J, Schumacher SE et al (2012b) Subgroup-specific structural variation across 1,000 medulloblastoma genomes. *Nature* 488: 49–56
- Northcott PA, Lee C, Zichner T, Stütz AM, Erkek S, Kawauchi D, Shih DJH, Hovestadt V, Zapatka M, Sturm D et al (2014) Enhancer hijacking activates GFI1 family oncogenes in medulloblastoma. *Nature* 511: 428–434
- Northcott PA, Buchhalter I, Morrissy AS, Hovestadt V, Weischenfeldt J, Ehrenberger T, Gröbner S, Segura-Wang M, Zichner T, Rudneva VA et al (2017) The whole-genome landscape of medulloblastoma subtypes. *Nature* 547: 311–317
- Pei Y, Moore CE, Wang J, Tewari AK, Eroshkin A, Cho Y-J, Witt H, Korshunov A, Read T-A, Sun JL et al (2012) An animal model of MYC-driven medulloblastoma. *Cancer Cell* 21: 155–167
- Peñuelas S, Anido J, Prieto-Sánchez RM, Folch G, Barba I, Cuartas I, García-Dorado D, Poca MA, Sahuquillo J, Baselga J et al (2009) TGF-beta increases glioma-initiating cell self-renewal through the induction of LIF in human glioblastoma. *Cancer Cell* 15: 315–327
- Raso A, Negri F, Gregorio A, Nozza P, Mascelli S, De Marco P, Merello E, Milanaccio C, Ravegnani M, Cama A et al (2008) Successful isolation and long-term establishment of a cell line with stem cell-like features from an anaplastic medulloblastoma. *Neuropathol Appl Neurobiol* 34: 306–315
- Ripoche D, Charbord J, Hennino A, Teinturier R, Bonnavaion R, Jaafar R, Goehrig D, Cordier-Bussat M, Ritvos O, Zhang CX et al (2015) ActivinB is induced in insulinoma to promote tumor plasticity through a  $\beta$ -cell-induced dedifferentiation. *Mol Cell Biol* 36: 756–764
- Rocques N, Abou Zeid N, Sii-Felice K, Lecoin L, Felder-Schmittbuhl MP, Eychene A, Pouponnot C (2007) GSK-3-mediated phosphorylation enhances Maf-transforming activity. *Mol Cell* 28: 584–597
- Rodón L, González-Juncà A, del Inda M, Sala-Hojman A, Martínez-Sáez E, Seoane J (2014) Active CREB1 promotes a malignant TGF $\beta$ 2 autocrine loop in glioblastoma. *Cancer Discov* 4: 1230–1241
- Ross S, Hill CS (2008) How the Smads regulate transcription. *Int J Biochem Cell Biol* 40: 383–408
- Santhana Kumar K, Neve A, Guerreiro Stucklin AS, Kuzan-Fischer CM, Rushing EJ, Taylor MD, Tripolitsioti D, Behrmann L, Kirschenbaum D, Grotzer MA et al (2018) TGF- $\beta$  determines the pro-migratory potential of bFGF signaling in medulloblastoma. *Cell Rep* 23: 3798–3812.e8
- Schwalbe EC, Lindsey JC, Nakjang S, Crosier S, Smith AJ, Hicks D, Rafiee G, Hill RM, Iliasova A, Stone T et al (2017) Novel molecular subgroups for clinical classification and outcome prediction in childhood medulloblastoma: a cohort study. *Lancet Oncol* 18: 958–971
- Seoane J, Pouponnot C, Staller P, Schader M, Eilers M, Massagué J (2001) TGFbeta influences Myc, Miz-1 and Smad to control the CDK inhibitor p15INK4b. *Nat Cell Biol* 3: 400–408
- Seoane J, Gomis RR (2017) TGF- $\beta$  family signaling in tumor suppression and cancer progression. *Cold Spring Harb Perspect Biol* 9: a022277
- Singha PK, Yeh I-T, Venkatachalam MA, Saikumar P (2010) Transforming growth factor-beta (TGF-beta)-inducible gene TMEPA1 converts TGF-beta from a tumor suppressor to a tumor promoter in breast cancer. *Cancer Res* 70: 6377–6383
- Taylor MD, Northcott PA, Korshunov A, Remke M, Cho Y-J, Clifford SC, Eberhart CG, Parsons DW, Rutkowski S, Gajjar A et al (2012) Molecular subgroups of medulloblastoma: the current consensus. *Acta Neuropathol* 123: 465–472
- Vassalli A, Matzuk MM, Gardner HA, Lee KF, Jaenisch R (1994) Activin/inhibin beta B subunit gene disruption leads to defects in eyelid development and female reproduction. *Genes Dev* 8: 414–427
- Vo Nguyen TT, Watanabe Y, Shiba A, Noguchi M, Itoh S, Kato M (2014) TMEPA1/PMEPA1 enhances tumorigenic activities in lung cancer cells. *Cancer Sci* 105: 334–341
- Wakefield LM, Hill CS (2013) Beyond TGF $\beta$ : roles of other TGF $\beta$  superfamily members in cancer. *Nat Rev Cancer* 13: 328–341
- Wang J, Garancher A, Ramaswamy V, Wechsler-Reya RJ (2018) Medulloblastoma: from molecular subgroups to molecular targeted therapies. *Annu Rev Neurosci* 41: 207–232
- Warner BJ, Blain SW, Seoane J, Massagué J (1999) Myc downregulation by transforming growth factor beta required for activation of the p15(Ink4b) G(1) arrest pathway. *Mol Cell Biol* 19: 5913–5922
- Watanabe Y, Itoh S, Goto T, Ohnishi E, Inamitsu M, Itoh F, Satoh K, Wiercinska E, Yang W, Shi L et al (2010) TMEPA1, a transmembrane TGF-beta-inducible protein, sequesters Smad proteins from active participation in TGF-beta signaling. *Mol Cell* 37: 123–134
- Wu MY, Hill CS (2009) Tgf-beta superfamily signaling in embryonic development and homeostasis. *Dev Cell* 16: 329–343
- Yan X, Xiong X, Chen Y-G (2018) Feedback regulation of TGF- $\beta$  signaling. *Acta Biochim Biophys Sin* 50: 37–50



**License:** This is an open access article under the terms of the Creative Commons Attribution 4.0 License, which permits use, distribution and reproduction in any medium, provided the original work is properly cited.